

**Crack Development and Acoustic Emission Studies  
in Potash Rock Loaded Under Uniaxial Compression**

by

Vincent William Mlakar, B.Sc.

Department of Mining and Metallurgical Engineering  
McGill University  
Montreal

March, 1992

A Thesis submitted to the Faculty of Graduate studies and Research in partial fulfillment of the requirements of the degree of Masters of Science



McGill

McGill University  
Department of Earth and Planetary Sciences  
380 University Street  
Montreal, Quebec H3T 2G4

Journal of Applied Geophysics  
Volume 50, Number 1, 1999

Montreal, March 10th 1999

The title above is hereby accepted for publication by the *Journal of Applied Geophysics*.

Acoustic Emission and Crack Development in Potash Rock

Mr. Vincent Mlakar  
McGill University  
Department of Mining and Metallurgical Engineering

June 2nd 1992, Montreal

To whom it may concern,

Please note that there is an error in the pagination / format on page 54 and page 55 of the manuscript. Both of the figures on these pages should be on the same page.

## Table of Contents

Abstract .....	i
Acknowledgements .....	ii
INTRODUCTION .....	1
1.1 Statement of the Problem .....	1
Petrology of Saline Rocks .....	3
2.1 Introduction .....	3
2.2 Mineralogical Components of Potash Rock .....	4
2.3 Identification and Characterization of Mineralogical Components Derived from Potash Rock .....	4
2.4 Mineralogy of Potash Rock .....	5
2.4.1 Halite .....	5
2.4.2 $\alpha$ Halite .....	6
2.4.3 $\beta$ Halite .....	6
2.4.4 Rimmed Sylvite .....	6
2.4.5 Red Rimless Sylvite .....	7
2.4.6 Insoluble Minerals and Substances .....	8
2.5 Textures .....	8
2.6 Principle Rock Types .....	10
2.6.1 Type "A" Potash Rock .....	10
2.6.2 Type "B" Potash Rock .....	11
2.6.3 Type "C" Potash Rock .....	12
2.6.4 Type "D" Potash Rock .....	13
2.7 Summary and Conclusion .....	14
Review of Methodology .....	30
3.1 Basic Measurement Techniques .....	30
3.2 Grain Size Measurements .....	32
3.3 Grain and Grain Boundary Density .....	33
3.4 Microstructural Anisotropy .....	33
3.5 Grain Matrix Relationships .....	34
3.6 Literature Review of Studies Relating Rock Texture and Composi- tion to Mechanical and Acoustic Emission Parameters .....	35
3.6.1 Grain Size and Grain Density .....	35
3.6.2 Grain Shape and Degree of Interlocking .....	35
3.6.3 Mineral Components .....	36
3.6.4 Grain Boundary Density .....	36
3.6.5 Textural Models .....	36
3.7 Analytical Results from Textural and Compositional Derived from Potash Rock .....	36
3.7.1 Average Grain Cross Section and Textural Homogeneity .....	36
3.7.2 Structural Interlocking .....	37
3.7.3 Textural Anisotropy .....	37
3.7.4 Mineral Composition .....	37
Uniaxial Compression Testing of Rock Under Laboratory Testing Condi- tions .....	36
4.1 Introduction .....	36
4.2 Review of Experimental Compression Testing of Rock Specimens .....	36
4.2.1 General Overview .....	36
4.2.2 Uniaxial Compression Testing .....	37
4.2.3 Influence of the Testing Machine Stiffness .....	38
4.2.4 Deformation of Rock .....	39
4.2.5 Determination of Elastic Constants .....	40

4.3 Factors Affecting the Stress-Strain Curves .....	42
4.3.1 Sample Geometry and Microstructure .....	42
4.3.2 Height to Diameter Ratio .....	42
4.3.3 The Effect of Grain Size .....	43
4.3.4 Platen Conditions .....	43
4.3.5 The Effect of Loading Rate .....	44
4.3.6 The Effect of Moisture and Humidity .....	44
4.3.7 Mineral Components and Texture Effects in Relation to the Mechanical Behavior of Evaporites .....	45
4.4 Elastic Plastic Transition .....	45
Laboratory Analysis of Acoustic Emission .....	56
5.1 Introduction .....	56
5.3 Signal Characteristics .....	58
5.3.1 Introduction .....	58
5.3.2 Summary and Representation of Acoustic Emission Parameters .....	58
5.4 Literature Review of Laboratory Studies of Acoustic Emission .....	59
5.4.1 Effects of Stress Level and Associated Acoustic Emission Trends Observed in Laboratory Testing Conditions .....	59
5.4.2 Acoustic Emission Trends Observed under Uniaxial Compressive Load .....	60
5.4.3 Acoustic Emission Trends Observed under Uniaxial Compressive Load With Respect to Other Physical Test Variables .....	62
5.4.4 Investigations into the Causes and Nature of Acoustic Emission .....	63
5.4.5 Acoustic Emission Studies in Relation to Strain .....	65
5.4.6 Acoustic Emission Response with Respect to Grain Size, Sample Size and Composition .....	68
5.4.7 Laboratory Studies and Application of Acoustic Emission Amplitude .....	69
5.4.7.1 The b-Value Parameter .....	70
5.4.7.2 The Time-Amplitude Statistical Method of Analysis of Acoustic Emission .....	74
5.4.7.3 The Amplitude Ratio Parameter .....	75
5.4.8 Acoustic Emissions Energy .....	76
5.4.9 Energy Parameters .....	76
5.5 Summary .....	78
Mechanisms of Brittle Fracture in Rocks .....	84
6.1 Introduction .....	84
6.2 Observation Techniques .....	84
6.3 Initial Microstructure .....	84
6.4 Basic Principles of Fracture Mechanics .....	86
6.5 Mechanisms and progressive Development of Fracture in Accordance to the Stress Strain Curve .....	87
6.6 Crack Interaction and Propagation Studies on the Basis of Fractographic Technique .....	89
6.7 Experimental Deformation of Evaporites .....	93
Procedure of Petrographic, Fractographic and Acoustic Emission Analysis .....	98
7.1 Petrography .....	98
7.2 Texture Analysis .....	98
7.3 Sample Preparation .....	99
7.3.1 Sampling and Specimen Preparation .....	99
7.3.2 Preparatory Stage .....	99
7.3.3 Secondary Stage - Sampling for Load and Acoustic Emission Testing Program .....	99

7.3.4 Third Stage - Specimen Preparation for Petrographic and Petrofabric Studies .....	100
7.3.4.1 Preparation of the Initial Slab .....	100
7.3.4.2 Development of polished sections .....	101
7.3.4.3 Specimens for the Study of Stress Induced Cracks .....	101
7.4 Measurement Apparatus .....	102
7.4.1 Requirements to Perform Measurements .....	102
7.4.2 Equipment Calibration .....	102
7.4.3 Data Storage and Processing .....	103
7.5 Acoustic Emission Monitoring Equipment .....	103
7.5.1 Acoustic Emission Monitoring and Processing Apparatus .....	103
7.5.1.1 System Description .....	103
7.5.1.2 Transducer .....	104
7.5.1.3 Preamplifier .....	105
7.5.1.4 Cables .....	106
7.5.1.5 Mainframe - Data Processor System .....	106
7.5.2 System Configuration Procedure for Per-Channel Monitoring .....	107
The Relationship of Petrographic to Strength Parameters of Potash Rock .....	123
8.1 Introduction .....	123
8.2 Summary of Macroscopic Petrographic Characteristics of Potash Rock .....	123
8.3 The Stress Strain Behavior of Potash Rock Loaded Under Uniaxial Compression .....	125
8.4 Statistical Relationship Showing the Influence of Texture to the Strength of Potash Rock .....	126
8.4.1 Introduction .....	126
8.4.2 Summary of Method of Linear Multiple Regression Analysis .....	126
8.4.2.1 Determination of the Multiple Regression Equation .....	127
8.4.2.1.1 Results of the First Stage of the Statistical Analysis .....	128
8.4.2.2 The Test of Significance of Multiple Regression .....	128
8.4.2.2.1 Interpretation and Assessment .....	129
8.4.2.3 Multiple Correlation Coefficient ( $R_{y123}$ ) .....	129
8.4.2.3.1 Assessment of Results of the Multiple Correlation Coefficient .....	130
8.4.2.4 The Standard Errors and Test of Significance for Partial Regression Coefficients .....	130
8.4.3 The Standard Partial Regression Coefficient .....	132
8.5 Summary .....	133
Analysis of Acoustic Emission of Potash Rock .....	140
9.1 Introduction .....	140
9.2 Acoustic Emission Rate .....	140
9.2.1 General Observations .....	140
9.2.2 General Observations of Acoustic Emission Rate in Relation to Increasing Uniaxial Load .....	141
9.2.3 Acoustic Emission Rate in Relation to the Petrographic Characteristics of Potash Rock .....	141
9.2.4 Acoustic Emission Rate Associated with Type "A" Potash Rock .....	141
9.2.5 Acoustic Emission Rate Associated with Type "B" Potash Rock .....	142
9.2.6 Acoustic Emission Rate Associated with Type "C" Potash Rock .....	143
9.2.7 Acoustic Emission Rate Associated with Type "D" Potash Rock .....	143
9.2.8 Summary .....	144
9.2.9 Comparative Study and Interpretation .....	145

9.3 Correlation of Acoustic Emission Activity to Inelastic Deformation ....	146
9.3.1 Comparative Study and Interpretation .....	147
9.4 Acoustic Emission Amplitude Parameter .....	147
9.4.1 Amplitude Characteristics .....	147
9.4.2 Amplitude Event Frequency Spectra .....	148
9.4.3 Microstructural Influence on Acoustic Emission Amplitude Char- acteristics .....	148
9.4.4 The b-Value Parameter .....	149
9.4.4.1 Introduction .....	149
9.4.4.2 The Physical Significance of the b-value .....	149
9.4.4.3 Computation of the b-Value .....	150
9.4.4.4 Representation of Functions Utilized for b-Value Computation .....	150
9.4.4.4.1 The Gutenberg-Richter Relationship .....	150
9.4.4.4.2 The Normal Distribution Function .....	151
9.4.4.4.3 The Power Law Function .....	151
9.4.4.4.4 The Least Squares Fit .....	151
9.4.4.5 Interpretation of the b-Value .....	152
9.4.4.6 Discussion and Comparison .....	153
9.5 Amplitude Distribution Ratio .....	154
9.6 Acoustic Emission Energy Analysis .....	156
9.6.1 Energy Parameter Frequency Characteristics .....	156
9.6.2 Cumulative Energy Distribution .....	156
9.7 Statistical Correlation Between Time Difference and Peak Amplitude Signals .....	157
9.7.1 Method of Analysis .....	158
9.7.2 Summary of Analysis .....	158
9.7.3 Results from the Chi Distribution and Contingency Table Analysis .....	159
9.8 The Relationship between Amplitude and Energy with Event Dura- tion and Time Difference .....	161
9.8.1 Observations .....	162
9.8.1.1 Amplitude - Event Duration .....	162
9.8.1.2 Energy - Event Duration .....	162
9.8.1.3 Energy - Time Difference .....	162
9.8.2 Summary .....	163
Fractographic Analysis of Potash Rock Loaded Under Uniaxial Compres- sion .....	201
10.1 Introduction .....	201
10.2 Classification .....	201
10.3 Crack Classification .....	202
10.3.1 Stage 1a HARC - LARC .....	202
10.3.2 Stage 2a Intercrystalline LARC A and B .....	203
10.3.3 Stage 3a Intracrystalline LARC and Stage 3a Transgranular A, B, and C Crack .....	205
10.3.4 Stage 3a Intragranular-Intracrystalline LARC .....	207
10.3.5 Stage 3b Intragranular-Intracrystalline LARC .....	208
10.3.6 Stage 3b Intracrystalline LARC .....	208
10.3.6.1 Stage 3b Cleavage A .....	208
10.3.6.1.1 Stage 3b Link A .....	209
10.3.6.1.2 Stage 3b Link B .....	209
10.3.7 Stage 3b Crack Development .....	210
10.3.7.1 Stage 3b Transgranular A .....	210
10.3.7.2 Stage 3b Transgranular B .....	210

10.3.7.3 Stage 3b Transgranular C .....	211
10.3.8 Stage 3b Intracrystalline A and B LARCs .....	211
10.3.9 Stage 3a and b Shear Cracks (subclasses 'i' and 'ii') .....	212
10.3.10 Stage 4 - Failure Crack Characteristics .....	212
Summary .....	236
CONCLUSION .....	239
BIBLIOGRAPHY .....	244

## ABSTRACT

Acoustic Emission (AE) techniques under laboratory testing conditions are used in order to understand the mechanical behavior and deformational processes of uniaxially compressed potash rock. Results obtained from the acoustic emission measurements are compared to crack development at preselected stress levels up to specimen failure.

It is observed that the fracture processes, mechanical behavior and acoustic emission response are dependent on the physical properties of potash rock. The mechanical behavior of potash rock displays two stress-strain trends under the same load conditions. Based on the acoustic emission rate, it was possible to delineate an approximate yield point of potash rock. However, a more detailed study of the acoustic emission amplitude and energy distributions showed that high amplitude events with long event durations are initially observed to occur near the yield point of the stress strain curves. These events are present prior to the yield point in specimens containing a high proportion of sylvite and after the yield point for monomineralic, halitic specimens. Finally, a classification scheme of crack morphology and systematic charts displaying the history of progressive crack development for all potash rock types has been developed.

## RESUME

Les techniques d'émission acoustique, dans des conditions de laboratoire favorables, sont utilisées afin de comprendre le comportement mécanique et les procédés de déformation de la roche potasse soumise à une compression uniaxe. Les résultats des données d'émission acoustique obtenus sont comparés au développement des fractures soumises à des présélections de niveaux de contrainte jusqu'à ce que la rupture du spécimen soit atteinte.

Il a été noté que le processus de fracturation, le comportement mécanique et la réaction des émissions acoustiques dépendent des propriétés physiques de la roche potasse. Le comportement mécanique de la roche potasse qui est soumise aux mêmes conditions de chargement, démontre deux tendances de la relation de contrainte-déformation. Il a été possible de discerner une approximation de la limite de résistance élastique de la roche potasse grâce au taux d'émission acoustique. De plus, une étude plus approfondie a démontré que des distributions d'amplitude et d'énergie d'émission acoustique à haute amplitude et longue durée ont lieu initialement près de la limite de résistance élastique des courbes de contrainte-déformation. Ces émissions apparaissent avant la limite de résistance élastique dans les spécimens contenant une forte proportion de sylvite, et après cette limite de résistance dans les spécimens contenant une forte proportion de halite. Finalement, un plan de classification de la morphologie des fractures ainsi qu'un tableau systématique révélant l'histoire du développement progressif des fractures sont présentés pour tous les genres de roche potasse.

## **ACKNOWLEDGEMENT**

The supervision and advice of Dr. F.P. Hassani, Dr. J.A. Szpunar of McGill University and Dr. P. Mottahed are gratefully acknowledged.

Special thanks goes to Mr. M. Momayez for developing the computer software for transferring and analyzing the acoustic emission data and his technical expertise in using the servo-controlled hydraulic machine press. Also, Mr. K. Shakitan for modifying the rock coring and saw cutting equipment in order to prepare samples suitable for testing.

The writer would also like to acknowledge the staff of PCS Cory, Saskatoon, for their guided tours through the mines and for the shipment of specifically selected potash rock samples from Saskatoon to Montreal.

The thesis would not have been carried out without exceptional encouragement and assistance from my wife Mariane, who helped with many aspects of the project including laboratory work and editing, proof reading and typing the last three drafts of the manuscript.

## INTRODUCTION

Monitoring acoustic emissions (AE) has been widely used as a precursor in assessing structural stability. In this study, acoustic emission techniques will be utilized in a laboratory setting to further understand the mechanical behavior and deformational processes of potash rock loaded under uniaxial compression.

Hardy (1977), Dreyer (1972), and Scholz (1968a, 1968b, 1968c) have indicated that acoustic emission response is dependent on material properties. They have suggested that inelastic deformation in geological materials may be due to microfracturing. Sources of acoustic emission activity appear to be associated to the development and propagation of microfractures through the microstructure of the material. Scholz (1968b), Pollock (1973, 1980), Graham (1976), Erlenkämper (1972), and Nakasa et al. (1979) have examined the acoustic emission amplitude distribution of events to discriminate source mechanisms and study the onset of unstable crack propagation in rocks.

Investigations into acoustic emission rate have also been used to delineate deformation stages in a load cycle [Montoto et al. (1984), Fonseka et al. (1985) and Knill et al. (1968)].

Therefore, an analysis of acoustic emission characteristics of potash rock, based on the current methods of testing, will be used to correlate acoustic emission data to various parameters. These parameters include the mechanical behavior during increased loading and the variable petrographic properties of potash rock. As a result, an attempt will be made to determine the sources of acoustic emission and assess the predictability of impending failure based on acoustic emission data.

### 1.1 Statement of the Problem

The purpose of this study is to investigate the relationship between acoustic emission parameters in order to obtain some insight into the microfracturing processes which occur at various stages in the load cycle of potash rock. The tests are conducted under uniaxial compression using a constant strain rate. The study will pursue the following objectives:

- 1) Investigate acoustic emission data generated from potash rock loaded under uniaxial compression in laboratory testing conditions.
- 2) Develop a classification scheme for potash rock via quantitative stereological methods and petrographic techniques.

- 3) Establish a relationship between acoustic emission parameters, microstructure and composition of potash rock.
- 4) Establish patterns relating the mechanical behavior of potash rock to the acoustic emission response.
- 5) Examine the stressed specimens for microscopic evidence of specimen damage and its possible source of acoustic emission. This latter objective will be a precursor to a future study into pattern recognition and source mechanism studies.

Parameters used to analyze data within the scope of this study can be summarized into four groups. These groups consist of acoustic emission, mechanical and textural parameters as well as mineralogical composition of the potash rock.

Variables under acoustic emission parameters that will be studied include: event count, acoustic emission rate, energy, amplitude, time difference between acoustic emission events and event duration. Mechanical parameters studied include stress, strain and elastic constants. Those studied for textural parameters include grain size, textural homogeneity and structural interlocking. Finally, the compositional ratios of minerals present in potash rock will be established.

## **Petrology of Saline Rocks**

### **2.1 Introduction**

Saline rocks are categorized under the group of rock types known as 'evaporites' [Nockolds et al. (1978)]. More specifically, this study deals with potash rock which is a saline rock. The term 'saline rock' is used to distinguish the group of deposits that are composed of sulfates and chloride mineral phases [Nockolds et al. (1978)]. These deposits originate from the process of precipitation and crystallization of concentrated brine solution.

Saline deposits occur as lenticular or irregular shaped masses containing interstratified layers with fragmental or organic sediment. Most deposits also display bedding structure. These deposits can be formed in both shallow and deep water environments. The isolated shallow water environments are restricted either by location on extensive shoaling shelves, or by the existence of a seaward reef or offshore bar. Those originating from deep water precipitation have also been proposed for saline deposits in association with sediments of deep water facies [Schmalz (1969)]. Based on this presumption, evaporite geology can be classified and modeled on the basis of its environmental relationships, particularly with respect to the underlying and overlying sedimentary sequences [Krumbein and Sloss (1964)].

The most important chemistry of saline deposits includes the chlorides and sulfates of sodium, potassium, magnesium and calcium (refer to table 2.1). These components can form simple salts, including halite and gypsum; but the development of double salts and more complex mineral species can also occur [Greensmith (1979)]. Primary mineralogy and texture of saline rocks are usually obscured by diagenesis. According to Nockolds et al. (1978), only halite and gypsum are precipitated in any abundance and occur as primary minerals in most ancient evaporite deposits.

The first part of this study concentrates on the petrographic analysis of potash rock derived from Saskatoon, Saskatchewan. The petrographic study of saline deposits includes the following topics: mineral constituents, mutual relationships of the crystalline constituents, microstructure, texture, diagenesis and sedimentary structures.

## **2.2 Mineralogical Components of Potash Rock**

The petrology of saline rocks refers to crystalline textures rather than particulate textures. From the mutual relationships of the mineral assemblages, it is possible to determine the order of crystallization and mineralogical alterations [Greensmith (1979), Nockolds et al. (1978) and Holter (1969)].

The mineral constituents of potash rock are composed of halides, and various insoluble phases coexisting with this rock type [Holter (1969) and Fuzesy (1983)].

Halite and sylvite are the predominant mineral phases in the potash rock. Sylvite is the primary ore deposit in the Saskatchewan region. The sylvite crystals are reported to have a distinct characteristic brick red to orange red color [Holter (1969) and Fuzesy (1983)]. Carnallite has also been reported to be observed in the Saskatchewan potash rock. It is present as a dominant secondary mineral phase although it has not been observed in the samples obtained for this study. Insoluble phases normally occur as distinct layers or as disseminations. These include clay, illite, dolomite, quartz, hematite and micas. Colors of these minerals vary from buff, brown, grey, green to red.

The potash rock can be categorized into several types based on the proportion of the existing mineral phases and the variability in grain size, shape and texture [Greensmith (1979) and Nockolds et al. (1978)].

The potash rock under investigation contains up to six characteristic mineral components which can be divided into four major potash rock types. As observed by standard petrographic techniques, these rock types are labelled as type "A" to type "D" [Greensmith (1979)]. Variations in the proportion of mineral constituents in the potash rock are also observed. A possibility of two or more types of potash rock can coexist within the same specimen. These variations are observed both vertically and horizontally. Petrographic changes occur gradually or abruptly, the latter producing an angular discontinuous structure.

## **2.3 Identification and Characterization of Mineralogical Components Derived from Potash Rock**

The mineralogy of potash rock is described in this section. The analysis is conducted using standard petrographic techniques. These techniques include optical microscopy and analysis of minerals as described by Greensmith (1978), Nockolds et al. (1978) and Williams et al. (1982).

In order to facilitate categorization, this section will describe the components of the potash rock in three parts. The first part will deal with the mineralogical characteristics of potash rock. The second part will deal with the texture of potash rock. The third part will classify the potash rock into types.

## **2.4 Mineralogy of Potash Rock**

In this section, the minerals which compose the potash rock will be described. There are three mineral constituents present: halite, sylvite and polymineralic clay material. Each mineral constituent also displays unique mineralogical characteristics, and can therefore be given another name within a subgroup of the same mineral species.

### **2.4.1 Halite**

Halite crystals occur as colorless grains. They are optically isotropic, display cubic cleavage and have low relief. Halite occurs in all four established potash rock types. Crystals vary in size, shape and crystallinity depending on the type. "Ghost" intracrystalline outlines of hopper crystals are apparent in types "A" and "D" potash rock [Nockolds et al. (1978)]. Figure 2.1 represents a microphotograph plate revealing this feature. Halite also occurs as the mineral phase with the highest proportion in relation to the other mineral phases present in potash rock.

Various intracrystalline microscopic features are observed in the texture of the potash rock. These include fluid inclusions which are transparent to pale green in color. They occur in clusters, isolated and aligned along crystallographically controlled planes. They are generally rectangular in shape, with the largest size observed with a diameter of 1.0 millimeter. Microscopic vacuoles are also present. Wispy to globule shaped material, varying in color from white to pale green are apparent. They are occasionally coated with red oxide along the exterior margins of the globules. Microcrystalline grains of red iron oxide material are also observed protruding into halite grains from the exterior margins. They are observed as thin hairline features projecting inwards from the grain boundary region. Elongated lathes of microcrystalline anhydrite, and doubly terminated quartz are also hosted by halite.

Patches and discontinuous clay bands occur both poikilitically enclosed within halite and intergranular with respect to halite.

Depending on the variety of potash rock, halite can exhibit two distinct textures. It can either form an interlocking equigranular mosaic with interstitial sylvite or, crystal grains supported by a predominant sylvite matrix. The former is observed in

potash rock types "A" and "D". In type "A", a pronounced petrofabric grain alignment is observed. The latter textural form shows halite occurring as euhedral and subhedral grains adjacent to sylvite. The sylvite conforms to the well developed halite faces of the grains.

#### **2.4.2 $\alpha$ Halite**

$\alpha$  halite is a secondary mineral phase in potash rock. Evidence of this mineral forming later appears by crosscutting textural relationships. Sharp truncations within sylvite grains occur. These truncations also occur along grain boundary areas adjacent to halite.

$\alpha$  halite is also observed as equidimensional shaped grains along the grain boundary, enclosed within sylvite or adjacent to halite.

#### **2.4.3 $\beta$ Halite**

$\beta$  halite, as in  $\alpha$  halite, is a secondary mineral phase. This variety displays the same textural occurrences as  $\alpha$  halite but the grains are smaller in size, transparent and anhedral to euhedral prismatic.

They occur along grain boundary areas impinging upon adjacent mineral phases and occur within halite and sylvite.

#### **2.4.4 Rimmed Sylvite**

Rimmed sylvite is the predominant mineral phase in type "B" and type "C" potash rock. Types "A" and "D" also contain this variety of sylvite but the zonation is not apparent.

Rimmed sylvite displays three distinct zones in a concentric geometric pattern, parallel to their outer surfaces (refer to figure 2.2). The center of the grain is usually white due to a high concentration of fluid inclusions. This is followed by a clear intermediate zone which gradually changes into a red iron-oxide rich exterior, forming the characteristic rimming. Under high magnification, the rims are composed of small hair-like fibres of goethite and small hexagonal plates of hematite. Halite does not show rimming, but rather an external coating of insoluble mineral phase. Holter (1969) has reported similar structures.

The crystals vary in size, shape and crystallinity with the respective types of potash rock. Types "A" and "D" potash rock display small to medium grained, anhedral and irregular shaped grains. Type "B" displays large to very large grained anhedral to

subhedral, poikilitic, equidimensional to irregular shaped grains. Type "C" potash rock displays small to medium grained, anhedral to subhedral, irregular shaped grains.

Sylvite is isotropic and displays low positive to low negative relief. The optical relief in sylvite is higher than that of halite.

Various intragranular features are associated with rimmed sylvite. Fluid inclusions are similar to those observed in halite. There are also high concentrations of vacuoles, located in the inner core area of the grains, predominantly in type "B" potash rock.

When clay is present in a high concentration, it is normally located along the grain boundaries of the sylvite, whereas halite hosts the clay. Some specimens of type "C" potash also display clay enclosed within sylvite grains indicating a secondary mineral phase.  $\beta$  Halite when observed with yellowish hue coloring, is found enclosed within sylvite.

Rimmed sylvite occurs in two textural positions. In types "B" and "C" potash rock, the sylvite forms an interlocking crystalline groundmass matrix. The rimming is restricted to the sylvite grains. The rims are continuous around the periphery of the grains even if the grain boundary is defined by two adjoining sylvite grains, indicating that the rimming is a secondary event, due to migration of iron rich fluids along the grain boundary areas. Sylvite in type "A" potash rock is interstitial.

Sylvite in type "D" potash rock is also located interstitially. The grains are anhedral and slightly larger. Grains of sylvite can also be found interlocked in type "D" potash rock whereas in type "A" they are generally isolated.

#### **2.4.5 Red Rimless Sylvite**

Red sylvite also occurs without the rimming pattern. The color varies from orange, red to dark red. The red coloration is uniform within the grains. Optical properties are the same as those of the rimmed sylvite.

Sylvite occurs with the rimmed sylvite and forms a granoblastic crystalline mosaic. Grain size varies with respect to the type of the potash rock. Red rimless sylvite is not present in type "D" potash rock. In general, they are smaller than the rimmed sylvite. The grains are anhedral and irregular in shape. Clay inclusions are found enclosed within some grains.

#### **2.4.6 Insoluble Minerals and Substances**

Insolubles are generally comprised of a clay component. They vary in color from a pale green to buff. Where the clay is hosted by halite, it is externally coated with a very thin film of iron oxide staining.

Clay is observed to occur in three textural positions. These include interstitial patches, layers of thin seams parallel to the bedding and contorted seams discordant to the bedding. The latter two occur in several configurations, being continuous, discontinuous, wavy irregular or straight (refer to figure 2.3).

Various structural features are associated with clay. A dominant structural feature includes fractures in clay patches. The fractures can be filled with red oxide or a fibrous crystalline growth of anhydrite perpendicular to the walls of the fracture. Intraclasts of clay and silt size clasts are also observed. The majority of these features are observed in type "B" and "C" potash rock. All four types of potash rock contain clay patches. Type "A" displays continuous clay layers parallel to bedding and poikilolitically enclosed in halite.

#### **2.5 Textures**

Texture refers to the physical makeup of a rock as distinct from its mineral or chemical composition. It is particular to its crystallinity, grain size and to the mutual relationship of the individual components [Greensmith (1979) and Williams et al. (1982)].

Potash rock consists of a crystalline mosaic of interlocking crystals of halite and sylvite. Depending on the grain size and proportions of minerals present in the rock, potash rock can form several textural variations ranging from equicrystalline to inequicrystalline to porphyroblastic. The former is composed of uniform grain size assemblages of sylvite and halite. The other extreme is defined by a texture of a wide range of grain sizes. This is predominantly observed in the type "B" potash rock. Type "B" potash rock displays large porphyroblasts of interlocked sylvite grains, laced around interstitial polycrystalline mosaic of halite. On several specimens, poikiloblastic sylvite hosts various types of inclusions and halite grains.

Type "A" potash rock displays pronounced petrofabric anisotropy. The anisotropy is defined by a preferred orientation of halite grains in a polycrystalline mosaic. Individual crystal grains range in shape from equant to elongated (refer to figure 2.5).

The grain boundaries of the texture of potash rock are generally smooth, regular to irregular. The general shape of sylvite crystal grains conform to the external morphology of adjacent halite grains. This observation is consistent with the four types of potash rock.

Crystal grains range widely in terms of size from fine to very coarsely grained. Grain size has been initially subjectively evaluated using Dreyer's (1972) classification scheme. This system was devised to categorize grain sizes for rocksalt.

Primary textural features of potash rocks have been described by Fuzesy (1983) in terms of variation in grain size, relationship between grain size, composition and grain shape. He also associated the depositional environment of the evaporites with textural criteria. Nockolds et al. (1978) describes the typical environment for the development of evaporites as consisting of halite appearing as rinds, cements and crust.

Several textural features present in the samples used for this study are indicative of primary origin. These include textures resulting from primary crystallization or sedimentation at, or just beneath, the sediment surface [Nockolds et al. (1978), Fuzesy (1983), Holter (1969) and Dean and Schreiber (1978)]. Primary fabrics usually form coarse layering. They can display alteration of saline layers with detrital layers and in some cases alternating layers of the same mineral showing different textures. These structures are frequently observed in type "B" and "C" potash rock. An equicrystalline texture gradually changes into a porphyroblastic texture. This is accompanied by a decrease in clay content (refer to figure 2.4).

The best examples of primary crystallization textures are shown by halite, whose crystallization takes place at the water-sediment interface. The various stages involved in the genesis of rocksalt by primary crystallization process is illustrated in Dean and Schreiber (1978).

The former produces hopper crystals which coalesce, form rafts, and sink to the bottom [Dellwig (1955)]. The latter occurs at the water-sediment interface and produces more continuous layers which have vertically elongated crystals coarsening in size upwards [Nockolds et al. (1978)]. Relic imprints of hopper crystals are frequently observed in type "A" and "D" potash rock. The external section of the grains are often recrystallized and appear as syntaxial overgrowths.

Phases of precipitation are terminated by detrital influx with an associated lowering of salinity. This is observed in the truncation of the halite fabric by a solution surface. It is apparent in all the types of potash rock observed in this study. The surface is often defined by laminae structure composed of insolubles and clay materials or, as a discontinuity surface. The band of potash rock directly occupying the layer above the discontinuity is often of a different variety from the layer below the solution surface (refer to figure 2.4).

Well defined banding of potash rock sometimes results from the alteration of clear bottom precipitated crystals, adjacent to a surface of precipitated crystals which are cloudy and abundant with fluid inclusions. The bands range in thickness from a few centimeters to a maximum of 25 centimeters. Each band normally displays uniform thickness and similar grain size.

Halite crystals may also grow in surface sediments by displacement and may coalesce to form a crystalline groundmass in which grains are floating.

In sediments which have undergone burial to depth of a few meters, displaced crystallization gives way to more interstitial cementation with the development of poikiloblastic texture which is evident in type "B" potash rock.

Halite is commonly associated with sylvite and carnallite. Crystals of halite are commonly coated with a thin layer of insolubles. Wardlaw and Schewerdtuer (1966) reported "chevron" crystals which occur as crystals with growth lines directed upwards towards a common vertical axis. In several cases, halite was found elongated, perpendicular to the bedding of the potash rock and truncated by anhydrite laminae.

## **2.6 Principle Rock Types**

### **2.6.1 Type "A" Potash Rock**

The type "A" potash rock is predominantly halitic in composition. It is composed of transparent to white, to light red shades of elongated halite grains forming a uniform crystalline anisotropic mosaic. Minute interstitial red sylvite, mottled with grey green clay patches occur widely dispersed in the mosaic (refer to figure 2.5). On large polished slabs (approximately 8" x 11") faint horizontal banding is evident. The bands range in thickness from a few centimeters to 20 centimeters. They are identified as faint variations in color of halite and red sylvite. Also, frequently bordering and oriented parallel to the bands are thin clay laminations.

The rock is equicrystalline, homogeneous and anisotropic. The mean grain size ranges from coarse grained to large grained. The external grain morphology of halite grains define an anisotropy. Anhedral to subhedral halite grains form a crystalline mosaic with intercrystalline small grained sylvite.

Several cut sections display a vertical decrease in grain size to as small as average grain size (refer to table 2.2). This change is accompanied by a loss in grain anisotropy, where the halite grains change in shape from elliptical to equidimensional. At regions where the grains reach their smallest grain size, the fabric becomes granoblastic. This sequential change is terminated by a truncation or a solution surface coated with clay laminae.

Clay also occurs intercrystalline to halite and intracrystalline hosted by halite. The latter forms discontinuous relic laminae traces normally found within recrystallized halite mosaic.

The grain size variation is observed as a loss in the pronounced fabric anisotropy, where the grains are equidimensional shaped rather than elliptical as is the case of anisotropic portions of the rock. The fluctuation in the sylvite content macroscopically appears as continuous rhythmic banding occurring parallel to the bedding.

Halite grains range in color from clear to hues of orange. In association with sylvite or clay, the crystals are frequently coated with a thin layer of either red oxides or clay material. Relic hopper zonation patterns within halite crystals are evident. These grains are recrystallized and show syntaxial overgrowths as well as straight intercrystalline boundaries.

Sylvite and clay are minor mineral phases in type "A" potash rock. Sylvite ranges in color from pale orange to red. The clay is buff to greenish grey in color. Both normally occur as widely dispersed intergranular patches in the halite mosaic. Also, where banding sequences are terminated, the sylvite can vary in proportion to occur as a major mineral constituent in association with clay laminations.

### **2.6.2 Type "B" Potash Rock**

The "B" type potash rock is composed of large porphyroblasts of sylvite. The crystal grains contain milky white centers with dark brick red concentric rims. Interstitial sections of this rock type consist of granoblastic clusters of white to transparent halite mosaic. There are also intergranular clots and patches of green grey to buff colored clay.

This rock is inequicrystalline and displays a distinct porphyroblastic texture. The mosaic consists of an interconnected branching pattern of large grained rimmed sylvite grains which are laced adjacent to granoblastic matrix regions. The matrix areas are composed primarily of medium grained halite and anhedral medium to small grained sylvite. Clay is often intermixed in the interfacial areas between the porphyroblasts and granoblastic areas (refer to figure 2.6).

The sylvite porphyroblasts are generally anhedral, equidimensional to irregular shaped. They normally conform to the external morphology of adjacent halite crystals, along granoblastic and porphyroblastic grain boundary regions.

The characteristic red rims are formed along the external periphery of the porphyroblasts, extending along the entire circumference of the grains. This even applies to grain boundaries between two adjacent porphyroblasts. The sylvite grains range in size from 1 centimeter to as large as 3 centimeters. The halite grains are generally subhedral and medium grained. Many grains display well developed faces. Sylvite and halite are intergranular to the matrix and to porphyroblastic areas.

Sylvite is the dominant mineral phase in type "B" potash rock. Halite occurs as a major mineral phase, mostly concentrated in matrix areas. Clay occurs in varied proportions in relation to the rest of the components in which a ratio of 4 to 1 can be noted. Clay occurs as laminae observed in various orientations and ranging from straight to wavy forms. Laminations range in thickness from a few millimeters to a few centimeters. The thicker layers also contains 'floating' grains of halite, sylvite and clay intraclast. The latter occur as sharp angular fragments. Red oxides deposits can be found concentrated between laminae.

### **2.6.3 Type "C" Potash Rock**

The type "C" potash rock is characterized by brick red to dark red colored sylvite, mottled with white halite. The rock is opaque and massive. Interstitial clots and films of green to grey clay are common and occur in variable amounts throughout interstitial regions of the rock.

The texture is equicrystalline and granoblastic. The fabric is developed by an interlocking polycrystalline mosaic composed of anhedral sylvite grains with subhedral halite grains. Sylvite varies in size from large grained to fine grained. This variation exhibits the fabric of the rock to range from an almost porphyroblastic texture to a fine grained groundmass matrix. The variation in grain size occurs gradationally

and controls the definition of the banding structure. Coarsening of sylvite grains increases vertically upwards. The grains of sylvite are generally equant in shape (refer to figure 2.7).

The crystallinity of halite is euhedral to subhedral. It forms equidimensional rectangular shaped grains displaying well developed cubic forms. Halite generally occurs as segregated grains supported in a sylvite groundmass. Polycrystalline monomineralic clusters composed of halite are evident. These clusters are relatively small and irregular shaped. The average diameter is of a few centimeters.

Clay and other insoluble phases are commonly located along grain boundary areas, and hosted by halite. The insoluble phases define a number of macrostructural features including clay seams and laminae. Both range in thickness, the largest measuring up to 8.0 centimeters. Similar features are associated with type "B" potash rock but occur more frequently in type "C" potash rock. Several specimens display secondary microcrystalline growth along relic linear cavities within clay layers. These growths appear to be composed of anhydrite and possibly calcite due to the crystal habit. They can develop as normal fibrous growth. The orientation of the layering varies from parallel to the bedding, to vertical, with many contortions, and it contains intraclasts of the wall rock.

#### **2.6.4 Type "D" Potash Rock**

Type "D" potash rock is relatively featureless in comparison to the other three types presented in this study. This rock consists of a mottled fabric of light orange sylvite interlocked with white grains of halite. Trace amounts of clay which appear as green grey specks located in interstitial areas of the rock can be observed.

The rock is composed of a homogeneous medium to coarse grained equicrystalline mosaic of interlocking anhedral halite grains with interstitial anhedral sylvite (refer to figure 2.8). Insoluble phases occur in trace amounts appearing as rounded minute patches located in interstitial and intragranular areas. The patches measure approximately 2 millimeters and are widely dispersed. Local horizontal pod shaped monomineralic clusters of sylvite are observed. They range in thickness from 1 to 3 centimeters. In most cases, the boundaries of the pods are poorly cemented possibly due to a solution surface.

Halite grains are medium grained, anhedral to subhedral. They form elliptical to equant shaped grains. Hopper zonation patterns are observed within many grains, along with syntaxial overgrowths.

The rock is predominantly composed of halite, minor amounts of intergranular sylvite and trace amount of clay patches. Lenticular pods of sylvite may be present, introducing local high concentrations of sylvite.

## **2.7 Summary and Conclusion**

Optical microscopic techniques used in this study are beneficial in identifying various elements of the potash rock types.

The volume fractions of the mineral constituents and grain sizes are observed to vary substantially over the range of the four types of potash rock. Potash rock of types "B" and "C" contain high contents of sylvite and clay as compared to that of types "A" and "D" potash rock.

Grain size also varies between the four types of potash rock. Lowest grain boundary density is predominant in type "B" potash rock due to the very large grain size. Type "C" and "D" potash rock show a medium to small grained crystallinity.

Petrofabric anisotropy is also a distinguishing factor between the different types of potash rock. Type "A" potash rock is the only variety which displays a strong anisotropic fabric.

Table 2.1: Sedimentary Chlorides and Sulfates [after Greensmith (1979)].

<b>Class</b>	<b>State</b>	<b>Species</b>	<b>Formula</b>
Chlorides	Anhydrous	Halite	NaCl
		Sylvite	KCl
Chlorides	Hydrous	Bischofite	MgCl <sub>2</sub> .6H <sub>2</sub> O
		Carnallite	KMgCl <sub>3</sub> .6H <sub>2</sub> O
Chlorides	Anhydrous	Glauberite	Na <sub>2</sub> SO <sub>4</sub> .CaSO <sub>4</sub>
		Anhydrite	CaSO <sub>4</sub>
		Barytes	BaSO <sub>4</sub>
		Langbeinite	K <sub>2</sub> SO <sub>4</sub> .2MgSO <sub>4</sub>
Sulfates	Hydrous	Mirabilite	Na <sub>2</sub> SO <sub>4</sub> .4H <sub>2</sub> O
		Kieserite	MgSO <sub>4</sub> .H <sub>2</sub> O
		Gypsum	CaSO <sub>4</sub> .2H <sub>2</sub> O
Sulfates	Hydrous	Polyhalite	Ca <sub>2</sub> K <sub>2</sub> Mg(SO <sub>4</sub> ) <sub>4</sub> .2H <sub>2</sub> O
		Hexahydrate	MgSO <sub>4</sub> .6H <sub>2</sub> O
		Epsomite	MgSO <sub>4</sub> .7H <sub>2</sub> O
		Kainite	4KCl.4MgSO <sub>4</sub> .11H <sub>2</sub> O

Table 2.2: Qualitative classification of grain size system utilized for rocksalt, equally applicable to potash rock [after Dreyer (1972)].

Mean Grain Diameter		Grain Density		Denomination
$d_m$		$z$		
(mm.)		(Grains / cm <sup>2</sup> )		
above	300	below	$-1.41 * 10^{-3}$	Gigantograined
30	300	$1.41 * 10^{-3}$	$-1.41 * 10^{-5}$	Very Large Grained
10	30	$-1.41 * 10^{-1}$	-1.27	Large Grained
3	10	1.27	$-1.41 * 10^1$	Coarse Grained
1	3	$1.41 * 10^1$	$-1.27 * 10^2$	Average Grained
0.3	1	$1.27 * 10^2$	$-1.41 * 10^3$	Small Grained
0.03	0.1	$1.27 * 10^4$	$-1.41 * 10^5$	Dense Grained
0.001	0.03	$1.41 * 10^5$	$-1.27 * 10^8$	Microcrystalline
0.0001	0.001	$1.27 * 10^8$	$-1.27 * 10^{10}$	Cryptocrystalline
0.000001	0.0001	$1.27 * 10^{10}$	$-1.27 * 10^{14}$	Radiocrystalline

**Figure 2.1:** Microphotograph displaying hopper zonation pattern hosted by halite crystal in type "A" potash rock. Photograph taken under 35 magnification in plane polarized light.

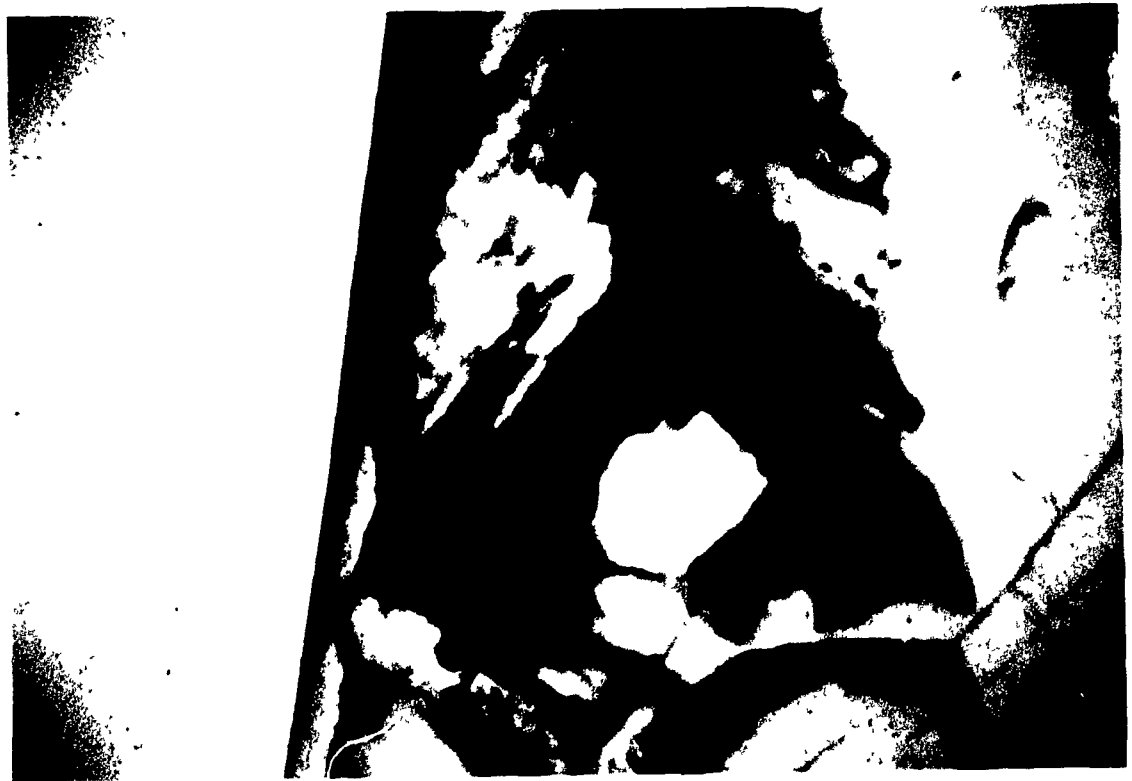
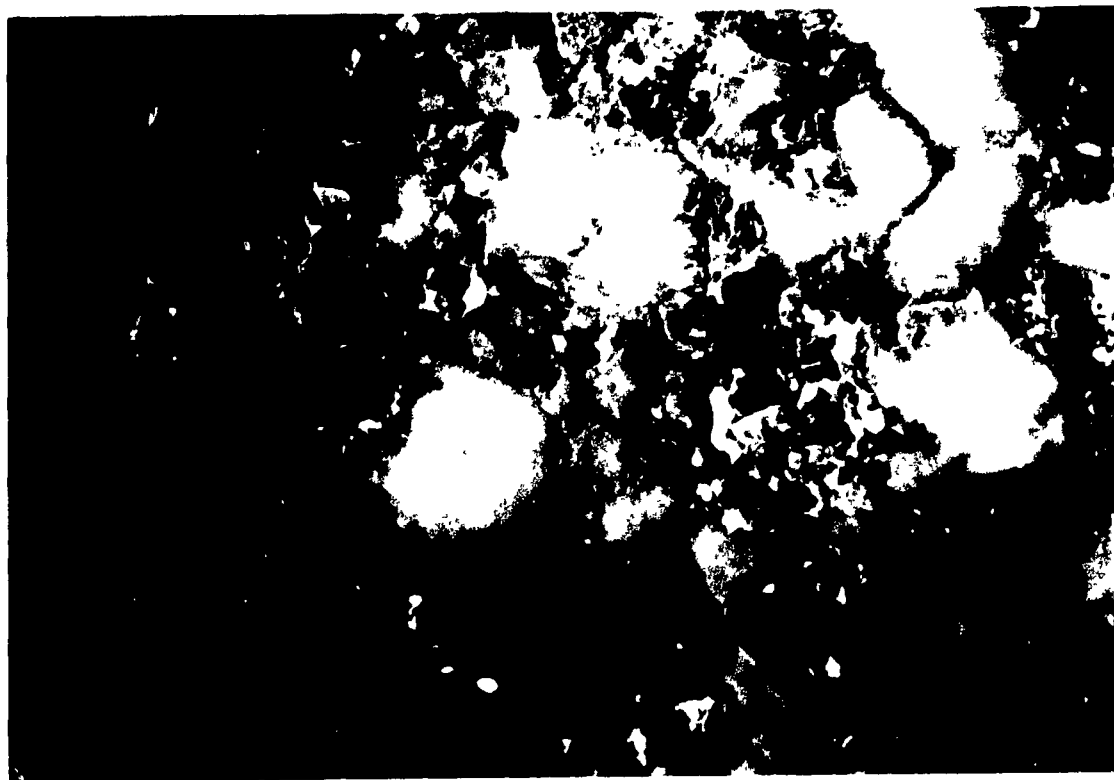


Figure 2.2: Microphotograph of type "B" potash rock. It shows the rimming pattern of sylvite porphyroblast. Photograph taken under 35 magnification in plane polarized light.



**Figure 2.3:** Photograph of type "C" potash rock. Illustrated are layers of clay-anhydrite seams. Clay is also observed protruding into adjacent crystalline layers. These protrusions show evidence of dissolution along the grain boundary regions of the crystalline mosaic.

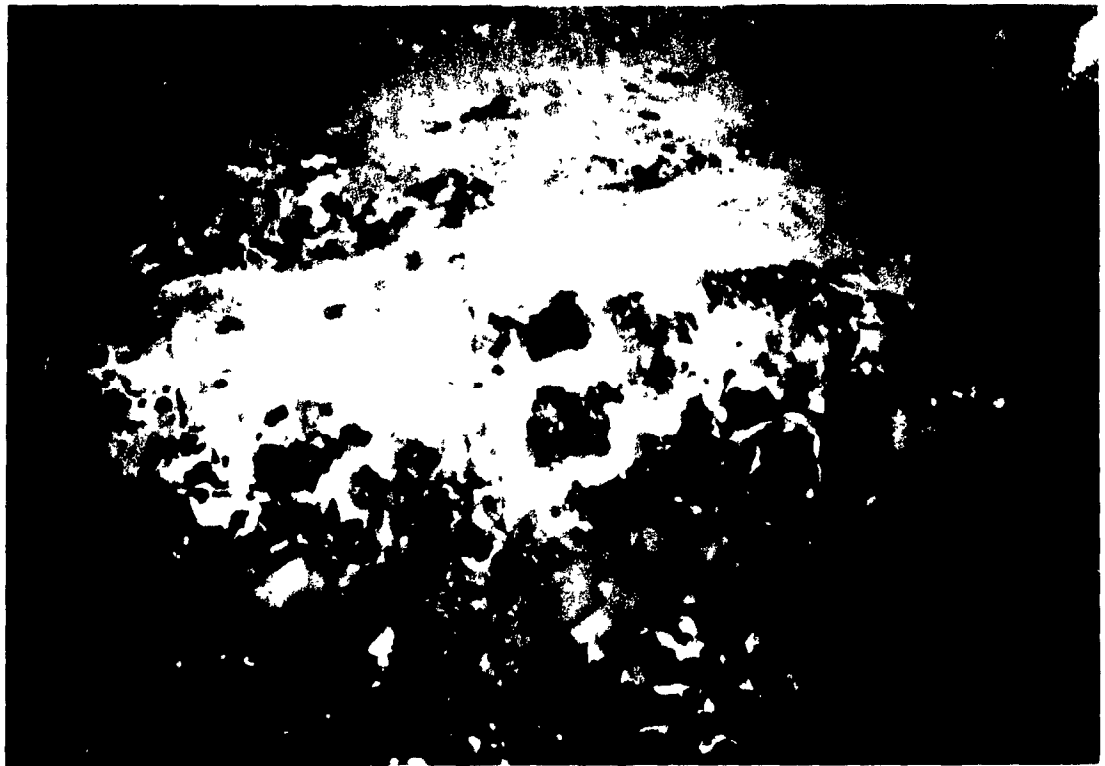
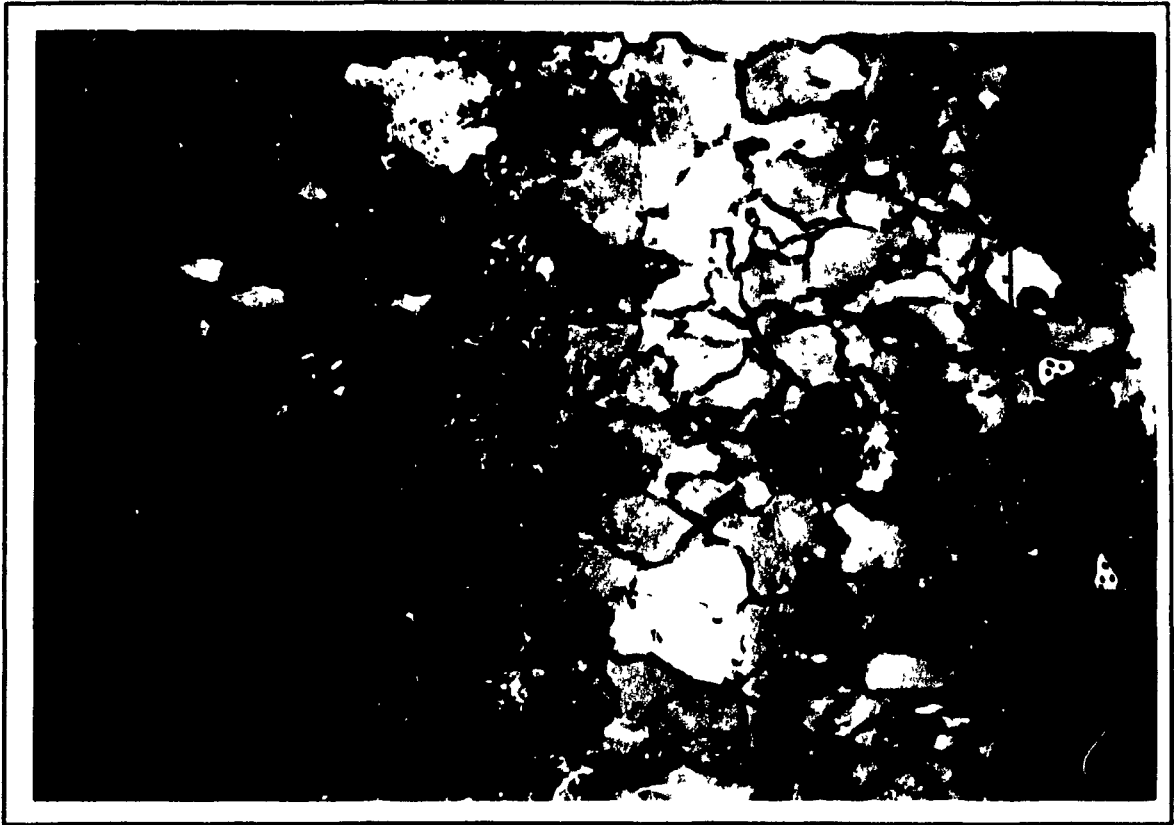
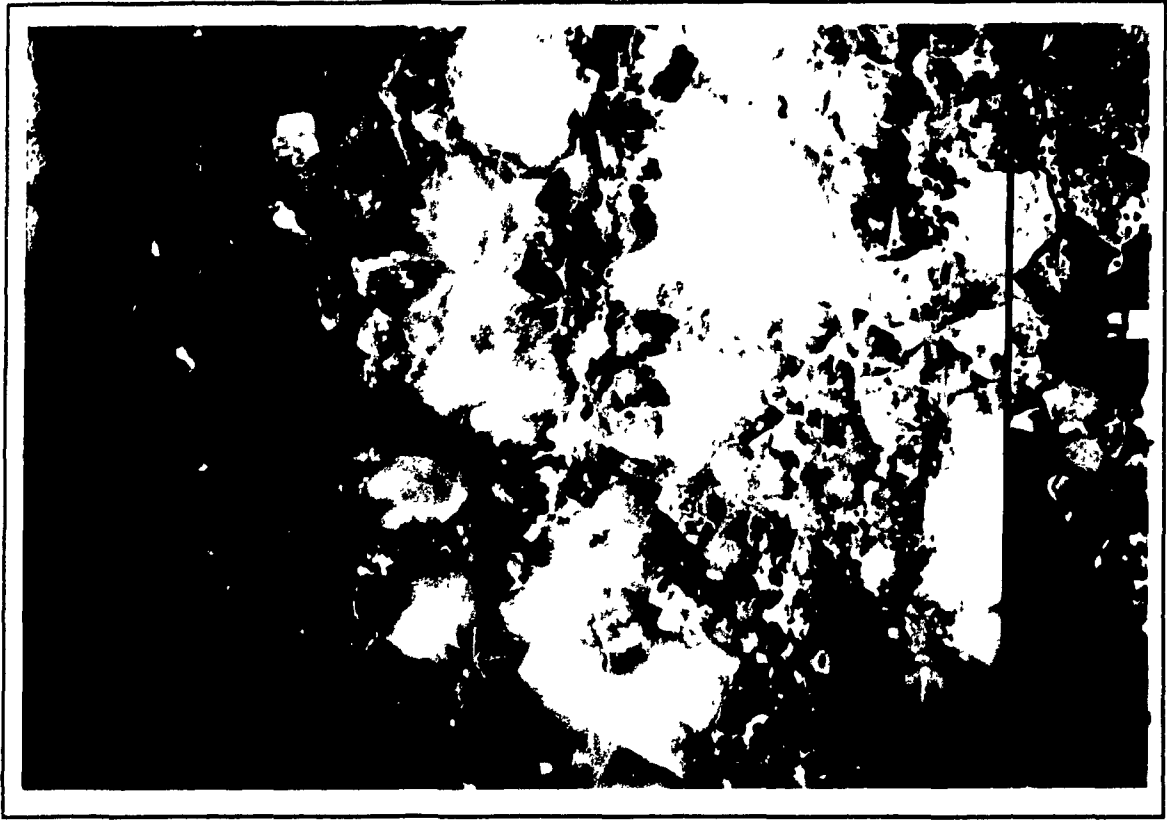


Figure 2.4: Photograph displaying a vertical change in grain size within a type "B" and "C" potash rock occurring over a vertical distance of 15 centimeters. Upper layers represent type "C" potash rock with the more consistent granoblastic mosaic. The lower extreme layer constitutes sylvite porphyroblasts and an inequicrystalline mosaic.





**Figure 2.5:** Displays a type "A" potash rock. It is principally composed of an anisotropic equicrystalline mosaic. It is mostly composed of anhedral halite grains (outlined) that are elongated in shape. Minor amounts of interstitial sylvite (black) and clay (stippled) are also present. Faint horizontal banding is apparent. Photograph is magnified 1.50X.



**Figure 2.6:** Displays a type "B" potash rock. It is composed of an inequicrystalline mosaic of anhydrous sylvite (black) poikiloblasts set in a fine to medium grained halite with sylvite granoblastic matrix. Interstitial clay (stippled) seams are present. Photograph is magnified at 1.25X.

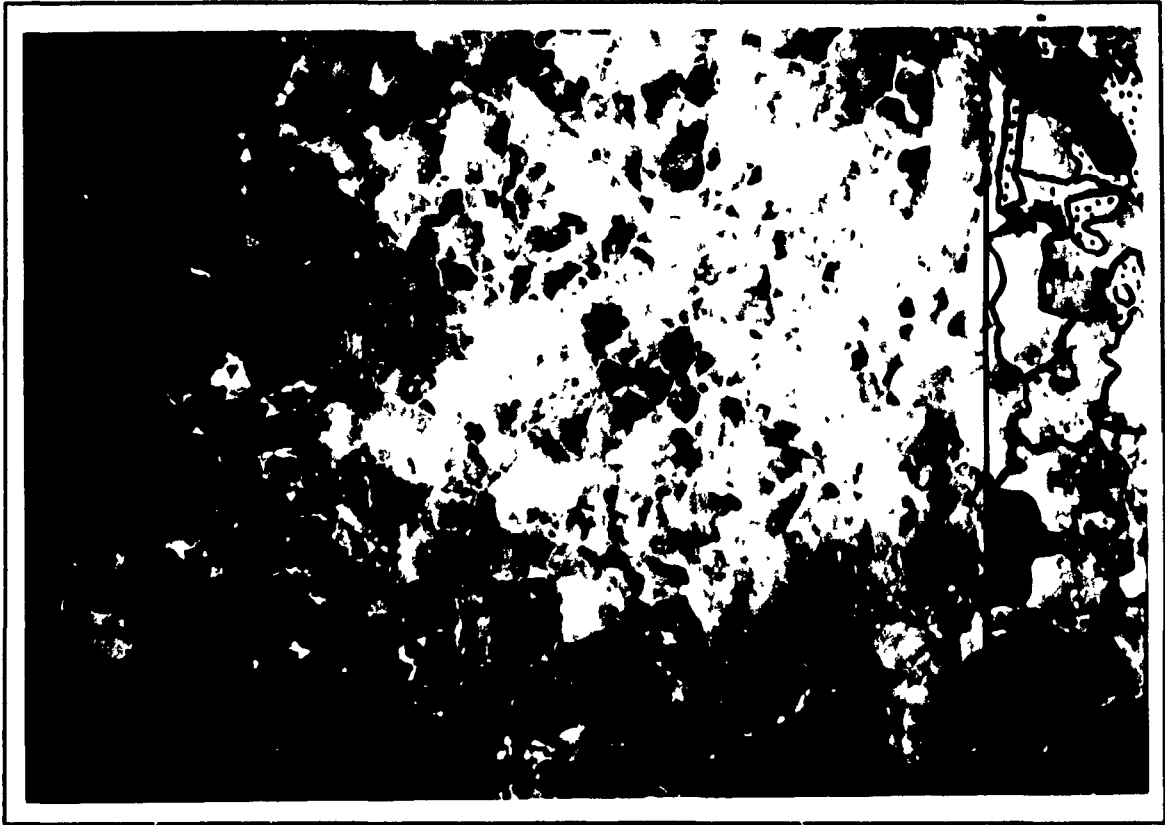


**Figure 2.7:** Displays a type "C" potash rock. It is principally composed of an equi-crystalline mosaic. A granoblastic mosaic of interlocked sylvite (black) and halite (outlined) grains constitutes the major mineral components of the rock. Interstitial clay (stippled) is also present. Photograph is magnified 1.50X.

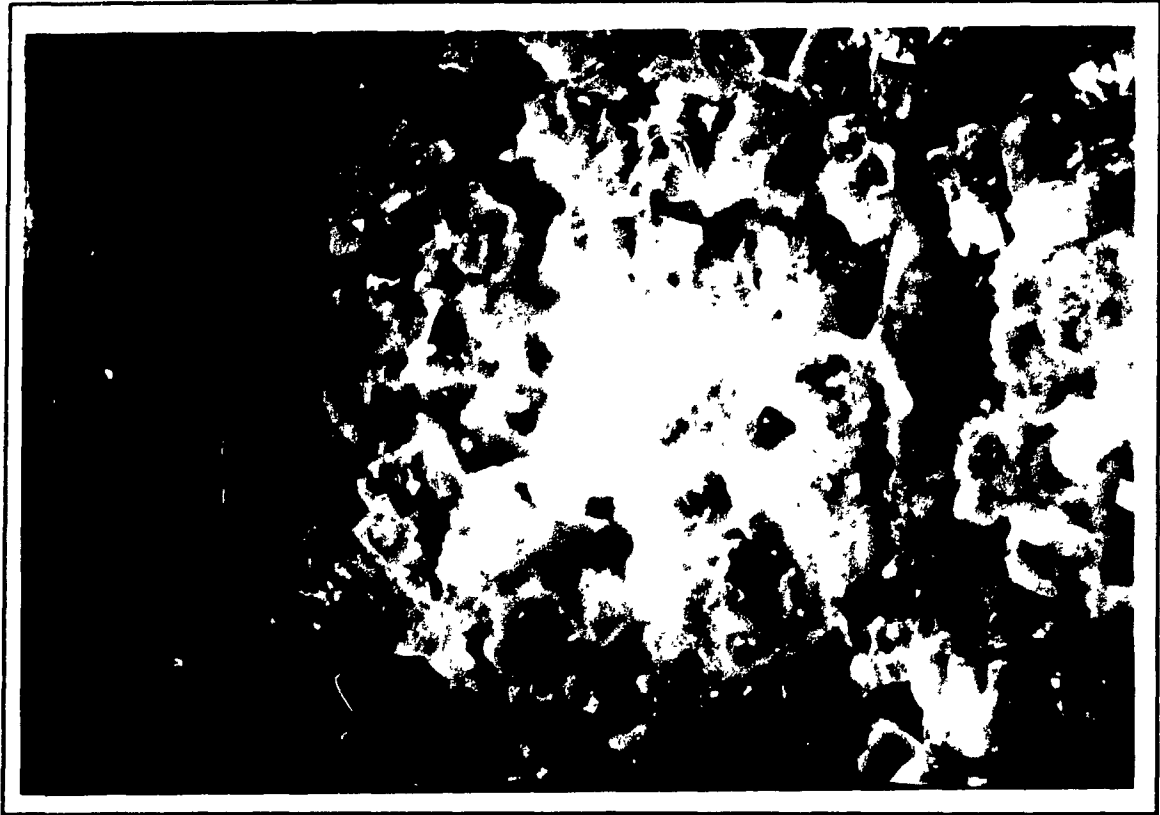


Figure 2.8: Displays a type "D" potash rock. It is principally composed of an equi-crystalline mosaic constituting a homogeneous distribution of anhedral sylvite (black) and anhedral to subhedral halite (outlined). Trace amounts of intercrystalline clay (stippled) is also present. Photograph is magnified 1.50X.

## **Quantitative Petrographic Analysis**

### **3.1 Review of Methodology**

Defects in rocks including grain boundary structure, mineralogical characteristics and structural features are possible sources of acoustic emission.

By using various techniques to measure certain petrographic parameters on polished rock slabs and thin sections, textural and compositional coefficients can be obtained.

Microstructural measurements including morphological grain parameters and degree of anisotropy can be examined by methods of quantitative stereology [DeHoff and Rhine (1968)]. Quantitative stereology is concerned with the quantitative characterization of microstructure in terms of its point, lineal and areal elements. By means of suitable two dimensional measurements on the plane of observation, statistically exact information can be obtained from various microstructural features in three dimensional space occupied by the rock [DeHoff and Rhine (1968)].

Measurements are performed with the aid of optical microphotographs of slabbed, etched and polished specimens representing the microstructure on the planer section. The data is then processed by digitizing the features from the microphotographs. Measurements taken include the percentage of area of grains and matrix; length, breadth and perimeter of each grain in the viewing window.

This section will review the techniques used to measure compositional, textural and microstructural parameters of potash rock.

### **3.2 Basic Measurement Techniques**

Basic measuring techniques of quantitative stereology involve reduced "unit operations" including: counting, size determination and area fraction measurement.

Counting methods can be accomplished by three different types of scanning modes. In quantitative stereology, scanning is essentially a sampling procedure used to produce a representative picture of the " population ". In this case, the population consists of all individual structural features.

The first type is called 'feature-to-feature scanning' which involves scanning every constituent without following a fixed pattern. The other two methods involve a systematic sampling procedure. In the first method, referred to as 'line scanning', the sampling points form a continuous line. This technique forms the basis of lineal analysis. In the second case, referred to as 'point counting', the sampling points are arranged at the intersection points of a rectangular grid.

Size determinations and areal fraction measurement methods will be used to determine grain size, textural homogeneity and structural interlocking. These parameters will be discussed in the following sections.

Quantitative stereology utilizes a standard set of symbols. These are acronyms of the word they represent, for example :'*L*' for Line, '*P*' for Point, '*A*' for Area, '*S*' for Space, '*V*' for Volume.

There is also the dual usage of symbols for both microstructural features and test quantities. The test quantities could be points, lines, surfaces, or volumes. The compound symbols represent a fraction in which the numerator refers to the microstructural quantity and the denominator pertains to the test or reference 'background' quantity [DeHoff and Rhine (1968) and Rodgers (1974)].

Two symbols are used for surfaces :'*A*' and '*S*', where '*A*' is for flat surfaces and '*S*' is for curved surfaces. Also note that the '*P*' stands for the number of points and '*N*' for the number of features.

There is a particular set of measurements that is routine in quantitative stereological work. These operations are all performed on two dimensional sections and involve simple, lineal and areal measurements [Dehoff and Rhine (1968)]. There are a total of seven basic operations.

The first is point counting '*P<sub>p</sub>*'. This term refers to test points that are counted in relation to areal feature of the microstructure on the section of plane.

The next term '*P<sub>L</sub>*', refers to the number of points (intersections) generated per unit length of test lines. These 'points' usually consist of intersections made by test lines with traces of surfaces on the polished plane.

The third parameter is '*N<sub>L</sub>*'. It defines the number of interceptions of features of a microstructure per unit length of test lines.

The fourth is a count of the number of points on a microstructure per unit area. It is abbreviated as '*P<sub>A</sub>*'. This measurement simply involves the total number of such 'points' counted within the chosen area which gives the ratio '*P/A*' or '*P<sub>A</sub>*'.

The fifth measurement involves counting the number of 'objects' in a section area of the microstructure. It is abbreviated as '*N<sub>A</sub>*'.

The areal analysis ('*A<sub>A</sub>*') methods, usually involves the determination of relative areas of a phase constituent per unit area of microstructure.

The final operation, referred to as a lineal analysis, is frequently used for measurements of grains forming a crystalline mosaic. This measurement involves intercepted lengths that are measured along straight lines across the micro structure. The divided lengths intercepted by particles or second phase regions are measured separately, added up, and compared to the total length of the transverse. The ratio ' $L_L$ ' for a particular phase is selected.

Various expressions have been derived from the basic measurement parameters. These are used to relate point, lines, surfaces and volumes in space, for measurements conducted on two dimensional surfaces [DeHoff and Rhine (1968) and Underwood (1970)].

Details on the procedures of these methods are described in Dehoff and Rhine (1968) and Underwood (1970). These methods are used in a number of metallurgical studies. Rodgeron (1974) used these methods extensively.

The equations relating the quantities can be expressed as follows:

$$V_V = A_A = L_L = P_P (mm) \quad 3-1$$

$$S_V = \left( \frac{4}{\pi} \right) \quad 3-2$$

$$L_A = 2P_L (mm) \quad 3-3$$

$$S_V = 2PAP_L (/mm^3) \quad 3-4$$

These equations relate the magnitude of lineal, areal, and volume densities from measurements made on a planer test section. The proofs and derivations of these relationships are shown in DeHoff and Rhine (1968) and Underwood (1970).

### 3.3 Grain Size Measurements

Measurement of grain size can be defined by various geometrical relationships. There are no exact solutions but, in all cases, the determinations are made on planer sections. The data is then either treated as a probability distribution problem or, measured by counting methods or by comparison methods.

In the former method determinations made by grain size distribution involve measuring individual grains accomplished by planimetric methods [DeHoff and Rhine (1968)]. The weight fraction of each grain size within a range must be determined. It is thus necessary that the measured values be grouped in order to calculate the distribution.

The application of grain size distribution methods has been extensively used by Dreyer (1972). The grain size parameter is referred to as the average grain cross sectional area. It is defined as followed :

$$M = \sum_{i=1}^N H_i F_i \quad 3-5$$

where ' $H_i$ ' is the frequency of occurrence (total count) of a particular grain size group, with a cross sectional area of ' $F_i$ ' measured in ' $mm^2$ '.

The counting method as the name implies, ' $\bar{N}_L$ ', involves measuring the average number of intercepts with a test line of unit length [Dehoff and Rhine (1968) and Underwood (1970)].

The last of the three methods know as the comparison method, involves comparing microscopic images with a standard series of templates on microphotographs.

### 3.4 Grain and Grain Boundary Density

The grain size shows a distinct relationship to the grain boundary density and grain density per unit. Grain density can be measured by ' $N_A$ ' which is simply the percentage ratio of the number of grains within a test area [Dehoff and Rhine (1968)]. Dreyer (1972) has defined grain density as the 'grain fineness' value. This value is the inverse of the average grain cross section ' $M$ '. Grain fineness is the measure of grain density 'z' as shown below :

$$z = \frac{1}{M} \quad 3-6$$

### 3.5 Microstructural Anisotropy

Potash rock concerned with this investigation displays varying degrees of fabric anisotropy. Anisotropy is defined by the alignment of grains observed along the grain boundary structure of the crystalline mosaic. The grain boundary traces can either form isotropic or partial orientation. In the latter system of grain boundary traces observed on a two dimensional plane, part of the total length of lines are oriented in a definite direction.

Depending on the orientation of the sectional plane, one can make a distinction between completely oriented structures and partially oriented structures. Of the possible types of orientations, there are three systems: systems of lines in a plane (two dimensional), systems of lines in space (three dimensional), and systems of surfaces in space.

DeHoff and Rhine (1968) and Underwood (1970) have developed a classification system to describe the structure and determine the degree of orientation which describes the anisotropy of the microstructure. The formulae utilized for several different types of scenarios to measure anisotropy in two and three dimensional systems are shown in DeHoff and Rhine (1968).

### 3.6 Grain Matrix Relationships

Dreyer (1972), Onodera et al. (1980), Howarth and Rowlands (1987), among other authors, have shown the importance of establishing a relationship between matrix-grain parameters and mechanical properties of rock. There are several useful measurable parameters that quantitatively evaluate spatial distribution of discrete grains. In most cases, the measurable value involves the relationship between the matrix and particle constituent-system or, a particle inter-relationship system.

Dreyer (1972) and Onodera et al. (1980) have used two parameters which characterize the matrix-grain relationship of rock types. These parameters are textural homogeneity and structural interlocking.

Spatial distribution of individual microstructural elements can be defined in terms of homogeneity [Dreyer (1972)]. A region is said to be homogeneous in certain structural elements, if subregions can be interchanged without affecting the attributes of the structure as a whole. Homogeneity is therefore governed by the size of the interchangeable subregions, because the distribution of structural elements becomes homogeneous as the size of the interchangeable subregions decreases. Dreyer (1972) defines the index of textural homogeneity as:

$$t = \frac{M}{\sqrt{\sum_{i=1}^N H_i (F_i - M)^2}} \quad 3-7$$

whereby, 't' when it is as large as the frequency distribution is determined by one grain size. Maximum homogeneity implies that the structure contains one size group. High variability in grain size corresponds to a low homogeneity index.

Secondly, structural interlocking ('g') in a two dimensional plane has also been defined by Dreyer (1972) as followed:

$$g = \frac{1}{n} \sum_{i=1}^n \left( \frac{U_i}{\sqrt{F_i}} \right) \quad 3-8$$

where ' $F_i$ ' is the grain sectional area ( $\text{mm}^2$ ) and ' $U_i$ ' is the length of grain segment in contact with neighboring grains. Structural interlocking measures the degree to which the grains are interlocked. Thus, if the mean of the grains display convex perimeters, the structural interlocking will be low. This measurement is dependent on the ratio of grain area per unit portion of grain in contact with adjacent grain.

### **3.7 Literature Review of Studies Relating Rock Texture and Composition to Mechanical and Acoustic Emission Parameters**

There are several different types of laboratory studies that investigate relationships between various parameters. For most studies, correlations are established between the inherent rock properties (ie. microstructure, texture and composition) and mechanical and acoustic emission parameters. This section will review literature related to several types of comparative studies.

#### **3.7.1 Grain Size and Grain Density**

Dreyer (1972) demonstrated that the cubical compressive strength of rocksalt increases with increasing grain density. He stated that the strength increases with the granular density, where it reaches a maximum compression strength value for a given surface density greater than 10 grains per  $\text{cm}^2$ . Olsson and Peng (1976) observed similar results, where the yield strength of marble increases linearly with increasing grain density. The grain density was defined as the inverse square root of the mean grain size. Onodera et al. (1980) and Hugman and Freeman (1979) also reported that there is a definite relationship that exists between grain size and the mechanical properties from the various rock types tested.

Various relationships between acoustic emission response with respect to grain size have been reported by Scholz (1968a), Mogi (1962) and Fonseka et al. (1985). The main emphasis of these studies is to establish a relationship between acoustic emission parameters (most often the acoustic emission rate, cumulative count and energy), grain size and composition.

Laboratory investigations conducted on rocksalt show that the grain size has an effect on the strength and the flow rate [Aubertin et al. (1987)]. The larger the grain size, the faster the deformation rate [Dreyer (1972) and Serata et al. (1978)]. Also, high plasticity has been observed to be associated with samples with larger grain size [Olsson and Peng (1976)]. The degree of strain hardening effects and strength, with respect to grain size, are lower for samples with smaller mean grain size.

Homogeneity, which is a function of grain size in a crystalline mosaic, displays a strong correlation with the cubical compressive strength of rocksalt [Dreyer (1972)].

### **3.7.2 Grain Shape and Degree of Interlocking**

The grain roughness coefficient, which was used by Onodera et al. (1980), showed that the axial stress on the sample approached the strength as the roughness value of the grain decreases. The roughness is defined as a function of the degree of the grain deviation from an inscribed circle. Dreyer (1972) reported that the cubical compressive strength of rocksalt decreases with increasing index of structural interlocking. Also, high interlocking values give rise to an increase in rock strength. Thus, it appears from these observations that there is a relationship between mechanical parameters and grain shape.

### **3.7.3 Mineral Components**

Mineral constituents in rock types have been evaluated either by determining the bulk chemical composition or by modal analysis using planimetric methods. An effective systematic study was conducted by Dreyer (1972) to determine the influence of mineralogy on the behavior of various types of rocksalt. In general, the strength of the rock decreases with increasing number of mineral components. This is primarily due to the elastic mismatch of adjacent differing mineral phases.

### **3.7.4 Grain Boundary Density**

Rodgerson (1974) has stated that in metallurgical materials, the grain boundary density along various orientations has an effect on the strength and deformational behavior. The fabric alignment of various rock types has a predominant effect on the fracture process and acoustic emission rate [Attewell and Sandford (1974a), (1974b) and (1974c)].

### **3.7.5 Textural Models**

Textural models are defined on the basis of multivariable regression analysis. In most instances, the models define coefficients of texture and composition with respect to the parameters previously discussed. Dreyer (1972) has given a detailed coverage of this subject. The models reported by Dreyer (1972) were developed specifically for rocksalt and indicate the combined effect of grain size, grain density and composition in determining the rock strength.

### **3.8 Results of the Textural and Compositional Analysis of Potash Rock**

#### **3.8.1 Average Grain Cross Section and Textural Homogeneity**

The average grain cross section representing a measure of grain size, was determined from black and white photographs of the specimens. Two to six times magnification was the optimal range to photograph and measure the features. When parameters were deemed to be difficult to measure, both the actual etched specimen and photograph would be used simultaneously to trace out the distinguishable features.

Three orientations of the same potash type were prepared to measure the features. These include two vertical planes, perpendicular to each other, and one horizontal plane. Type "A" potash rock displays on average, a slightly smaller grain size along the horizontal plane, as compared to the vertical planes. Observations along heavily banded samples display biased results, since bands can display variation in grain size between adjacent bands. The values for average grain cross section, textural homogeneity and structural interlocking for the four types of potash rock are tabulated in table 3.1.

The values for average grain cross sections are well represented for types "A", "C" and "D" potash rock. This can be said since the textural homogeneity values are indicative of uniform grain distributions. The value of textural homogeneity is low for type "B" potash, coinciding with a bimodal grain size distribution. Type "B" and "C" show similar average grain cross section values although their distinction is established by the textural homogeneity value, it being much lower in type "B" than in type "C" potash rock.

#### **3.8.2 Structural Interlocking**

Structural interlocking values have also been measured from the photographs. The values obtained for type "B" potash display values three to four times greater than the other three types (refer to table 3.1). This indicates that type "B" potash rock shows grains predominantly with highly convex perimeters. This observation is clearly indicative by the highly irregular shaped porphyroblasts of sylvite grains forming the groundmass of the rock. Low values, as measured for types "A", "C" and "D" coincide with crystal grains that are roughly equidimensional in shape (refer to tables 3.1 and 3.2)

### **3.8.3 Textural Anisotropy**

Type "A" potash rock is the only rock type in the spectrum of this study that displays external grain shape anisotropy. The anisotropy is characterized by grains elongated parallel to the vertical planes. This structural grain deformity is consistent throughout the cut plane of the specimen. A cross sectional cut along the horizontal plane displays uniform equidimensional circular grain shapes. The anisotropy can be categorized as linear-planar according to Underwood (1970).

### **3.8.4 Mineral Composition**

Variations of mineral composition of the four types of potash rock is not pronounced. Type "B", "C" and "D" potash rock show similar values of sylvite and halite in a ratio of approximately 2 to 1. Type "A" potash rock is generally halitic, composed of halite and minor amounts of sylvite. Clay occurs in minor to trace amounts in all four types of potash rock.

The distinction between the grain characteristics within each mineral phase was not determined. That is to say for example, the distinction between red sylvite and red rimmed sylvite was not made, but simply measured as a single constituent. This distinction is not significant in this study, but the relevance of mineral concentrations are. According to Dreyer (1972), textural properties and composition of a rock display a correlation with its mechanical properties.

Structural banding, lenses, clots and monomineralic aggregate clusters did not affect the results. Area fraction measurements were conducted on specimens with large measuring surface area. Mineralogical values for each type of potash were normalized and are shown in table 3.1.

Table 3.1: Textural parameters and mineralogical ratios of various types of potash rock.

Rock Type	Average Grain Cross Section (mm)	Grain Density (1 / M)	Structural Interlocking	Textural Homogeneity	
Type "A"	28.57	0.0350	9.19	1.71	
Type "B"	33.57	0.0298	26.73	0.41	
Type "C"	27.53	0.0360	7.22	1.67	
Type "D"	25.53	0.0392	6.53	1.85	
MINERALOGICAL COMPONENTS		GRAIN SIZE VARIATION OF DIFFERENT TYPES OF POTASH ROCK			
		"A"	"B"	"C"	"D"
Halite		large	coarse	coarse	coarse
$\alpha$ Halite		medium	med-crse	medium	coarse
$\beta$ Halite		small	small	small	---
Rimmed Sylvite		small	v.large	medium	medium
Uniform Sylvite		small	medium	small	---
Clay insolubles (patches)		fine-med.	fine-med.	fine-med.	fine-med.
MINERALOGICAL COMPONENTS		PERCENTAGE OF MINERAL COMPONENT PRESENT IN DIFFERENT POTASH ROCK TYPES			
		"A"	"B"	"C"	"D"
Halite ( $\alpha$ Ha, $\beta$ Ha, Ha)		97.14	28.63	33.65	70.13
Sylvite		2.43	68.41	63.13	28.82
Insolubles (Clay)		0.44	2.96	3.22	1.05

Table 3.2: Petrofabrics and variation in the grain shape of different potash rock types.

POTASH TYPE	GRANULARITY	TEXTURE		
"A"	equicrystalline	anisotropic halite mosaic		
"B"	inequicrystalline porphyritic	poikiotopic sylvite groundmass dispersed halite		
"C"	equicrystalline	interlocked sylvite groundmass monocrystalline clusters of halite		
"D"	equicrystalline	polycrystalline halite mosaic		
MINERALOGICAL COMPONENTS	POTASH TYPE			
	"A"	"B"	"C"	"D"
Halite	elongated	equidim.	equidim.	equidim. to irreg.
@-Halite	irreg.	rect./ irreg./ rounded	rect./ irreg./ rounded	equidim. to irreg.
B-Halite	rounded	rect./ irreg./ rounded	rect./ irreg./ rounded	----
Rimmed Sylvite	irreg.	equidim./ irreg.	equidim./ irreg.	irreg.
Uniform Sylvite	irreg.	equidim./ irreg.	equidim / irreg.	----
Clay insolubles (patches)	irreg. to laminations	irreg. to laminations	irreg. to lamination	irreg.

## **Uniaxial Compression Testing of Rock Under Laboratory Testing Conditions**

### **4.1 Introduction**

This chapter reviews the elements involved in testing the mechanical properties of rock under laboratory testing conditions. Potash rock displays various petrographic properties that control the mechanical behavior under various loading conditions [Dreyer (1972) and Aubertin (1987)]. Michel (1966) and Serata (1964) have shown that saline rock displays a homogeneous and isotropic behavior although, various textural anisotropies exist on the grain size scale. Most reported results from these studies also show a non-linear stress-strain relationship. Serata (1968) conducted uniaxial compression tests and noted brittle behavior in salt rock. Under increasing confining pressure and temperature more ductile conditions were prevalent. Baar (1977), Odé (1968), Dreyer (1972) and Spencer (1977) noted that rocksalt has a low elastic limit. Dreyer (1972) has also conducted a detailed study on rocksalt behavior as it is affected by mineralogical and textural nature, relative humidity, loading rate and tempering. Rocksalt is also a very soft material which facilitates sample preparation for testing. However, cautionary measures must be taken to ensure proper sample preparation due to the mineralogical components, cleavage properties and solubility effects [Baar (1977)].

### **4.2 Review of Experimental Compression Testing of Rock Specimens**

#### **4.2.1 General Overview**

This study will conduct uniaxial compression tests on potash. Three types of compression experiments are frequently used to investigate rock deformation under laboratory testing conditions [Spencer (1977)]. These tests include the creep, stress-strain and strain rate. The creep test involves an axial stress built up rapidly on the specimen. It is then held constant as the sample deforms. Strain is measured as a function of time. In the stress-strain test, the rate of strain or stress is constant. The changes with the applied stress are plotted against displacement. Finally, in the strain rate test a constant stress is applied and the strain rate is measured. Stress is displayed as a function of strain rate [Spencer (1977)].

The usual procedure in designing an experiment is to control all the variables, except one, and observe the effects when changing that variable. Variables fall into two categories: the environment of deformation ( pressure, stress, strain rate) and, the nature of the rock material (composition, grain size, homogeneity and texture) [Spencer (1977)].

The stress-strain test is considered for this investigation. The dependent variable will be load (stress), which will rise to the samples' ultimate strength and then diminish in the post failure region. It is possible to obtain a complete stress-strain relationship due to a 'controlled' failure, on a servo controlled hydraulic press. This is accomplished by a total control of, the stored strain energy from the machine and rate of displacement applied to the sample [Hassani (1980)]. A constant displacement rate is maintained by the closed loop operation of the servo-system which continuously adjusts the actual displacement [Brady and Brown (1985)].

#### 4.2.2 Uniaxial Compression Testing

A pure uniaxial compressive state of stress must satisfy the following conditions [Dreyer (1972)]:

$$\sigma_1 = 0, \sigma_2 = 0, \sigma_3 = -\sigma \quad 4-1.$$

where ' $\sigma$ ' denotes the magnitude of the uniaxial stress. Pure uniaxial compression implies that the same state of stress prevails in the specimen, in every homogeneous and isotropic 'element'. The applied stress to the sample is equal to the average stress in each portion of the sample [Dreyer (1972)]. In general, the axial force is recorded throughout the test. The initial cross-sectional area of the specimen divided by the axial force, will give as a result the axial stress. The stress is then plotted as a function of strain. This graphical representation shows the behavior of the material.

The stress distribution in the sample is non-uniform due to the end effects associated with the elastic mismatch between the rock and the testing apparatus. The specimen is restrained near its ends, and prevented from deforming uniformly. A sample being compressed in a uniaxial state of stress tends to expand laterally, as it is subjected to shortening due to the Poisson effect [Dreyer (1972)].

Due to the end effects, the stress distribution varies throughout the sample and is a function of sample geometry. As the height to diameter ratio ( $H/D$ ) increases, a greater proportion of the sample volume is subjected to an approximately uniform state of uniaxial stress. Stress distributions can be visualized as contour lines of equal principle stress for samples with different height to diameter ratios. Lama and Vutukuri (1978b) observed the stress distribution under uniaxial load, and concluded that there are two major regions. The first region contains biaxial compressive stresses near the contact surfaces of the sample and the other region, the platen, contains

tensile stresses in one axis. Radial shear lines originate from the ends. The compressional biaxial stresses induce a strengthening effect while the tensile stresses produce a weakening effect. It is for this reason that the sample height to diameter ratio should be of at least 2.0 [Lama and Vutukuri (1978a)].

Platens, with the same diameter as the sample, produce a more uniform stress field than those that are larger than the samples. Insertion of materials or lubricants have also been placed along the sample-platen interface in order to ensure a uniform stress field. [Lama and Vutukuri (1978b)]

Samples loaded under uniaxial compression display three modes of failure: the conical wedge shaped end segments of the failed sample, the slabbing effect in which the major cracks develop parallel to the direction of the applied force and, the shear or failure oblique plane effect which is due to platen rotation or lateral translation.

Cone shaped specimens formed under uniaxial compression are accounted by the platens producing a lateral constraint within the hatched zone (refer to figure 4.1). A lateral stress inhibits crack growth thus producing the double ended cone shaped samples. Since axial stress is greatest at the center, fractures will be initiated in that area. Areas outside the hatched zone develop an intermesh of branching cracks oriented parallel to the axial load. However, due to the radial constraint, these cracks should not penetrate the hatch zone, but rather contribute to the total fracture along lines intersecting the diagonals of the sample [Lama and Vutukuri (1978a)].

#### **4.2.3 Influence of the Testing Machine Stiffness**

The deformational characteristics of the sample are dependent on the relative stiffness of the sample and the testing machine [Hassani (1980)]. Figure 4.2 depicts the interaction between the sample and the testing machine. In order to understand the sample machine interaction, it is necessary to assume that this interaction is a spring loaded system in parallel orientation. Also, one must assume that the machine is represented by a linear elastic spring of constant longitudinal stiffness, ' $k_m$ ', and that the specimen has a non-linear response with a varying stiffness, ' $k_s$ '. When the specimen is loaded in compression, the springs of the machine extend and the sample is compressed. Note that by convention, deformation and forces are positive in compression and negative in tension (refer to figure 4.3). The stiffness is defined as followed:

$$k_i = \frac{dF}{dX_i}$$

4-2.

where 'i' can be either machine (m) or specimen (s); 'k' stiffness and 'F' the force. The linear system can be represented by the formula used by Hassani (1980) and Brady and Brown (1985):

$$F = -k_m \cdot x_m \quad 4-3.$$

and the specimen as :

$$dF = k_s \cdot dx_s \quad 4-4.$$

Note that these signs are reversed after post-peak strength of the material.

The total work strain energy, ' $W_m$ ', done by the machine can be represented as the area under the curve (refer to figure 4.4), as seen below:

$$W_m = \int_0^{x_i} -F_m dx \quad 4-5.$$

Similarly, for the sample, the total strain energy is given by the following:

$$W_s = \int_0^{x_i} F_s dx \quad 4-6.$$

The system in equilibrium is represented by the following relationship [Hassani (1980)]:

$$-k_m \cdot x_m = k_s \cdot dx_s \quad 4-7.$$

When the peak strength is reached, there are two situations that can occur depending if the testing machine is 'stiff' or 'soft' with respect to the specimen being tested. In the former case, the stiffness of the machine is greater than the sample i.e. it has a higher machine stiffness value and a steep gradient defining the slope. It is represented as:

$$k_m > k_s \cdot dx_s \quad 4-8.$$

In such a case, the total strain energy of the machine is less than the total strain energy of the sample. The excess energy needed in order to deform the specimen must be supplied. As a result, a post peak deformation pattern with decreasing load is observed. But, if the specimen is stiffer than the test machine; ( $k_m \leq k_s \cdot dx_s$ ), the post peak displacement,  $\Delta x$ , occurs from point A, and only to point B (see figure 4.4). The released stored energy of the machine is much greater than the specimen and as a result, due to this greater release of energy, a catastrophic failure occurs.

#### 4.2.4 Deformation of Rock

Representations of characteristic deformation patterns of rocks are seen by plotting the stress or stress difference ( $\sigma_1 - \sigma_3$ ) against strain.

On the basis of the stress-strain curves three patterns of mechanical behavior can occur. The first pattern is the linear elastic relationship, the second is the relationship whereby a pronounced strain is observed for every increment of increasing stress and the third is a slow increase in strain with every increasing increment of stress. The second type of pattern displays a high modulus of elasticity at early stages of the load cycle and then decreases continuously. The third type of behavior is typical of rocksalt and is referred to as the strain hardening effect by Dreyer (1972) and Spencer (1977).

At room temperature rocksalt shows a brittle behavior. The fracture pattern corresponds to a noticeable absence of plastic deformation at loads which have reached specimen failure. Under uniaxial compression the failure point is well defined [Serata and Gloyma (1960) and Baar (1977)]. Gilbert and Farmer (1981) have shown the strength of salt by Q-P diagrams, whereby 'Q' corresponds to the deviatoric stress and 'P' is the average stress in triaxial compression. They can also be expressed as followed:

$$Q = P(\sigma_1 - \sigma_3) = \frac{3}{2} \tau_{oct} \quad 4-9.$$

$$P = \frac{1}{3}(\sigma_1 + 2\sigma_3) = \sigma_m \quad 4-10.$$

According to Dreyer (1972) tempering can be used to remove the in-situ loading effects. A period of 8 hours is required to erase the previous stress memory. He also observed that faster loading rates were associated with smaller measurable deformations. More explicit details of the results are shown and discussed in the above reference.

#### 4.2.5 Determination of Elastic Constants

Many laboratory investigations of evaporites reported elastic constants. The most common parameters described are uniaxial compressive strength, modulus of elasticity, stem modulus and Poisson's ratio. The uniaxial compressive strength is the stress value at failure and is defined as followed:

$$\sigma_c = \frac{F}{A} \quad 4-11.$$

where ' $\sigma_c$ ' is the uniaxial compressive strength, ' $F$ ' is the applied force at failure and ' $A$ ' is the initial cross sectional area.

The relationship between the stress-strain curves can be represented by constants which are called the elastic constants [Lama and Vutukuri (1978b)]. These include the Young's modulus of elasticity (symbolized as 'E'). For rocksalt, the modulus is only defined for the elastic portion of the stress-strain curve and it is found to be very low. According to Dreyer (1972) after 8Kp/cm<sup>2</sup> the strain increases nonlinearly under uniaxial load conditions. The initial Young's modulus ('E') is calculated from the slope angle of theta (θ) as shown in figure 4.5. The Young's constant 'E' can be derived from the secant or tangent value. The tangent value can be calculated as follows:

$$E_t = \left( \frac{d\sigma}{d\epsilon} \right) \cdot \sigma_1 \quad 4-12.$$

The 'E<sub>p</sub>' corresponding to the plastic region is then defined as 'Δσ' and 'Δε' of the sample upon unloading [Dreyer (1972)]:

$$E_p = \frac{\Delta\sigma}{\Delta\epsilon} \quad 4-13.$$

The elastic modulus in the plastic region is defined as:

$$E_p = t_\sigma \delta \quad 4-14.$$

where 'E<sub>p</sub>' is the slope of the tangent to the unloading curve at any stress level.

Figure 4.5 defines the region of the curves.

The shear or bulk modulus has also been measured. It is defined as the value of hydrostatic pressure divided by the volumetric strain.

Material property values for rocksalt are variable. The reported values for uniaxial compressive strength range from 19 to 30MPa.

The value for the Young's modulus of elasticity for evaporites displays the most variability. Reported values range from less than 3GPa to as high as 35GPa with an average of 25GPa. According to Dreyer (1972), the relationship between the Young's modulus of elasticity and the applied stress varies due to rock ductility, and it is therefore not suitable for true elastic modulus values of the rock. Lama and Vutukuri (1978b) have attributed modulus increase to the collapse of pores and closure of microcracks. They have also stated that the increase in 'E' with increasing stress was due to extensive crystal deformation in the form of dislocation and cleavage.

The Poisson ratio values reported are also variable, ranging from 0.17 to 0.45. The shear modulus also shows a wide range of values from 1.6 GPa to 32.2GPa.

### 4.3 Factors Affecting the Stress-Strain Curves

#### 4.3.1 Sample Geometry and Microstructure

According to Lama and Vutukuri (1978b), test samples can be cylindrical, prismatic or cubic in shape. Cylindrical shaped samples are preferable because they are easier to prepare and their shape dimensions are accurate. As for the effect of shape on the strength of the rock, various results have been reported. Rock samples which do not contain much inherent microstructure do not vary significantly in terms of the modulus of elasticity. Lama and Vutukuri (1978b) reviewed tests on marble with various height to diameter ratios ranging from 0.33 to 3.0. Results for Young's modulus of elasticity were similar: using samples with different diameters will not significantly change the results. A change in the size of non-homogeneous rock specimens will likely introduce the number and type of defects present in the sample thus, producing variable results. The influence of shape becomes significant when the height to diameter ratio is greater than three.

#### 4.3.2 Height to Diameter Ratio

The ratio of the height to diameter of samples influences the test results. Stress distribution in samples with ratios near unity tend to exhibit a high compressive strength. Large height to diameter ratios fail prematurely due to instability. Lama and Vutukuri (1978b) presented results for potash samples with height to diameter ratios ranging from 0.5 to 4.0. The following experimental relationship was established for the test results:

$$\sigma_c = a \left( \frac{d}{h} \right)^b + C \quad 4-15.$$

Where 'a' ranges from 10 to 24 MPa; 'b' ranges between 1.1 to 2.1 and 'c' ranges from 16 to 28 MPa. For rectangular shaped samples, the variation in height effects is much greater than changes in the lateral dimension of the specimen [Dreyer (1972)]. The strength decreases with increasing height for a certain cross sectional distance along the specimen. For weak rocks, it is difficult to obtain samples having an appropriate height to diameter ratio. In such cases, in order to calculate the compressive strength, the ratio is determined by extrapolating and inserting the data into an empirical relationship. This relationship, presented below, has been reported by Dreyer (1972):

$$\sigma_c = C \left( \frac{d}{h} \right)^n \quad 4-16.$$

where the values of 'C' and 'n' are defined as constants.

Height to diameter ratios for rocksalt have been studied by Serata (1964). He observed that there is an increase in strength with increasing height to diameter ratios. For graphical representation of the test results, one can refer to the above reference.

#### 4.3.3 The Effect of Grain Size

Laboratory investigations conducted on rocksalt have shown that the flow rate is dependent on grain size. Dreyer (1972) and Le Compte (1965) observed that faster deformation occurs with larger grain size. Stokes (1966) noted that high plasticity was associated with large grain sizes of the specimens. The degree of hardening and strength, in relation to larger grain sizes within individual samples, were also lower than those found in samples with smaller grain sizes. Brace (1961) also observed the same trend for various other rock types. A relationship was developed to show this correlation and is commonly referred to as the Hall-Petch [Aubertine et al. (1987)]:

$$\sigma = \sigma_0 + k d^{\frac{1}{2}} \quad 4-17.$$

where ' $\sigma$ ' is the failure stress, ' $\sigma_0$ ' and ' $k$ ' are material constants and ' $d$ ' is the average grain size. It was also noted by Hardy (1982) that samples with a characteristic large grain size also fragment easily along the edges of the specimen during sample preparation.

Dreyer (1972) stated that the strength of cylindrical samples of polycrystalline rocksalt increases when the granular density (grains per cm<sup>2</sup>) increases. It reaches a maximum uniaxial compressive strength at 60 grains per cm<sup>2</sup>. This is applicable for average grain diameters of 6.2 mm. Such a value was derived by establishing a correlation between the cubical compressive strength and the number of grains per unit area of a sample. After an initial increase, the curve asymptotically approaches the value of 60 grains per cm<sup>2</sup>. In similar tests, Serata (1964) suggests at least 1000 grains per sample. Brady and Brown (1985) suggest that the sample diameter should be at least ten times the largest grain size in the specimen.

#### 4.3.4 Platen Conditions

According to Lama and Vutukuri (1978b), the end contacts between the platen and sample develop friction. It can be measured as the coefficient of friction between the plate and the specimen surface.

Various types of materials and platen surface textures have been considered for testing. Surfaces can be rough, smooth, rigid, brush or relative in diameter with respect to the specimen. Rough platens induce high friction and high confinement regions extending into the specimen in which the stress distribution is non-uniform [Lama and Vutukuri (1978b)].

#### **4.3.5 The Effect of Loading Rate**

The compressive strength and brittleness of rocksalt are increased with increasing rate of load. According to Dreyer (1972) and, Carter and Heard (1970), an increase in the modulus of elasticity, and higher strength are also present. Serata et al. (1978) and Dreyer (1972) observed that the strength decreases, when the rate is continually increased.

The load can be applied under strain or stress control mode. In general, a relationship was developed by Lama and Vutukuri (1978b) to establish the loading rate, it reads as followed:

$$\text{stress rate} = (\text{strain rate}) (E) \quad 4-18.$$

It was observed that the modulus can rise for different loading rates. The effect of strain rate, in post yield curves of evaporites, is also increased with increasing temperature. Lama and Vutukuri (1978b) found that strain hardening increases rapidly with increasing strain rate.

Homogeneous, strong rocks with low porosity which display linear elastic behavior, will not be affected by increased strain rate [Lama and Vutukuri (1978b)]. Rocks that show transitional and ductile deformation with increasing compressive load, show an increase in Young's modulus or, no increase with strain.

The ISRM Commission (1979) recommends that a loading rate of 0.5 to 1.0 MPa per second be used in uniaxial compression tests. This corresponds in time to the attainment of peak strength in the order of 5 to 10 minutes. The times to peak strength correspond to axial strain rates in the order of  $10^{-5}$  to  $10^{-4}$  per seconds. For evaporites, departures from the prescribed strain rates by 1 or 2 orders of magnitude produce minor differences [Brady and Brown (1985)].

#### **4.3.6 The Effect of Moisture and Humidity**

Depending on the humidity of the testing and storage environment, salt can behave as a 'hygroscopic' material, in the sense that it can absorb water from the atmosphere [Lama and Vutukuri (1978b)]. This is known as the 'Joffé Effect'. This effect is prevalent when the humidity is greater than 75%.

The Joffé Effect is a surface effect in which partial surface recrystallization occurs along the external region of the specimen. This raises the plasticity by lowering the elastic limit [Mendelson (1962)]. Water absorbed on the surface stops the reaction between the air and salt, and can thus weaken the surface by generating a barrier in the crystalline structure.

Immersing the specimen into a solution leads to recrystallization, forming an external ring, which results in an increase deformation rate and shorter time to failure [Varo and Passaris (1977)].

According to Lama and Vutukuri (1978b), moisture content in the sample has an effect on reducing the compressive strength of the rock. Also, increasing the humidity increases the deformation rate. They have suggested to store the samples 5 to 6 days in an environment of  $20 \pm 2^\circ C$  with a 20% relative humidity. The moisture conditions should also be noted.

#### **4.3.7 Mineral Components and Texture Effects in Relation to the Mechanical Behavior of Evaporites**

A systematic study was conducted by Dreyer (1972) to determine the influence of texture and mineralogy on the behavior of various rocksalt types. The uniaxial compressive strength of rocksalt increases with increasing content of secondary minerals. The amount of secondary minerals must exceed 1.5% in order to have any effect on the strength. This relationship is shown below:

$$\sigma_c = D(1.00 + 0.0115K + 0.0071A + 0.0079P) \quad 4-19.$$

where 'K', 'A', 'P' are the strengths of keirsentite, anhydrite and polyhalite respectively.

It was also reported by Dawson and Munson (1983) and Serata (1968) that the flow rate decreases with increasing amount of impurities in the specimen. This is due to the brittleness of the secondary and minor mineral components. It was also shown by Dreyer (1972) and Serata (1968) that the texture and grain size affect the flow behavior of rocksalt.

#### **4.4 Elastic Plastic Transition**

Several studies conducted on rocksalt loaded at constant strain rate display four regions along the stress-strain curve. These include the following regions:

- 1) region of elastic deformation
- 2) transient region whereby strain hardening effects occur
- 3) region of steady state flow at constant stress

4) region of decrease in stress until unstable fracture propagation occurs

Strain hardening of polycrystalline solids has been proposed to be due to dislocation mechanisms activated in crystals. These crystals deform in this manner because of imperfections which lead to glide at low shear stresses. Plastic deformation requires that a large amount of dislocation occurs. In most cases, it is also responsible for the low shear strength of individual crystal grains [Dreyer (1972) and Spencer (1977)].

Models for dislocation theory consider strain hardening to take effect with increasing deformation. The effect is due to the interaction of pre-existing defects in crystal lattice structure.

Spencer (1977) proposes five groups based on the percentage of strain produced in a given sample under uniaxial load conditions. The spectrum is presented from the transition of brittle to ductile deformation as shown in figure 4.6. The time factor varies with rock deformation. This can be observed in two types of testing conditions: creep and constant strain rate. In the former type of testing, the differential stress is maintained and strain against time is plotted. In the latter type of testing, the strain rate is constant.

There are four stages of creep which can be defined. Instantaneous elastic deformation, transient creep, steady state creep (with a steady strain rate) and accelerated creep (strain rate increases) [Spencer (1977)]. These stages are depicted on a 'rheogram', which is a graphical plot of a flow diagram. It represents the cyclic time deformation relationship of specimens loaded to various stress levels [Aubertin et al. (1987)]. The stress remains constant for each load level until the material stops deforming. The stages are divided on the basis of changing deformation rates [Aubertin et al. (1987)]. Figure 4.7 diagrammatically represents the components and stages identified on a flow diagram. According to Hardy (1982), Serata (1960) and Butcher (1980), a more detailed subdivision of the stages along the flow curves can be identified. These include the primary flow, secondary or stationary flow and rupture or tertiary flow. When the load is removed, partial recovery of the elastic strain portion, or stage one of transient creep, takes place.

The second type of test configuration (constant strain rate) can also be used to show the rheological behavior of materials and once again the four stages can be identified on curves defined by ' $\sigma_1 - \sigma_3$ ' plotted over the strain rate ' $\dot{\epsilon}$ ', [Aubertin et al. (1987)]. Micromechanisms of creep within rock include fracturing, recrystallization, gliding, dislocation pile-up and grain boundary adjustments.

The majority of these plots can take the form of empirical relationships between stress versus time and/or strain. Various models are summarized in Spencer (1977). These models are based on material behavior. These are grouped as elastic, viscous and plastic. Various combinations of these ideal behavioral bodies are arranged in different orders depending on the behavior up to a particular stress, strain or time level. Complex models have been used to model the ideal material behavior. Components of total strain can contain purely elastic components, time dependent nonelastic and nonrecoverable components, elastic and viscous afterworking and viscous components. Some researchers have used 'pictograms' to show the model. These include the spring (for elastic components), the dashpot (for viscous components) and the slip surface (for plastic behavior).

Rocksalt displays elastic behavior until the differential stress is surpassed. Beyond this stage, the rock salt displays plastic deformation. This level is reported to be in the range of 3.5 to 5.3 MPa. Salt is considered to be an elastoplastic material with a well defined flow limit [Spencer (1977)]. According to Lama and Vutukuri (1978b), behavior of rock salt appears to conform to the majority of other rock types. Hardy (1982) has measured the compressional wave velocity of rock salt compressed under uniaxial load, and has observed that the compressional wave velocity decreases with increasing deformation, but appears only at the limit of the onset of dilatancy.

There are many factors which affect the brittle-ductile transition of rock salt which have not been covered since they do not pertain to the scope of this project. Such factors include rock porosity, temperature environment and confining pressure which affect the Young's modulus of elasticity as well as the creep properties.

Figure 4.1: Illustration of fracture pattern in compression of specimens. (a) shows the stress patterns; (b) shows the conical failure [after Lama and Vutukuri (1978b)].

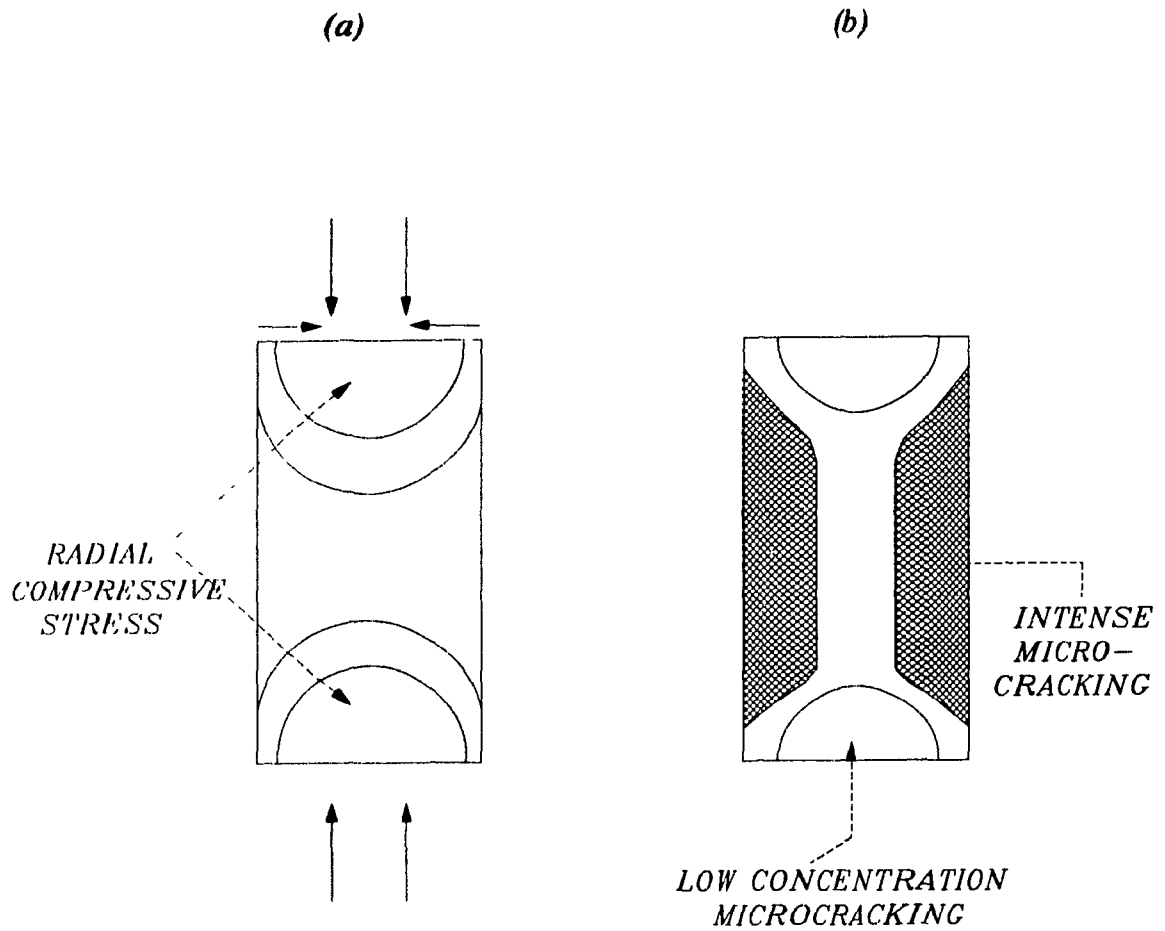


Figure 4.2: Spring analogy illustrating machine-specimen interaction [after Brady and Brown (1985)].

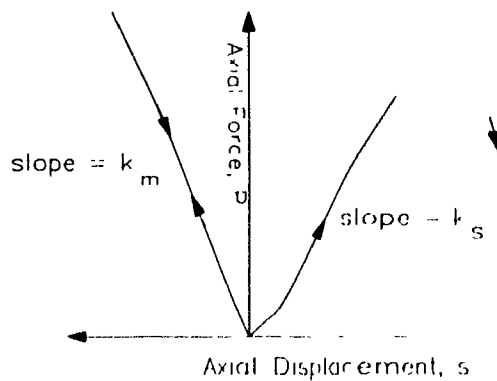
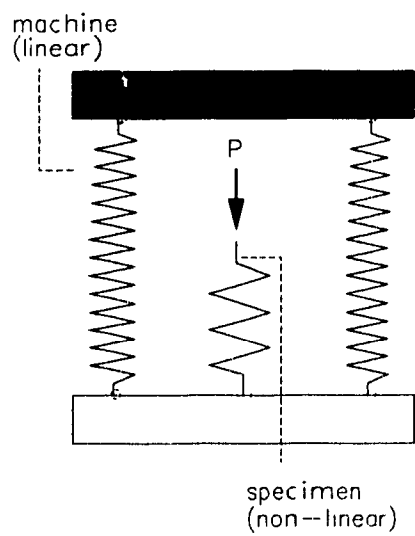


Figure 4.3: Illustration of the effect of variation in machine stiffness with respect to specimen failure.

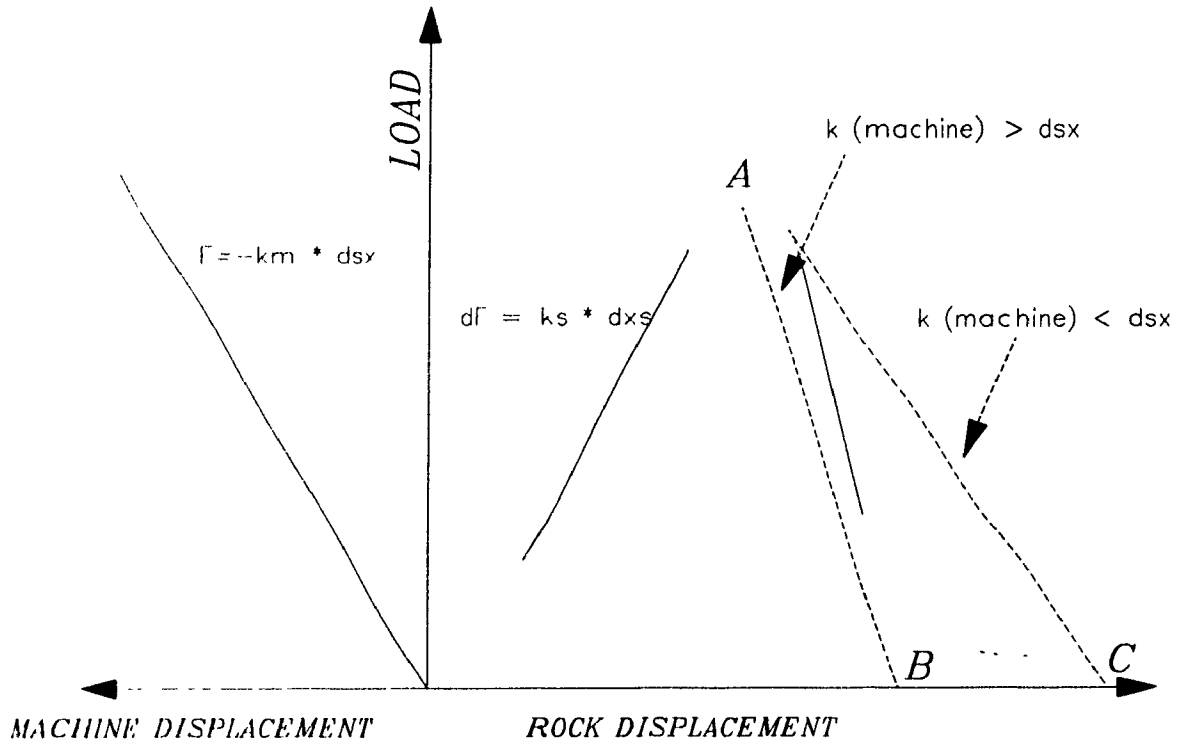
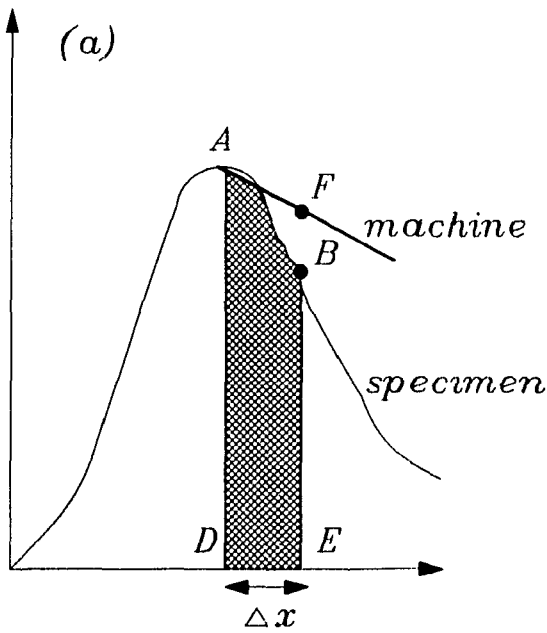


Figure 4.4: Post-peak unloading using machines that are (a) soft and (b) stiff, with respect to the specimen [after Brady and Brown (1985)].

(a)

$$\Delta W_s = ABED$$

$$\Delta W_m = \Delta W_s + AFB$$



(b)

$$\Delta W_s = ABED$$

$$\Delta W_m = \Delta W_s - ABC$$

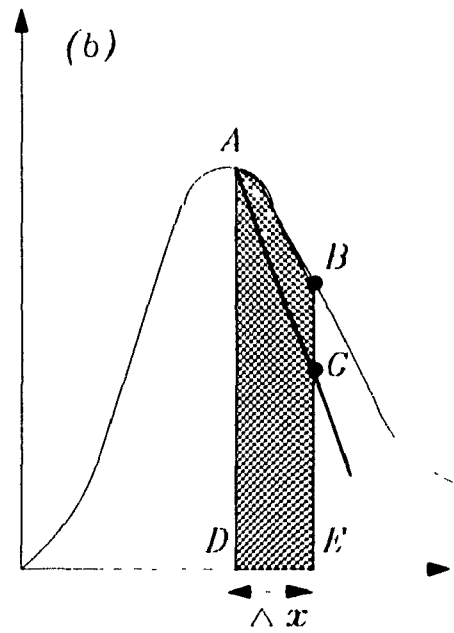
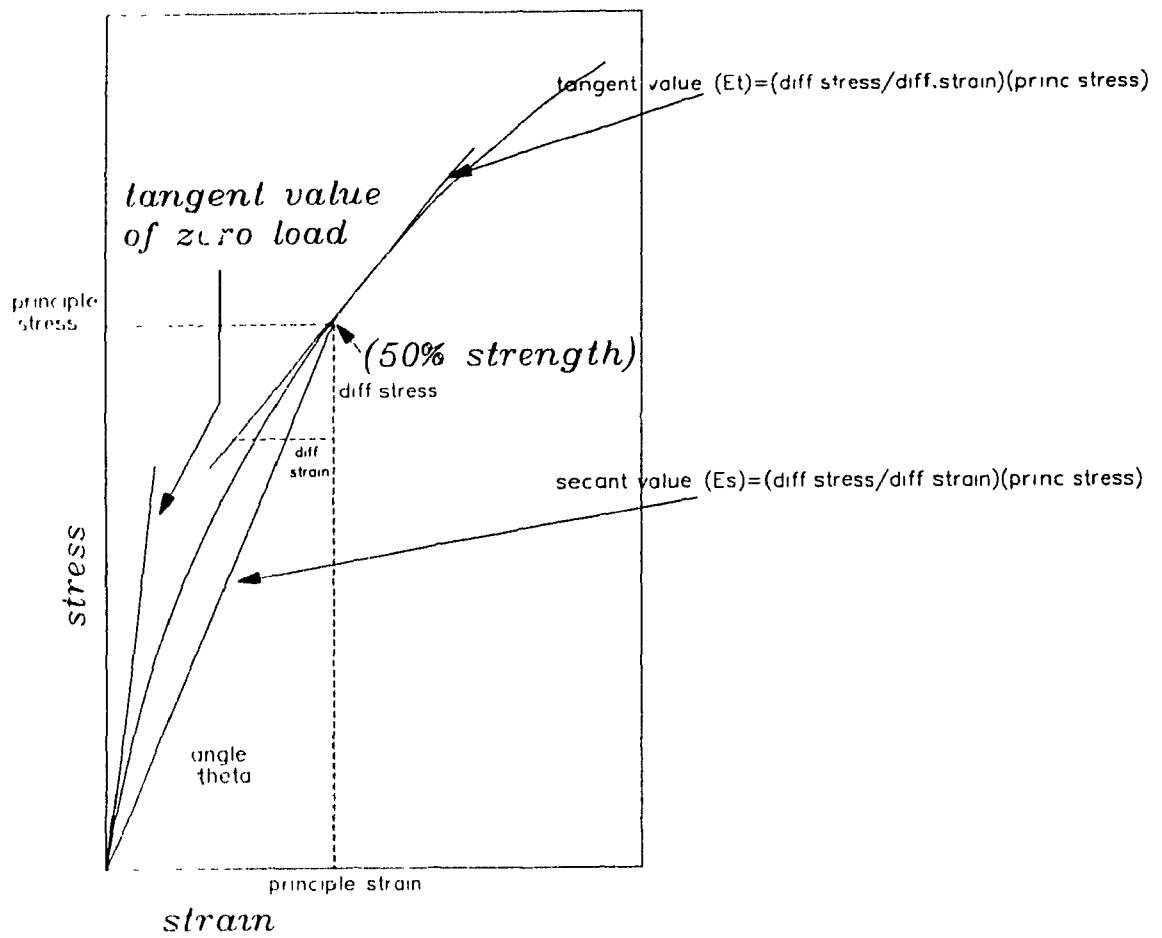


Figure 4.5: Illustration of the determination of the modulus of elasticity ( $E_p$ ) of rocksalt from stress-strain curves [after Dreyer (1972)].



**Figure 4.6:** Schematic representation of the spectrum from brittle fracture to ductile flow. The hatched areas of the stress-strain curves indicate the variation within each case and the overlap in cases 3, 4, and 5 [after Spencer (1977)]. Note that case 1 and 2 respectively represent ' $\sigma_1 > \sigma_2 = \sigma_3$ ' and ' $\sigma_3 < \sigma_1 = \sigma_2$ '. Case 3 represents the stress axis of the curves by ' $(\sigma_1 - \sigma_3)'$ '.

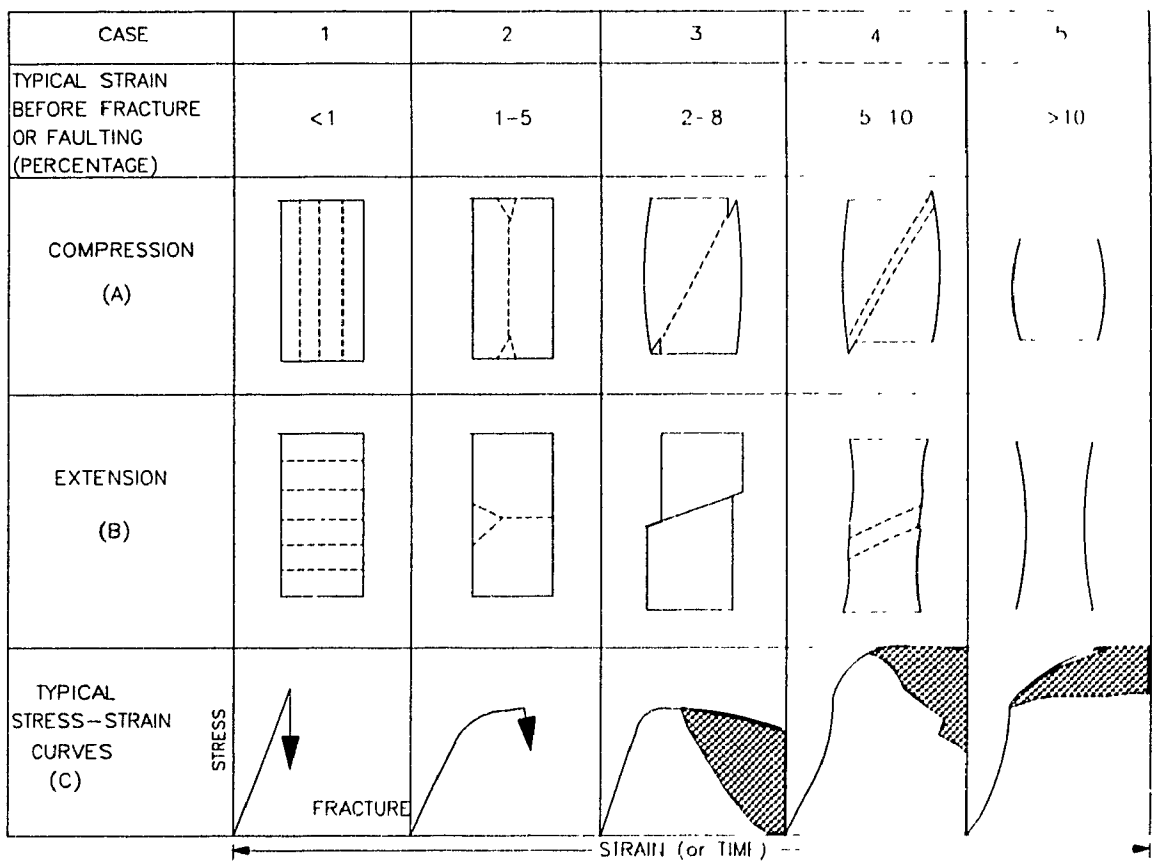
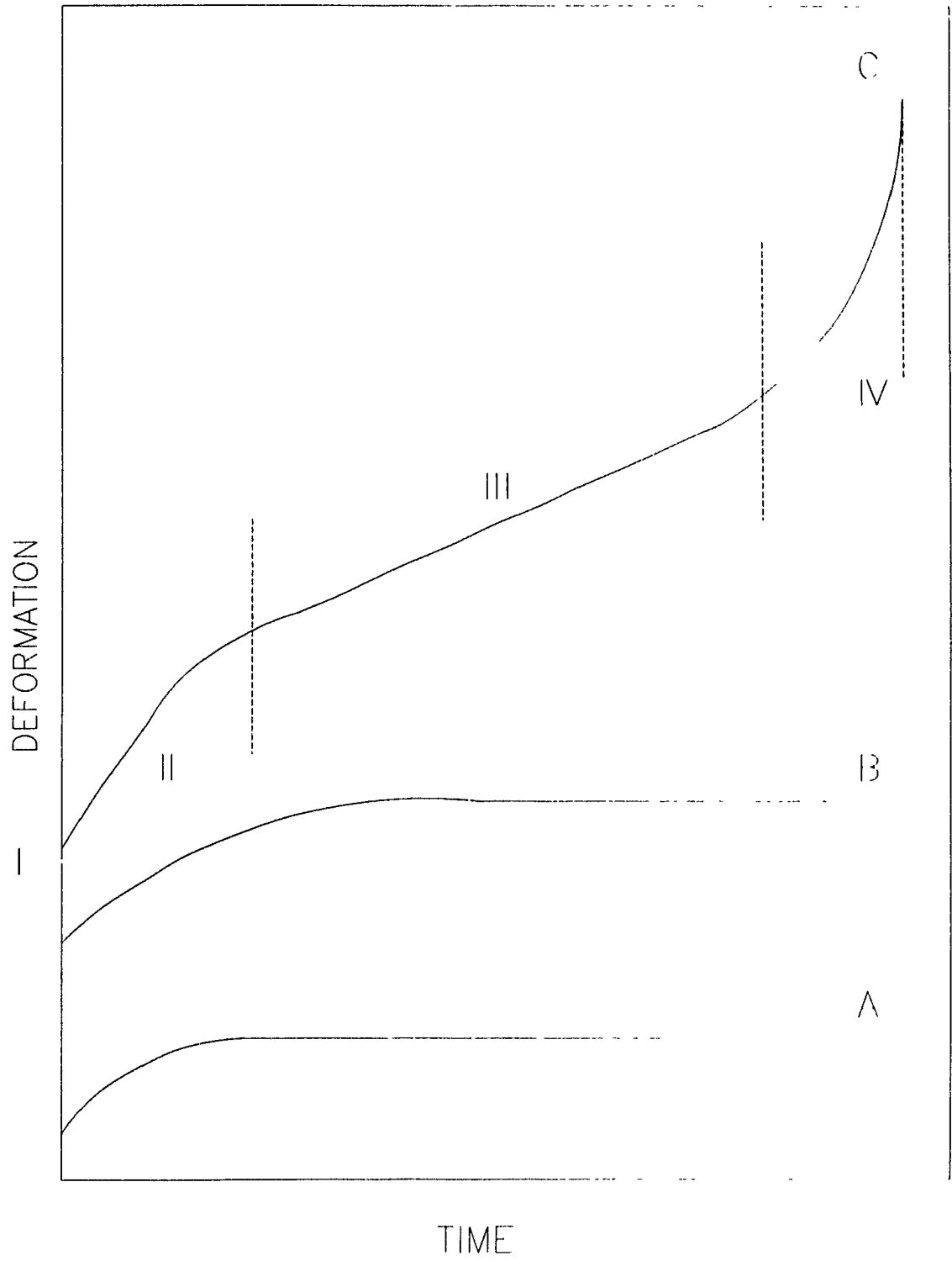


Figure 4.7: Schematic representation of the various stages of creep on the flow diagram; (I) instantaneous creep, (II) transitory creep (III) stationary creep and (IV) rupture. The three different curves correspond to different loading rates and testing temperature [after Aubertin et al. (1987)].



## **Laboratory Analysis of Acoustic Emission**

### **5.1 Introduction**

Acoustic emission monitoring has been used to evaluate the mechanical behavior of geologic materials in both laboratory and field conditions.

Acoustic emission is a class of phenomena whereby transient elastic waves are generated by the rapid release of energy via localized sources, sources within the material, or the elastic waves so generated [ASTM 610-77 (1978)]. These waves travel from the location, where the displacement or flaw was activated, to a boundary where it is measured as acoustic emission or microseismic event. There are a variety of terms used in acoustic emission literature to describe these events. A partial listing includes acoustic emission, microseismic activity, stress wave emission, elastic radiation and elastic shocks.

Laboratory studies have generally focussed on determining the fundamental material properties related to microfracturing phenomena and failure. Such techniques have been used for acoustic emission studies performed on polycrystalline and single crystals of both, rocks and metals. The rock types used include intrusive and extrusive igneous rocks (such as gabbros, granites, syenites, tuffs, and andesites), sedimentary rocks (such as sandstones, coal and evaporites, mainly rock salt), and metamorphic rocks (such as schists and gneisses). Various pure substances such as aluminum, copper and various types of alloys are used to investigate acoustic emission in metallurgical studies.

Various testing configurations, in a laboratory environment, are used to investigate acoustic emission. Uniaxial and triaxial compressive loading conditions are the most commonly reported testing conditions. Others include the three-point bending test, temperature controlled tests and tension loading conditions.

Field studies in acoustic emission are conducted on both surface and underground locations. More commonly reported are acoustic emission phenomena related to mining induced seismicity. The development of an underground opening introduces a new stress regime to the adjacent host rock. Field studies have concentrated on studying the mechanics of seismic events and rockburst phenomena as well as the structure and design in mines.

Acoustic emission analysis and monitoring are similar for both field and laboratory investigations. But, the frequency range, magnitude and occurrence over which these events are recorded are different [Hardy and Leighton (1984)]. Also, the

equipment used to monitor the events is different. In laboratory experiments, the acoustic emission rate and number of events are several orders of magnitude greater than in tests conducted under field conditions. As shown in figure 5.1, the frequency range of acoustic emission data collected in laboratory testing conditions are generally greater than  $10^2$  Hz, and those collected in field studies show ranges of less than  $10^4$  Hz.

Field and laboratory acoustic emission studies can be categorized into seven major groups. Each group covers a particular topic dealing with acoustic emission and a test environment.

The first group pertains to the effects of stress level with respect to acoustic emission trends. These trends are generally observed as acoustic emission rate, acoustic emission energy and/or acoustic emission event duration in relation to progressive changes in stress, environment and temperature. [Scholz (1968a), Montoto et al. (1984), Fonseka et al. (1985), Khair (1984), Roberts (1980), Knill et al. (1968), and Richardson (1980)].

The second group relates to acoustic emission source mechanisms. The third group deals with the relationship of acoustic emission with strain behavior due to various stress conditions. Scholz (1968b) and Sano et al. (1982) covered this subject in detail.

The fourth group is represented by the acoustic emission amplitude and energy distribution analysis. Pollock (1977) and (1980), Nakamura (1977), Mogi (1962), Scholz (1968a), Graham (1976), and Nakasa (1970) present this topic in detail.

The fifth group relates fractographic studies to corresponding acoustic emission data. The sixth group discusses the frequency spectra of acoustic emission. These acoustic emission studies include pattern recognition of events. A brief description of this analytical technique is presented in Matthews (1983).

Finally, the seventh group deals with source location studies. These studies are generally conducted in the fields but, laboratory experiments are also performed.

Only some of the groups pertaining to this study will be further elaborated in the literature review. The topics discussed include acoustic emission rate observed under uniaxial compression of rocks, acoustic emission source mechanisms, acoustic emission in relation to strain, as well as acoustic emission amplitude and energy. A brief discussion of acoustic emission response with respect to sample grain size and composition will also be presented.

## **5.3 Signal Characteristics**

### **5.3.1 Introduction**

When interpreting acoustic emission signals, it is necessary to understand the nature of the flaws of the material under investigation. The primary objective of acoustic emission work is to relate acoustic emission phenomena to mechanisms responsible for their generation [Matthews (1983)]

The analysis of acoustic emission may involve a study in the form of individual signals although more often, a study of the average properties of samples of emissions are taken over a finite time span. Types of measurements associated with an acoustic emission are shown in figure 5.2. Acoustic emission signals can be represented in frequency domain or more often in the time domain. Signal characteristics can take on many forms depending on the material and its failure mechanisms. Acoustic emission events generated from microstructure in metals and rocks (under laboratory testing conditions) generally carry information at frequencies ranging from  $10^2$  Hz to  $10^6$  Hz. An original signal that is transmitted through the material is diffracted and attenuated by the inherent properties of the material's structure. Attenuation has been thought of, as a small consequence, due to the small sample size used under laboratory testing conditions. [Matthews (1983)].

Acoustic emission signals display relatively short time duration (up to 1 micro-seconds), reach a maximum amplitude early in the signal (usually the first cycle), and decay nearly in an exponential fashion to the background noise level.

Acoustic emission signals can be classified into two types: burst and continuous emissions. The burst emissions are discrete signals related to individual emission events occurring within the material. Continuous emissions are defined qualitatively as a sustained signal level produced by rapidly occurring acoustic emission events [ASTM E610-77 (1978)].

### **5.3.2 Summary and Representation of Acoustic Emission Parameters**

Acoustic emission signal processing is based on signal characteristics including frequency, magnitude and other waveform parameters. Acoustic emission parameters are defined by events integrated over a selected time base or, measured as a cumulative value. These parameters can be interpreted and analyzed numerically and graphically.

Acoustic emissions are quantified by counting the number of times the sensor voltage exceeds a preset threshold voltage. This measurement is referred to as 'ring-down count' ('N'), and is measurable for burst type emissions [Matthews (1983)].

Parameters can be defined by discrete signal characteristics which include acoustic emission rate and energy. As well, the total count can be defined by the following parameters: rise time, events, ringdown counts, peak amplitude and event duration. The procedure for event parameter counting involves setting a threshold voltage in much the same manner as for ringdown counting. When an event of sufficient amplitude occurs, a trigger is fired and the counter increases by an increment of one. To avoid counting the same signal twice, the trigger is reset only after a time delay exceeds the ringdown time [Acoustic Emission Technology Corp. (1988)]. In most reported investigations, acoustic emission parameters are considered as a function of various physical parameters (ie. stress, strain, time, etc.).

Another group displaying the 'mean' of parameters is defined as the sum of acoustic emission data counts, divided by the number of events in that interval. These are less frequently reported. The most commonly reported is the mean or accumulated energy, ( $\Sigma$ ). The average per event or the total average can be represented by ringdown counts, event duration, rise time slope, peak amplitude and energy.

Acoustic emission sources from polycrystalline material yield different signal characteristics due to the inherent microstructure. Acoustic emission parameters have more recently been used in signal discrimination techniques including investigations into the acoustic emission event duration, ringdown counts, peak amplitude, slope, energy and rise time [Pollock (1980) and Graham (1976)]. Acoustic emission amplitude and energy distributions are used to describe more explicitly, the nature of a sample of emission data. If, as suggested by Pollock (1980), Nakamura (1977), Graham (1976), Scholz (1968a), Fonseka et al., (1985) and Mogi (1962), the gradient of the distribution of an acoustic emission parameter is related to certain mechanical and physical characteristics of the material, it may well prove to be a reliable signal analysis technique. Distribution analysis involves enumerating acoustic emission signals according to their magnitude and/or duration value.

## **5.4 Literature Review of Laboratory Studies of Acoustic Emission**

### **5.4.1 Effects of Stress Level and Associated Acoustic Emission Trends Observed in Laboratory Testing Conditions**

The purpose of such an investigation is to observe the acoustic emission response of a material in relation to the physical testing conditions.

Analysis of acoustic emission trends can involve a graphical interpretation of various acoustic emission parameters plotted as a function of load, deformation, temperature or time.

Acoustic emission trends are observed as acoustic emission event count ( $N_e$ ) or acoustic emission event count rate ( $N$ ). The acoustic emission event count refers to the number obtained by counting each discernable acoustic emission event once. The acoustic emission event count rate is defined as the time rate of the event count [Hardy and Leighton (1984)]. Stress, strain and temperature have also been measured with the corresponding time of the event count rate. Fonseka et al (1985), Montoto et al (1984), Wu and Thomsen (1975) among other authors have used these analytical techniques to observe acoustic emission trends.

#### **5.4.2 Acoustic Emission Trends Observed under Uniaxial Compressive Load**

Montoto et al. (1984) and Scholz (1968b) have observed acoustic emission rate ( $N$ ) of hard 'brittle' rocks. Three 'stages', defined by the acoustic emission rate, can be distinguished for specimens loaded to failure under uniaxial loading conditions. Stage one consists of high acoustic emission activity. Stage two is characterized by a decrease in acoustic emission activity and/or a quiescent period, corresponding to the linear-elastic behavior of the rock. It is reported to occur between 30% to 60% of the failure strength. Stage three is characterized by limited acoustic emission activity observed up until 70% to 80% of failure strength. This is followed by an accelerated increase in acoustic emission rate near sample failure, coinciding with dilatation and volumetric increase of the specimen. New cracks, crack interactions, coalescing and shear movement are observed.

Fonseka et al. (1985) observed a similar trend as the one described above, however they reported five stages rather than three: a rapid increase in acoustic emission rate at the onset of loading; a decrease in acoustic emission rate; a quiescent period over a loading range of 25% to 75% of the ultimate strength; an onset of exponentially increasing acoustic emission rate and finally, a very high acoustic emission rate culminating at failure. Constant stress-rate loading conditions show a different response from constant strain-rate experiments. The latter is characterized by static fatigue development associated with slow subcritical crack growth. In terms of acoustic emission rate, it remains steady until prior to failure where it increases sharply. Both Montoto et al. (1984) and Fonseka et al. (1985) provide visual microphotographic evidence of the associated deformational stress induced features.

Khair (1984) tested granite and coal under similar loading conditions. Granite showed three distinct phases of acoustic emission rate: an initial low rate, a gradually increasing rate, and a very high rate. The acoustic emission rate indicated random peaks due to local over stressing. Acoustic emission generated during deformation of these rocks was mostly controlled by the fracture surface, crystal size and brittle nature. Testing of coal, under uniaxial compression, also displayed acoustic emission rate characterized by the three stages as reported by Montoto et al. (1984) and Scholz (1968b).

Roberts (1980) measured acoustic emission in salt under uniaxial incremental load. He found a decrease in acoustic emission rate with time after loading. During the secondary stage, acoustic emission rate decreased much slower than during primary creep.

Reymond (1980) observed acoustic emission in rock and concrete. He showed that his results of acoustic emission event count versus volumetric strain follow the results of Scholz (1968a), which can be defined by the power law relationship. Fracture initiation was observed at 50%, whereas Scholz (1968b) observed this phenomena at 90% of the failure strength. A U-shaped distribution characterizing the three stages of acoustic emission with respect to time was observed.

Knill et al. (1968) found that an increase in the size and proportion of coarse aggregate in concrete, increased the spread of the emission rate-time distribution. Knill et al. (1968) and Reymond (1980) suggested that further studies of this type may increase the knowledge of the relationship between heterogeneity, deformation and strength of materials.

Vance (1983) reported acoustic emission data of potash rocksalt. Presentation of event count versus applied load shows a steadily increasing curve. Cumulative event versus applied load is shown to have a similar shape to the stress versus axial strain curve.

Richardson (1980) investigated acoustic emission in polycrystalline rocksalt and single salt crystals. He showed that the loading mode for single crystal studies would affect the location of peak acoustic emission rate. Constant stress loading conditions show peak acoustic emission rate located in the post yield zone. With constant strain rate, the peak acoustic emission rate was in the yield region. Using various threshold settings, he found that the highest number of events occurred near the yield point, making it possible to delineate the yield point. No deflections were observed for test

results pertaining to polycrystalline rocksalt. Both polycrystalline rocksalt and single salt crystals behave differently, although deformation processes in single crystals are similar to those of individual grains in polycrystalline rocksalt.

Other researchers explored acoustic emission response by considering the frequency content of the microseismic events. Rothman (1977) observed acoustic emission in sandstone stressed to failure, under uniaxial compression, and measured corresponding acoustic emission. He used P-wave velocity measurement in  $x$ ,  $y$ ,  $z$  directions to conclude that void space (in the form of microcracking) is developed parallel to axial load. Results showed that the velocity along the 'z' plane ( $V_z$ ) increases with increasing load.  $V_x$  and  $V_y$  remained constant up to 50% of failure strength. They then decrease, coinciding with a volumetric decrease of the sample due to increasing stress. From this point on, rock volume increased due to dilatancy. Just prior to failure, the rock volume increases close to its unloaded value. The velocity data indicated that cracks closed parallel to, and opened perpendicular to, applied load.

Dunning and Dunn (1980) studied acoustic emission in single quartz crystal under incremental loading. They monitored crack propagation, amplitude and frequency of acoustic emission events. Cracks associated with acoustic emission corresponded to maximum surface strains during stable crack propagation. No acoustic emission was observed during loading and unloading, up until 90% of failure stress. Also, the observed frequency is the result of direct travel along the [0001] crystallographic plane. The reflection occurred from the crack surface and from side to side (the latter adjacent to the accelerometer). The predicted frequency occurred with the measured amplitude peak. They based acoustic emission results only on intragranular crack propagation.

#### **5.4.3 Acoustic Emission Trends Observed under Uniaxial Compressive Load With Respect to Other Physical Test Variables**

Observed acoustic emission trends have been reported for rocks tested under uniaxial compression. However, these studies have either pretreated the specimen by tempering (eg. water permeation or cyclic loading) or exposed the specimen to high temperature conditions. Under variable testing conditions and/or pre-treatment of the specimens different acoustic emission response is obtained and procedures of such investigations will be discussed in the following section.

Wu and Thomsen (1975) measured acoustic emission in terms of  $\sum(\sqrt{E})$  parameter which is a rough measure of the sum divided by all the events of the square root of energy. Tests were conducted for water permeated Westerly granite under constant uniaxial stress and under various temperature conditions ranging from room temperature to 150° Celsius. Experimental results revealed three stages of acoustic emission and deformation. The first stage (transient creep) showed a rapid increase in axial, radial and volumetric strain associated with an increase in the total energy of acoustic emission events. The second stage showed a linearly increasing volumetric, radial and axial strains, but  $\sum(\sqrt{E})$  increased exponentially. The third stage showed that strains increased at an accelerated rate coinciding with an increase in  $\sum(\sqrt{E})$  at a supra-exponential rate. A decrease in microfracturing activity, indicated by low acoustic emission activity, was apparent in samples permeated with water. This is due to water films forming in the crack surfaces and facilitating dislocation without generating acoustic emission.

Haimson and Kim (1977) observed acoustic emission rate for rock stressed under four different types of loading configurations. Cyclic loading tests of two rock types showed different acoustic emission response. High acoustic emission activity in granite was observed in the first load cycle up to 80% of the failure strength. The next two cycles showed no acoustic emission activity. These loading cycles were accompanied by crack development. Acoustic emission increased in the last stage of the loading cycle. This response is indicative of various mechanisms including micro-crack growth which progresses into coalescing, fracturing, and sudden unstable crack growth. Acoustic emission in granite begins at the onset of dilatancy, and increases to failure, whereas acoustic emission in marble accumulates in a stepwise fashion without any dramatic change near failure.

#### **5.4.4 Investigations into the Causes and Nature of Acoustic Emission**

This section will present reported observations of sources responsible for acoustic emission generation under laboratory loading conditions. Most of these reports are based on fractography. This method provides visual criteria of deformational features generated during the loading process. The features are post-deformational such that a correlation with time, strain or acoustic emission parameters is an indirect one.

This section will also review the general mechanisms reported in the literature. It will include rock types, test configurations and possible deformation mechanisms responsible for the generation of acoustic emission.

Geological materials are polycrystalline in nature [Hardy and Leighton (1984)]. Acoustic emission can originate at three levels: microlevel, macrolevel and megalevel. They originate at a microlevel as a result of dislocation. At a macrolevel, they result from twinning, grain boundary movements and fracture development through and between mineral grains. At a megalevel, acoustic emission can originate from fracturing and failure of the material or from relative motion between structural units.

Eisenblätter (1979) stated that acoustic emission occurs in materials when elastic energy is released. These releases are due to variable causes such as plastic deformation, gliding, dislocation and twinning of crystal grains.

Fonseka et al. (1985) conducted acoustic emission studies in conjunction with scanning electron microscopy techniques in order to identify stress induced features. Uniaxial and triaxial tests were conducted on marble, diorite and microgranite. The study was conducted in several stages. Initially identification of inherent microstructure prior to sample preparation and surface features were observed. Various stress induced features were observed after loading on surfaces along which failure had occurred.

Microscopic imperfections contribute to the flaws which promote fractures and generation of acoustic emission. Montoto et al. (1984) conducted uniaxial compressive tests on granites with different degrees of alteration. This affected the rock's cohesiveness and granularity. The associated acoustic emission rate showed that a higher rate and cumulative count were observed in samples that were highly weathered. The initial stage of loading and acoustic emission recorded was stated as being due to the formation of new cracks. The final stage (at failure) was due to coalescing of fractures and the development of shear movements.

Khair (1984) conducted compression tests on coal and granite. On large samples he observed that the fracture planes were controlled by texture and fabric. Fractures normally occurred along grain boundary areas.

Scholz (1968b) conducted compressive tests on tuff and granite. He noted that more activity was associated with tuff as compared to granite in the initial stages of

loading. The difference is accountable by the rock porosity. Although this observation is made, it is assumed that the average size of microfracturing events remains constant and the accumulated frequency of events is proportional to the inelastic volumetric strain.

Scholz (1968c) also conducted a source location study and in the process noted two varieties of waveforms. One is due to microfracturing the other is due to the transducer response.

Various conclusions have been drawn from single crystal studies of geologic material. Richardson (1980) investigated single and polycrystalline salt behavior associated with acoustic emission rate peak for samples loaded under uniaxial compression. He suggested that weakening by dislocation from pinning points was the likely source mechanism for acoustic emission generation. Acoustic emission associated with polycrystalline samples was specifically the sum of acoustic emission activity originating from a complex deformation pattern involving grain boundary interaction, propagation of microcracks and dislocation motion resulting in intergranular slip.

Dunn and Dunning (1980) concluded that acoustic emission only occurs during crack propagation. Their study was conducted on single crystals of quartz loaded under uniaxial compression and it showed that crack propagation was the only intra-granular phenomena that contributed to the generation of acoustic emission.

#### **5.4.5 Acoustic Emission Studies in Relation to Strain**

This section will outline studies which demonstrate that cumulative acoustic emission event count, with increasing stress, is related to deformation. Scholz (1968b), Sano et al (1982), Onhaka (1983), Raymond (1980) and Barron (1970) showed that inelastic volumetric strain is related to cumulative acoustic emission counts, for various stress levels of a load cycle. The total volumetric strain is usually determined from axial and circumferential strain measurements. Inelastic volumetric strain is obtained by subtracting an extrapolated linear portion of the stress-strain curve from the total volumetric strain, as shown in equation 5.3. Inelastic volumetric strain shows a distinct correlation with cumulative event counts. In the later stages of the load cycle where failure is approached, acoustic emission cumulative count deviates from the depicted correlation due to rapid acceleration of acoustic emission activity. These relationships are based on the assumption that if the average size of

microfracturing remains constant, the sum of the accumulated activity is directly proportional to the inelastic volumetric strain. These relationships also show that each acoustic emission event contributes to a small increment 'n' to the volumetric strain.

Scholz (1968b) stated that rock is inelastic at high stress levels and it shows a characteristic decrease in the modulus of elasticity by dilatancy. The model of accumulated frequency of microfracturing is defined by:

$$N(\bar{\sigma}) = \frac{1}{2\pi k_2 \bar{\sigma}} \int_{-\infty}^S \exp\left[\frac{-(\sigma - \bar{\sigma})^2}{2(k_2 \bar{\sigma})^2}\right] d\sigma \quad 5-1.$$

where 'N( $\bar{\sigma}$ )' is the accumulated frequency of events, 'k<sub>2</sub>' is a constant and 'S' is the strength. He demonstrated that the function satisfies experimental data. The fit is good for data between 50% to 95% of fracture strength, above which it is speculated that there is a change in the deformation mechanism.

Sano et al. (1982) investigated the effects of strain rates on the strength of rock based on Scholz's (1968b) hypothesis. According to Sano et al. (1982), the strength of rock can be expressed by the power law function which is dependent on axial strain rate and dilatant strain rate. The experiments were conducted on granite under constant axial strain rate and constant volumetric strain rate. Volumetric strain was calculated as follows:

$$\epsilon_v = \epsilon_{ax} + 2\epsilon_{cir} \quad 5-2.$$

The inelastic volumetric strain, ' $\epsilon_v$ ', is defined by:

$$\Delta = \epsilon_v - \left(\frac{1-2\nu}{E} \sigma + \epsilon_o\right) \quad 5-3.$$

where ' $\sigma$ ' is the applied stress and 'E' is a constant. The model reported by Sano et al. (1982) was developed to show the relationship where acoustic emission activity is dependent on strain rate. This relationship is dependent on several parameters including stress and strain rates and is expressed as:

$$\sigma_{max} \propto \Delta \frac{1}{\eta} \quad 5-4.$$

where 'n' is the stress corrosion index and ' $\sigma_{max}$ ' is the maximum applied stress reached at a certain time, ' $t^*$ ', defined as:

$$\Delta^* = \Delta t^* \quad 5-5.$$

The applied stress reaches its maximum when the dilatant strain reaches a critical dilatancy. Dilatant volumetric strain is defined as:

$$\Delta = \eta \frac{dN}{dt} \quad 5-6.$$

where ' $n$ ' is the average contribution of microfracturing to the increase in dilatant strain and ' $dN/dt$ ' is the microfracturing rate.

' $\sigma_{max}$ ' is defined by:

$$\sigma_{max} = \alpha \frac{1}{\epsilon^{n+1}} \quad 5-7.$$

where ' $\epsilon$ ' is the axial strain rate, given for granite by:

$$\sigma = E \epsilon t \quad 5-8.$$

where ' $E$ ' is Young's modulus, independent of strain rate.

When the dilatant strain rate is held constant, this produces the stress corrosion index to be approximately of the same value as the dilatant strain rate (refer to equation 5-7).

Reymond (1980) concluded that the initiation of unstable cracking for experiments conducted under uniaxial compression for rocks and concrete, occurs at approximately 50% of the failure strength of the material; whereas Scholz (1968b) observed this trend to take place at 90%.

Onhaka (1983) conducted experiments on granite and monitored acoustic emission through low and high pass filters. He reported that a relationship exists between inelastic volumetric strain and cumulative event counts. When failure approaches, there is a rapid increase in acoustic emission activity.

The acoustic emission rate for low frequency range events increases more rapidly than that of higher frequency range events. Two possibilities exist for frequency dependence in the tertiary phase of creep, due to larger crack developments and to the attenuation of higher frequencies. As noted by Scholz (1968a) and Saro et al. (1982), the cracking mechanism which contributes to the number of incremental crack growth, is due to inelastic volumetric strains formed during crack opening, causing dilatation. This influences the attenuation of higher frequencies.

Roberts (1980) conducted acoustic emission measurements on rocksalt during creep loading. Loading was incremental (under constant load rate), and was maintained at a stress level until the strain rate approached zero or 24 hours had elapsed.

In contrast to other authors including Scholz (1968b), Sano et al. (1982) and Reymond (1980); Roberts (1980) correlated acoustic emission rate to axial strain rate by the power law relationship:

$$A = b \epsilon^m \quad 5-9.$$

where ' $\epsilon$ ' is the axial strain and ' $A$ ' the acoustic emission rate, and ' $b$ ' and ' $m$ ' are constants.

Barron (1970) conducted tests by triaxial configuration for various rock types and measured various associated acoustic emission parameters. Results indicated that for syenite (confined at  $\sigma_3 = 85 \text{ kg/m}^2$ ), acoustic emission and volumetric strain coincide at the indicated load levels. Similar test results were obtained for quartzite, and granite. Siltstone showed no acoustic emission activity, possibly due to out of range frequencies which were unable to be detected by the monitoring equipment.

#### **5.4.6 Acoustic Emission Response with Respect to Grain Size, Sample Size and Composition**

Hardy and Leighton (1984), Scholz (1968), Mogi (1962), Tandon and Tangri (1975), Erenkämper (1979), Pollock (1980) observed that acoustic emission response varies due to the difference in grain size of geological materials. Similarly, the impurity of rocks is also associated with a characteristic acoustic emission response. Acoustic emission response can be measured in terms of amplitude or energy, event count and rate. Acoustic emission parameters, stress, strain or temperature can be correlated to material properties including grain size, anisotropy, texture, porosity and composition. The relationship can be used to predict stress levels in the rock, and delineate dominant deformation mechanisms. Scholz (1968), Mogi (1962), Tandon and Tangri (1975), Erenkämper (1979), Fonseka et al. (1985), Baram and Rosen (1980), Mintzer et al. (1978), Ohira et al. (1979), Sondergeld et al. (1981) and Matthews (1983) have reported pertinent observations affecting acoustic emission with respect to grain size, sample size, and sample purity. A summary of their findings will now be presented.

- 1) Pure monocrystalline materials show an increase in acoustic emission activity with increasing grain size.
- 2) In pure materials, most dislocation occurs along grain boundary areas. An increase in the grain size results in less grain boundary area, thus reducing potential sources for acoustic emission.

- 3) Reducing grain size increases yield stress. Dislocation in fine grained samples are subjected to higher stress when plastic flow begins as compared to coarse grain samples. Higher stress will increase dislocation velocity.
- 4) Variable grain size changes the shape of load-time curve. The dependence of strain-rate on time depends on the shape of the load-time curve and grain size. Since acoustic emission is strain rate dependent, the rate of acoustic emission will be affected as well.
- 5) Acoustic emission varies due to impure or secondary mineral phases.
- 6) Reducing grain size decreases glide distance and increases dislocation velocity, which results in a shorter glide time for dislocation packets.
- 7) Acoustic emission energy increases with grain size. As purity decreases, the maximum acoustic emission activity is observed in smaller grain sizes. The grain size at which maximum acoustic emission activity is observed may be less than the finest grain size. Maximum acoustic emission activity occurs at the onset of plastic flow, then falls off.

Sample size is another factor controlling acoustic emission output. In general, burst rate should be proportional to sample volume [Sondergeld (1981)]. Kim et al. (1979) studied the effect of specimen size on acoustic emission for two salt single crystals. The amplitude distribution was measured and the relation between the number of pulses ' $N_i$ ' and amplitude ' $V_i$ ' was found to be:

$$N_i = AV_i^{-m} \quad 5-10.$$

where ' $A$ ' and ' $m$ ' are constants. Acoustic emission rate was found to decrease with increasing strain. It was also observed that acoustic emission rate was smaller for larger specimens at the same strain level.

#### **5.4.7 Laboratory Studies and Application of Acoustic Emission Amplitude**

Acoustic emission can be analyzed in terms of its amplitude. The acoustic emission amplitude is studied as a distribution of events. More precisely referred to as the cumulative acoustic emission event amplitude distribution, it is defined as a display of the number of acoustic emission events with signals that exceed an arbitrary amplitude as a function of amplitude [Hardy and Leighton (1984)].

The differential amplitude distribution is also studied. It is defined as a display of the number of times the acoustic emission signal peak amplitude falls between ' $V$ ' and ' $V + \Delta V$ ' as a function of the amplitude ' $V$ '. ' $f(V)$ ' is the absolute value of the differential of the cumulative amplitude distribution [Hardy and Leighton (1984)].

The amplitude distributions provide a tool to manipulate and normalize acoustic emission data. Also, as it will be further discussed in this section the acoustic emission amplitude distributions provide a means of discriminating between various source mechanisms. Finally, changes in the amplitude distributions due to changing stress or temperature conditions can show precursors to the failure of the material. Thus, prediction of failure or unstable crack propagation is possible.

Within the scope of this study, three methods of analyzing amplitude distribution are investigated. Each of these techniques define parameters derived from the amplitude distribution. These parameters include the b-value parameter, the amplitude ratio parameter and the analysis of time and amplitude statistics.

#### 5.4.7.1 The b-Value Parameter

The b-value parameter is derived from a function that defines the amplitude distribution. Amplitude distribution data is normally plotted as the number of events having a peak amplitude greater than a 'threshold' value [Pollock (1976)]. According to results presented in the literature, the data points usually appear on a straight line. The b-value is derived from the slope of these points (refer to figure 5.3).

The derivation of magnitude in a microseismic event is described by Richter (1958), where the amplitude distribution analysis is applied to earthquakes. The magnitude of an earthquake event ' $M$ ' is defined as:

$$M = \log A - \log A_0 \quad 5-11.$$

where ' $A$ ' is a recorded trace and ' $A_0$ ' is a selected standard. ' $M$ ' is characteristic of an earthquake. When analyzing seismic events, usage of the magnitude scale implies that the data at a given distance is all alike except for amplitude.

The frequency distribution of earthquakes over a range of amplitudes can be represented by:

$$\log N = A - bM \quad 5-12.$$

(or)

$$N = 10^A * 10^{(-bM)} \quad 5-13.$$

where ' $N$ ' is the number of shocks of magnitude ' $M$ '. Both ' $A$ ' and ' $-b$ ' are constants for ' $dN/dM$ '. This relationship can be reformulated as:

$$\log(-N) = A - bM \quad 5-14.$$

On the other hand, Mogi (1986) noted that the method presented by Richter (1958) is not valid for deep focus earthquakes. The total amount of earthquakes with magnitude ' $M$ ' can be expressed as:

$$N(M) = \int_M^{\infty} n(M)d(M) \quad 5-15.$$

thus the relationship between 'N(M)' and 'M' is represented as:

$$\text{Log } N(M) = A - bM \quad 5-16.$$

where ' $n(M)d(M)$ ' is the frequency of earthquakes and their magnitudes from 'M' to 'M+dM'.

Ishimoto-Iida [after Fonseka et al. (1985)] developed a relationship between ' $n(A)$ ' and 'A' for the amplitude recorded from the time 'A' to 'A+dA'. It states that the number of events of amplitude 'A' is a set of ' $n(A)d(A)$ ' and is represented as:

$$n(A) = kA^{-m} \quad 5-17.$$

where 'k' and '-m' are constants [Mogi (1962)]. Fonseka et al. (1985) demonstrated that as far as magnitude is concerned both formulae are identical and are as followed:

$$m = b + 1 \quad 5-18.$$

Suzuki (1959) proved the relationship of 'b' to 'm' to be:

$$b = m - 1 \quad 5-19.$$

Acoustic emission amplitude distribution analysis has been introduced by Scholz (1968a) and Mogi (1962). Scholz (1968a) reported the dependence of the b-value on stress and also stated that the b-value varies for different rock types. This analysis involves considering the frequency of occurrence of events as a function of amplitude. Data is plotted on log coordinates where the ordinate represents the frequency of occurrence of events and the abscissa displays the maximum trace amplitude. A strong linearity fitting the power law function was noted earlier referred as the 'Ishimoto-Iida' relationship. Results for various rock types showed a consistent decrease of b-values with increasing stress. Marble exhibited a frequency-magnitude relationship similar to brittle rocks but linearity is more consistent than in the other rock types.

Fonseka et al. (1985) reported similar b-values measured for various types of rocks. They concluded that the b-value decreases towards unity (ie.  $b = 0$ ), as failure is approached when loading under constant strain rate.

A model presented by Scholz (1968a) pertaining to the physical significance of the b-value involves the stress 'regime' as explained by a probability function ' $F(S:\sigma)$ '. The development of local stress increase is due to fracture growth in which a redistribution of the stress field occurs. Pollock (1980) expressed it as being:

$$b = \frac{2}{3} V (1 - F) \quad 5-20.$$

where 'F' is a function of stress, which includes the stress field fluctuations.

Pollock (1980) also discussed the physical significance of the b-value reported by Mogi (1962). It was assumed that the arrest of rapid fracturing governs the emission amplitude. This will be initiated by barriers in the stress field usually observed in rocks characterized by a degree of inhomogeneity. The b-value then emerges as a product of three factors shown by:

$$b = V k_3 K \quad 5-21.$$

where 'V' is the exponent relating acoustic emission energy to amplitudes, 'k<sub>3</sub>' is the proportionality constant and 'K' is the degree of spatial fluctuation of stress distribution.

Both authors emphasized that the b-value is controlled by small scale fluctuations in stress due to rock textural inhomogeneity. Mogi (1962) reported that the m-value ( where  $m = b + 1$  ) varies from 0.3 to 2.7 depending on the structure and the degree of inhomogeneity.

Recent publications of laboratory based investigations, discussed below, have reported the b-value measurement with respect to various loading conditions of geologic materials.

Sano et al. (1982) showed that a linear relationship exists between cumulative acoustic emission events and volumetric strain until the maximum fracture stress is reached. Beyond this point, acoustic emission increases rapidly and the associated b-value decreases as macro-faults are formed. Part of the study observed b-values for various tests. When the axial strain rate was constant, the b-value decreased with increasing stress. When the dilatant strain rate was constant the b-value remained constant. An increase in the strain rate coincided with similar b-values but the slope lines were located at lower levels. As a result, a decrease in b-value indicates higher dilatant strain rate and therefore the b-value is useful in predicting the fracture density in the rock. It was observed from this analysis that the b-value was stress and strain rate dependent.

Atkinson et al. (1984) reported that Westerly granite displays a thermal Kaiser effect when heated in slow cycles up to 500° Celsius. The critical stress concentration factor is reduced by heat treatment in response to an increase in bulk micro-

crack density. Amplitude distribution varies with the stress intensity factor. The b-value decreases with increasing temperature of every heating cycle. The amplitude distribution in this case is defined by the power law function:

$$n(V) = \left( \frac{V}{V_0} \right)^{-b} \quad 5-22.$$

where ' $V/V_0$ ' is the amplitude whose peak (in Voltage) ' $V$ ' exceeds ' $V_0$ '. The b-value was obtained for every heating cycle. The observed trend signifies that the emission population is characterized by a greater number of smaller amplitude events at lower temperatures.

The physical significance of the b-value can also be associated with particular deformation mechanisms. These are a characteristic of the material with a unique texture and stress level. In the following papers, the b-value is interpreted as a function of grain size and as a correlation representing dominant primary deformational processes occurring during fracture experiments. The amplitude distribution in these cases are defined by functions, in order to accommodate the fit of the cumulative amplitude distribution. Models of amplitude distribution should be related to the understanding of the material properties and deformation processes [Pollock (1979)].

Holt and Evans (1976) conducted measurements and presented an interpretation of the amplitude distribution of acoustic emission signals. They used this technique as a means of studying fundamental characteristics of acoustic emission sources. They showed that a basic log-normal distribution could be used to fit their acoustic emission amplitude data. Furthermore, they proved that this distribution approximates the power law relationship for large amplitudes. Their tests were conducted on two different types of materials; the first was a tensile test of a fiberglass specimen and the second the emissions from an oxidized tensile test sample of Magnox pressure vessel steel. They have presented the distribution function of a parameter ' $x$ ' in the form of:

$$N(x) = \frac{B}{x\sigma} \exp - \frac{(\ln x - \ln \bar{x})^2}{2\sigma^2} \quad 5-23.$$

where ' $B$ ' is a constant and ' $\sigma$ ' is the standard deviation of the normal distribution of ' $\ln x$ '. This model fits with the large b-values usually observed in plastic zones.

The log-normal form presented by Holt and Evans (1976) is not the only alternative to the power law function. Graham (1976) has also proposed the statistics of extrema formula as a model for the explanation of cumulative distribution.

Graham (1976) showed that acoustic emission signal characteristics are dependent on the microstructure of the material. Acoustic emission measurements which included amplitude distributions of three types of graphite epoxy composites that were fractured in bending showed a difference in the distribution between aged and unaged samples. Both displayed maximum peak amplitudes early in the test. 'Steady state' amplitudes of events were smaller for the aged samples. Aged specimens displayed different amplitude distribution from unaged specimen.

The extrema value function fits the amplitude distribution, more so than the standard power law function. This is represented as:

$$F(V) = F(o) \left\{ 1 - e^{-\frac{V^{-b}}{V_o^{-b}}} \right\} \quad 5-24.$$

The distribution function also represents the dominant fracture mechanism which occurs during the load test. Therefore, the parameters of the equation take on a new significance. ' $F(o)$ ' is the relative number of events associated with different mechanisms during the same time interval; ' $V_o$ ' is a measure of the event amplitudes generated from the deformation mechanisms and ' $b$ ' is the shape factor or 'spread' of the distribution. Distribution analysis of acoustic emission amplitude parameter can delineate the complex nature of fracture processes which occur in the material. This observation was substantiated by visual microscopic evidence of the fracture process with respect to increasing stress.

#### 5.4.7.2 The Time-Amplitude Statistical Method of Analysis of Acoustic Emission

Erlenkämper (1979) presented a method of analyzing acoustic emission amplitude with time difference data, derived from testing carbon and aluminum alloys. By using contingency tables which defined the distribution of acoustic emission data, he used the Chi square distribution analysis to do a statistical inference. The inference was to test for acoustic emission source mechanism's dependence or independence. The acoustic emission data within the contingency tables are defined by the amplitude of the event (' $A_o$ ') and their corresponding time difference (' $T_A$ ') between two consecutive events.

The inference tests for the dependence or independence arises from the fact that there are two types of acoustic emissions that can be emitted from either carbon or aluminum alloys. A series of dependent events, known as poly-a-process, were exhibited by the aluminum alloy. Independent events, which are known as the Poisson process, were observed to be emitted from the carbon steel. The poly-a-process

displays at first a strong event which in turn induces a series of smaller dependent events. The Poisson process is the result of events emitted independently of each other.

A statistical correlation between time difference and peak amplitude (' $A_{max}$ ' and ' $T_A$ ') respectively, is established by using contingency tables for the two parameters. The Chi square value ' $\chi^2$ ' was calculated from :

$$\chi^2 = n \sum_{i=1}^r \sum_{k=1}^s \frac{(n_{ik} - n_{i \cdot} \cdot n_{\cdot k})^2}{n_{i \cdot} \cdot n_{\cdot k}} \quad 5-25.$$

where ' $n_{i \cdot}$ ' and ' $n_{\cdot k}$ ' are the partial sums defined by:

$$n_{i \cdot} = \sum_{k=1}^s n_{ik} \quad 5-26.$$

$$n_{\cdot k} = \sum_{i=1}^r n_{ik} \quad 5-27.$$

The calculated Chi square value was compared with values in the table of the Chi square distribution. The null hypothesis which stated an independence of time difference and amplitude was rejected.

Closer observation of the contingency table revealed patterns. These patterns were observed as high concentration areas within the contingency table representing time difference and amplitude data. It was observed that a large number of small amplitude events with small time differences were apparent, however, large amplitude events with large time differences were not present.

Also, larger amplitude events with small time differences and smaller amplitude events with larger time differences occurred often. From this observation, it was concluded that the time difference of acoustic emission signals are inversely proportional to the peak acoustic emission amplitude.

#### 5.4.7.3 The Amplitude Ratio Parameter

Pollock (1973) defined the amplitude ratio parameter. Acoustic emission amplitude data has been collected for four types of steels. The results show the dependence of the amplitude distribution on the material and deformation mechanism.

The amplitude ratio parameter is defined as the ratio of the number of events exceeding a predefined amplitude level to an arbitrary number of events exceeding a reference amplitude level [Pollock (1973)]. In other terms, this is a numerical measure of the amplitude distribution generated over the entire range of stress history.

He also used this type of analysis to show that the amplitude parameter displays a marked change as failure of the sample is reached. This trend is indicated by an increase in the proportion of high amplitude events over the total population of events. Such observations show that this type of analysis could be used as a precursor in predicting failure in some materials.

The author goes on to explain the possible source mechanisms responsible for the change in the amplitude ratio with respect to increasing stress.

The advantage of using this method is to isolate discrete changes in amplitude ratio thus, delineating the changes in the source mechanisms. This method appears to be more effective and less time consuming than the determination and interpretation of the b-value parameter.

#### **5.4.8 Acoustic Emissions Energy**

Acoustic emission energy has been analyzed using several techniques. One method of studying acoustic emission energy is more commonly used in analyzing metals and developing relationships between acoustic emission energy and incremental crack growth. Tests are designed to extrude the material and measure the corresponding crack velocity, area and opening. These measurements are routinely considered in fracture mechanics experiments of single stress-induced crack growth.

Another type of analysis considers the various factors affecting the acoustic emission energy that is received and processed. This involves the development of the source, transfer and receiver functions. This method produces results which will interpret source mechanisms.

Acoustic emission energy can also be analyzed as a distribution of events. The treatment in this latter case is analogous to the amplitude distribution analysis technique.

Energy is defined by ASTM (610-77) (1977) as the square of the event amplitude in arbitrary units. The AET 5500 system measures energy by taking into account two parameters: the peak event amplitude and the event duration. It is calculated as:

$$E = \text{peak amplitude} + \log_{10} (\text{event duration}) \quad 5-28.$$

#### **5.4.9 Energy Parameters**

The energy of acoustic emission can be established by various analytical methods. This section discusses basic acoustic emission measurements used to define acoustic emission energy. Various definitions of energy have been reported by different authors.

Analysis of the energy data has taken on many forms. These include methods of determining an 'E-value' parameter from a distribution function, determining the acoustic emission energy as a function of stress, strain or time and, demonstrating the relationship of energy to characteristic deformational patterns based on material properties [Pollock (1977)].

Baram and Rosen (1980) defined acoustic emission energy as being computed from  $\Sigma C / \Sigma E'$  (ie. the average number of counts per acoustic emission event). This investigation involves the effect of grain size in acoustic emission of aluminum samples. The objective of their study was to correlate acoustic emission with samples of different grain sizes, tested at various strain rates, with energy released due to acceleration or deceleration of moving dislocations. Increased acoustic emission activity was associated with higher strain rates. Acoustic emission energy attained maximum peak values which were closer to the yield point for coarser grained samples. A model for relating energy per unit screw dislocation, per unit volume was stated as being:

$$\frac{dW'}{L} = \Lambda \quad 5-29.$$

where ' $dW'$ ' is the strain energy density of moving dislocations, ' $\Lambda$ ' is the mean free path, and ' $L$ ' is a constant. It was shown that ' $\Lambda$ ' increases with increasing grain size; the mobile dislocation density decreases with grain size.

Acoustic emission characteristics are important for the assessment of structural integrity of piping components, steel pressure vessels and gas storage tanks [Nakasa (1979)]. The amplitude distribution function parameter (m-value) can be used to derive total event count and total event energy. Acoustic emission amplitude is described by the power law function as:

$$f(x) \propto x^{-m} \propto x \quad 5-30.$$

where:

$$x = \frac{V_p}{V_0} \quad 5-31.$$

This slope can be used to discriminate acoustic emission signals due to characteristic deformation and/or cracking by defining the unique m-value. m-values are high for plastic deformation and increase as work hardening goes on. m-values also decrease as cracking goes on. The quantity ' $e$ ' is affected by both material properties and instrument settings.

Calder et al. (1988) showed that a signal energy parameter called the 'energy sum' displayed results that have the capability of monitoring changes in stress, in a localized area of the rock mass. This investigation was conducted in a field study. The value is calculated in the frequency domain by summing up the RMS voltage magnitude values:

$$E \Sigma = \int V(f) df \quad 5-32.$$

### 5.5 Summary

Although there are many acoustic emission signal analysis techniques, there are only a particular group of acoustic emission parameters that can be used to determine if they are affected by inherent material properties.

Event counting and acoustic emission rate criteria have been used to observe trends with respect to increasing stress level and microfracturing phenomena, as evident by microscopic analysis. A relationship between material properties and acoustic emission counting parameters can at best be qualitative. In general, for most rock types the rate typically accelerates at the onset of failure. But, several studies have shown this not to be true. Roberts (1980), Richardson (1980) and Fonseka et al. (1985) have presented results for various rocks that have visco-elastic behavioral properties in which no apparent change in acoustic emission rate was observed. Preliminary testing of potash rock showed the acoustic emission rate to decrease with increasing stress.

The main purpose of determining the acoustic emission rate was so that it could be used as a precursor to predict the onset of failure. In field studies, this method has also proved to be unsuccessful. Trombik and Zuberek (1977) reported inconsistent results, where the acoustic emission rate changes occurred with no accompanying failure and in some cases, failure sometimes occurred with no apparent warning.

Also, it should be noted that the acoustic emission rate is controlled by load testing conditions and stress level. Results include tension and various compressional loading modes (such as creep, constant stress, or constant strain) which yield different acoustic emission rates and counts. As a result, the acoustic emission response obtained is significant only in relative terms, and an interpretation of the data can not be directly correlated to material properties.

Cumulative event counts have been successfully applied to establish empirical relationships with deformation of the material under investigation. These statistical correlations between strain and event count have been introduced by Scholz (1968b). Several researchers have used this technique to develop similar relationships to various other rock types, most of which follow the power law function [Roberts (1980) and Sano et al. (1982)]. In most cases, the function does not fit all of the data points, especially near failure. These studies deal with the fundamental material properties and in many cases, the workers' objectives are to model failure under laboratory testing conditions, rather than establishing the mechanisms leading to material deformation and failure.

The amplitude distribution and the characteristic 'b-value' have been used to delineate the mechanism and the nature of the acoustic emission signal. This value can be correlated to material properties in order to observe microstructural (or compositional) parameters that would effect the acoustic emission response. Pollock (1980), Graham (1976), Scholz (1968), Mogi (1962), Holt and Evans (1976), Sano et al. (1982), and Nakasa (1979) have demonstrated that the b-value parameter is a valuable parameter in assessing possible failure mechanisms in geologic materials, metallic materials and structures, and in developing the criteria necessary to determine if failure is imminent when this mechanism is in operation. Field test studies have also provided exceptional results in order to assess high and low stress concentration areas in pillars and thus potentially unstable pillars [Trombik and Zuberek (1977) and Semadeni and Calder (1988)].

The physical significance of the b-value can be interpreted in two different ways. Various authors have emphasized that the b-value is governed by small scale fluctuations in stress due to material microstructure and stress level. Some workers have placed more importance on the latter point. The fact that the deformation mechanism is a function of stress level causes the b-value to decrease as the stressed material approaches failure [Scholz (1968) and Sano et al. (1982)]. The physical significance of the b-value can also be addressed as being linked to specific deformation mechanisms which are dependent on the inherent material properties [Pollock (1980)].

The b-value is derived from the slope of the number of events having peak amplitude<sup>d</sup> events greater than the voltage threshold level as a function of voltage,

observed on a logarithmic scale. Erlenkämper (1979), Holt and Evans (1976), Graham (1976) and Pollock (1977) have also reported to use different distribution functions other than the power law function to fit the data points.

Amplitude distribution function is characteristic of the material and its deformational mechanism. Similarly, analogous functions based on energy can be readily defined [Pollock (1977)]. Up until now, various studies have used the acoustic emission energy parameter as being accompanied by incremental crack growth. Theoretical relationships can be derived connecting acoustic emission energy with crack incremental growth and mechanical parameters of a testing system.

The absolute amplitude and energy of acoustic emission events depend upon several factors such as, distance from the source and attenuation characteristics of the material. The relative distribution of the events is independent of these factors. Therefore, this data has a high potential of supplying information on the emission mechanisms at the source [Nakamura (1977)].

Relatively few laboratory studies have been done using source location. In general, the purpose of such studies has been to observe if the source locations coincide with the failure region in the specimen.

A number of authors have considered the frequency characteristics of individual acoustic emission events. Such investigations are used to determine a relationship between frequency content and other physical parameters. It has been shown by Greenfield (1977), Niwa et al. (1984) and Eisenblätter (1979) that the observed spectra changes as the stress level increases, with a general shift towards higher frequencies. These techniques are still in the preliminary stage. With the present availability of equipment, there is no advantage over the analysis of acoustic emission amplitude or energy distribution methods in discriminating the dominant deformational features or stress level in geologic materials.

**Figure 5.1: Frequency range for acoustic emission or microseismic events [after Vladut (1988)].**

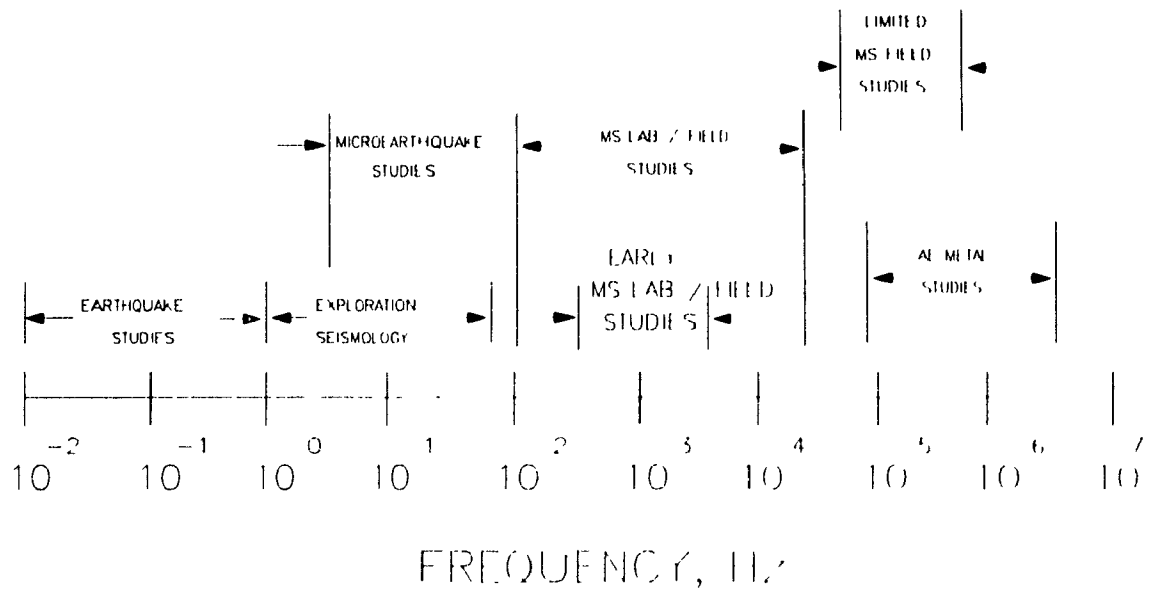
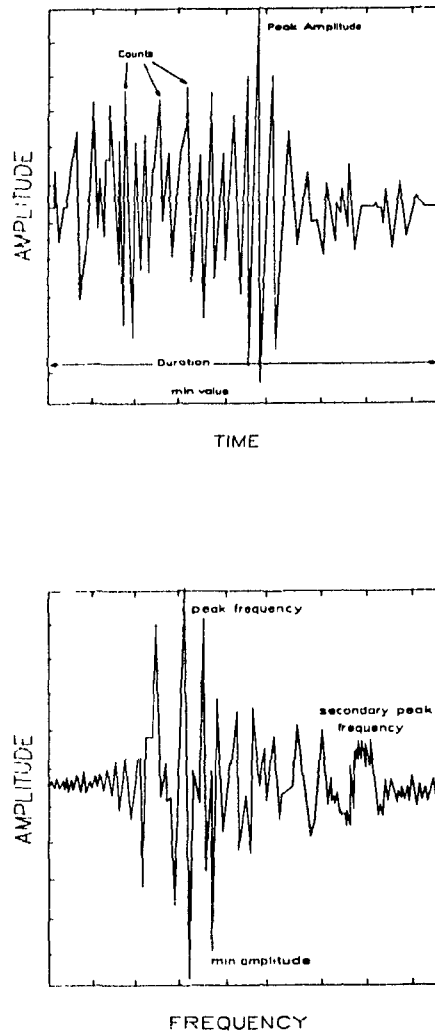


Figure 5.2: Acoustic emission signal represented in (a) time domain and (b) frequency domain. (a) displays peak amplitude, minimum value, rise time, signal duration, counts, energy, RMS value, all specified by predefined threshold. (b) displays peak frequency, maximum and minimum amplitude, various slopes defined by frequency peaks and RMS [after Matthews (1983)].





## **Mechanisms of Brittle Fracture in Rocks**

### **6.1 Introduction**

Microscopic observations are performed in order to obtain direct evidence of stress induced features. Various techniques are available to conduct this type of study. Methods used are limited by the degree of magnification required. Structurally inhomogeneous rock can limit the study under low magnification in order to isolate localized cracking. The following sections will cover the technique of microscopic observations and types of structures observed in pre-stressed and stressed materials under unique testing conditions.

### **6.2 Observation Techniques**

Optical microscopy is the most frequently used technique to observe microstructure in rock samples. Thick, thin and polished sections are used to observe cracks and microstructure under various magnification ranges. Problems arise when attempts are made to distinguish original cracks from those induced by sample preparation. Thicker sections can sometimes be useful in determining artificially produced structures from real structures by observing the structure within the sample [Simmons and Richer (1976), Fonseka et al. (1985)].

Fonseka et al. (1985) and Lux and Rokahr (1984) have used decorative techniques in order to exaggerate the crack features. This is done by introducing fluorescent dyes and by sample etching. These techniques are useful for larger intra and intergranular structures.

With electron microscopy, crack characteristics and other microstructures can be studied with greater detail. Various electron microscopic techniques and modes can be applied to observe microstructures.

### **6.3 Initial Microstructure**

Initial microstructure in rock is an important factor to be studied. According to Brace (1961), Fonseka et al. (1985) and Kranz (1979) initial microstructures are potential sites for the development of fractures. The features frequently include grain, twin boundaries and microcavities.

Among microcavities, it is necessary to distinguish between pores and microcracks [Brace (1962) and Fonseka et al. (1985)]. Pores are equidimensional spaces existing in inter and intragranular regions of a rock, along grain boundaries or fluid inclusions. Pore space can be further categorized on the basis of size, shape and relation to other pores including intergranular, connective and micropores [Caruso et al.

(1985)]. Intergranular pores are large, irregularly shaped to equidimensional. Connective pores are smaller and narrower than intergranular pores. Finally, micropores are defined as pores with dimensions equal to or smaller than a few microns. Pores are mainly responsible for the permeability in rocks. It has been noted by Sprunt and Brace (1974) that crystalline evaporites contain intragranular void spaces referred to as fluid inclusions, and vacuoles.

Microcracks, that are part of the original system of the rock, are developed in post deformational stages of the rock due to tectonic and structural activity. Microcrack features include cleavages, fractures and partings at original intact grains. These are narrow relative to their length and may be the main source of porosity and permeability in rocks with low permeability [Sprunt and Brace (1974)]. Microcracks can also be categorized into HARC's and LARC's [Kranz (1979)]. HARC's and LARC's are the abbreviations for High and Low Aspect Ratio Cracks respectively. Studies into crack phenomena have also been performed in terms of their density distributions and their orientation in rocks [Scholz (1968c) and Bieniawski (1968)]. Others including Kranz (1979), Sprunt and Brace (1974), Tapponier and Brace (1976), Peng and Johnson (1972) and Bieniawski (1967) have attached importance on lengths, aspect ratio, connectivity and spacing of cracks.

Microcracks can develop in all sizes. According to Peng and Johnson (1972) and Bieniawski (1967), microcracks are the principle features responsible for the behavior of brittle rock under stress.

Via scanning electron microscopy, various features are observed which are not apparent by optical microscopy [Brace (1961)]. It has been noted by Fonseka et al. (1985) that cracks studied optically may be artifacts due to sample preparation.

In order to identify the initial microstructure a summary has been presented of the most pertinent morphological features reported:

- 1) Long narrow sharp ended cracks are rare. These cracks vary in size and aspect ratios, the maximum not being more than 100 [Brace (1961), Simmons and Richter (1976)].
- 2) Elongated cavities or pores are commonly located along grain boundaries. Crack like cavities are rare, and more apparent in minerals with good cleavage.
- 3) The ends of elongated cavities are rounded and appear to be formed by bridging of a longer cavity [Sprunt and Brace (1974)].

- 4) Equant cavities located along intergranular and intragranular regions may consist of vacuoles or fluid inclusions.

#### **6.4 Basic Principles of Fracture Mechanics**

In this section, the common principles concerning fracture mechanics are examined. It is necessary to examine and understand the fracture process criteria. Kranz (1979) summarized the important aspects of fracture propagation.

Cracks, in a structure, develop due to application of repeated loads. There are three basic theories that govern the direction in which a crack will propagate. Knowledge of these parameters enables one to predict crack growth and fracture

The first theory articulates that a crack tends to propagate in a direction perpendicular to the maximum tensile stress along the region surrounding the crack tip. The second theory states that a crack will propagate in a direction which enhances the subsequent energy release rate. Finally, the third theory states that a crack will propagate in a direction along which the strain energy density is the lowest. Normally, in terms of fracture mechanic principles the first theory is defined by the Stress Intensity Factor (K), the second by the Crack Extension Force (G) and the third by the Strain Energy Density (S).

According to Kranz (1979), from these theories four principles can be derived. The first states: " Looking out from the propagating crack tip, further propagation will generally be directed toward the local maximum principle stress and perpendicular to the local minimum principle stress. " From this, three modes of crack development can occur: mode I (Extension Mode), whereby displacement is perpendicular to the crack plane, mode II (Sliding Mode), whereby displacement is in the plane of the crack and, mode III (Tearing Mode), whereby the displacements are in the plane of the crack and parallel to the leading edge of the crack. The three modes of crack propagation are illustrated in figure 6.1. The general case of crack development involves superimposing all three modes. The stresses associated with the crack field can be subdivided into mode I, II and III components and each mode has associated with it, a stress tensor. The criterion for crack growth is demonstrated by the Griffith Crack theory. The theory is related to propagation of cracks originating from flaws, cracks or foreign matter [Brace (1960)].

The second principle states that: " if a crack is not aligned with the principle stress, it will be subjected to a combination of stresses (ie. modes I, II and III). Therefore, the fracture propagation corresponds to the tensor sum of the stresses involved. Such a combined mechanism can produce a complex fracture. For example,

if a crack is subjected to modes II and III stresses the imposed shear deflects the crack away from planer propagation into a direction where shear is minimized. In this sense, the shear stresses may be seen as playing a corrective role restoring cracks that deviate to a stable path in the direction of the greatest principle tensile stress of the applied field" [Lawn and Wilshaw (1975)].

The third principle states that: " a crack will propagate in its own plane unless subjected to a shear stress" [Kranz (1979)].

The final principle states that: " the zone of influence around a pore or cavity will change the extent and/or the orientation if the stresses applied to the cavity are changed." If a crack propagates in the zone of influence of cavities, the crack may be prone to changes in the local stress field and thus change its direction.

### **6.5 Mechanisms and Progressive Development of Fractures in Accordance to the Stress-Strain Curve**

Bieniawski (1967), Peng and Johnson (1972) and Lux and Rokahr (1984) have identified the fracture in rock to correspond to stages of increasing load. Materials tested range from sandstones to granites, marbles and evaporites. In the majority of these studies, the authors have discovered that there can be a breakdown of four regions of crack development with respect to the stress-strain curve. These include closing of pre-existing cracks, elastic deformation, stable and unstable fracture propagation. In the majority of materials, cracks are generated due to pre-existing cracks characterized by void space, grain boundary and other microstructures [Wawersik and Brace (1971)].

Sarfaraz and Ghosh (1987) elaborated on three possibilities in which fractures can propagate in polycrystalline material. Microcracks can be initiated in intragranular regions and propagate transgranularly by intersecting slip bands or blockage of slip bands by a second particle. Secondly, microcracks can also develop in the presence of voids or along grain boundaries due to second phase embrittlement. In the latter case, the abundance of the second phase can influence the degree of cracking. When the phases possess cleavage characteristics, the energy required for crack nucleation decreases as the second phase increases. As a result, the second phase assists in the cracking process. If cleavage planes are favorably oriented with respect to the second phase, the cracks cross the particle matrix transition more easily. Finally, microcracks can develop at grain boundaries due to misorientation of adjacent mineral grains.

Initial crack closure takes place in the rock during the first portion of the loading cycle [Bieniawski (1967), Tapponier and Brace (1976)]. This is characterized by an initial curvi-linear trend along the stress-strain curve. For potash rock, the initial stage of pore closure is higher due to the porous nature of the rock. This region of the stress-strain curve is small in comparison to the remaining portion of the stress-strain curve.

After crack closure, the stress strain curve is linear and displays a constant modulus of elasticity. According to Bieniawski (1967), sliding takes places between adjacent crack faces. This results in the development of short tensile cracks forming along the length of the crack face. This is due to frictional phenomena. The application of Stroh's Model contributes to the mechanism of development of these cracks. In this model, cracks nucleate from a wedge crack due to a pile up of dislocations or slip planes [Sarfraz and Ghosh (1987)].

According to Olsson and Peng (1976), the glide lamellae are blocked by obstacles resulting in fracture development. The obstacles are usually grain boundary regions. The stress along the lamellae of the grains are relieved by two possible scenarios. In the first case, the stress ahead of the lamellae tip is resolved on to a glide plane. In the second, if the stress is not large enough for the slip to occur, the minimum stress field may nucleate a crack. Figure 6.2 shows an explanatory diagram of the possible situations. Salt crystals have several possible glide planes. These can be activated under particular stress and temperature conditions [Baar (1977)].

Due to the irregularity of the surfaces of crack faces, frictional shear resistance is produced. Points of contact do not move until they are sheared off. The distance between these interlocked points acts as Griffith Crack openings. Fracture initiation progresses as the crack's tips grow. They grow by propagating under compressive shear. The initial cracks form at a small angle to the direction of maximum compressive stress, eventually becoming stabilized. This results from shear movements of the crack faces. At this stage, the stress-strain curve is characterized by an increase in volumetric strain, a departure from linearity from the stress-strain curve and a drastic increase in acoustic emission activity [Fonseka et al. (1985), Sprunt and Brace (1974), Peng and Johnson (1970), Tapponier and Brace (1976) and Kranz (1979)]. From within this stage, short vertical cracks are developed due to irregularities of the crack surface. Continuous shear movement of the crack faces results in stable extension of the cracks located near the tip of the initial crack. At this point there is a

departure from linearity on the stress-strain curve. Chains of small cracks along the grain boundary have also been reported by Fonseka et al. (1985), in microgranodiorite, for samples loaded to 75% of failure stress.

The next stage consists of the region of stable fracture propagation. It is characterized by cracks that develop in a direction parallel to the direction of maximum stress. According to Bieniawski (1967), a uniform distribution of cracks can not be observed due to the anisotropic nature of the rock. Also, various interactions of cracks can develop due to favorably oriented array of pre-stressed crack openings.

In this stage various crack interactions occur. With increasing stress, all cracks eventually coalesce with different crack arrays joining, however the principle failure mode is still parallel to the direction of maximum stress [Tapponier and Brace (1976)].

A change takes place in the pattern of crack development such that there is a shattering of grains. The Critical Energy Release reaches a crucial value [Bieniawski (1967)]. The onset of unstable fracture propagation begins at this point.

From this point on, unstable fracture propagation predominates the deformation of the rock. It is characterized by high velocity of fracture development. The increase is asymptotic as defined by the generation of acoustic emission. This is also referred to as the terminal velocity [Bieniawski (1967)].

At the maximum strength of the rock, the terminal velocity is achieved. Beyond this point, there is macroscopic fracturing, characterized by forking and coalescing of cracks, leading to specimen rupture.

## **6.6 Crack Interaction and Propagation Studies on the Basis of Fractographic Technique**

Prior to 1970, reports concerning fractography were minimal, with much speculation. Models have been postulated on the basis of analogous studies of homogeneous materials [Tapponier and Brace (1976) and Bombolakis (1973)]. Since the late 1970's, studies on deformed specimens have been approached in two ways. The first consists of fractographic techniques on specimens loaded to a predetermined stress level. The second consisting of scanning electron microscopy studies at higher resolutions. For the latter, surfaces of thin sections were etched in order to remove superficial features [Fonseka et al. (1985)]. Studies have been conducted in a variety of

load configurations and material types. The scope of this study will cover only those considered to have contributed to pertinent observations in identifying, characterizing and interpreting microfracture phenomena.

The majority of the studies indicated that cracks were of both intra and intergranular in nature. Supportive evidence has been reported by Wawersik and Brace (1971), Kranz (1979), Tapponier and Brace (1976), and Sprunt and Brace (1974). These studies are based on samples of granite loaded to a predetermined level of load.

Several common observations were reported. It was found that an increase in the amount of grain boundary cracking occurred along ruptured bridges of original elongated cavities and through the development of new cavities.

Kowallis et al. (1982) and Fonseka et al. (1985) found that cracks originated along tectonically annealed cracks. Newly formed cleavage cracks occurred in feldspars of granite. This was apparent at the onset of dilatancy. At higher stresses, transgranularly axial cracks began to proliferate, starting at pores and at transverse grain boundaries. Also, transgranular cracks were observed to occur through preexisting elongated cavities and axial cracks originating at shear cracks.

Similarly, Kranz (1979) also observed the formation of microcracks and macrocracks derived from the intersection and coalescing of microcavities. He observed two basic types of linkages. These were termed 'en-echelon' and 'en-passant'. The former develops as a result of large shear stress concentrations between the crack tips in an arranged array. Figures 6.3a and 6.3b illustrate two modes of fracture linking. Linkages are in a vertical direction as branch cracks grow towards maximum stress. When the cracks approach at some small angle to the applied stress, shear linkages are observed. The latter occurs when two cracks approach each other from different planes.

Kranz (1979) further added that crack propagation directions can be deflected from their preferred path due to the influence of nearby pore or void space. Cleavage cracks are not susceptible to zones surrounded by void space. They occur on planes which have low tensile strength and would require mode II and III stress as to deviate the crack from its plane. Cleavage steps occur when cleavage cracks pass through a region containing dislocation with a screw component as a twist boundary. In this instance, both 'en-echelon' and 'en-passant' interactions occur together.

Cleavage cracks are easily formed in specimens that are loaded with high strain rates and low temperatures. Cleavage fractures can be categorically grouped and microscopically identified in four ways [Ewalds et al. (1984) and Knott et al. (1973)].

The first type occurs when cleavage cracks grow in parallel sets which are overlapped by secondary cleavage sets or aligned in the shear plane. This produces an 'en-echelon' interaction. The second occurs when cleavage cracks are oriented in perpendicular planes or cleavage steps by screw dislocation. The third type forms when the step is parallel to the crack propagation direction and perpendicular to the crack plane in which a twist boundary is present at an angle. Merging of cleavage steps typical of the third type can dictate the direction of local crack propagation. The fourth type is referred to as 'cleavage tongues'. These are easily developed during sample preparation. The grains involved are twinned. In these cases, the twins first form due to a high deformation rate in the form of an advancing crack. The crack will migrate along the twin then return to the original crack plane.

Similarly, Fonseca et al. (1985) followed the example of Kranz (1979) however, they categorically distinguished two types of cracks: grain boundary cracks and intragranular cracks. The former consists of chains of small cracks lying along the grain boundaries. Their nature is similar to those observed by Tapponier and Brace (1976) and Wawersik and Brace (1971) called LARCs. The latter have been broken down into 'en-passant' and 'en-echelon' crack interactions. Both result from crack propagation out of the plane with initial repulsion upon overlapping (refer to figure 6.3d). Kranz (1979), Fonseca et al. (1985) and Montoto et al. (1984) have also conducted acoustic emission testing and have indirectly associated crack development to microfracture development in the rock.

In a polycrystalline system of a rock consisting of cubic mineral phases, cracks that meet along grain boundaries will contain a stress field which extends into adjacent grains. Due to the change in the crystallographic orientation of adjacent grains, some slip systems will be activated with respect to the crack in neighboring grains. These slip systems will operate and release localized stresses at the tip of the propagating crack. The crack can also deflect to propagate into adjacent grains due to favorable cleavage orientation. Microcrack nucleation and propagation that have been activated by such systems have been reported by Olssen and Peng (1976) for marble loaded in triaxial compression configuration.

Four types of microcrack nucleation mechanisms have been identified, in which the glide is activated by an obstacle. Types I and II operate at the intersection of glide lamellae with grain boundaries. Microcracks resulting from type III mechanism form at the intersection of the lamellae. Type IV mechanism is caused by a wedging action from a combination of strong and weak grains. Mechanisms I, III and IV were reported to lead to microcracks oriented parallel to the direction of maximum compression. Mechanism II produces cracks lying in a plane of high shear stress. Faults are composed of 'en-echelon' arrays of subaxial cracks connected by packets of inclined twinned lamellae.

Tapponier and Brace (1976) observed microcracks development in Westerly granite loaded in a triaxial load configuration. Cracks were distinguishable from other features in the rock. Cracks were long, straight and narrow with sharp ends, in contrast to natural cavities which were round, bridged and with blunt ends. The cracks were grouped into two categories. The first having a transgranular nature, termed type "B"; and those associated with pre-existing arrays of grain boundary LARCs (low aspect ratio cavities), cleavage planes or healed cracks, termed type "A".

The former variety was further subdivided into three groups. Those located in intragranular pores, those starting at high angle grain boundaries of different minerals and those starting along grain boundary LARCs inclined from 20 to 60 degrees to the load direction of compression. At loads up to 75% of failure strength, new cracks formed along grain boundaries whereby compositionally different mineral grains were present. These cracks occurred at high angles to the maximum stress.

According to Sangha et al. (1974), microcracks in sandstone loaded under uniaxial compression were not controlled by local sample structural heterogeneity. Due to the lack of uniformity in the rock, variations in fracture modes were not apparent with respect to the axis of symmetry. It was observed that failure throughout the entirety of the sample occurred along the cement matrix rather than along the grain at all loading rates and stress levels. Failure was associated with an increase in the number of uniformly spaced short cracks rather than increasing propagating cracks. Samples displaying a high degree of bedding due to grain size variation showed no change in the form of crack propagation, but rather a slight irregular distribution of similar cracks was noted.

## 6.7 Experimental Deformation of Evaporites

Evaporites are composed of crystalline aggregates. Their deformation is dependent on various textural and compositional factors. Passaris (1980) noted that halite grains display an anisotropic behavior when arranged in a regular pattern due to the regular crystallographic arrangement of each crystal grain in an aggregate. An irregular arrangement of the grains would produce an isotropic behavior of the rock. Yet, important insights of the behavior of the rock may be obtained by studying the deformational characteristics and mechanisms of individual grains.

Baar (1977), Nockolds et al. (1978) and Greensmith (1979) have presented in the literature, the mineralogical components of the evaporite group of rocks. In general, these include: halite, sylvite, carnallite, langbeinite, kainite, kierserite, epsomite, polyhalite, bischofite, gypsum.

Calcite, dolomite, anhydrite are also minerals that occur in evaporites but they behave differently than the minerals listed above. These display brittle fractures even above average loads.

The halides contain a unique crystalline structure referred to as FCC (or Face Centered Cubic structure) as in the case of halite and sylvite [Phillips and Griffen (1981)]. Note that a rock containing a high proportion of sylvite is referred to as potash. This observation was considered important to Dreyer (1972) who believed that the behavior of the rock was controlled by its composition and texture.

The mechanisms that activate deformational processes are due to the presence of intracrystalline defects such as fluid inclusions or crystallographic defects [Spencer (1977) and Dreyer (1972)]. The test conditions are controlled by the loading conditions and the external temperature under which deformation proceeds to control the active deformation mechanism. The prominent mechanisms are listed and briefly explained below:

1. Fracture: this is the form of deformation most frequently observed. It is the most common mode of deformation due to high loading rate at room temperature. Various explanations of crack development and interaction have been reported and are explained in the previous section.
2. Granulation: Crushing of the crystal which does not allow openings to form.

3. Slip: Displacements produced by intracrystalline slip. Sometimes the slip is limited to a plane or a set of parallel planes. In other instances, a displacement band, kink or lamellae are formed within each rotation relative to the material outside the band along which it occurs.
4. Translational gliding: A form of intracrystalline slip in which displacements along some lattice direction occurs without loss of cohesion.
5. Twin gliding: a slip mechanism by which a crystal is mechanically twinned.
6. Kinking: a type of deformation band in which the lattice is changed or deflected by gliding along slip planes.
7. Partings: breakage of a crystal along a plane of weakness caused by deformations resulting in twin planes.

The latter five mechanisms are prevalent under special loading conditions. Dreyer (1972) described single crystal deformation mechanism of rocksalt at room temperature as brittle. Natural crystals lose their 'brittleness' after tempering to 600° Celsius and at a critical shear stress of 7 to 10 kp/cm<sup>2</sup>. Beyond this temperature and pressure conditions, samples glide and crystal translations are observed. The crystals can also sustain several levels of straining even after maximum strength has been attained. Glide mechanisms increase with increasing temperature in a shearing apparatus in which individual salt crystals are oriented to display maximum glide. Finally, the brittleness of crystals can be reduced at room temperature by decreasing the loading rate.

Figure 6.1: Schematic figure illustrating the three modes of fracture.

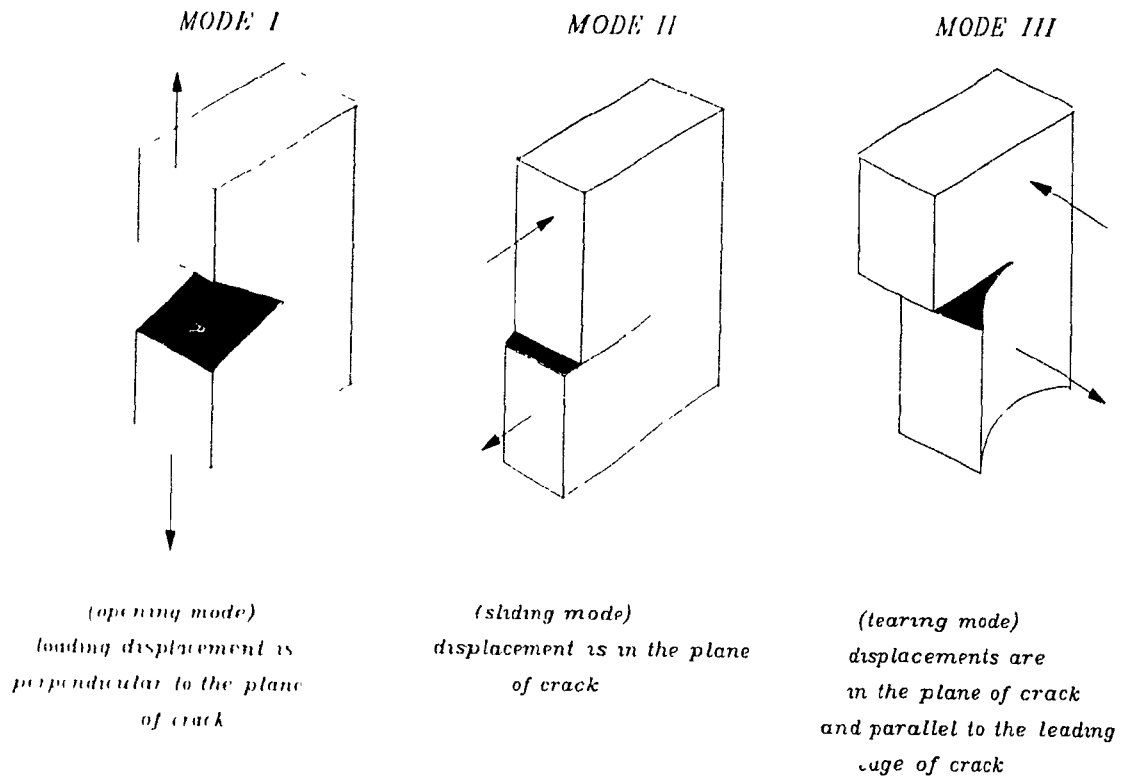


Figure 6.2: Four types of microcrack nucleation mechanisms have been identified in which the glide is activated by an obstacle. Types I and II operate at the intersection of glide lamellae with grain boundaries. In type I, the cracks form at a high angle to the lamellae. In type II, the cracks form parallel to the lamellae, where a component of normal stress in the glide plane is removed to form a crack.

Microcracks resulting from type III mechanism form at the intersection of the lamellae. Type IV is caused by a wedging action from a combination of strong and weak grains. Mechanisms I, III and IV were reported to lead to microcracks oriented parallel to the direction of maximum compression. Mechanism II produces cracks lying in a plane of high shear stress. Faults are composed of 'en-echelon' arrays of sub-axial cracks connected by packets of inclined twinned lamellae. According to the report, types I and IV were most frequently observed just beyond maximum stress [after Olsson and Peng (1976)].

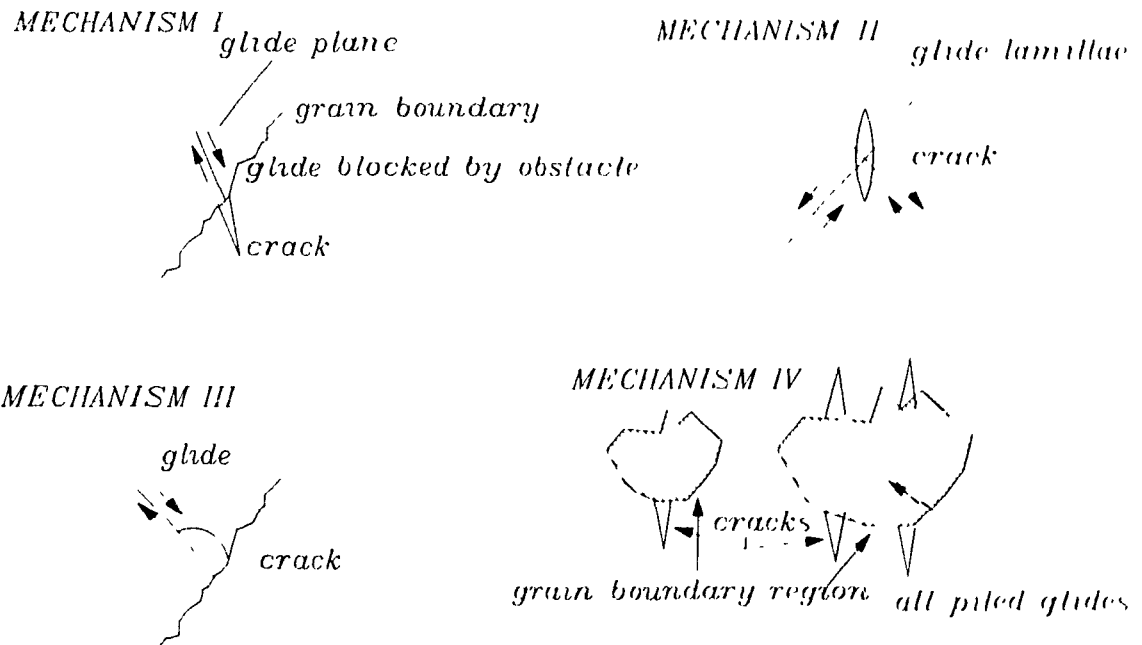
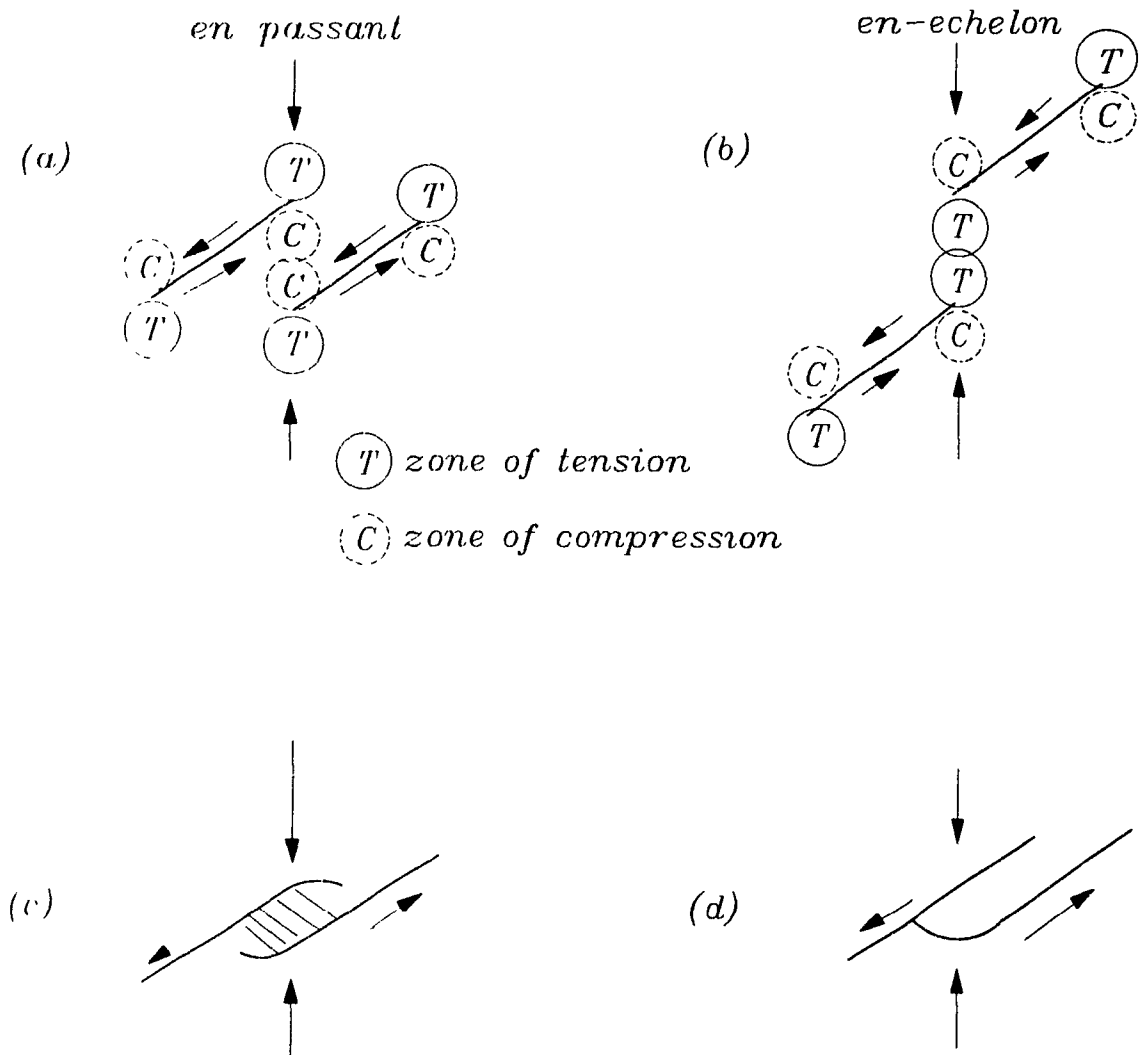


Figure 6.3: Schematic illustration of two types of crack interactions between overlapping cracks: (a) displays the 'en-passant' configuration. This produces adjacent regions of compression ('C'), (b) shows the 'en-echelon' configuration. The latter interaction brings together two regions of tension ('T'). The development of such interactions produce a sliver of material (shown hatched in (c) which acts as a double-ended cantilever eventually snapping at one end, as shown in (d)) [after Fonseca et al. (1985)].



## **Procedure of Petrographic, Fractographic and Acoustic Emission Analysis**

### **7.1 Petrography**

Petrographic analysis is necessary in order to identify the rock forming components of petrophysical significance. One hundred and fifteen (115) polished thin sections and fifty (50) polished planer slabs were photographed, catalogued and analyzed for grain and pore structure, texture and mineralogy.

Microscopic observation of internal rock structure and composition was performed using planer polished specimens. Specimens were observed under both optical and electron microscopy in order to observe the rock texture, structure, mineralogy, porosity, alteration (diagenesis) and microfractography. Figure 7.1 derived from Montoto et al. (1984) summarizes the techniques made available to study the specimens' components.

### **7.2 Texture Analysis**

Textural analysis involves characterizing the rock structure by its grain size distribution, textural homogeneity and structural interlocking [Dreyer (1972)]. This was accomplished by digitizing these measurable microstructural features off photographic prints of polished specimen surfaces.

In certain cases, insufficient detail of microstructural features of the specimens were observed on the photographic prints of the specimen. In such situations, the samples were chemically etched prior to being photographed. Also, in photographing the specimens, red filters were employed to increase the contrast between the grain and grain boundary regions.

Photographs were noted for their orientation, sample number and scale with respect to a predetermined reference. The black and white prints measured 8.5 by 11 inches in size. The photographs were taped onto the digitizer tablet (Jandel Corp., 1989), and the grain boundary regions were traced out using the magnetic tracing device. The circumference of each grain was traced out individually corresponding to the grain boundary area. The data collected from this measurement included the perimeter distance and the area of the grain. The data was transferred to a computer disk and stored in ASCII format.

A similar technique was used to determine the mineralogical percentage of each specimen. In this case, the surface area of a particular mineral phase divided by the total area was measured. Both the total surface area of the plane of observation and the mineral phases were traced out.

A total of sixty (60) polished specimen surfaces were photographed and measured. On average, a total of one hundred and fifty (150) grains were measured.

### **7.3 Sample Preparation**

#### **7.3.1 Sampling and Specimen Preparation**

Block shaped specimens of potash and salt rock (originally sized between 35 to 50 cubic centimeters) were obtained from PCS, Saskatoon (Cory Division), pre-packed in styrofoam and sealed in plastic wrapping. Based on grain size and percentage of mineral components, four variations of potash sample types were selected from ore horizons of the mine area located at the head of the drift 2.95 along 2000 entries. The extent of the mine plan was drafted in April 1988.

The sample preparation program involves several stages of cutting, coring, grinding, sectioning and polishing. All sectioned and slabbed specimens have been noted for their orientation, relative to the position of the structural features on the original block sample. The predominant features include bedding laminations and banding. Samples were utilized for petrographic, textural, load-acoustic emission and fractographic studies.

#### **7.3.2 Preparatory Stage**

The original block was initially trimmed down to form a well dimensioned rectangular block (refer to figure 7.2). Two vertical planes (cut at right angles to each other), and one upper and lower horizontal planer slab were cut along the external faces of the original block. The planer slabs represent three orthogonal planes of the sample. Each sample is approximately 0.50 cm in thickness and the surfacial area of the plane coincides with the area of the block along the same designated cutting face (refer to Figure 7.3). The cut is accomplished using a rotary diamond blade saw with a constant cutting rate of 0.25 cm/min. in a dry medium. It was noted that cutting the sample manually introduced artificial structures along the cutting face of the sample. The use of lubricants would also alter the appearance of the sample structure by permeating into the rock along the grain boundary areas. The slabs were then vacuum sealed in polyurethane bags until they were further developed for testing.

#### **7.3.3 Secondary Stage - Sampling for Load and Acoustic Emission Testing Program**

Figure 7.3 summarizes the stages involved in preparing the remaining portion of the block to be used to prepare samples for the load-acoustic emission testing pro-

gram. All tests were performed on right cylindrical shaped samples with an average diameter to height ratio of 1.78. Sample size was limited by natural macroscopic discontinuities observed in the samples (refer to figure 7.4).

Sample diameters of 7 centimeters and 15 centimeters were considered for load and acoustic emission testing. The smaller sample size was developed by cutting the prepared block into smaller equispaced rectangular samples. The samples were then ground down into a right cylinder shaped sample using a machine lathe rotating at an extremely low grinding speed, so as not to introduce any artificial structure (refer to figures 7.5 and 7.6).

The larger size samples were cored out directly from the original block. This cut was accomplished using a 4 inch diamond-tipped core barrel mounted on a drill press. Ground rock debris developed from the cutting had to be expelled from the cutting front in order to efficiently cut out the complete length of the core. Since all cutting had to be done in a dry medium, expelling of the ground material was accomplished by developing an air flow system within the core barrel. The configuration of the equipment utilized for sample preparation is shown in figures 7.7.

The orientation of each specimen was cut out in a direction perpendicular to the banding observed in the original block. All samples were clamped down during cutting and coring to avoid vibration and movement.

Even and smooth ended specimens were achieved using a machine lathe then hand lapped and polished using Silicon Carbide grit paper. The ends were ground within 0.008 mm of parallel, using a surface grinding machine. Final polishing was achieved at 200 grit size and finished at 800 grit size. A visual examination of each sample was made, paying particular attention to structural and lithological characteristics that would likely influence the acoustic emission response and the behavior of the sample under load.

After numbering and cataloging, the specimens were stored in an environmentally controlled room to be pre-conditioned.

### **7.3.4 Third Stage - Specimen Preparation for Petrographic and Petrofabric Studies**

#### **7.3.4.1 Preparation of the Initial Slab**

All petrographic and textural observations were performed from the polished slabs by electron and optical microscopy. Planer polished slabs were also used to study the macroscopic structure, microstructural and grain size analysis.

The planer slabs were cut along three axis to represent orthogonal sections. The slabs cut from the source block were marked to conform with the imposed reference frame. Slabs were assigned top and bottom surfaces to correspond with the surfaces of the blocks from which they were cut from. As shown in figure 7.3, the zero orientation line for x-direction slabs are in the xz-plane of the +z side; the line for the y-direction slabs are in the yz plane on the +z side; and the line for the z-direction slab is in the xz-plane on the -x side.

#### **7.3.4.2 Development of polished sections**

Strips were cut from the planer slab to produce the polished thick and thin sections. An approximate 4 cm width strip was cut off the entire external perimeter of the planer slab. The remaining portion of the slab was polished and etched using formic acid in order to display a strong contrast between the grain and grain boundary area.

The polished slab were photographed and catalogued. The photographs were used to determine the petrofabric, grain size analysis and mineralogical composition of the rock types present.

To develop polished thin sections, several evenly spaced cuts, perpendicular to the length of the strip were preformed. The area of each rectangular specimen approximates the area of a standard thin section. Fine cuts to develop a thin slice of the specimen were accomplished using an Isomet Low Damage Low Speed Precision Saw (Buehler Ltd., Evans, Illinois, 60204), and then successive polishing with alcohol solution starting at 600 grit and ending with almost dry 0.3  $\mu\text{m}$  alumina were performed. Finally, scratches were 'painted' off the surface with a moist, soft, camel's hair brush. This surface was epoxied down on a glass microscope slide. The process was repeated on the other side to provide an uncovered thin section of 300  $\mu\text{m}$  of the rock specimen.

#### **7.3.4.3 Specimens for the Study of Stress Induced Cracks**

Specimens used for the study of cracks and pores in rock were derived from both pre and post-deformation of the rock specimens.

Samples were first vacuum impregnated with epoxy resin, cleaned and cut. Comparisons were then made by both optical microscopy and scanning electron microscopy of surfaces formed by; fracture alone, low speed diamond sawing and polishing.

Specimens observed by scanning electron microscopy were coated with carbon, (200 angstroms thickness), prior to observation in order to prevent surface charging under the electron beam of the scanning electron microscope.

#### **7.4 Measurement Apparatus**

Many qualitative descriptions of rock textures are available but quantified analysis of textural parameters such as grain size, orientation, and grain matrix relationships are few. This is due to the difficulty of obtaining adequate data in a short period of time. It is for this reason alone that the measurement equipment utilized for this investigation involves digitizing the individual elements of the rock fabric. Two dimensional measurements are preformed via the Jandel Scientific electromagnetic digitizing tablet. The hardware is linked up to a micro-computer system under software control by the 'Sigma Scan' program system. The data measured by this system can be grouped as shown in table 7.1.

A 16-key puck is implemented to trace out the microstructural features. Each key can be preprogrammed to store different variable types (measured values) in specified blocks of the data worksheet file.

##### **7.4.1 Requirements to Preform Measurements**

Scaled microphotographic prints were developed to measure out the necessary parameters. Initially, an etched specimen was photographed under magnification ranging from 2 to 20 times (depending on the grain size). Thirty to one hundred grains were observed on individual prints. In order to enhance certain microstructural elements and mineral grain constituents, color filters and polarizers were used to produce both color and black and white 8" x 11" prints. This is the standard size required to preform the measurements effectively on the tablet.

##### **7.4.2 Equipment Calibration**

Each measurement requires its own calibration mode. Several situations also require that the user establish a calibration for the same measurement, since various prints were photographed at different scales. The program supplies the user with an option which enables one to create and save a calibration in a file. The specific types of calibrations include the angle, area, distance, slope and tally counting x and y cartesian or polar coordinates to measure two known points.

The accuracy is limited both by the digitizer's resolution and measurement technique. In order to minimize error in calibrations and data measurements, a large as possible standard should be used.

### **7.4.3 Data Storage and Processing**

There are two stages involved in producing the final result. Once the parameters of all the elements have been measured, digitized and recorded; the newly formed data file can be interfaced with various statistical software for calculation purposes.

Although only one measurement mode can be invoked at a time, the Sigma Scan system can collect more than one type of data at any given time. When measurements are made and processed, the data is stored on a data worksheet. This worksheet is composed of a spreadsheet with rows and columns. The data can be reorganized once it has been collected.

### **7.5 Acoustic Emission Monitoring Equipment**

#### **7.5.1 Acoustic Emission Monitoring and Processing Apparatus**

This section presents the equipment used to measure acoustic emission parameters with the AET 5500 system installed at McGill University.

##### **7.5.1.1 System Description**

The laboratory monitoring system consists of the following components:

Pre / post amplifier	Emission sensor Amplification of signal Discriminator (used to differentiate between invalid signals)
Processor	Parameterization stage (where signal pulse are processed and recognized as an event) Conditioning and recording the signal (for parameterization)
Recorder	Recording of the parameters and other physical test data

The AET Model 5500 system is a two-component interconnected system composed of an 8-channel mainframe unit and a MS-DOS based microcomputer terminal. The mainframe input and control components are located at the rear and front panel. The rear panel contains the sensor connector inputs to and from the computer terminal. All processing takes place within the mainframe. Test parameters including physical parameters (load, displacement, temperature, etc...) are transferred through an analog input located in the mainframe. Data is stored in a hard-disk and/or floppy disk system located in the computer terminal. Figure 7.8 illustrates the interconnected system used to preform acoustic emission measurements.

### 7.5.1.2 Transducer

Acoustic emission sensors are used to detect signals. These sensors, commonly referred to as 'transducers', are input devices that convert the mechanical energy of the elastic wave into an electrical signal [Matthews (1983)].

The selection of the transducer is based on several criteria including: sensitivity, impedance, resolution, range and durability. The former two parameters are frequency dependent [Malott (1984)]. Sensitivity is defined as the ratio of the charge in the output, to the charge in the input. High sensitivity is desirable since the frequency range is greater and as a result, less amplification is required [Malott (1984)].

There are basically two varieties of microseismic transducers used in acoustic emission testing. These include the geophone (or velocity gauge) and the piezoelectric accelerometer; the latter type is frequently considered for laboratory testing conditions [Matthews (1983)].

The advantages of using accelerometers are that they are more sensitive. They exhibit a greater output voltage than velocity detectors when both are excited with a constant velocity signal [Vladut (1988)]. Also, they have better resolution, a broader frequency range response and a greater dynamic range showing similar frequency ranges that are generated and observed in laboratory rock specimens. A limited low frequency response is present in accelerometers. This is due to the input resistance of the amplifier [Malott (1984)].

The piezoelectric transducer is constructed of a mass-spring system where a seismically active geologic material is attached to the back of the piezoelectric plate, acting as a couplant spring (refer to figure 7.9). The piezoelectric effect results from a crystal subjected to pressure to the plate and as a result, a current flows through the plates and the encircling metal bond. The pressure is a deflection reading, which is transformed to a voltage time output [Vladut (1988) and Matthews (1983)].

The transducer is a capacity device which has a high impedance stated as a capacitive value. To match the high impedance output of the transducer, a charge amplifier or a voltage amplifier with a high input impedance must be used [Vladut (1988)].

Transducers are capable of responding in two modes. These include undamped, with the element backed by air; and damped, whereby a damping material backs the element. The undamping mode yields a resonant type transducer, sensitive to a large range of high frequencies, with a peak effect at the mechanical resonant frequency of

the seismic mass coupled to the transducer. The damped mode yields a broadband transducer, sensitive over a broader range, but does not show a satisfactory flat frequency response over that range. It also distorts the input acoustic signal.

A couplant (such as SC6 Silicon grease ) transmits acoustic emission waves from the sample to the transducer. The couplant should be smeared on the shoe of the sensor in a light layer, in an amount sufficient to flow out slightly from under the sensor shoe when it is pressed against the sample. The shoe should be in contact with the specimen. The sensor cable should be attached to the transducer prior to installation. Finally, in order to affix the sensor firmly to the sample, adhesive tape and rubber bands are used in order to avoid sensor movement during the test.

Acoustic emission sensors need to fit with the test sample in a practical fashion in order to yield appropriate results. Their size must be in proportion to the surfacial contact of the specimen. The couplant and surface condition of the specimen are both important interfaces. The surface of the specimen should be clean and abraded [ASTM 650-78 (1979)].

A piezoelectric accelerometer was chosen for this study, the specifications of which are presented in table 7.2.

### **7.5.1.3 Preamplifier**

Virtually all microseismic installations use a preamplifier which is located at the sensor. It provides the first stage of amplification of the low voltage signal derived from the output voltage of the transducer. Its major function is to convert the sensor impedance to a suitable range for driving the signal along the 25 foot transmission lines and any other electrical components. The input impedance of the preamplifier forms the load for the sensor. The proper magnitude and phase angle of the input impedance is governed by the sensor requirements. Impedance between the sensor and the preamplifier must be matched in order to prevent power loss and noise generation. [Malott (1984) and Matthews (1983)]

The Physical Acoustics 1220A Series preamplifier was utilized for this study. The preamplifier has user variable settings, allowing high pass, low pass, or bandpass filters, single ended or differential input, variable 40 dB or 60 dB gain settings and the choice of three output configurations as shown in figure 7.10. The specifications for the preamplifier model 1220A are shown in table 7.2.

#### **7.5.1.4 Cables**

Cables are the transmission lines required to relay input signals to the signal processor. A long transmission line acts as a low pass filter with loss. A high frequency signal (with a fast rise time) becomes more rounded and attenuated as it transmits down the line. The resistance of the cable also causes an overall reduction in signal amplitude. These combined effects limit the frequency response that can be transmitted by a given type and length of cable. The larger the wire or gage size the less the resistance and capacitance. Twenty five foot cables are used in this study. They are interconnected to the sensor and to various other components as shown in figure 7.11.

#### **7.5.1.5 Mainframe - Data Processor System**

Once the event is detected by the transducer, converted into an electrical signal and preamplified, it is then transmitted to the multi-channel processing system. The system is composed of two main components including the main frame and the personal computer terminal. The former contains several built-in modules to parameterize the data immediately.

The AET 5500 system consists of a wide array of output control options in order to control the signal parameterization. Its controls are located on the front panel which consist of a Hi/Low switch gain control, a gain volume control, a LED event indicator, an output connector to link with an oscilloscope, a headphone jack input and an 8-channel selector.

The rear panel is reserved for various input and output connectors. In general, the channel inputs are reserved for the sensor connections. The analog inputs are the links that receive and process the acoustic emission and load/deformation data that is transferred to the data storage disk in the computer terminal.

The computer based acoustic emission monitoring system is software rather than hardware oriented. Acoustic emission data can be collected from all 8 channels, measuring signals independently. Two other test modes are designed specifically for source location techniques.

The signal processor unit is equipped with a threshold-counting instrument. This requires the signal amplitude to exceed a threshold voltage to be recognized and recorded. Counting is performed by rate and summation. Accuracy depends upon the accuracy of the comparator clock frequency.

The AET's Model 208 Signal Processor Unit is equipped with a dual channel signal conditioner. This post amplifier and signal conditioner provides an adjustable gain, from total attenuation to 40dB.

Threshold is set to provide maximum discrimination between background noise and valid events. The threshold voltage may be set in 0.01 volt increments between 0.0 to 10.00 Volts.

The digitizing section consists of two modules including the ringdown counter / event duration module (REM) and the amplitude / rise time module (ARM) (AET Corp., 1988).

Acoustic emission is characterized by high amplitude, rapid rise time and exponential decay. The ringdown counter / event duration module contains an event detector which turns on, when the first threshold crossing occurs. At the same time, the event duration clock begins counting the pulses, which are defined by a user variable time-base.

The ringdown counter/event duration module counts each threshold crossing in the event and stores that count. It will turn off when no event crossings occur within a 256-count limit of the event duration clock. This 256-count is the amount of time that an event detector waits to ensure that the event is over. Both the duration and ringdown counts are transferred to the processor.

The amplitude / rise time module obtains the raw signal from the preamplifier before it undergoes post-processing. The peak amplitude determinations are made with the same gain, and expressed in decibel units. The rise time is determined by the number of pulses of the rise time clock. The clock turns on when the REM event detector signals that the event is in progress. It turns off when the event reaches the highest peak amplitude. The AET 5500 calculates the slope by converting the peak amplitude to millivolts and dividing the rise time in microseconds. Based on these two parameters the AET 5500 can compute energy by:

$$\text{Energy} = \text{Peak Amplitude} + 10 \log (\text{event duration}) \quad 7-1.$$

### **7.5.2 System Configuration Procedure for Per-Channel Monitoring**

An MS-DOS computer is used to input acoustic emission parameters, set-up displays and store acoustic emission data. All processing takes place in the 5500 system and is then transferred to the microcomputer hard disk for storage.

There are two general procedures available. The "SENSOR" procedure, specifically used to set-up parameters to monitor and record acoustic emission signal events under a per-channel mode; and the "TEST" procedure which is used for source location technique.

The present study considers the analysis of acoustic emission parameters obtained under the 'sensor' test procedure. The initial set-up, testing and recording procedures consist of several steps:

- 1) Set up and interconnect the components/apparatus.
  - a) This includes attachment of the signal cable to the sensor and on the other end to the preamplifier.
  - b) Couple the sensor to the sample.
  - c) Attach the cable to the mainframe rear panel input into the appropriate pre-amplifier input.
  - d) Activate the system.
  - e) Load the system.
- 2) Set threshold and adjust gain.
- 3) Set up parameters for the SENSOR.
- 4) Record procedures.
- 5) Set-up display.
- 6) Perform run.
- 7) Stop recording procedures.

To determine the system settings, a number of pilot test runs were performed at different loading rates and sample sizes. It was also observed that reproducibility of results was improved by maintaining a constant location of the coupled transducer. This location was at the mid-diametrical region of the cylindrically shaped specimens.

Uniaxial testing is conducted using the RDP HOWDEN servo-controlled stiff testing machine. The specimens are loaded under uniaxial compression, at a constant rate of strain. Rigid steel platens with the same diameter as the specimens were used. Any initial non-parallelism was adjusted for by an upper spherically seated platen. This test set-up is shown in figure 7.12.

Table 7.1: Measurement parameters used for quantitative petrographic analysis.

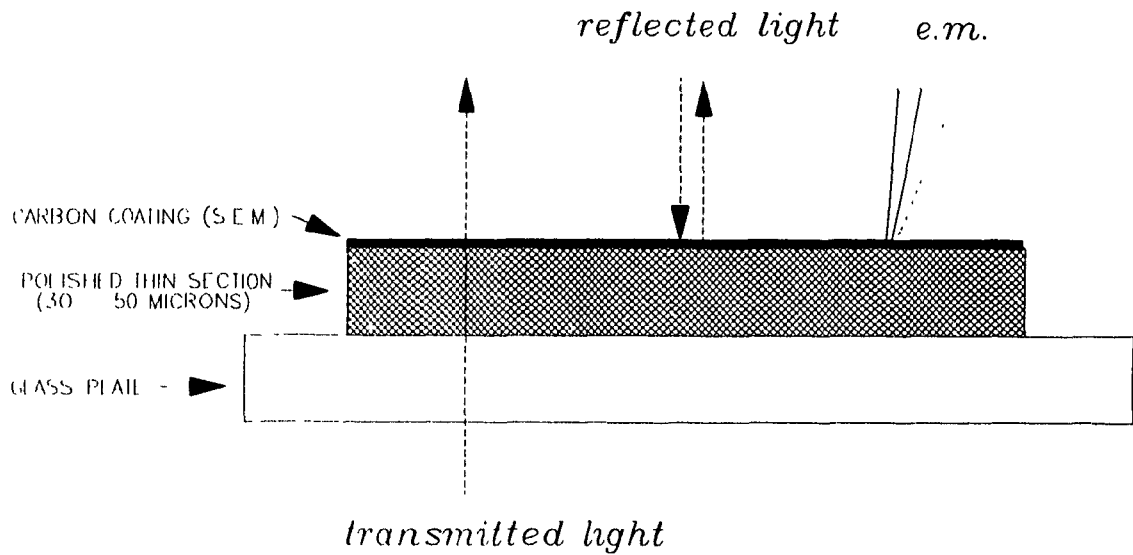
MEASUREMENT	PURPOSE OF MEASUREMENT
X, Y coordinate measurement	reference marker for orientation analysis
distance measurement	i- lineal intercept measurement used to measure anisotropy ii-grain size / homogeneity / structural interlocking
area measurement	grain size / homogeneity / structural interlocking
tallying of multiple groups	in conjunction with lineal intercept measurements
polar coordinate measure	construction for rose diagram

Table 7.2: Equipment and specimen specifications used to test potash rock.

TEST PARAMETER	SPECIFIED CALIBRATION OR SET VALUE
Rock type	Potash rock
Location of Origin	Saskatoon (PCS)
Length (2 sizes)	170 mm / 120 mm
Diameter (2 sizes)	101.64 mm / 75.5 mm
Test Type	Uniaxial
Control Mode	Displacement (constant rate of strain)
Mode rate	$1.538 \times 10^{-3}$
Number of loading cycles	1
Number of acoustic emission Sensors	1
Sensor Type	PAC 15-2358
Resonant Frequency	150 kHz
Pre-Amplifier Gain	40 dB
Post-Amplifier Gain	1 (amplification factor)
Pre-Amplifier Filter	100 - 300 kHz. (Band-pass)
Threshold	1.50 V (fixed)
Load Scale	500

Figure 7.1: Polished thin section and various microscopic techniques used to observe specimen morphology [after Montoto et al. (1984)].

<b>Rock Forming Components to be Observed</b>	<b>Mineralogy</b> Texture State of diagenetic alteration Macro-Sedimentary structure	<b>Fractography</b>	<b>Mineralogy</b> Porosity Grain Boundary Morphology Fractography
<b>Observational Technique</b>	Transmitted Plane and Polarized Light Reflective Light	Transmitted Plane and Polarized Light Reflective Light	Transmitted Plane and Polarized Light Reflective Light S.E.M. E.M.P.A.



**Figure 7.2** Initial cut of slab from the original shipped block. The slab is approximately 1cm thick. It has been noted for its orientation with respect to the original position of the sample block.



Figure 7.3: Schematic breakdown of various sample components to be used for the various stages of the test program.

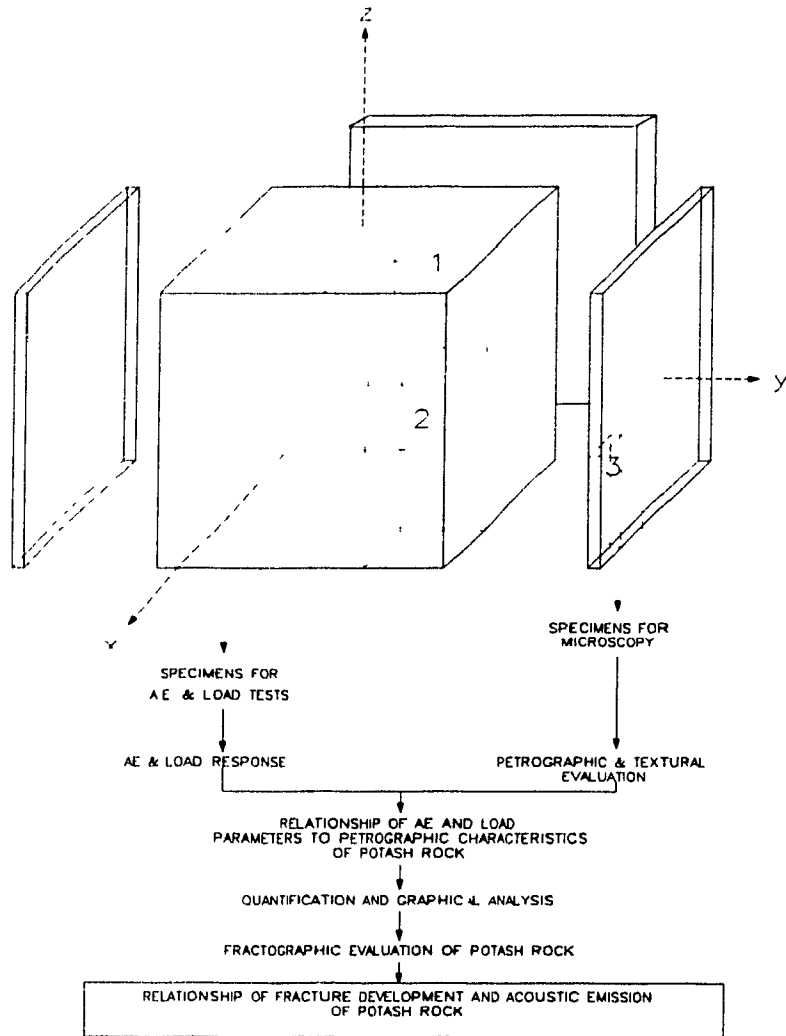


**Figure 7.4:** Photograph of potash sample after they have been cored, displaying natural horizontal discontinuities.



Figure 7.5: Photograph displaying the setup used to shape cylindrical sample developed via machine lathe. Figure 7.6 shows the end result sample.

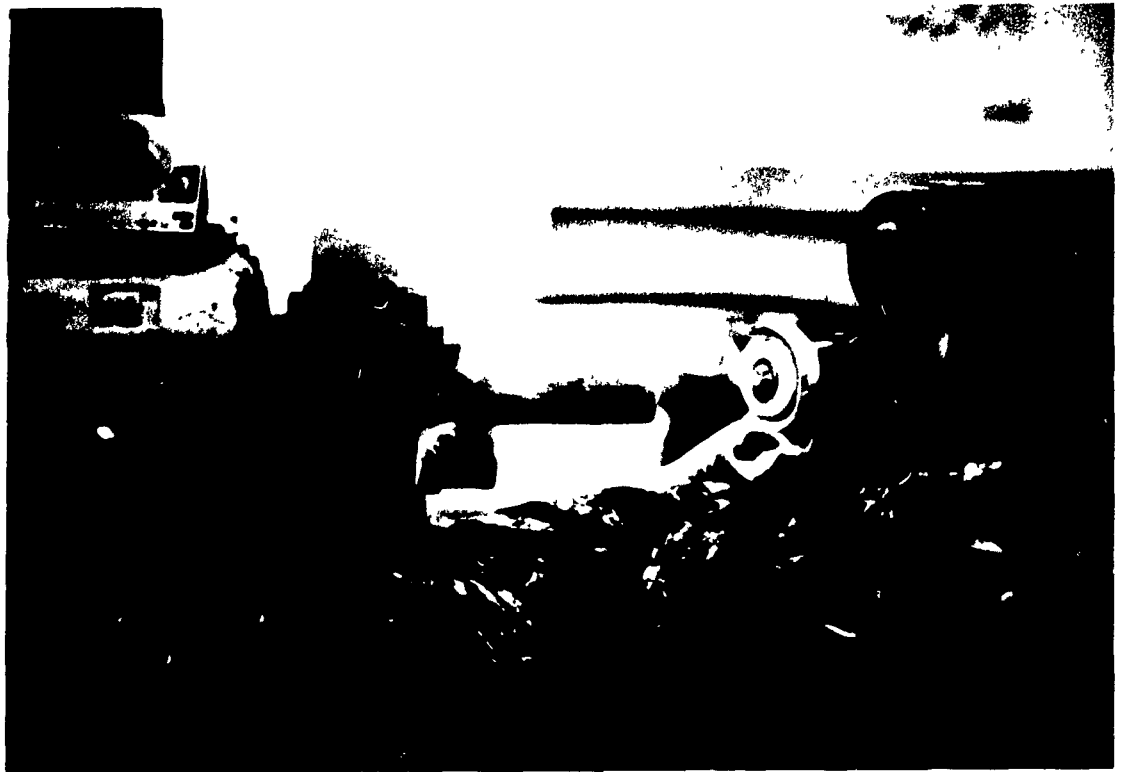


Figure 7.6: Photograph displaying the end result sample used for testing.



Figure 7.7: Photograph of setup utilized to core out specimen of potash. Coring was accomplished in a dry medium. An adaptor coupled between the shaft and core barrel was devised to feed compressed air into the barrel during cutting.

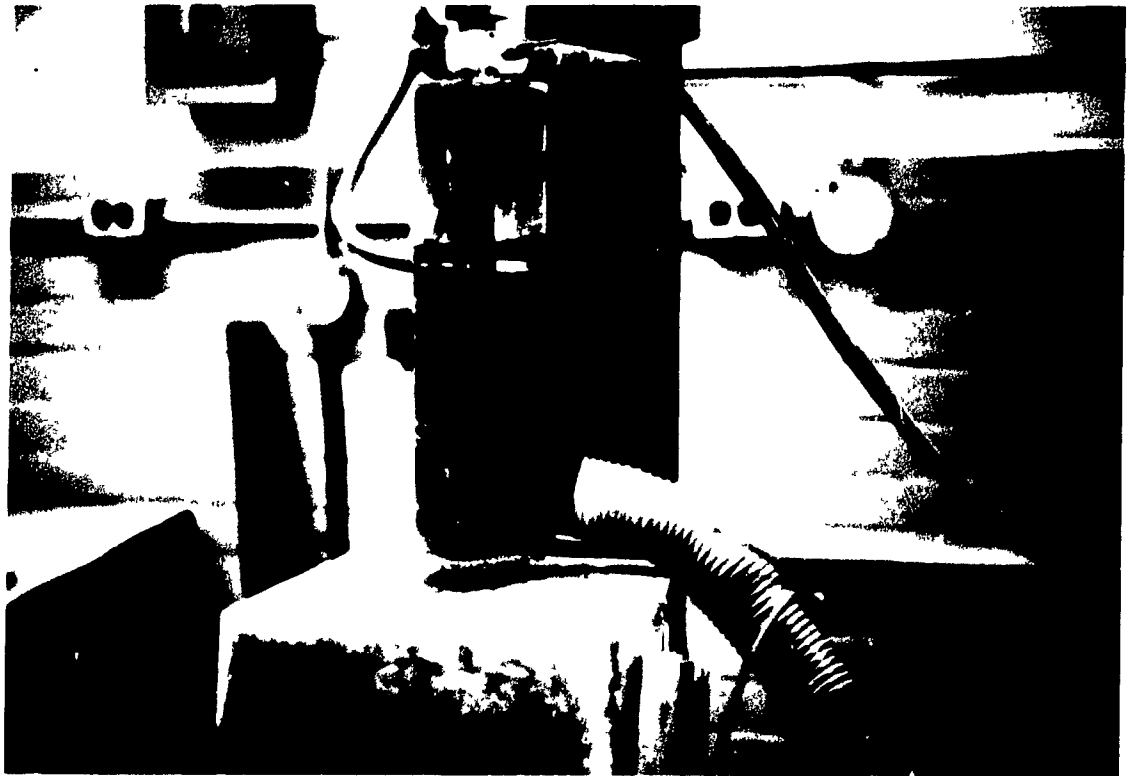


Figure 7.8: Diagrammatic representation illustrating interconnected system (courtesy of AE Technology Corp, 1988).

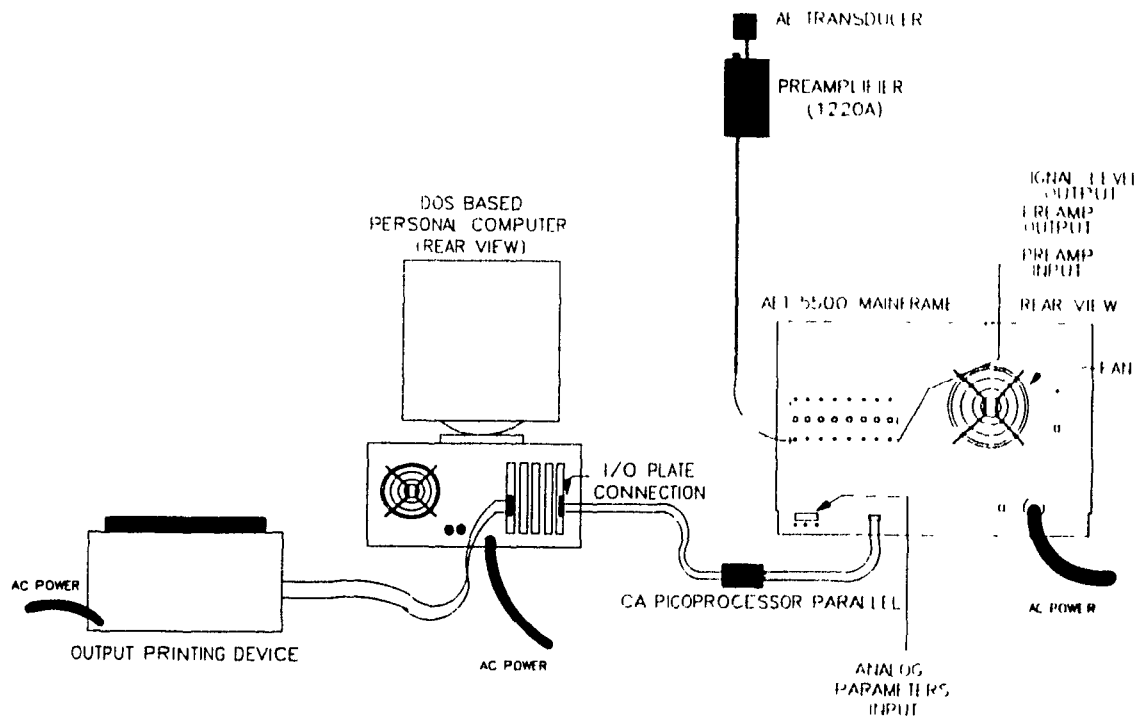


Figure 7.9: Schematic of piezoelectric transducer [Vladut (1988)].

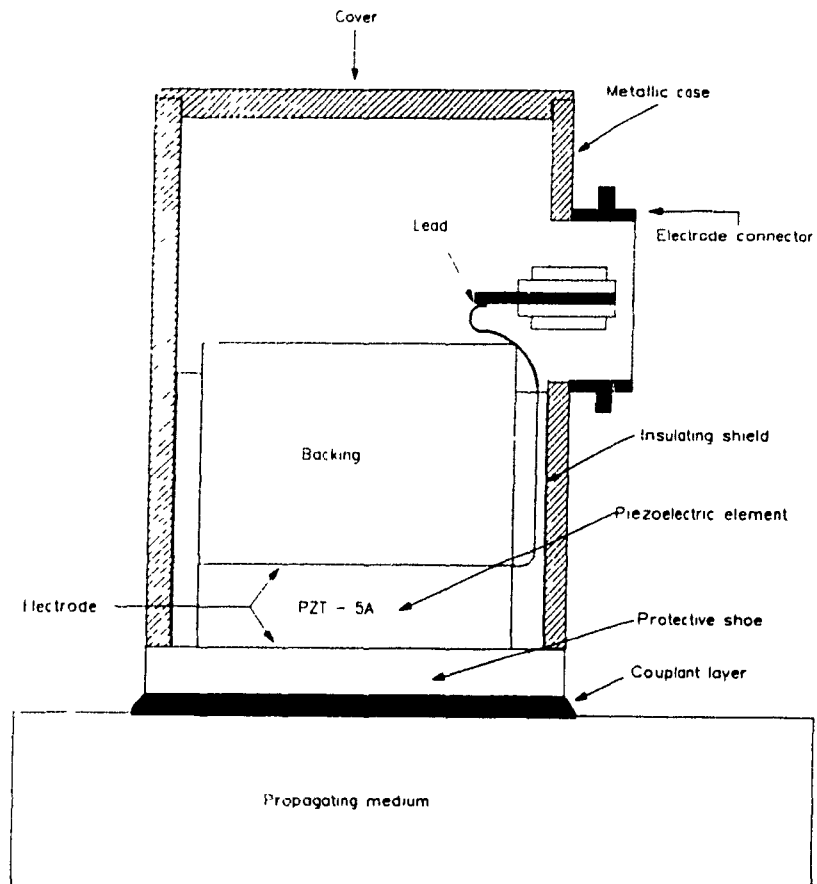


Figure 7.10: Schematic of the 1220A preamplifier, external connectors and controls (courtesy of Physical Acoustics Corp, 1984):

- 1) Acoustic emission single ended input connector
- 2) Acoustic emission input select switch
- 3) Acoustic emission differential input connector
- 4) Power signal cable
- 5) Gain select

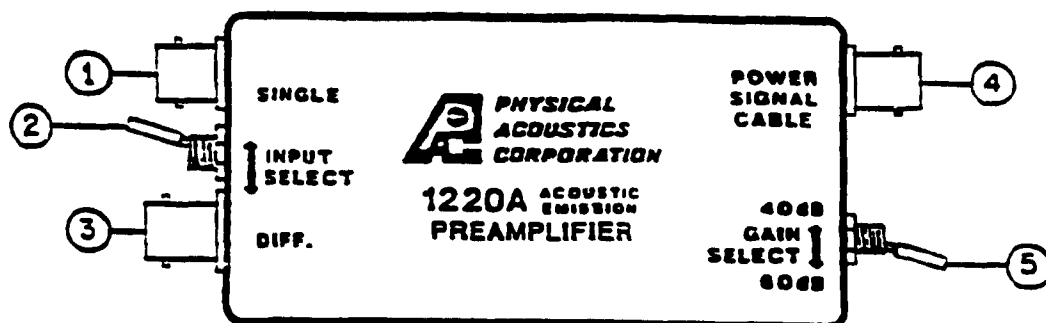


Figure 7.11: Wire connections of the preamplifier and sensor to signal processor/mainframe unit.

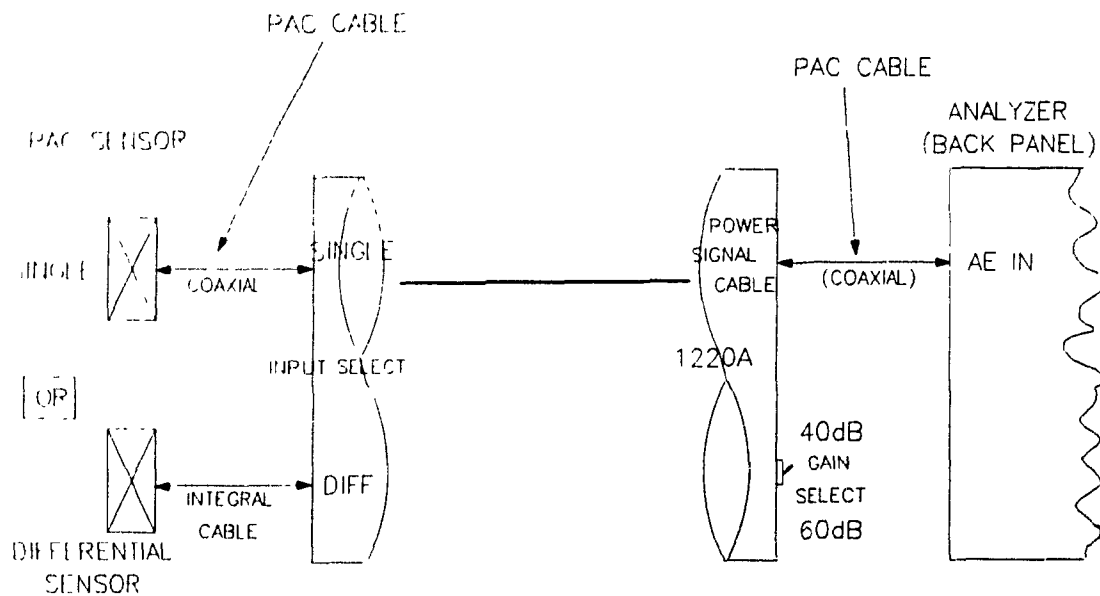


Figure 7.12: Photograph of sample seated between platens on servo-controlled hydraulic press. Also, shown is the acoustic emission transducer.



## **The Relationship of Petrographic to Strength Parameters of Potash Rock**

### **8.1 Introduction**

This chapter deals with a statistical correlation which establishes the relationship between texture and rock strength. The approach considered for the analysis involves using the multiple regression technique. Following a brief summary describing the petrography and load deformation characteristics of potash rock used for this study, a statistical analysis showing the dependence of uniaxial compressive strength to petrographic parameters will be discussed.

The dependent variables including textural homogeneity and structural interlocking, previously defined by Dreyer (1972), were measured from two-dimensional polished surfaces and from polished thin sections. Other dependent parameters that were measured include the mineral composition and average grain cross section.

The mineral composition measured for potash rock specimens displays a variable distribution. Samples contain visible inhomogeneous structure. Specimens were prepared for reflective light optical microscopy. Major and accessory minerals were identified and grain size distribution was assessed. Two geometric measurements including grain perimeter and the area of each mineral specimen were also measured. The final mineralogical ratios were determined from normalized values of combined measurements of several potash samples of the same type. The percentage of sylvite was determined by the areal analysis method. This method determines the percentage of the total relative area of sylvite with respect to the total area of the specimen surface area, as shown in equation 8.3.

### **8.2 Summary of Macroscopic Petrographic Characteristics of Potash Rock**

The potash rock under investigation has been categorized into four types. The distinctions are apparent from the color, mineral ratios, texture, grain size and structure of the specimens. Extensive details on the various petrographic features are described in chapter 2.

On the basis of color, the principle rock types are divisible into two groups. Types "B" and "C" display a brick red color, with variable dark to lighter shades. The red color was identified as sylvite, which is the dominant mineral phase in types "B" and "C" potash. Also, interstitial clots and lamillae of green clay are commonly present in these specimens. Types "A" and "D" potash rock on the other hand, are light orange to clear white in color with minor interstitial specs of green clay.

Mineralogical differences are also distinguishable between the four types of potash. Types "B" and "C" are composed of a high percentage of sylvite in relation to types "A" and "B" potash. Type "A" contains up to 5% of sylvite whereas type "D" may contain up to 30% of it. The clay is considered as a minor mineral constituent in all four types of potash rock, although it can occur up to 10% in some samples, particularly in types "B" and "C".

Texturally, all four types of potash rock are different. Type "A" displays an equigranular crystalline mosaic of interlocked anhedral halite grains. The majority of the samples of type "A" potash display a strong grain alignment perpendicular to the bedding plane. The average grain cross section is 20 mm also referred to as large grained [Dreyer (1972)]. Type "B" potash rock is inequicrystalline and porphyroblastic. It is composed of laced anhedral poikiloblasts of rimmed sylvite grains interlocked with granoblastic clusters of halite. The average grain cross sections range from 1mm for halite grains, to 45mm for sylvite porphyroblasts.

Type "C" potash rock is composed of a homogeneous, equicrystalline granoblastic mosaic of sylvite matrix interlocked with granoblastic clusters of halite. The average grain cross section is 20 mm, referred to as coarse to large grained. Type "D" potash rock is texturally homogeneous equicrystalline and isotropic. It is composed of a granoblastic mosaic of halite with interstitial anhedral grains of sylvite. The average grain cross section is 10mm or less. It is designated as coarse grained.

Macroscopic structure obstructs the homogeneity of the rock, predominantly in the form of clay films adjacent to remnant solution surfaces. These form in areas whereby there is lateral grain size variation and monomineralic banding or layering. These features are frequently observed in types "B" and "C" potash rock. The films of clay range in thickness from a few millimeters to 5 cm. These layers are usually oriented horizontally in relation to inherent bedding. As previously mentioned, variation in grain size is associated with the clay layers, often increasing in size upwards. This feature gives the rock a layered appearance.

Three types of measurements were performed, these include textural homogeneity, structural interlocking and average grain cross section based on Dreyer (1972) and Onodera et al. (1980). Types "A", "C" and "D" potash display high values of textural homogeneity. Structural interlocking is distinctively high for type "B" potash rock. The high value of structural interlocking is primarily due to the irregular shaped sylvite porphyroblasts in type "B" potash rock. However, types "A", "C", and

"D" show lower structural interlocking values which is indicative of more regular shaped grains. These values will be used in this next section to demonstrate the influence of inherent rock properties to load when loaded under uniaxial compression.

### **8.3 The Stress-Strain Behavior of Potash Rock Loaded under Uniaxial Compression**

There is slight variation in the stress-strain behavior between the four types of potash rock. Differences in the behavior are observed in the extent of the linear elastic region, the strain hardening region and the load attained prior to sample failure.

At less than 1MPa of pressure, a pre-load adjustment is observed. The stress-strain curve is non-linear. This occurs before the elastic zone. The initial concave upward nature of the function is due primarily to pore closure located at the grain boundary areas. At 3% of the failure stress, linear elastic deformation is observed. The linearity is strong up to approximately 50% of the uniaxial compressive strength. At this point, the curve deviates. An increase strain rate is observed with increasing load, thus displaying a concave downward direction of the stress-strain curve. The Young's modulus of elasticity was calculated using the linear portion of the curve. The proceeding portion of the curve continues on a pseudo-linear trend displaying an increase in uniaxial strain with respect to a shorter incremental increase in stress. This behavior was typically observed in rocksalt specimens. It is commonly referred to as the strain hardening region [Dreyer (1972), Roberts (1980) and Richardson (1980)]. This trend is observed up to specimen failure.

Notable differences in the stress-strain relationship are apparent. Figure 8.1 illustrates representative examples of the stress-strain curves for the four types of potash rock loaded under uniaxial compression. Three dissimilarities are noticeable among types "A", "B", "C" and "D" potash rock. The elastic limit and the region of linear elasticity are both higher and longer for types "A" and "D", in comparison to types "B" and "C". The elastic limit for potash rock in type "A" and "D" ranges between 14 to 16MPa, in comparison to only 8 to 11 MPa for types "B" and "C". Secondly, there is a more definitive linearity associated with types "A" and "D", followed by a sharp deviation in the stress-strain curve to the strain hardening region. The linearity is also apparent in types "B" and "C" but, the strain hardening region is both shorter and imperfectly elucidated. Finally, the uniaxial compressive strength is higher for types "A" and "D" as compared to the other two types of potash rock.

## 8.4 Statistical Relationship Showing the Influence of Texture to the Uniaxial Strength of Potash Rock

### 8.4.1 Introduction

Potash rock samples were tested for acoustic emission response. They were loaded under uniaxial compression up to specimen failure. It was noted that the uniaxial compressive strength values varied with respect to petrographic type. A correlation was established showing the dependence of textural parameters and sylvite concentration of potash rock on the uniaxial compressive strength.

The determination of the textural parameters was previously described in chapter 3. The measurements include structural interlocking and textural homogeneity. The formulae corresponding to these variables are presented below:

Structural interlocking

$$g = \frac{1}{n} \sum_{i=1}^n \left( \frac{U_i}{\sqrt{F_i}} \right) \quad 8-1.$$

whereby  $F_i$  is the grain sectional area in  $\text{mm}^2$  and  $U_i$  is the length of grain in contact with neighboring grains.

Textural homogeneity

$$t = \frac{M}{\sqrt{\sum_{i=1}^n H_i * (F_i * M)^2}} \quad 8-2.$$

whereby  $M$  is the average grain cross section and  $H_i$  is the frequency of occurrence of a particular grain size cross section.

The mineral composition and grain size were also measured for potash rock specimens. Two geometric measurements including grain perimeter and area of each mineral type were obtained. The final values for mineral compositional ratio were determined for each specimen. The percentage of sylvite in potash rock was calculated as follows:

$$\text{Percentage } KCl = A_A = \frac{A_{KCl}(\text{mm}^2)}{A_{\text{total specimen surface}}(\text{mm}^2)} * (100\%) \quad 8-3.$$

whereby  $A$  refers to the area of the constituent in  $\text{mm}^2$ .

### 8.4.2 Summary of Method of Linear Multiple Regression Analysis

The linear multiple regression analysis involves several stages of calculations and statistical inferences in order to evaluate the regression coefficients. The technique and analysis of data are best described by Lindgren (1976).

In general, the problem involves solving the following:

- 1) Determine the  $Y$ ,  $X_1$ ,  $X_2$ , and  $X_3$  regression coefficients by regression of  $Y$  upon  $X_1$ ,  $X_2$  and  $X_3$ . The coefficients are identified in table 8.1.
- 2) Test the coefficients  $b_1$ ,  $b_2$  and  $b_3$  for significance by using the  $F$  and  $t$  tests.
- 3) Determine the multiple correlation coefficient.
- 4) Test the significance of the multiple regression.
- 5) Calculate the standard error of estimate and the standard error for regression coefficients.

#### 8.4.2.1 Determination of the Multiple Regression Equation

The main regression equation relating the observed values of the uniaxial compressive strength ( $\sigma_c$ ) was calculated using three parameters: structural interlocking, textural homogeneity and ratio of impurity. Using the estimated regression coefficients, one can define the fitted values by the following equation:

$$\hat{Y} = a + b_1 x_1 + b_2 x_2 + b_3 x_3 \quad 8-4.$$

$$\hat{Y} = \bar{Y} + b_1 x_1 + b_2 x_2 + b_3 x_3 \quad 8-5.$$

$$\text{where } : x_n = (x_n - \bar{x}_n) \quad 8-6.$$

In order to solve the coefficients  $b_1$ ,  $b_2$  and  $b_3$ , a set of normal equations are established. These include the following:

$$V_1 \quad b_1 \sum x_1^2 + b_2 \sum x_1 x_2 + b_3 \sum x_1 x_3 = \sum x_1 y \quad 8-7.$$

$$V_2 \quad b_1 \sum x_1 x_2 + b_2 \sum x_2^2 + b_3 \sum x_2 x_3 = \sum x_2 y \quad 8-8.$$

$$V_3 \quad b_1 \sum x_1 x_3 + b_2 \sum x_2 x_3 + b_3 \sum x_3^2 = \sum x_3 y \quad 8-9.$$

The variables of the normal equations are the result of the sum of products and the simple correlation coefficients which are determined from the initial given data shown in table 8.1. The sum of products are represented as follows:

$$\sum x_1^2 = \sum x_1^2 - \left( \frac{(\sum X)^2}{n} \right) \quad 8-10.$$

$$\sum x_1 y = \sum x_1 y - \left( \frac{\sum X_i \sum Y}{n} \right) \quad 8-11.$$

$$\sum x_1 x_2 = \sum x_1 x_2 - \left( \frac{\sum X_i \sum X_j}{n} \right) \quad 8-12.$$

Also, a simple correlation is defined by the following:

$$r_{ij} = \frac{\sum x_i y_j}{\sqrt{\sum y^2 \sum x^2}}$$

8-13.

The method of determining the coefficient  $b_1$ ,  $b_2$  and  $b_3$  can be done by various methods. Two methods include the Gaussian elimination and / or the Cramer method. The latter method involves using determinants of values  $b_1$ ,  $b_2$  and  $b_3$ , utilized in the normal equations.

#### 8.4.2.1 Results of the First Stage of the Statistical Analysis

Table 8.2a shows the resulting calculations of the sum of products and simple correlation. The coefficients of regression  $b_1$ ,  $b_2$  and  $b_3$  were calculated using the method previously described. It can be noted that extra decimal places were used for this type of calculation, so that the round off error in preceding calculations are reduced by a sizeable margin. The results of the calculation are presented below:

$$b_1 = -0.15138018 \quad 8-14.$$

$$b_2 = -1.96503816 \quad 8-15.$$

$$b_3 = -0.09886834 \quad 8-16.$$

The multiple regression analysis techniques have established relationships between the uniaxial compressive strength, ' $\sigma_c$ ' and various petrographic parameters including structural interlocking, 'g'; textural homogeneity, 'H'; and percentage of sylvite, 'KCl'. It is expressed in the following equation:

$$\sigma_c = 30.2820 - 0.1514g - 1.9650H - 0.0989KCl \quad 8-17.$$

The equation for the regression of sum of squares (RSS) is expressed as follows:

$$RSS = b_1 \sum x_1 y + b_2 \sum x_2 y + b_3 \sum x_3 y \quad 8-18.$$

$$RSS = 539.0588 \quad 8-19.$$

#### 8.4.2.2 The Test of Significance of Multiple Regression

The test of significance is a test statistic whereby the random variables values will be considered in order to render a decision on if the hypothesis tested is true. In this case, the hypothesis involves the reductions of the sums of squares which are attributable to the regression. These can be evaluated by the F-value. The F-value is determined by the following equation:

$$F = \frac{\frac{\sum_{i=1}^n (x_i - \bar{x})^2 \cdot \sum_{i=1}^n (y_i - \bar{y})^2}{m}}{\frac{\sum_{i=1}^n (x_i - \bar{x})^2}{n - m - 1}} \quad 8-20.$$

This calculation can be simplified in table form, whereby reduced calculations are used to determine the F-value. Table 8.2b presents this simplified format. F-values determined from the tables of the F-distribution are presented for two levels of confidence:

$$F_{0.05} = 2.84 \quad 8-21.$$

$$F_{0.01} = 4.31 \quad 8-22.$$

#### 8.4.2.2.1 Interpretation and Assessment

The calculated F-value of 8.314 falls outside the critical region at 95% and 98% confidence intervals. The decision based on these results implies rejection of the null hypothesis, whereby, the null hypothesis is  $H_0: (B_1 = B_2 = B_3 = 0)$ . Although none of the individual variables have significant explanatory power, the entire set of variables explain a significant part of the variation in the uniaxial compressive strength.

#### 8.4.2.3 Multiple Correlation Coefficient ( $R_{y123}$ )

The multiple correlation coefficient displays the measure of the combined effect of the independent variables  $X_1, X_2, X_3$  on the dependency of Y. The numerical value of the multiple correlation coefficient is always at least equivalent to the simple or partial correlation. The correlation coefficient ( $R^*$ ) is represented by the following formula:

$$R_{y123} = \sqrt{\frac{\sum y^2}{\sum y^2}} \quad 8-23.$$

Utilizing the values from this study, the multiple correlation coefficient result is :

$$R_{y123} = 0.6150 \quad 8-24.$$

The inference about the correlation coefficient is performed. The calculated ' $R^*$ ' is compared to two critical values of ' $R$ ' extracted from tables.

$$R_{0.05} = 0.4190 \quad 8-25.$$

$$R_{0.01} = 0.4940 \quad 8-26.$$

### 8.4.2.3.1 Assessment of Results of the Multiple Correlation Coefficient

The inference about the multiple linear correlation coefficient shows that  $R^*$  is greater than the table value of  $R$ . The decision based on this data, results in a rejection of the null hypothesis ( $H_0: (B_1 = B_2 = B_3 = 0)$ ). This result indicates that the uniaxial compressive strength is related to the textural homogeneity, structural interlocking and percentage of sylvite in each rock type specimen.

### 8.4.2.4 The Standard Errors and Test of Significance for Partial Regression Coefficients

The standard error of the estimate of the population of y-value is given by :

$$S_{y..1..k} = \sqrt{\frac{\sum(y-\hat{y})^2}{n-k-1}} \quad 8-27.$$

whereby :

$$\sum(y-\hat{y})^2 = \sum y^2 - \sum b_i(\sum x_i y) \quad 8-28.$$

The standard error is a means of estimating the variance of the error about the regression. The standard error of estimate of the population of y-value is calculated to be  $S_{y_{123}} = 4.6489$  (MPa), referring to the uniaxial compressive strength.

In order to obtain the standard errors for the partial regression coefficient, it is necessary to obtain the inverse of the determinant 'D'. The inverse of 'D' can be obtained as follows:

$$D^{-1} = \det \begin{pmatrix} a_{11} & a_{12} & a_{13} \\ a_{21} & a_{22} & a_{23} \\ a_{31} & a_{32} & a_{33} \end{pmatrix} \quad 8-29.$$

$$\alpha_{11} = \frac{(a_{22}a_{33} - a_{32}a_{23})}{D} \quad 8-30.$$

Whereby each variable is represented by the following:

$$\alpha_{21} = \frac{(a_{31}a_{23} - a_{21}a_{33})}{D} \quad 8-31. \quad \alpha_{32} = \frac{(a_{31}a_{12} - a_{11}a_{32})}{D} \quad 8-32.$$

$$\alpha_{31} = \frac{(a_{21}a_{32} - a_{31}a_{22})}{D} \quad 8-33. \quad \alpha_{13} = \frac{(a_{12}a_{21} - a_{21}a_{11})}{D} \quad 8-34.$$

$$\alpha_{12} = \frac{(a_{32}a_{13} - a_{12}a_{33})}{D} \quad 8-35. \quad \alpha_{23} = \frac{(a_{21}a_{11} - a_{11}a_{21})}{D} \quad 8-36.$$

$$\alpha_{22} = \frac{(a_{11}a_{33} - a_{31}a_{13})}{D} \quad 8-37. \quad \alpha_{33} = \frac{(a_{11}a_{22} - a_{21}a_{12})}{D} \quad 8-38.$$

A general expression for the standard errors of partial regression coefficients is given as:

$$S_{b_i} = \sqrt{\alpha_{ii} S_{y_{123}}^2} \quad 8-39.$$

Given the data used for this study, the inverse values were calculated :

$$\alpha_{11} = 0.00138877 \quad 8-40.$$

$$\alpha_{22} = 0.21223810 \quad 8-41.$$

$$\alpha_{33} = 0.00006957 \quad 8-42.$$

Based on these values the standard errors of the partial regression coefficients were determined:

$$S_{b_1} = \sqrt{\alpha_{11} S_{y_{123}}^2} = 0.08035054 \quad 8-43.$$

$$S_{b_2} = \sqrt{\alpha_{22} S_{y_{123}}^2} = 0.99331448 \quad 8-44.$$

$$S_{b_3} = \sqrt{\alpha_{33} S_{y_{123}}^2} = 0.01798401 \quad 8-45.$$

The significance of partial regression coefficients were tested with the student t-test, whereby:

$$H_o = \beta_1 = \beta_{10} = 0 \quad 8-46.$$

The null hypothesis ( $H_o$ ) to be tested is  $\beta_i$  (the slope of the relationship in the population) is  $\emptyset$ . If  $\beta_i = \emptyset$ , then the linear equation is irrelevant.

Also, it is suspected that the slope of the regression equation is negative and therefore stating the alternate hypothesis ( $H_a$ ) includes the following:

$$H_a: B_1 < 0, B_2 < 0, B_3 < 0, \quad 8-47.$$

The test of significance will be a two-tailed test in which the critical region will be evaluated for both the 0.005 and  $0.025 \frac{\alpha}{2}$  degrees of freedom.

Representation of the t-test value is given by:

$$t = \frac{b_i - \beta_{io} df - n - k - 1}{S_{bi}} \quad 8-48.$$

These values are tabulated for :  $t = \frac{b_1}{S_{b_1}}$ ,  $t = \frac{b_2}{S_{b_2}}$ ,  $t = \frac{b_3}{S_{b_3}}$ . These values are compared to the table values. The inference of the test statistic will show the relevance of the regression coefficient by showing significantly higher values than the critical table values.

The values were calculate as follows:

$$t = \frac{b_1}{S_{b_1}} = -1.88399704 \quad 8-49.$$

$$t = \frac{b_2}{S_{b_2}} = -1.97826387 \quad 8-50.$$

$$t = \frac{b_3}{S_{b_3}} = -5.49756903 \quad 8-51.$$

Given the degrees of freedom ( $df$ ) =  $45 - 3 - 1 = 41$ , the table values were determined as follows:

$$t_{0.025} = 2.021 \quad 8-52.$$

$$t_{0.005} = 2.704 \quad 8-53.$$

Since the calculated 't' value falls outside the range set by the critical 't' value for  $X_3$ , but near the critical boundary for  $X_2$  and  $X_1$ , it can be observed that the contribution to the regression equation by all three variables is significant to determine a better value of Y. Also, the conclusion is to reject  $H_0$ , the null hypothesis, based on these results.

#### 8.4.3 The Standard Partial Regression Coefficient

The standard partial regression coefficients are independent values of the original units of measurement and are therefore a comparison of the coefficient which indicate the relative importance of the independent variables. These are formulated as:

$$b_i' = b_i \frac{S_i}{S_y} = \frac{b_i \sqrt{\frac{\sum x_i^2}{df}}}{\sqrt{\frac{\sum y^2}{df}}} \quad 8-54.$$

$$b_1' = -0.21719668 \quad 8-55.$$

$$b_2' = -0.16185644$$

8-56.

$$b_3' = -0.50929915$$

8-57.

From  $b_1'$ ,  $b_2'$  and  $b_3'$ , it can be observed that  $X_3$  is 2.3 times as useful as  $X_1$ , and 3.2 times as useful as  $X_2$  in estimating  $Y$ . Whereas,  $X_1$  is approximately twice as useful as  $X_2$  in estimating  $Y$ . Therefore,  $X_1$  and  $X_3$  are more influential in estimating  $Y$ .

### 8.5 Summary

In this stage of the project the potash rock specimens were tested under uniaxial compression up to specimen failure. It was observed that the uniaxial compressive strength varied in relation to the specimens' textural characteristics and percentage of sylvite content in the sample.

The purpose of this chapter of the project was to determine if a dependency of textural parameters and composition on the uniaxial compressive strength of potash rock exists.

Three independent variables were set up. These include textural homogeneity, structural interlocking and compositional ratio of sylvite in each rock type. A multiple linear correlation analysis was performed to determine if the relationship exists.

The analysis determined the following:

- 1) The regression coefficients by the regression of  $Y$  upon  $X_1$ ,  $X_2$  and  $X_3$  was resolved. The regression equation was shown to be:

$$\sigma_c = 30.2820 - 0.1514g - 1.9650H - 0.0989KCl \quad 8-58.$$

- 2) The t-test and F-test inferences were performed to prove if the test coefficients are significant in the regression equation and that they show a relationship with uniaxial compressive strength.

The hypothesis  $H_0: b_1 = b_2 = b_3 = 0$ , whereby the null hypothesis states that "the four variables are linearly unrelated" was tested for.

The results of the statistical inferences via the t and F-tests were contrary. The F-test has shown that the table value does not fall in the critical region, for both 95% and 98 % confidence interval range, for one-tailed distribution. Thus, the conclusion is rejection of the null hypothesis, and therefore the petrographic variables are significant in predicting the uniaxial compressive strength.

Testing the significance of partial regression coefficients was performed with the t-test. The null hypothesis comprises the same statement as was the case for the F-test statistical inference. The alternate hypothesis is also stated as :

$$H_a : B_{i_0} < 0 \quad 8-59.$$

The alternate hypothesis is considered for a two-tailed test. Also, the alternate hypothesis considers  $B_{i_0}$  as less than zero since it is suspected that the slope of the regression equation is negative.

The formula used to calculate the t-statistic for inferences about the slope is given by:

$$t = \frac{b_i - \beta_i}{S_{b_i}} \quad 8-60.$$

The t-value determined from the tables were:

$$t_{0.025} = 2.021 \quad 8-61.$$

$$t_{0.005} = 2.704 \quad 8-62.$$

The contribution of  $X_3$  is significant in predicting Y. Although,  $X_1$  and  $X_2$  fall within the critical region thus failing to reject  $H_0$ , they fall very close to the limit.

- 3) The multiple regression coefficient was determined to be  $R_{y_{123}} = 0.6150$ . It is less than the tabular value of  $R_{y_{123}}^*$  thus indicative that the combined effect of  $X_1$ ,  $X_2$  and  $X_3$  can be effective in predicting Y.
- 4) Finally, the standard error of estimate and the standard error of the correlation coefficient were determined. The standard error of estimate of the population of Y value is calculated to be  $S_{y_{123}} = 4.6489$  MPa, referring to the uniaxial compressive strength.

The slope,  $\beta_i$ , of the regression function of the population can be estimated by means of a confidence interval given by:

$$b_i \pm t\left(n-2, \frac{\alpha}{2}\right) \cdot S_{b_i} \quad 8-63.$$

thus, with the tabulation of the standard errors of the partial regression,  $S_{b_1}$ ,  $S_{b_2}$ ,  $S_{b_3}$ , the confidence intervals (at the 95% interval), for each coefficient is given by;

$$b_1: 0.0110 \text{ to } 0.3144 \quad 8-64.$$

$b_2$ : 0.0425 to 3.9725

8-65.

$b_3$ : 0.0625 to 0.1352

8-66.

These values represent the slope of the line of best fit from which the sample is drawn with 95% confidence.

**Table 8.1: Compilation of data including textural parameters and uniaxial compressive strength values.**

SAMPLE NUMBER	STRUCTURAL INTERLOCKING	TEXTURAL HOMOGENEITY	RATIO OF IMPURITY	UNIAXIAL COMPRESSIVE STRENGTH	Specimen
	X1	X2	X3	Y	n
S1A7	9.19	1.71	2.87	25.92	1
S2A1	8.90	1.71	2.87	28.80	2
S2A2	8.90	1.71	2.87	29.00	3
S2A4	9.01	1.71	2.87	28.89	4
S5A2	9.20	1.71	2.87	26.09	5
S5A3	9.00	1.71	2.87	27.65	6
S5A4	9.19	1.50	2.87	15.60	7
S5A6	8.70	1.50	2.87	29.00	8
S5A7	8.90	1.60	2.87	29.99	9
S5A8	8.92	1.60	2.87	29.20	10
S6A1	8.60	1.40	8.77	31.20	11
S1B1	26.50	0.41	74.74	16.56	12
S1B2	30.00	0.50	75.61	19.47	13
S1B3	31.00	0.30	74.91	14.26	14
S6B1	26.70	0.70	71.37	17.35	15
S1C1	10.20	1.37	36.87	16.66	16
S1C2	10.20	1.53	36.87	16.71	17
S1C3	8.10	1.65	36.87	22.18	18
S1C4	8.00	1.67	36.87	21.39	19
S7C1	8.70	1.68	36.87	20.00	20
S1D1	6.87	1.85	68.39	24.96	21
S1D2	7.20	1.85	68.39	22.97	22
S1A1	1.70	2.87	8.77	9.19	23
S1A3	9.19	1.70	2.87	25.73	24
S2A3	8.50	1.70	2.87	28.67	25
S2A6	8.50	1.68	2.87	28.80	26
S4A1	8.30	1.60	2.87	29.93	27
S4A2	8.80	1.70	2.87	27.61	28
S4A3	8.80	1.71	2.87	27.26	29
S4A4	8.50	1.75	2.87	29.10	30

Table 8.1: (Continuation)

SAMPLE NUMBER	STRUCTURAL INTERLOCKING	TEXTURAL HOMOGENEITY	RATIO OF IMPURITY	UNIAXIAL COMPRESSIVE STRENGTH	Specimen
	<b>X1</b>	<b>X2</b>	<b>X3</b>	<b>Y</b>	<b>n</b>
S4A6	9.19	1.70	2.87	25.88	31
S5A1	9.19	1.63	2.87	15.64	32
S5A5	9.00	1.71	2.87	27.86	33
S5A9	9.19	1.70	2.87	15.63	34
S9C1	26.73	0.41	36.87	17.40	35
S9C2	11.10	1.50	36.87	20.60	36
S9C5	8.50	1.50	36.87	20.31	37
S9C6	12.50	1.65	36.87	18.59	38
S9C7	12.70	1.71	36.87	21.62	39
S9B1	26.73	1.68	71.37	18.25	40
S9B2	28.21	1.43	71.37	15.75	41
S9B3	25.85	1.69	71.37	18.05	42
S9B4	27.00	1.78	71.37	16.21	43
S9B5	23.45	1.80	71.37	19.14	44
S9BC1	27.10	0.50	71.37	16.75	45

	STRUCTURAL INTERLOCKING	TEXTURAL HOMOGENEITY	RATIO OF IMPURITY	UNIAXIAL COMPRESSIVE STRENGTH	
	<b>X1</b>	<b>X2</b>	<b>X3</b>	<b>Y</b>	
$\sum x_i$	600.70	68.47	1308.14	1007.82	
$\bar{x}$	13.35	1.52	29.07	22.40	
$\sum x_i^2$	10952.52	113.85	75845.34	23996.32	

$$\sum x_1 x_2$$

795.3226

$$\sum x_1 x_3$$

25670.7004

$$\sum x_1 y$$

12430.7961

$$\sum x_2 x_3$$

1706.5846

$$\sum x_2 y$$

1560.4768

$$\sum x_3 y$$

24873.2131

Table 8.2: Part a) displays the tabulation of the sum of products and simple correlations. Part b) shows the analysis of the variance of the test of significance of regression.

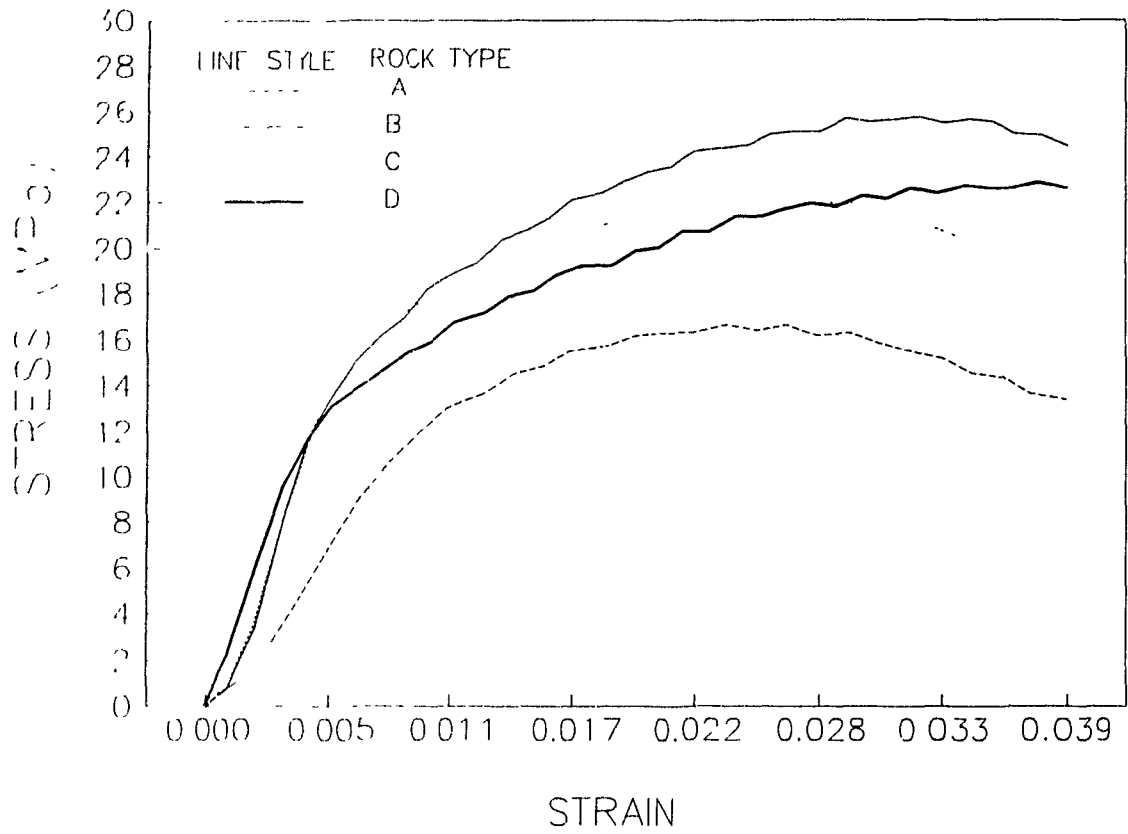
**Part a)**

$X_1$	$\sum x_1^2 = 2933.84$	$\sum x_1 x_2 = -118.68$ $r_{12} = -0.71$	$\sum x_1 x_3 = 8208.85$ $r_{13} = 0.78$	$\sum x_1 y$ $r_{1y} = -0.50$
$X_2$		$\sum x_2^2 = 9.67$	$\sum x_2 x_3 = -283.82$ $r_{23} = -0.47$	$\sum x_2 y = 27.06$ $r_{2y} = 0.23$
$X_3$			$\sum x_3^2 = 37818.0$	$\sum x_3 y = -1123.89$ $r_{3y} = -0.60$
$Y$				$\sum y^2 = 1425.17$

**Part b)**

SOURCE	SYMBOLIC		DATA	FROM	TABLE	
	degrees of freedom (d.f.)	S.S.	d.f.	S.S.	$MS = \frac{SS}{df}$ M.S.	F
Regression on constant variables	$k$	$\sum b_i (\sum x_i y)$	3	539.0588	179.6863	8.3140
Residual	$n - k - 1$	<i>by subtraction</i>	41	886.1145	21.6125	
Totals	$n - 1$	$\sum y^2$	44	1425.1733		

Figure 8.1: The stress - strain behavior of four types of potash rock loaded under uniaxial compression.



## **Analysis of Acoustic Emission of Potash Rock**

### **9.1 Introduction**

Analysis of acoustic emission generated in polycrystalline samples of potash rock will be presented in this chapter. The specimens were loaded under uniaxial compression, under a constant strain rate mode of load. The specifications of the loading parameters are shown in table 7.2. Acoustic emission was monitored with the acoustic emission sensor coupled to the vertical face of the specimen. A schematic representation of the test setup is shown in figures 9.1a, 9.1b and 7.12.

Various acoustic emission parameters were measured, analyzed and will be discussed in this chapter. These include acoustic emission rate, amplitude, energy and event duration.

### **9.2 Acoustic Emission Rate**

Acoustic emission rate in potash rock is presented in two parts. It is examined in relation to an increase in load and its distinctions with respect to petrographic characteristics.

#### **9.2.1 General Observations**

Acoustic emission rate in relation to stress and strain are analyzed. Figures 9.2 to 9.5 display representative graphs of acoustic emission rate against stress for all types of potash rock.

The threshold setting to measure acoustic emission counts was determined by trial and error. A range of 1.4V to 1.8V settings were tested. It was found that 1.5V would be the optimal level. Levels over 1.5V (fixed) resulted in insignificant registration of acoustic emission data, particularly for potash rock types "A" and "D". Threshold levels set under 1.5V resulted in the saturation of the equipment. This was most apparent for types "B" and "C" potash rock. Several peaks present in amplitude distribution histograms were observed as a result of noise. Raising the threshold eliminated the noise.

The results display significant patterns when observing acoustic emission rate in relation to load. In the graph shown in figure 9.6, changes observed in acoustic emission rate correspond to distinct inflections along the stress and strain curves. Only minor variations are observed in acoustic emission rate when it is presented as a function of increasing stress and strain.

### **9.2.2 General Observations of Acoustic Emission Rate in Relation to Increasing Uniaxial Load**

Based on graphical analysis, four distinct regions of acoustic emission activity can be defined (refer to figures 9.2 to 9.6). The regions are labelled as 'A', 'B', 'C' and 'D' which correspond to regions 1, 2, 3 and 4, respectively. Region one, located at the onset of applied load, shows low acoustic emission activity. Any minor peaks observed at less than 1 MPa of stress are due to adjustments of the platen sample interface. With increasing load the sample shows elastic deformation with low acoustic emission activity, this zone defines region two. Region three is the region prior to the elastic limit whereby the acoustic emission activity increases to a high rate. Region four is located after the elastic limit. Three areas within this last region along the stress-strain curve can be distinguished: the strain hardening region, the peak load sustained by the sample and the post peak load region. The acoustic emission rate remains at a peak level from region three located at the yield point, and remains constant throughout the three regions of region four, with minor fluctuations observed. The acoustic emission rate is observed to trend in three forms, either it gradually decreases, remains steady throughout the test or decreases to a very low level.

### **9.2.3 Acoustic Emission Rate in Relation to the Petrographic Characteristics of Potash Rock**

Minor variations are apparent when observing the graphical representations of acoustic emission rate with respect to increase stress. Variable structure, texture or composition contained in the samples may cause differing deformation mechanisms to be activated.

The general statistics show that the maximum rate that can be observed is 180 events per unit strain. The cut off acoustic emission rate is less than 10 events per unit strain. The events recorded at every increment of strain are consistent within their own petrographic types. Types "A" and "D" show the highest consistency, while "C" and "B" display the least. Differing fracture and deformation patterns associated with these rates are also observed. The latter observations are presented in chapter 10.

### **9.2.4 Acoustic Emission Rate Associated with Type "A" Potash Rock**

Type "A" potash rock displays three patterns of acoustic emission rate in relation to increasing stress. Table 9.1 categorizes the samples according to type "1A", "2A" and "3A".

Type "1A" potash rock, displays an initial rise in acoustic emission rate observed as a peak recorded at approximately 10 events. This is measured at a stress level of 2 to 4 MPa. The acoustic emission rate then drops to 5 events per unit of strain. Low acoustic emission activity is associated with the linear elastic range. This region occurs between 4 to 14 MPa. At the upper extreme limit of the elastic range, there is a sharp increase in acoustic emission rate to 40 events per unit of strain. This high rate remains steady through the strain hardening region, sample failure limit and post failure. Minor structural variations in this type of potash rock are observed. These include late stage diagenetic discontinuous bands of clay and sylvite occurring interstitially. They are oriented sub-horizontally with respect to the sample shape and the direction of the load. They range in thickness from 1 to 8mm.

Type "2A" potash rock, is similar to type "1A". However, it does not show an initial rise of acoustic emission rate corresponding to the preload level. These samples display a uniform homogeneous crystalline mosaic of halite with no discordant structure.

Type "3A" potash rock, shows a similar trend to type "2A" but the acoustic emission rate in the post-peak region decreases to 5 events per unit strain. There are no notable petrographic differences existing between the latter two types. The decreases are accountable by slabbing of the sample and thus, a loss of full contact of transducers to the sample.

#### **9.2.5 Acoustic Emission Rate Associated with Type "B" Potash Rock**

Type "B" potash rock displays four patterns when observing the acoustic emission rate stress relationships. The maximum acoustic emission rate ranges from 60 to 140 events. This rock displays two to four times more activity than type "A" potash rock. Also, the point of rapid increase in acoustic emission rate corresponding with the elastic limit is less evident than in type "A" potash rock. The non-linear region in type "B" potash rock is less constant than type "A" potash rock. Referring to figure 9.7, the specimens deform in three distinct regions of the stress-strain curve; a linear elastic region in which the acoustic emission activity resumes from nil (region 'A') and gradually increases to a maximum within the plastic region in which the acoustic emission rate attains a maximum at some point (region 'B') and then remain at that level or decreases gradually (region 'C'). No obvious peaks or inflections on the curve relating acoustic emission rate to stress were evident.

Four distinct patterns can be observed in type "B" potash rock and are categorized accordingly in table 9.1. Type "1B" shows a steady increase in acoustic emission rate at a constant slope to a maximum of 100 events per unit strain.

Petrographic features of the samples include sub-horizontal contorted anhydrite clay seams ranging in thickness from 1 to 3 cm. Also, a large variation in grain size is observed within each sample. Gradational change in grain size from small to large grained polycrystalline mosaic composed of sylvite and halite is also present. These features are not apparent in the other groups of type "B" potash rock.

Type "2B" potash rock displays an inflection of acoustic emission rate at 2 MPa. The increase from this point on is steady up to 11MPa, where it peaks to 70 events per unit strain. The inflection to peak acoustic emission activity corresponds to a better defined yield point on the stress-strain curve. The acoustic emission rate generally remains high after this point, with a subtle but steady decrease. Type "2B" displays no variations in structure and texture to the norm of type "B" potash rock.

Types "3B" and "4B" show similar acoustic emission rate trends to type "2B". Both display a steady increase of acoustic emission rate to a maximum level corresponding to 60 to 140 events per unit strain. The increase of acoustic emission rate starts at 0.7 to 7 MPa, with the exception of samples S9B5 and S9B4, where the maximum acoustic emission rate is reached at 2.8 MPa. Type "3B" samples then steadily decrease in acoustic emission rate to 60 events per unit strain, whereas type "4B" acoustic emission rate remains high.

Specimens corresponding to this type of behavior have the same petrographic elements as type "2B" potash rock.

#### **9.2.6 Acoustic Emission Rate Associated with Type "C" Potash Rock**

The acoustic emission rate in type "C" potash rock are similar to that of type "B". The maximum acoustic emission rate ranges from 100 to 130 events and up to 200 events for sample S1C2. Table 9.1 shows the samples and corresponding groupings. Type "C" potash rock does not display any petrographic variations within its own type except for sample S7C1 which is composed of numerous clay seams.

#### **9.2.7 Acoustic Emission Rate Associated with Type "D" Potash Rock**

Type "D" potash rock displays similar acoustic emission rate patterns as those of type "A" potash rock. The acoustic emission rate displays a rapid increase to peak rate at the yield point of its load history. The peak acoustic emission activity ranges from 90 to 120 events per unit of increasing strain. The high activity is maintained

throughout the duration of the test. The stress-strain curve for type "D" potash rock is incongruous from that of type "A" potash rock. The difference lies in the region of the curve after the elastic limit, in that the proceeding region or the strain hardening region is poorly defined in type "D".

### 9.2.8 Summary

Various conclusions can be drawn from the treatment of observing acoustic emission rate in relation to the stress-strain curves. The pattern of acoustic emission rate and the stress-strain curves are an expression of their own petrographic groups.

The acoustic emission rate as a function of stress, can be divided into four stages. These stages are irrespective of petrographic types, except for minor variations in macro or microstructural features. The majority of the test results display no difference in patterns prior to the elastic limit, although dissimilarities are present after the yield point. The four stages can be summarized as follows:

- 1) **Initial Stage**                      The presence of no acoustic emission activity, or the development of very low activity present at the onset of loading which quickly decreases as the elastic region is approached.
- 2) **Primary Stage or elastic deformation**      The presence of relatively low acoustic emission activity but accelerated acoustic emission rate within the elastic range.
- 3) **Secondary Stage**                A rapid increase of acoustic emission activity slightly before, or at the elastic limit. It is possible to delineate the yield point of types "A" and "D" potash rock as indicated by the increase in acoustic emission activity.
- 4) **Final Stage**                      At the post yield point of the loading cycle the acoustic emission activity remains steadily high or decreases after the maximum strength of the sample has been reached.

The number of acoustic emission events recorded at peak rate varies between different sample types. In general, types "B" and "C" potash rock have higher peak acoustic emission rates as compared to types "A" and "D". The major distinction between these samples is the higher percentages of sylvite and clay present in the

former two types of potash rock. Also, although types "A" and "D" display similar acoustic emission rate patterns, type "D" displays a peak acoustic emission rate that is twice as high as that of type "A", possibly due to low concentration of sylvite.

### **9.2.9 Comparative Study and Interpretation**

The primary analysis of acoustic emission rate involves interpreting and describing the trend via a graphical plot of acoustic emission rate versus stress and strain.

The results presented in this study are generally contradictory to other published results dealing with hard rock. In terms of regions or stages in acoustic emission activity, in relation to hard or brittle rocks, three stages can be defined. These consist of a high initial rate, followed by a decrease in activity which corresponds to the linear elastic stage, and finally an accelerated increase in activity which corresponds to sample failure [Montoto et al. (1984), Khair (1984), Scholz (1968a), and Fonseka et al. (1985)]. The acoustic emission rate for potash behaves similarly within the elastic range, where low activity was recorded. This is indicative that the fracture processes have not been initiated. The low, although pronounced increase in acoustic emission activity would appear to correspond to a period of reduced volumetric compressibility and elastic behavior of the stress-strain conditions [Khair (1985)]. Also, the behavior at this stage is due to heterogeneities and discontinuities present in the rock. Such structural features give rise to local stress concentrations and localized failure. The differences in acoustic emission response are accountable by the different structures observed in each of the potash rock types. Peak acoustic emission activity corresponding to the yield point and not to the sample failure at maximum strengths was reported by Fonseka et al. (1985), Scholz (1968b), Sano et al. (1982) and Montoto et al. (1984).

Vance (1983) and Richardson (1980) reported a steady increase in acoustic emission activity in potash rock and polycrystalline rocksalt. The latter author also reported results of single crystal tests. He reported that peak acoustic emission rate coincides with the yield point of the specimen loaded under uniaxial compression.

Richardson (1980), Knill et al. (1968), Atkinson (1984) and Khair (1984) reported that based on granularity, acoustic emission rate increases with decreasing grain size and increasing grain density. Acoustic emission rate results were contrary

to this observation. It was observed that higher activity was present in samples containing a higher concentration of sylvite. Also, samples with a higher degree of heterogeneity displayed higher rates. Similar observations were reported by Khair (1984) and Montoto et al. (1984).

A study by Matthews (1983) reveals several conclusive similarities and differences. According to the author and coinciding with the observation of potash rock, increased acoustic emission activity is associated with an increase in grain size.

Reducing the grain size increases the yield stress. Strain hardening region exists at higher stresses for fine grained samples. Higher stress will increase dislocation velocity which results in a steady high acoustic emission rate.

Variation in acoustic emission due to impurities or secondary minerals does not necessarily change the acoustic emission rate trend in relation to stress. But the frequency of acoustic emission events recorded due to increase uniaxial load varies.

Acoustic emission energy increases with grain size. Maximum acoustic emission for pure materials occurs for the largest grain size or in a single crystal. As purity decreases the maximum acoustic emission rate, acoustic emission is observed at smaller grain sizes. The grain size at which maximum acoustic emission rate is observed may be less than the finest grain size. Maximum acoustic emission occurs at the onset of plastic flow, then falls off [Mintzer et al. (1978), Ohira et al. (1979) and Sondergeld et al. (1984)].

### **9.3 Correlation of Acoustic Emission Activity to Inelastic Deformation**

Although lateral deformation was not measured, it is still apparent from the shape of the stress-strain curve that potash rock generally exhibits elasto-plastic behavior. The correlation between inelastic behavior and acoustic emission activity will be discussed in this section. It has been shown by Scholz (1968b) and Sano et al. (1982) that there is a strong correlation between axial strain and corresponding accumulated acoustic emission activity. This data was obtained and treated by computer fitted curves. The results are graphically represented by cumulative acoustic emission activity versus axial strain. An example is shown in figure 9.8. It displays a prominent linear relationship between the two parameters. The straight line shown in this figure has been calculated utilizing the least squares formula.

The results confirm that there is a strong correlation between axial deformation and acoustic emission activity. As presented in this study, the major contributor to detectable acoustic emission activity appears to be the initiation and propagation of

fractures. The results of the test show that the slope of the line conforming to the linear least squares equation are lower for types "A" and "D" potash rock, and larger for the other two types. This indicates that more acoustic emission activity (disregarding the frequency of the acoustic emission waves) is generated for types "B" and "C" at every increment of increasing strain.

### **9.3.1 Comparative Study and Interpretation**

The correlation between acoustic emission activity and inelastic behavior appears to coincide with the concepts of material behavior described by Brace (1960), Scholz (1968b) and Bieniawski (1967). In most cases, it is believed that this relationship holds true upon fracture initiation of the sample. The point at which acoustic emission cumulative count is related to strain varies upon rock type. For Scholz (1968b), the results held true at 50% of the failure strength.

Similarly for potash rock, this distribution was apparent up to the elastic limit. For types "B" and "C" potash rock, the linear relationship could actually hold true from within the elastic limit, thus indicating that fracture initiation could occur within this zone. The latter would conform more accurately to Vance (1983), who reported that a linear relationship between axial strain and cumulative event count occurs from very low levels of stress even within the elastic zone. Richardson (1980) tested polycrystalline rocksalt and observed that acoustic emission activity with increasing strain showed no inflection.

### **9.4 Acoustic Emission Amplitude Parameter**

In this section the acoustic emission amplitude and the amplitude distribution derived from potash rock are analyzed. The amplitude distribution analysis provides a factor establishing the discrimination between various source mechanisms of the deformation of the material.

The acoustic emission amplitude data was analyzed at two stages in the loading cycle including the elastic limit and specimen failure. An attempt is made to discriminate differences in the amplitude distribution in terms of sample load level, petrographic type and sample size. A variation in amplitude event frequency spectra could indicate that different fracture mechanisms operate at different levels of load and specimen type with respect to the texture of the rock [Pollock (1980)].

#### **9.4.1 Amplitude Characteristics**

The amplitude measured consists of recorded data over the cut off threshold level set to 1.50 Volts. Acoustic emission was monitored in the 100 to 300 kHz range.

Amplitudes recorded with these equipment settings are of a range of 77 to 99dB. This range was present in both large and small specimens of all four types of potash rock at stress levels measured up to the elastic limit and sample failure.

#### **9.4.2 Amplitude Event Frequency Spectra**

Representation of peak amplitudes of the individual emissions vary over several orders of magnitude. The graphical plot of amplitude and frequency characterizes the amplitude distribution. Any change in the distribution histogram is an indication of different operating fracture mechanism [Nakasa (1979)]. Graphs were plotted for all sample types and separated in terms of load range for events recorded to the elastic limit and sample failure, petrographic type and size category (refer to figures 9.9 and 9.10).

#### **9.4.3 Microstructural Influence on Acoustic Emission Amplitude Characteristics**

Several fracture mechanisms can occur simultaneously as suggested by the amplitude distribution histogram. The abundance and distribution of events are different for measurements recorded to the elastic limit and post yield limit. The analysis of the amplitude distribution can be utilized to provide a preliminary insight on the deformation processes occurring at different stress levels [Pollock (1977,1980), Graham (1976) and Nakasa (1979)].

Referring to figure 9.9, the majority of the signals are evenly distributed throughout the amplitude range. This is evident for all four types of potash rock. Types "B" and "C" though, display a slightly larger amount of signals occurring at small amplitude (refer to figures 9.9 and 9.10). At the other end of the amplitude range, a large amount of signals are also concentrated at the high end of the spectra (refer to figure 9.10). The latter population of signals are not dispersed, rather they are concentrated under the 97 dB amplitude level.

Figures 9.10 displays the amplitude distribution for specimens loaded to failure. The acoustic emission amplitude distributions display a concentration of acoustic emission events at low amplitude range of 85 dB and at a higher amplitude range of 97dB.

The presence of these concentrations of events would indicate that there is a large number of events due to deformation mechanisms generating low amplitude. These acoustic emission waves increase excessively in concentration after the yield point. A wide range of high amplitude events which are generated in significant amounts are existent within the elastic and plastic regions.

The number of signals generated with respect to the elastic limit increases to as much as four times for readings measured to the failure point of the specimen. This observation is predominant in types "B" and "C" potash rock.

Finally, the overall distribution of acoustic emission signals with respect to sample size is not affected. The distribution and the peaks are more pronounced in the larger samples.

#### **9.4.4 The b-Value Parameter**

##### **9.4.4.1 Introduction**

The b-value parameter is a value derived from a function defining the cumulative amplitude distribution. The amplitude distributions of acoustic emissions often appear on a straight line when they are plotted on logarithmic axes [Pollock (1980)]. The distribution defines the number of acoustic emission events having a peak amplitude greater than a voltage which is plotted as a function of voltage.

The b-value as it was earlier described, is characteristic of the material and the deformation mechanisms. It should also be independent of the distance from the source of the deformation to the sensor [Pollock (1980)], thus other factors that would affect the results are disregarded.

Changes in the b-value are due to the deformation mechanisms as it is a function of stress. The b-value typically decreases as the stress level of the material approaches failure. This is due to the fact that higher amplitude events are generated as failure of the specimen is approached.

##### **9.4.4.2 The Physical Significance of the b-value**

Pollock (1980), with reference to Scholz (1968a) and Mogi (1962); appropriately defines the physical significance of the b-value. According to Mogi (1962) the b-value is related to the heterogeneity of the material. It is believed that the crack arrest process characterizes the emission amplitude. The crack path can be altered due to heterogeneities in the material. The material texture also creates local anomalies in the distribution of the stress field. Thus, a propagating fracture path and the material are considered as a function of the fracturing volume. The b-value is controlled by three factors represented by:

$$b = \nu \lambda_{\beta} \kappa$$

9-1.

whereby,  $\nu$  is the exponent value relating acoustic emission energy to amplitude, and is predefined as '2',  $\lambda_{\beta}$  is a proportionality constant and  $\kappa$  is the degree of spatial fluctuation of the stress distribution.

The model presented by Scholz (1968a) differs slightly from Pollock (1980). The fracture arrest is represented, in this case, as an areal effect; and the energy release as a volume effect. Scholz (1968a) defines a probability :

$$F(S; \sigma) \quad 9-2.$$

whereby the probability is that the local non-uniform stress ( $\sigma$ ), exceeds the material strength ( $S$ ). The local stress field increments by the presence of fracture growth. The expression for 'b' with respect to the model presented by Mogi (1962) is defined as:

$$b = \frac{2}{3} \sqrt{1 - F} \quad 9-3.$$

whereby 'F' represents the stress field anomalies and  $\frac{2}{3}$  is a factor introduced due to the area effect of the fracture and volume effect with respect to the energy release.

Pollock (1980) further explains that several other authors relate the b-value to specific material deformation mechanisms. The models for the amplitude distribution should be related to an understanding of the material itself. The computation of the b-value is a significant parameter in interpreting the deformation mechanisms of the material.

#### 9.4.4.3 Computation of the b-Value

The representation of the amplitude distribution can be described by the distribution function of peak amplitude. The function  $n(a)$  can be defined as the fraction of emission population whose peak amplitude exceeds 'a'. Secondly, one can define a function  $m(a)$  such that the fraction of emission population whose amplitude falls between  $a$  and  $(a + \Delta a)$  is given by:

$$\int_a^{a+\Delta a} m(a) da \quad 9-4.$$

It is found that experimental data approximates several applicable functions. Several functions were tested. Acoustic emission data recorded up to 80% of the failure strength was considered for this type of analysis. The functional fit to experimental data displays a substantial deviation for acoustic emission data collected over 80% of the failure strength.

#### 9.4.4.4 Representation of Functions Utilized for b-Value Computation

##### 9.4.4.4.1 The Gutenberg-Richter Relationship

This relationship, used for the determination of the b-value is defined as:

$$\log N(M) = A - bM \quad 9-5.$$

whereby, 'N', is the number of acoustic emission events of magnitude 'M'. Both 'A' and '-b' are constants. This function was used by Fonseca et al. (1985), Scholz (1968b), Mogi (1962), Sano et al. (1982), and Nakasa (1979). The function was fitted to amplitude data distribution and cumulative amplitude distribution.

#### 9.4.4.4.2 The Normal Distribution Function

The normal distribution function is chosen to represent b-values for amplitude distribution, since the function fits acoustic emission data. This was pertinent since low amplitude data did not follow a linear trend when plotted on a cumulative distribution but instead exhibited a log normal distribution. The distribution is expressed in its final form as :

$$\ln N(V) = D - E c^2 \quad 9-6.$$

whereby 'N(V)' is the peak amplitude distribution function or, the number of acoustic emission events with peak amplitudes in the range of  $V + dV$ . The variable 'c' is the amplitude recorded from time 'A' to 'A + dA'. 'D' and 'E' are constants, characteristic of the distribution. They are synonymous to the b-value. The function was successfully used by Holt and Evans (1976).

#### 9.4.4.4.3 The Power Law Function

The power law function was used by Nakasa (1979) and Pollock (1979, 1980). The function is expressed as:

$$N(A) = k A^{-m} \quad 9-7.$$

This relationship is also called the Ishimoto-Iida [Fonseca et al. (1985)]. It expresses the relationship between the amplitude distribution 'N(A)' and 'A' from the amplitude recorded from the time 'A' to 'A + dA'. It states that the number of events of amplitude 'A' is a set of  $n(A)d(A)$ , whereby 'k' and 'm' are constants. Suzuki (1959) proved the following relationship:

$$b = m - 1 \quad 9-8.$$

thus defining the b-value. Acoustic emission pertaining to this function must tend to follow a linear trend in order to display a good representation.

#### 9.4.4.4.4 The Least Squares Fit

The Least Square function was demonstrated by Sano et al. (1982) to fit a cumulative distribution of acoustic emission amplitude. It is represented by:

$$\ln(N) = Ax^b + B$$

9.9.

This function is similar to the power law function. ' $N$ ' is the amplitude distribution, ' $x$ ' is the amplitude recorded from the time ' $A$ ' to ' $A + dA$ '. ' $A$ ' and ' $B$ ' are constants. ' $b$ ' is the value defining the characteristics of the amplitude distribution.

The  $b$ -values measured for samples tested under uniaxial compression are tabulated in tables 9.2a, 9.2b, 9.3a and 9.3b.  $b$ -value computations were determined for data measured up to the elastic limit and 80 % of specimen failure. These are in good agreement with the  $b$ -values obtained using the methods described above. Figures 9.11 to 9.14 illustrate examples of samples and their distribution for each sample loaded to the elastic limit and failure.

#### 9.4.4.5 Interpretation of the $b$ -Value

The range of the  $b$ -values is dependent on the fit of the functions described in section 9.4.4.4. The differences in the  $b$ -value are dependent on the deformational mechanisms in the rock under various levels of uniaxial load. For example, type "A" potash rock should have significantly higher  $b$ -values due to increased work hardening region which is the dominant behavior of this type of rock. Evidence is supported by multiple intergranular mode II and III slip and shear movements. Type "B" potash rock was observed to contain a large number of brittle transgranular cracks, which should be evident by a lower  $b$ -value [Nakasa (1979) and Pollock (1980)]. The details on the fracture characteristics will be discussed in chapter 10.

Each function showed a marginal range of dispersion of  $b$ -values. The Gutenberg-Richter relationship for amplitude distribution showed an average fit for amplitude values from 85 to 96 dB. As previously mentioned in the literature review, the  $b$ -value in the elastic range is higher than the data measured to failure. This observation holds true for all of the other equations used to show  $b$ -value analysis. All of the equations excluding the Holt Evans normal distribution function [after Holt and Evans (1976)], also represent a good fit to the experimental data to an accuracy of 95%. The function is dependent on the linearity, and therefore a high range of amplitude data tends to deviate from the calculated values. The normal distribution function, which is a quadratic form, can also represent experimental data on the upper amplitude range. The constants for the normal distribution function ' $D$ '

and 'E' are representative of the b-value. Concentrating on the 'D' value it can be noted that these values are recognizably lower for acoustic emission data calculated up to the elastic limit.

#### **9.4.4.6 Discussion and Comparison**

As observed by Mogi (1962), Scholz (1968a), Pollock (1977, 1980) and Fonseca et al. (1985), the amplitude distribution function of the potash rock appears as straight lines when plotted on a log scale. The b-values reported for potash rock are less than one. In general, this finding falls well within the range of b-values reported for rock.

The variation in the b-value was considered due to the fact that fractographic studies of potash rock loaded under uniaxial compression have shown deformation mechanisms with respect to its own type. Minor variations in the b-value between the different types of potash rocks are apparent for data measured to failure. But upon establishing a correlation of b-values to petrographic parameters, there was no corresponding relationship with fracture characteristics of potash rock. Consistent b-values are not apparent for data calculated within the elastic range. Pollock (1980) stated that deformation mechanisms are a function of stress, and thus cause the b-value to change. This may be indicative that differing textures of individual samples tested, have anomalous local stress fields which produce differences in the fracture pattern. All four types of potash rock show a decrease in b-value as the samples are stressed to failure.

Fonseca et al. (1985) and Nakasa (1979) have shown that rocks that are less brittle display constant b-values maintained until failure. Potash, which qualifies as a brittle rock, should comply to this fact. But based on the results presented in tables 9.2a, 9.2b, 9.3a and 9.3b, the b-values are lower at 80% of the failure stress, thus being indicative of brittle rock behavior. Stronger evidence of decreases in the b-value, as failure of the specimen is approached, was demonstrated by Pollock (1973) who used an amplitude ratio parameter measured for samples loaded at various levels of increasing stress.

Holt and Evans (1976) further investigated the log-normal form which approximates the power law function for large amplitudes. In this case, the amplitude distribution is governed by particle size distribution and there is no upper limit on the b-value. This model was useful in fitting the large b-values usually associated with plastic deformation, as in type "A" potash rock. It was shown that the log-normal form was a useful alternative to the power law function.

The physical significance of the b-value has been investigated in two manners. Primarily to relate it to a stochastic theory of fracture arrest in an inhomogeneous stress field and secondly, to show the effect of microstructure on the fracture mechanisms.

The former shows the dependence of the 'b' parameter on stress. The relationship for events which accompany frictional sliding and deformation of ductile rocks was found to have a higher b-value after the yield point. This analysis also attempted to demonstrate the dependence of the b-value on rock texture. The latter point was also observed by establishing a correlation of b-values to petrographic parameters. The correlation does not exist, at least on the scale of variability of texture. Local variation was observed, however it appears insignificant to the relationship.

The second point requiring clarification is that the b-value relationship sharply distinguishes two processes. The first occurs at low stresses up to the yield point and the second occurs after the yield point. It will be shown in chapter 10 that the dominant fracture processes in all four types of potash rock varies. This differentiation is not observable in the b-value.

### **9.5 Amplitude Distribution Ratio**

Pollock (1973) has shown that a change in amplitude distribution prior to failure exists (refer to table 9.4). This is of significance since a change in the distribution of amplitudes over the entire range indicates a change in the type of cracking phenomena. In this study, it was believed that the texture of potash rock would dictate the deformational mechanisms active under uniaxial load. Apparently, it was observed that the texture does not contribute significantly to the variation, yet changes in the b-value are apparent between various load levels. It is observed that the calculated b-value decreases with increasing load, signifying that the proportion of high amplitude signals are increased towards failure. A smooth fit of the cumulative amplitude distribution indicates that a single mechanism may be responsible for producing large and small cracks [Pollock (1973)].

A study performed by Pollock (1973), has shown a practical application of amplitude analysis, particularly, the change in amplitude distribution prior to failure. Table 9.4 shows a concise tabulation of amplitude ranges forming predefined levels. Each level consists of three groups of amplitude ranges starting from 75dB up to 99dB. The parameter in the last column defines the ratio of the number of events over 84dB to the total number of events. It can also be represented as follows:

$$A.R. = \frac{4+5+6+7+8}{1+2+3+4+5+6+7+8}$$

9-10.

Whereby 1 through 8 represents the amplitude levels. The distribution is a numerical measurement of amplitude distribution. Table 9.4 and figures 9.15 and 9.16 show the changes occurring in the amplitude distribution parameter. It can be observed that the changes in amplitude distribution are different with respect to large and small samples. The small samples display a marked change in the amplitude parameter at approximately 50 to 60% of the failure strength. Marked changes in large specimens are only apparent at the onset of loading between 10 to 20% of the failure strength. This is preceded by a gradual increase in the ratio which is indicative of an increase in the proportion of high amplitude emissions. The changes in the amplitude ratio parameter occur near the elastic limit of the specimens.

The changes in amplitude occurs significantly at the yield point of the sample load. Prior to the elastic limit, low amplitude acoustic emission activity is present. After the elastic limit, high amplitude acoustic emission activity is the dominant type. This feature is more apparent in types "B", "C" and "D" potash where more sylvite is present in the rock. Grain embrittlement causing intragranular cracking development is due to elastic mismatch of adjacent grains. This observation is also apparent in type "A" potash.

Figure 9.17 shows graphical representations of acoustic emission rate for each amplitude window. It can be observed that low amplitude acoustic emission is actively present at regions prior to the elastic limit. They are also apparent at the post failure region of the sample under uniaxial load. Low amplitude ranges are defined by events between 75dB and 81dB.

Very low to nil activity is observed at the 82 and 83dB levels. High acoustic emission activity of high amplitude acoustic emission events occur from the elastic limit to the peak strength of the rock. The effect described above, whereby a shift towards high emissions amplitudes as failure is approached has been described by several authors and appears to be present in many materials [Nakasa (1979), Scholz (1968a) and Fonseka et al. (1985)].

Schoiz (1968a), Nakasa (1979), Graham (1976) and Pollock (1980) have indicated that the b-value is closely related to the heterogeneity of the material. Experimental evidence from the tests presented in this study supports this statement.

## 9.6 Acoustic Emission Energy Analysis

An attempt has been made to observe acoustic emission energy parameter with respect to the four types of potash rock. The energy of an event is determined by the AET 5500 System by the following function:

$$E = \text{peak.amplitude} + \log 10(t) \quad 9-11.$$

where 'E' is the energy and 't' is the event duration. The cumulative energy distribution was analyzed in the same manner as that of the determination and analysis of the b-value amplitude parameter. The units of energy are represented by decibels (dB).

### 9.6.1 Energy Parameter Frequency Characteristics

Representation of peak energy of individual events vary over several orders of magnitude for the entire range of samples tested. The plot of peak energy versus frequency (number of events) is illustrated in figures 9.18 and 9.19, for samples loaded to failure.

The majority of the specimens tested showed that the distribution occurs over an energy range of 82 to 130 decibels. The distribution of events recorded to failure is similar for all four types of potash rock. This distribution consists of three peaks: a large amount of signals recorded at 85 to 86 dB, a smaller peak at 90 dB and a larger peak occurring at 100 to 112 dB. This latter peak is distributed in two forms. It is either normally distributed or positively skewed, the latter type producing a fourth peak at 126 dB. The largest peaks of the energy distribution are associated with heterogeneous samples of type "B" and "C" potash rock.

### 9.6.2 Cumulative Energy Distribution

As was the case for amplitude, the cumulative energy distribution is a display of the number of times an acoustic emission signal energy exceeds an arbitrary level as a function of energy  $F(E)$ :

$$N(E) = \int_E^{k+\delta E} F(E) dE \quad 9-12.$$

The normal distribution function is the model used to relate these variables. Erenkämper (1979) proposed the function presented below which was modified for energy:

$$F(E) = \frac{(N_c)}{(\sigma\sqrt{2\pi})} * \left(\frac{(1)}{(E_{max})}\right) * \exp\left(-\ln^2\left(\frac{\left(\frac{(t_{max}) * \sigma^2}{(t_{max})}\right)}{(?)}\right)\right) \quad 9-13.$$

It represents the model for the cumulative distribution function. ' $N_G$ ' represents the total number of acoustic emission events, ' $\sigma$ ' the standard deviation, ' $E_{max}$ ' the mean energy and, ' $\bar{E}_{max}$ ' the median. These are all variables.

In this case, the model is characterized by the distributions' mean and median. A shift in the median would indicate that there is a deviation of the total event population from the norm. This is indicative of acoustic emission events with different energy characteristics resulting from different deformational mechanisms. The model was applied to each sample. Figure 9.20 displays an example of the log-normal distribution with respect to cumulative acoustic emission energy data. It can be observed that the variation in the 'E' value was insignificant.

As proposed by Pollock (1980), Holt and Evans (1976) and Graham (1976), the triple peak distribution from potash rock should be related to understanding the material deformational properties. Each of the peaks represent a deformation mechanism. The peaks of the energy distribution are located in similar positions along the spectra of the energy distribution for all four types of potash rock.

A difference lies in the number of events recorded for each sample tested, whereby the distribution remains the same, but the peaks can be composed of double the number of events. Data recorded to the elastic limit shows a similar distribution, however the three peaks seen on the energy distribution are present although less apparent. This indicates that the same mechanisms are operating within the elastic stage of the load cycle.

### **9.7 Statistical Correlation Between Time Difference and Peak Amplitude Signals**

In accordance to Erlenkämper (1979), an attempt is made in this section to interpret acoustic emission amplitude and its time difference. According to this author, a series of signals from different types of materials can occur in the two types of processes. The first is referred to as the Poisson process, whereby the time difference between two consecutive signals is recorded at regular intervals. The second is called the poly-a-process, whereby acoustic emission signals are characteristically recorded in clusters. This process is indicative of a primary process of dependent events, setting off chains of smaller events to follow.

In this section, an attempt is made to associate fracture development to one of the two processes described above. If the cracks are of a Poisson process, they are generally intergranular in origin. If they tend to be of a poly-a-process, they are most likely related to multiple intragranular crack interaction process. Both types of cracks are observed in all four types of potash. The purpose of this section is to isolate the

dominant process with respect to the potash rock type by using a statistical inference and more specifically to test the inference concerning contingency tables of the acoustic emission amplitude and time difference.

### 9.7.1 Method of Analysis

In order to determine if a process is dominant in a sample, a statistical treatment of the data is considered [Erlenkämper (1979)]. The Chi square distribution will be used to test the hypothesis concerning enumerative data. This type of test will use the contingency table. It will be used to compare experimental results with expected results in order to determine independence of events with respect to time difference.

The contingency table is an arrangement of data in a two-way classification. The data consists of frequency counts of acoustic emission events. The table is made up of two variables which are of interest to a statistical investigation. These include time difference between two events, and amplitude. Such tables are used to indicate if the two variables are independent or dependent. A hypothesis test is used to determine independence of one data set to the other. In this case the Chi square distribution,  $\chi^2$ , is used.

### 9.7.2 Summary of Analysis

In general, the analysis involves five stages:

- Stage 1) The statistical inference will test for the independence between amplitude ( $A_{max}$ ) and time difference ( $t_d$ ) by the analysis of the contingency table.
- Stage 2) The contingency table shows the frequency of acoustic emission amplitude found in categories or cells of time differences. In order to adequately display a representative distribution, the contingency table consists of amplitude categories in intervals of 1 increment, in units of decibels. Their frequencies are represented by time difference categories. The classes of time difference are devised in increments of less than 0.0005 milliseconds which increase by doubling each interval. The final interval class is composed of events with greater than 4.096 milliseconds time difference. The amplitude ranges from 74 to 105 decibels. Thus, the contingency table consists of on average 15 rows and 15 columns. Table 9.5 displays the layout of the contingency table. Sample calculations corresponding to the method of the contingency table are also shown in table 9.5.
- Stage 3) The hypothesis will be tested for independence. The null hypothesis states:

Ho: The generation of consecutive acoustic emission events with characteristic amplitudes are independent of their time differences.

Ha: The amplitudes are not independent of their time differences.

Stage 4) The Chi square distribution will be used to test this hypothesis. The analysis is based on the fact that the variance is equal to its mean value for measured variables of independent events. Deviations occur by chance with random tests, the limits being determined by the dispersion index Chi, 'X'. For the two parameters, amplitude and time difference, ( $A_{max}$ ,  $T_A$ ), the Chi value, 'X', is calculated from:

$$\chi^2 = n \sum_{i=1}^r \sum_{k=1}^s \frac{(n_{ik} - \frac{n_i n_k}{n})^2}{\frac{n_i n_k}{n}} \quad 9-14.$$

where ' $n_i$ ' and ' $n_k$ ' are the partial sums defined by:

$$n_i = \sum_{k=1}^s n_{ik} \quad 9-15. \quad n_k = \sum_{i=1}^r n_{ik} \quad 9-16.$$

An assessment by testing the independence for the Chi square coefficient is preformed. The inference about the Chi value is then accomplished. The calculated Chi square value is compared to the critical Chi value derived from the table of Chi values.

Stage 5) Due to the type of distribution, the test of independence uses a one-tailed critical region. It is also, the right handed tail of the Chi distribution. The critical Chi square value is determined from a table for the Chi distribution with degrees of freedom defined by:

$$(r - 1)(s - 1) \quad 9-17.$$

whereby 'r' and 's' represent the number of rows and columns of the contingency table.

If the calculated Chi value does not fall into the critical region then one fails to reject the null hypothesis and therefore, the conclusion is that there exists an independence between amplitude and time difference.

### 9.7.3 Results from the Chi Distribution and Contingency Table Analysis

Results are tabulated in table 9.6. Values do not show a tendency to occur in a particular range, but higher Chi square values are found to be associated with type

"B" and "C" potash rock and lower values with the other two types. Both sets of calculated Chi values fall within the critical range of the distribution limits. The lower observed values show a tendency to be closer in agreement to the theoretical frequency, while the larger observed values indicate a disagreement in comparison to the theoretical frequency [Erlenkämper (1979)].

The Chi square value,  $\chi^2$ , determined from the tables were taken for a confidence interval of alpha, ' $\alpha$ ', set at 0.05. The degrees of freedom were given at:

$$(r - 1)(s - 1) \sim 196 \qquad 9-18.$$

$$(14)(14) \sim 196 \qquad 9-19.$$

An approximation of the number of degrees of freedom is dependent to the size variation with respect to the acoustic emission data observed within the contingency tables. The initial hypothesis is only  $P = 0.1\%$ . In order to fail to reject the null hypothesis, the samples must show the following probability:

$$P = P(\chi^2 < 2.40) \qquad 9-20.$$

The test statistics shown in table 9.6 fall within the critical region of the Chi distribution. Under these conditions, a decision is taken to fail to reject the null hypothesis. Failing to reject the null hypothesis indicates that an independence between the amplitude and time difference,  $(A_{max}, T_A)$ , exists, regardless of petrographic type.

By displaying a contour diagram of the frequency of acoustic emission events, as observed on a contingency table, various patterns are revealed. These patterns appear due to higher concentrations of events within the contingency table (refer to figure 9.21).

The distribution of event clusters is similar over the entire range of tests. Minor differences exist between potash rock types. These differences are not observable with respect to size, except for potash type "B" whereby the total number of events is lower by a factor of three for small samples tested.

The distribution consists of a large number of events of low amplitude (84 dB) with moderately low time differences. A secondary concentration of high amplitude events (98dB) with moderate low time differences also exists. A third concentration at moderately high amplitudes with moderate time differences, is observable for samples S5A8, S5A2, S4A6, S5A9 and S9B1.

Within the large specimens of types "B" and "C" potash rock, a large number of low amplitude with low time differences are observable in samples S9B3, S9B2, S9B1, S9B4, S9B5 and S9C6, S9C2 and S9C1.

In all cases, high frequency of acoustic emissions occur at 0.016 milliseconds to the 0.032 milliseconds of the time difference interval. This range is considered to be moderate low. The secondary peak observed at low time differences corresponds to values of 0.0005 to 0.0001 milliseconds.

Several samples display low event counts between the 96 to 98 dB amplitude range spanning over the entire time difference range. These include samples S1A7, S2A1, S5A4, S4A4, S9C7, S1C2 and S1D2.

Finally, several samples display relatively large number of events with small time differences over the entire amplitude range. These include samples S2A4, S1C1, S1C3, S1C4, S9B4, S9B5, S9B6, S9B1, S9B2, S9B3, S9C6, S9C1, S9C2, and S1D1. Although these variations exist, differences in the petrography of potash rock are minor.

Based on the inference with respect to the Chi square distribution properties, samples which fail to reject the null hypothesis, ( $H_0$ ), are indicative of acoustic emission events which are generated by a polya-process type. On the other hand, the samples in which the decision was to reject the null hypothesis indicate that the majority of events are of the Poisson process type. Closer observation of the contingency tables also supports these results.

The polya-process would be observed as a complex process of intragranular crack interactions. These processes occur in sylvite grains of types "B" and "C" potash rock. They occur within the early stages of plastic deformation.

This type of crack development is less apparent in types "A" and "D" potash rock. They occur in the late stages of plastic deformation.

It follows from this analysis, that the degree of dependence of acoustic emission signals occurring in a series of events, represents an important property characteristic of the material. This analysis is substantiated by visual evidence of crack development in the specimens loaded under uniaxial compression. The associated fracture development observed in potash rock will be discussed in chapter 10.

## **9.8 The Relationship between Amplitude and Energy with Event Duration and Time Difference**

The relationship established with these parameters was analyzed by contour dia-

grams displaying the density of events relating two parameters. The purpose of this analysis is to determine the acoustic emission signal characteristics in terms of the load history. The acoustic emission data used for this analysis was measured to sample failure.

### **9.8.1 Observations**

#### **9.8.1.1 Amplitude - Event Duration**

Figure 9.22 displays characteristic examples of the frequency of events between event duration and amplitude. The concentrations of events observed on the contour diagrams are similar for all four types of potash rock. There are three concentration clusters, all of which display similar distributions. The first concentration occurs at the 86 to 89 dB levels. In which the lower amplitudes contain three times more events than the higher range amplitudes. Both levels are representative of events that contain less than 5 to 20 milliseconds event durations.

The second concentration of events occurs between 90 to 96 dB. It contains event durations between 50 to 150 milliseconds. These concentrations of events produces a thin longitudinal distribution.

The third concentration of events occurs at the 98 dB level. The events form a concentration along a narrow range of 250 to greater than 450 milliseconds.

#### **9.8.1.2 Energy - Event Duration**

Figure 9.24 displays examples of contour diagrams showing the concentration of events with energy versus event duration. The distribution shows minor irregularities, but in general, it displays a pattern of concentration of events along a diagonal trend. This diagonal trend consists of three internal signal concentrations.

From the contour diagram, the low energy events consist of short event durations of 10 to 40 milliseconds. The middle concentration along the diagonal consists of moderate energy events ranging from 150 to 250 milliseconds event duration. These events correspond to amplitude levels of 90 to 96 dB. The high energy events contain event durations of greater than 450 milliseconds.

#### **9.8.1.3 Energy - Time Difference**

The energy versus time difference distribution of events show similar distribution patterns to the amplitude versus time difference contour diagram (refer to figure 9.23). However, the former contour diagram shows a more condensed distribution than the amplitude versus time difference diagram. The major concentration for all ranges of energy of events varies from 0.016 to 0.032 milliseconds time difference. As

was the case for amplitude, a secondary minor concentration of events with 0.0001 to 0.0004 millisecond time difference also exists. The highest concentration of events with 0.016 to 0.032 millisecond time difference occurs between the 105 to 107 dB level. The concentration of events with the same time difference decreases with increasing energy level of events.

### **9.8.2 Summary**

A subjective conclusion was drawn from the analysis presented in table 9.7. A comparison between event duration, amplitude and energy along with time difference was performed in order to associate signal characteristics within a particular region in the loading history. Table 9.7 summarizes and interrelates the signal characteristics based on event concentration of the contour diagrams.

Figure 9.1a: Schematic of experimental setup for samples tested under uniaxial compression and acoustic emission.

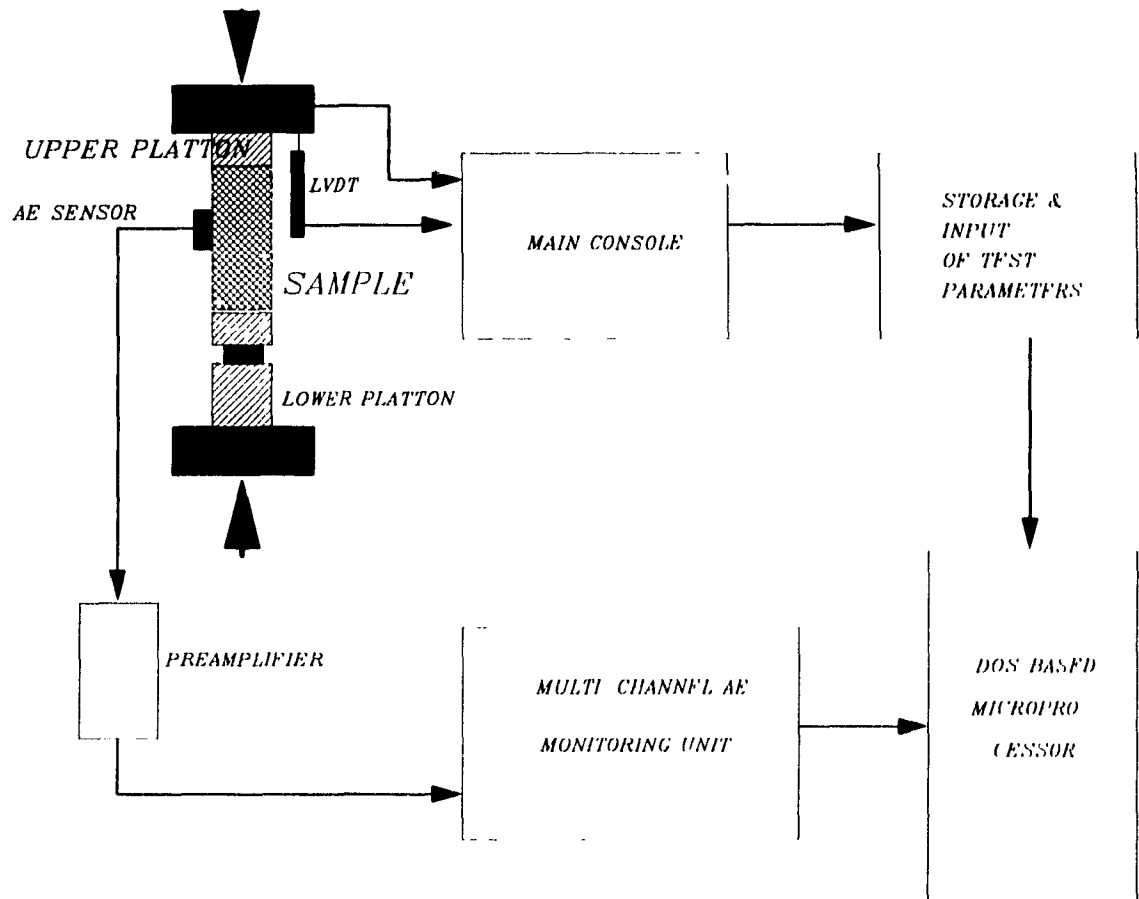


Figure 9.1b: Photograph of experimental setup of sample for uniaxial compression and acoustic emission tests.

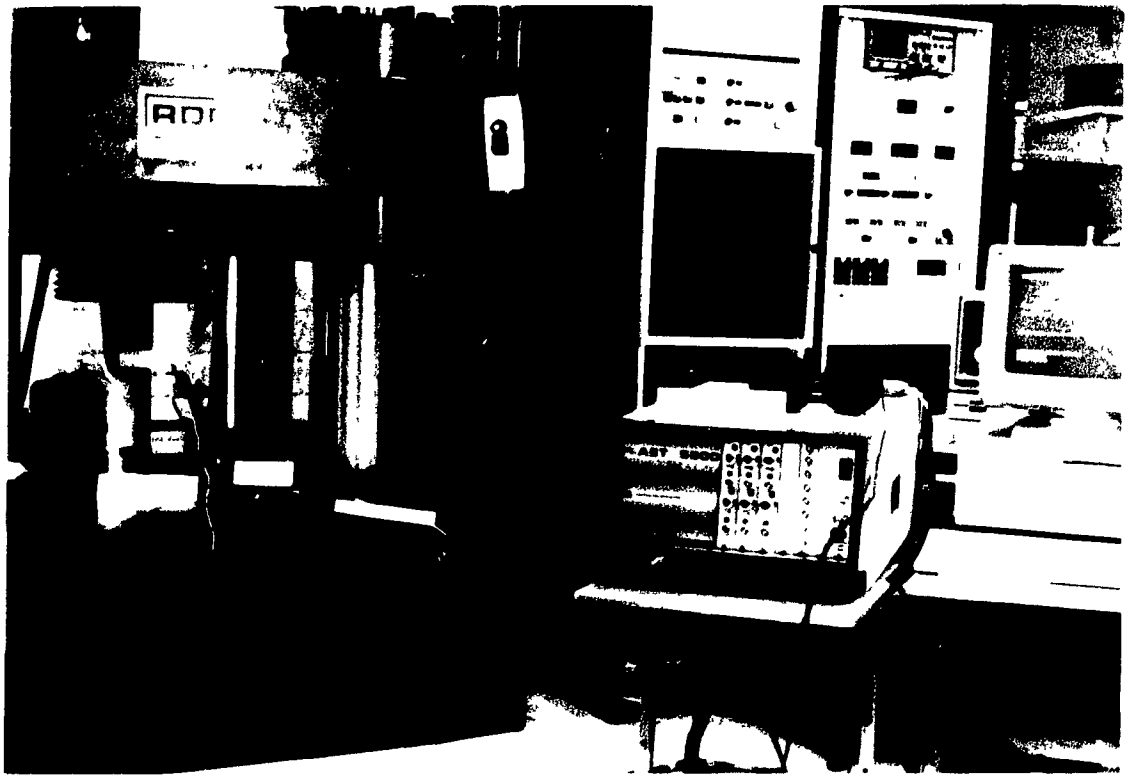


Figure 9.2: Representative plot of acoustic emission rate versus stress for type "A" potash rock.

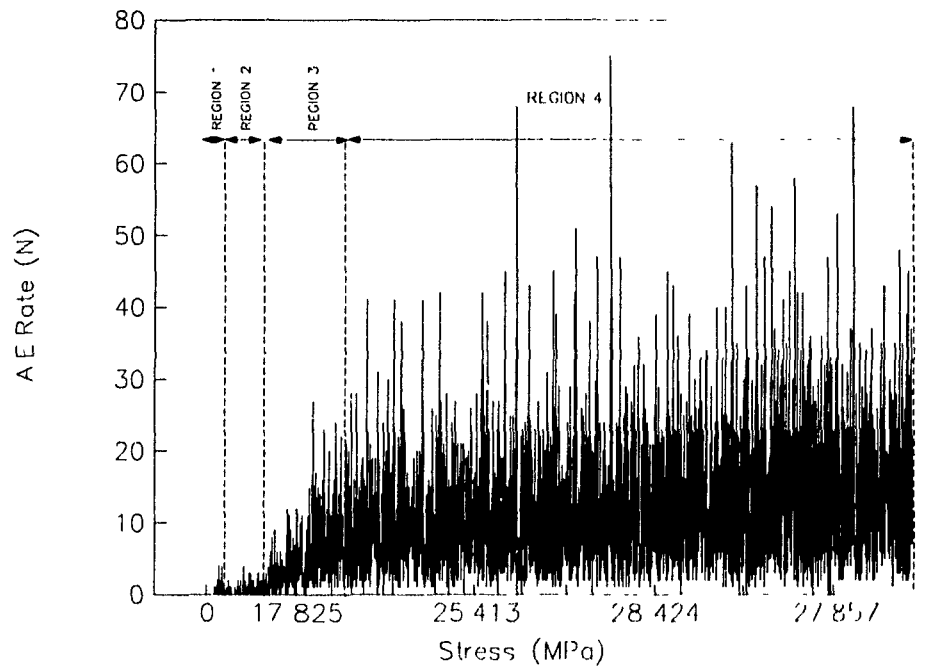


Figure 9.3: Representative plot of acoustic emission rate versus stress for type "B" potash rock.

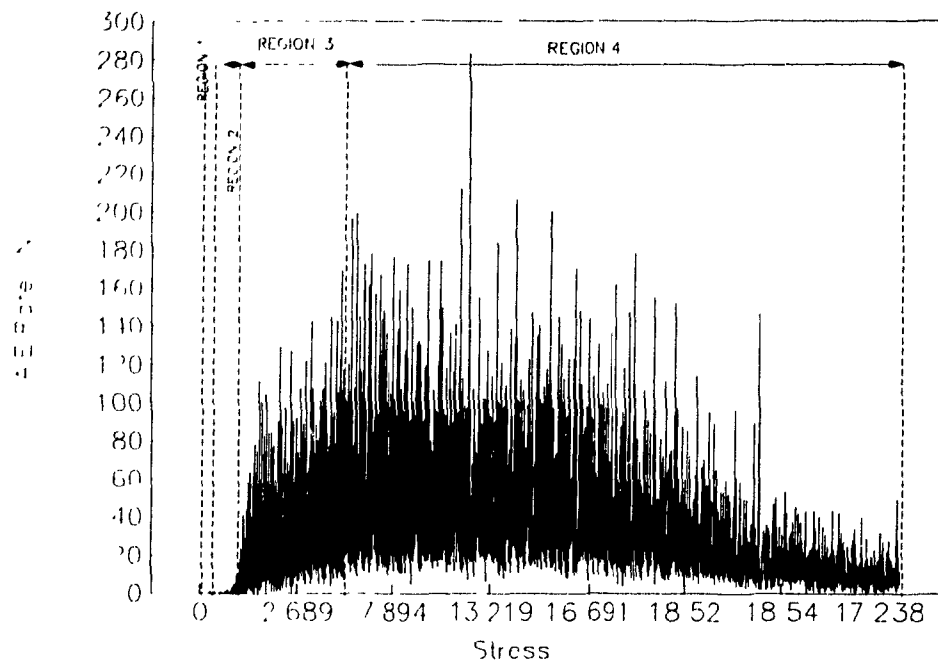


Figure 9.4: Representative plot of acoustic emission rate versus stress for type "C" potash rock.

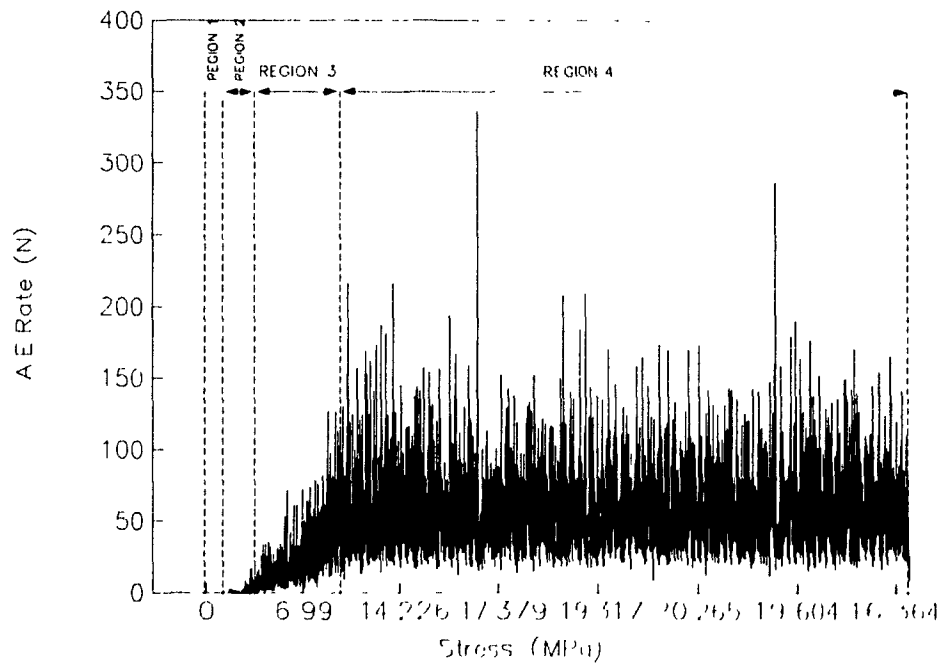


Figure 9.5: Representative plot of acoustic emission rate versus stress for type "D" potash rock.

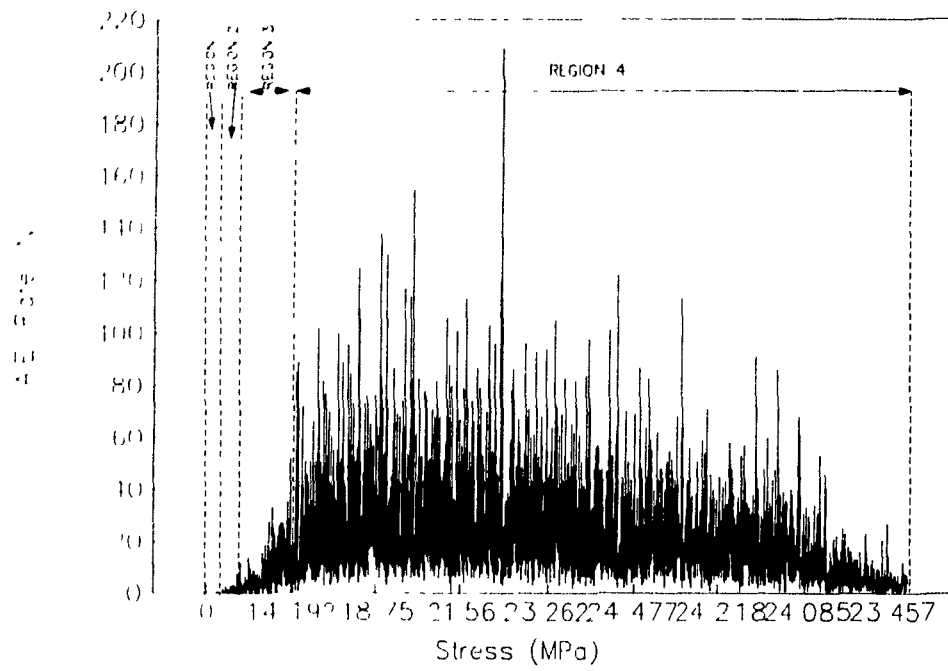


Figure 9.6: Graphical representation of type "A" potash rock displaying the relationship between acoustic emission rate versus stress and strain for sample S1A3. The four regions corresponding to changing acoustic emission activity are also shown.

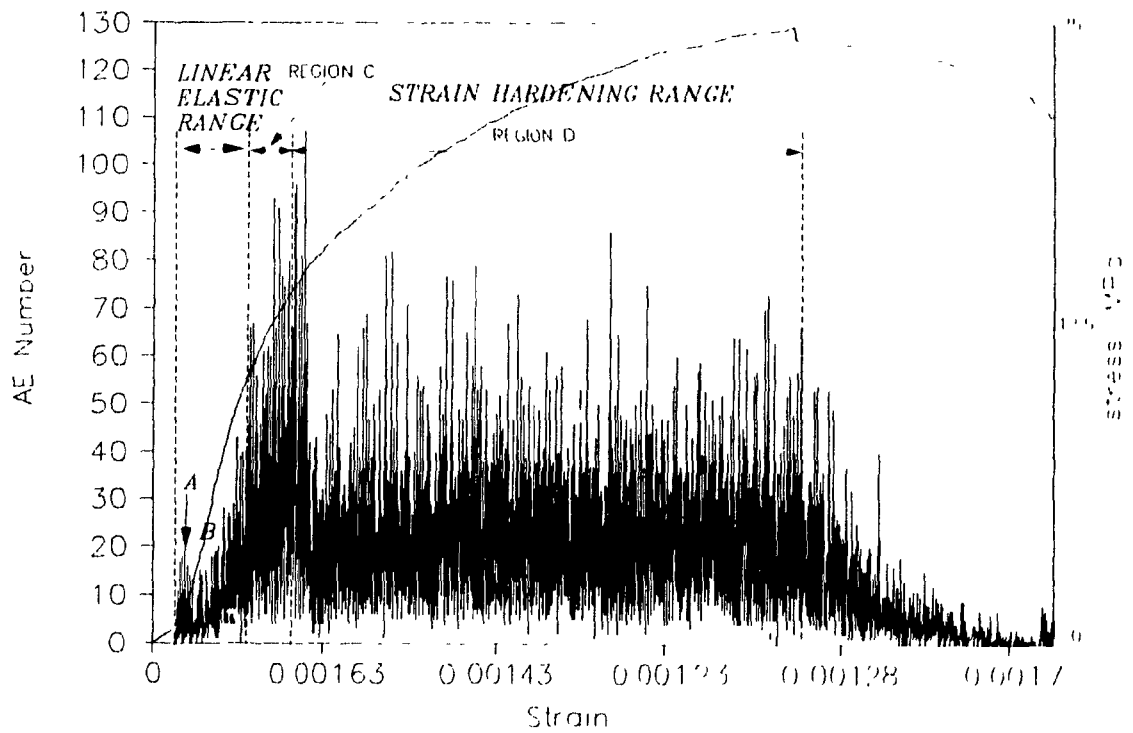


Table 9.1: Subdivisional group types of each potash rock type, based on acoustic emission rate response (refer to text for explanation).

**Type "A" potash rock**

Type "1A"		Type "2A"		Type "3A"
S1A3	S5A7	S1A7	S2A2	S2A1
S6A1	S5A9	S5A6	S5A2	S2A6
S2A3	S4A1	S5A8	S4A6	S5A1
	S4A4		S5A3	S4A2

**Type "B" potash rock**

Type "1B"	Type "2B"	Type "3B"	Type "4B"
S1B1	S1C6	S9C5	S9B4
S1B2	S1B2		S9B2
S1B3			S9B1
			S9BC1

**Type "C" potash rock**

Type "1C"	Type "2C"	Type "3C"
ALL SAMPLES EXCLUDING THE SPECIMENS INDICATED TO THE RIGHT OF THE TABLE	S1C4 S1C3 S9C6	S7C1

Figure 9.7: Graphical representation of type "1B" relationship between acoustic emission rate versus stress and strain for sample S1B1.

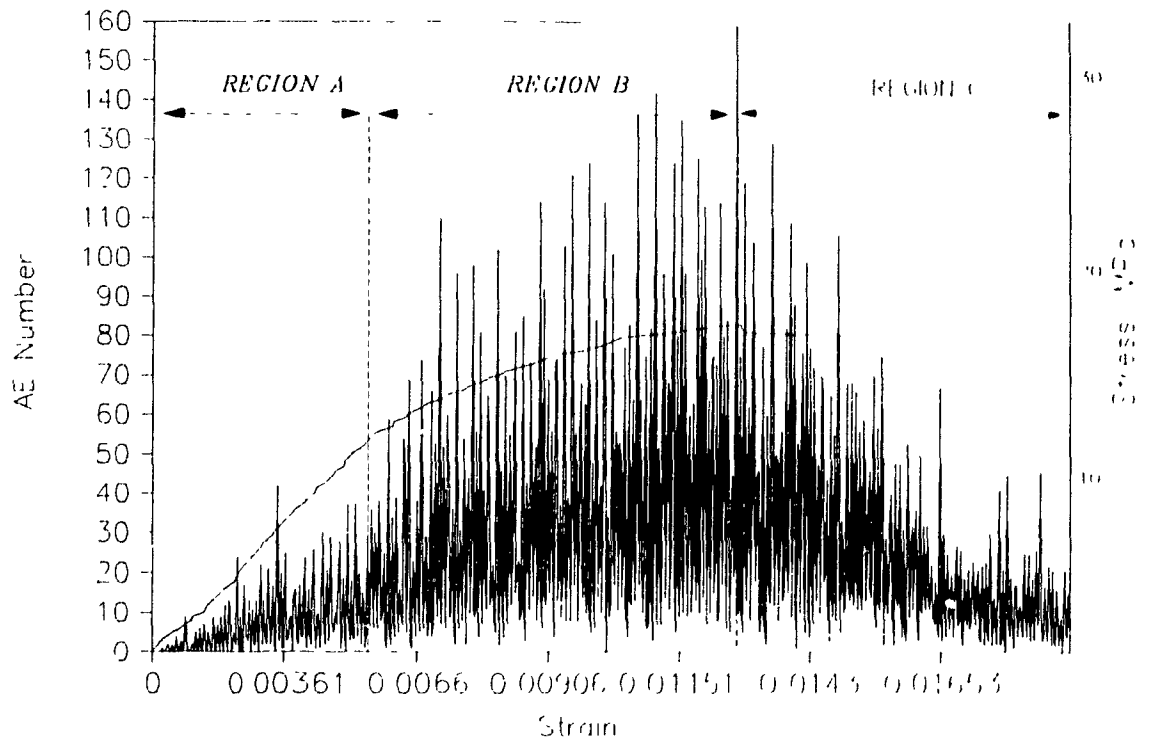
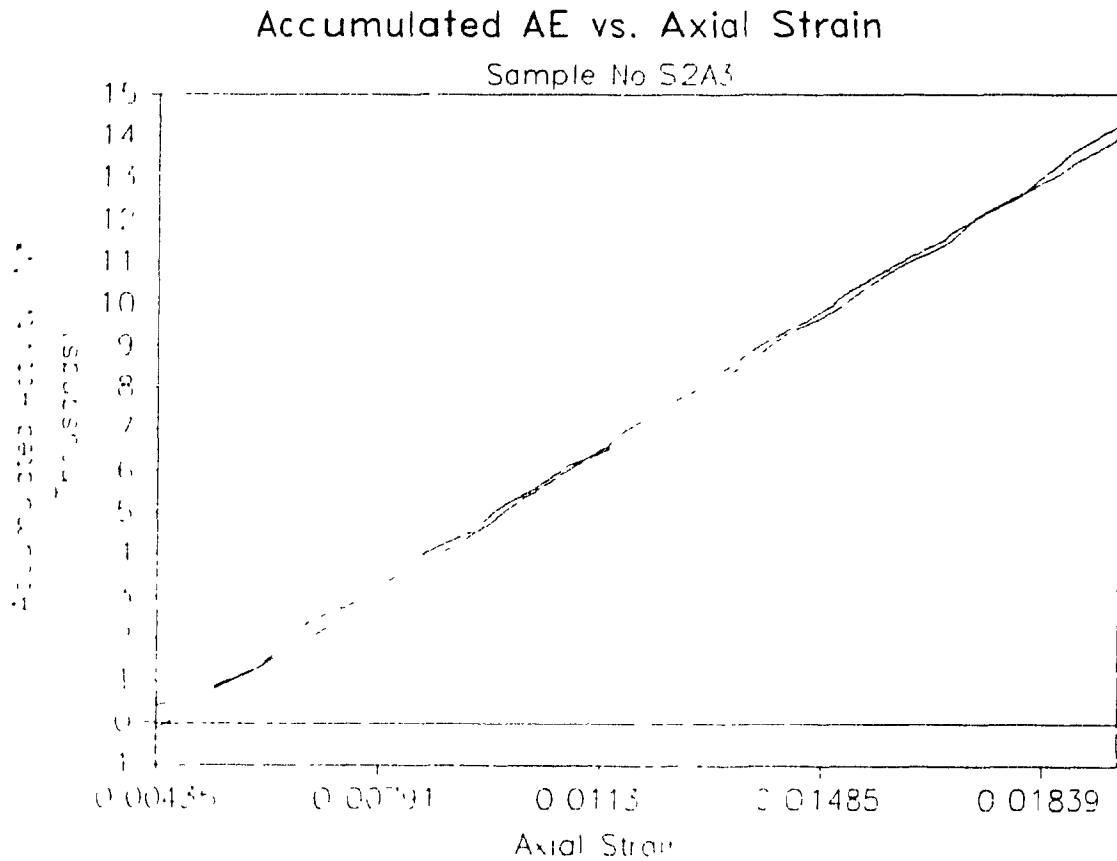


Figure 9.8: Typical curves displaying the variation of cumulative acoustic emission activity in relation to axial strain. The dashed line falling below the zero level represents the least squares fit relating uniaxial strain and acoustic emission activity, ( $N_e = A + Be$ ). The other solid line represents the actual cumulative acoustic emission data.



**Figure 9.9:** An example of an amplitude distribution histogram for a small selection of specimens loaded to the elastic range. Distributions are shown for samples S5A4, S1B2, S1C3 and S1D1.

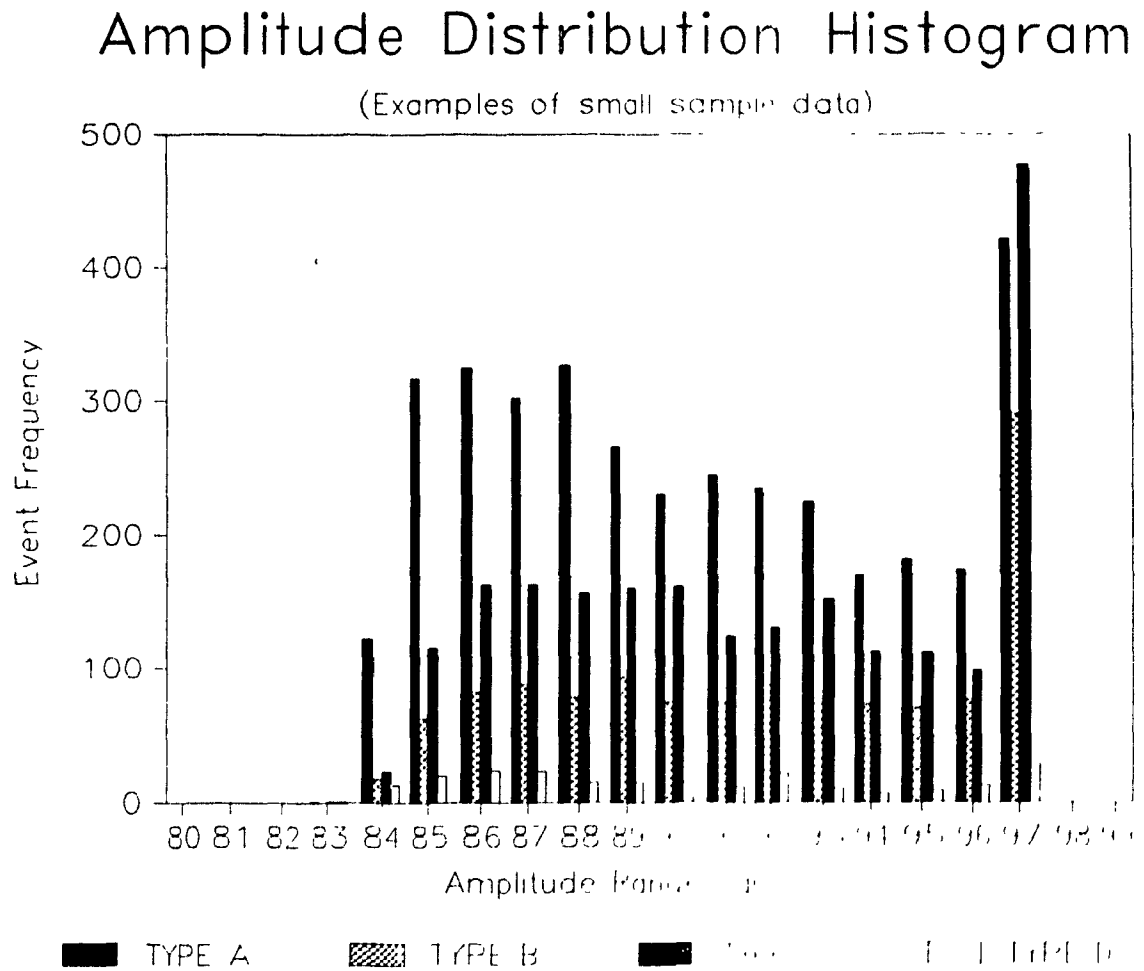
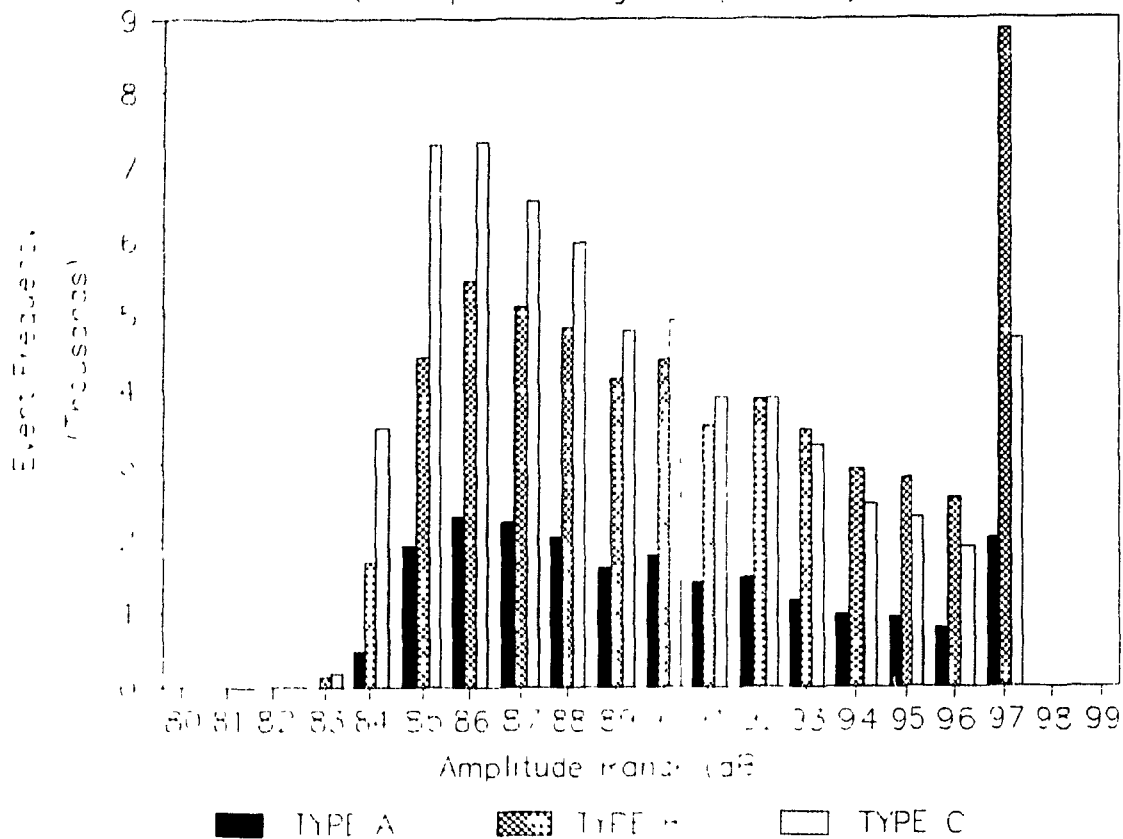


Figure 9.10: An example of an amplitude distribution histogram for a large selection of specimens loaded to the failure range. Distributions are shown for samples S2A6, S9B5 and S9C5.

## Amplitude Distribution Histogram

(Examples of large sample data)



**Table 9.2a: Tabulation of b-values using formulae defined by various authors. Acoustic emission data corresponds to sample failure.**

	Power Law Function	Least Squares Fit (Sano et al 1982)	Gutenberg-Richter Relationship	Gutenberg-Richter Relationship	Holt-Evans Distr function	
	$N(A) = kA^{-m}$	$\ln(N) = Ax^b + B$	$\log(N) = A + bM$ using $\ln(N) = A + bM$	$\log(N) = A + b(B - M)$ using $\ln(N) = A + b(B - M)$	$\ln(f) = D - E \lambda^2$	
	Cumulative Ampl Value	Cumulative Ampl Value	Cumulative Ampl Value	Cumulative Ampl Value	Cumulative Ampl Value	
	Note b = m-1	Note b = m-1				
SAMPLE NO	to failure	to failure	to failure	to failure	to failure	
					D	E
S1A7	0.2292	0.2276	-0.2322	0.2322	18 7786	0 001308
S2A1	0.4064	0.2777	-0.2322	0.2322	18 7786	0 001308
S2A2	0.3935	0.3222	-0.1798	0.1798	15 2979	0 000842
S2A4	0.2734	0.2691	-0.2004	0.2004	15 7133	0 000937
S5A2	0.2839	21.6840	-0.1404	0.1404	13 9160	0 000590
S5A3	0.3649	0.3620	-0.1518	0.1518	13.9628	0 000641
S5A4	0.1885	4.8078	-0.1663	0.1663	16.1451	0 000773
S5A6	0.2815	0.2562	-0.1748	0.1748	15 2585	0 000874
S5A7	0.2853	0.3637	-0.1455	0.1455	14 1326	0 000658
S5A8	0.3549	2.3036	-0.1565	0.1565	14 3097	0 000659
S6A1	0.3762	0.3474	-0.1629	0.1629	15.2937	0 000759
S1B1	0.2908	0.2327	-0.1439	0.1439	13 6314	0 000621
S1B2	0.2082	0.2577	-0.1306	0.1306	13.7763	0 000603
S1B3	0.2340	0.3691	-0.1412	0.1412	13 5694	0 000653
S6B1	0.3200	0.3298	-0.1483	0.1483	14 5840	0 000739
S1C1	0.4186	0.4281	-0.1211	0.1211	14 4686	0 000559
S1C2	0.1901	0.3572	-0.1320	0.1320	14 7113	0 000608
S1C3	0.3504	0.2851	-0.1995	0.1995	15 6430	0 000920
S1C4	0.2037	0.4536	-0.1482	0.1482	14.7531	0 000683
S7C1	0.3148	0.3273	-0.1749	0.1749	14 8217	0 000818
S1D1	0.2882	0.6504	-0.1790	0.1790	16 0585	0 000843
S1D2	0.2877	0.2889	-0.1903	0.1903	16.3331	0 000950

Table 9.2b: Tabulation of b-values using formulae defined by various authors.  
Acoustic emission data corresponds to sample failure.

	Power Law Function	Least Squares Fit (Sano et al 1982)	Gutenberg-Richter Relationship	Gutenberg-Richter Relationship	Holt-Evans Distr function	
	$N(A) = kA^{-m}$	$\ln(N) = Ax^b + B$	$\log(N) = A + bM$ using $\ln(N) = A + bM$	$\log(N) = A + b(B - M)$ using $\ln(N) = A + b(B - M)$	$\ln(V) = D - Ex^2$	
	Cumulative Ampl Value	Cumulative Ampl Value	Cumulative Ampl Value	Cumulative Ampl Value	Cumulative Ampl Value	
	Note $b = m - 1$	Note $b = m - 1$				
SAMPLE NO	to failure	to failure	to failure	to failure	to failure	
					D	E
S1A1	0.3205	0.4104	-0.1685	0.1685	16.4941	0.000988
S1A3	0.2073	0.3559	-0.1441	0.1441	15.6918	0.000820
S2A3	0.4090	0.3522	-0.1665	0.1665	15.6581	0.000826
S2A6	0.4064	9.3590	-0.1695	0.1695	15.4019	0.000784
S4A1	0.4220	0.3377	-0.1653	0.1653	15.6151	0.000762
S4A2	0.3015	0.4107	-0.1679	0.1679	15.0163	0.000783
S4A3	0.3802	0.2359	-0.1881	0.1881	17.1394	0.001060
S4A4	0.3568	0.3958	-0.1784	0.1784	15.9949	0.000823
S4A6	0.1961	0.3356	-0.1500	0.1500	15.0855	0.000693
S5A1	0.3217	0.2753	-0.1875	0.1875	15.4134	0.000869
S5A5	0.3775	3.4331	-0.1790	0.1790	15.9715	0.000832
S5A9	0.2882	0.3062	-0.1838	0.1838	15.0578	0.000813
S9C1	0.4453	0.3104	-0.1832	0.1832	17.4653	0.000812
S9C2	0.4656	0.3087	-0.1827	0.1827	17.3796	0.000866
S9C5	0.2228	0.3206	-0.1876	0.1876	17.1310	0.000879
S9C6	0.2704	0.3485	-0.1887	0.1887	16.04677	0.000797
S9C7	0.2242	0.3211	-0.1895	0.1895	17.3225	0.000949
S9B1	0.2810	0.5047	-0.1874	0.1874	15.7732	0.000928
S9B2	0.3275	0.2962	-0.1598	0.1598	15.6209	0.000749
S9B3	0.2621	0.1187	-0.1926	0.1926	16.3491	0.000913
S9B4	0.3003	0.2555	-0.1335	0.1335	15.3694	0.000625
S9B5	0.3325	0.3096	-0.1359	0.1359	15.3586	0.000633
S9BC1	0.3793	0.4195	-0.1524	0.1524	15.66592	0.000766

Table 9.3a: Compilation of b-values using formulae defined by various authors. Acoustic emission data corresponds to samples tested to the elastic range.

	Power Law Function	Least Squares Fit (Sano et al 1982)	Gutenberg-Richter Relationship	Gutenberg-Richter Relationship	Holt-Evans Distr function	
	$N(A) = kA^{-m}$	$\ln(N) = Ax^b + B$	$\log(N) = A + bM$ using $\ln(N) = A + bM$	$\log(N) = A + b(B - M)$ using $\ln(N) = A + b(B - M)$	$\ln(f) = D - kx^c$	
	Cumulative Ampl Value	Cumulative Ampl Value	Cumulative Ampl Value	Cumulative Ampl Value	Cumulative Ampl Value	
	Note b = m-1	Note b = m-1				
SAMPLE NO	to elastic range	to elastic range	to elastic range	to elastic range	to elastic range	
					D	F
S1A7	0.3532	-0.3869	-0.1268	0.1268	11.1949	0.00070358
S2A1	0.3088	-0.2536	-0.1522	0.1522	11.5454	0.00084900
S2A2	0.3852	-0.6289	-0.1500	0.1600	11.5065	0.00089417
S2A4	0.3889	-0.2687	-0.2046	0.2046	12.6892	0.00114131
S5A2	0.3271	-0.2495	-0.1489	0.1489	12.1522	0.00082605
S5A3	0.3820	-0.2910	-0.1330	0.1330	11.1130	0.00073781
S5A4	0.4047	-0.3172	-0.1491	0.1491	14.1643	0.00083190
S5A6	0.4886	-0.2476	-0.1604	0.1604	11.3931	0.00088972
S5A7	0.2622	-0.2547	-0.1445	0.1445	11.2939	0.00079710
S5A8	0.4588	-0.2750	-0.1760	0.1760	12.4893	0.00097907
S6A1	0.3047	-0.2398	-0.1218	0.1218	10.5952	0.00067486
S1B1	0.3625	-0.3552	-0.1192	0.1192	11.9716	0.00066045
S1B2	0.1504	-0.4071	-0.1099	0.1099	11.5772	0.00060912
S1B3	0.3381	-0.3640	-0.1369	0.1369	13.3130	0.00075917
S6B1	0.3197	-0.3375	-0.1356	0.1356	12.4874	0.00075562
S1C1	0.4684	-0.3861	-0.1040	0.1040	11.3934	0.00057652
S1C2	0.3786	-0.3564	-0.1174	0.1174	12.4167	0.00065050
S1C3	0.4402	-0.2757	-0.1791	0.1791	12.5367	0.00092272
S1C4	0.3866	-0.2262	-0.1538	0.1538	12.0972	0.00085285
S7C1	0.3443	-0.3347	-0.1491	0.1491	11.8985	0.00083100
S1D1	0.3698	-0.2626	-0.1473	0.1473	11.3271	0.00081575
S1D2	0.4450	-0.2640	-0.1682	0.1682	12.5591	0.00093779

Table 9.3b: Compilation of b-values using formulae defined by various authors. Acoustic emission data corresponds to samples tested to the elastic range.

	Power Law Function	Least Squares Fit (Sano et al 1982)	Gutenberg-Richter Relationship	Gutenberg-Richter Relationship	Holt-Evans Distr function	
	$N(A) = \lambda A^{-m}$	$\ln(N) = Ax^b + B$	$\log(N) = A + bM$ using $\ln(N) = A + bM$	$\log(N) = A + b(B - M)$ using $\ln(N) = A + b(B - M)$	$\ln(V) = D - Ex^2$	
	Cumulative Ampl Value	Cumulative Ampl Value	Cumulative Ampl Value	Cumulative Ampl Value	Cumulative Ampl Value	
	Note b = m-1	Note b = m-1				
SAMPLE NO	to elastic range	to elastic range	to elastic range	to elastic range	to elastic range	
					D	E
S1A1	0.3333	-0.2930	-0.1523	0.1523	14.2443	0.00086356
S1A3	0.5915	-0.2979	-0.1440	0.1440	12.2331	0.00081633
S2A3	0.4086	-0.2990	-0.1646	0.1646	13.4446	0.00091301
S2A6	0.4563	-0.2775	-0.1455	0.1455	11.2747	0.00080581
S4A1	0.2762	-0.2514	-0.1470	0.1470	12.0960	0.00081324
S4A2	0.3866	-0.3670	-0.1445	0.1445	13.4099	0.00080686
S4A3	0.3712	-0.3134	-0.1710	0.1710	14.6599	0.00097016
S4A4	0.4432	-0.2697	-0.1636	0.1636	12.7110	0.00090650
S4A6	0.3664	-0.3243	-0.1448	0.1448	12.7907	0.00080267
S5A1	0.6601	-0.2665	-0.1651	0.1651	12.7540	0.00091519
S5A5	0.4507	-0.2782	-0.1650	0.1650	14.2858	0.00092073
S5A9	0.4793	-0.2436	-0.1731	0.1731	12.9258	0.00096536
S9C1	0.2677	-0.3455	-0.1454	0.1454	14.4764	0.00084344
S9C2	0.2587	-0.3628	-0.1456	0.1456	14.3131	0.00081163
S9C5	0.2959	-0.3977	-0.1508	0.1508	14.3667	0.00084058
S9C6	0.3143	-0.3580	-0.1681	0.1681	15.5915	0.00092632
S9C7	0.2965	-0.3514	-0.1720	0.1720	15.8187	0.00095894
S9B1	0.4214	-0.2807	-0.1878	0.1878	14.443883	0.00104849
S9B2	0.3354	-0.3896	-0.1435	0.1435	14.073374	0.00080256
S9B3	0.3641	-0.2171	-0.1759	0.1759	16.013309	0.00098099
S9B4	0.4085	-0.4363	-0.1107	0.1107	14.279509	0.00061688
S9B5	0.3265	-0.4555	-0.1195	0.1195	15.206778	0.00066600
S9BC1	0.2275	-0.2536	-0.1356	0.1356	13.643742	0.00075595

**Figure 9.11:** Cumulative distribution functions and corresponding plots for the power law function (1), the log normal distribution function (2), the Gutenberg-Richter model (3), the Gutenberg-Richter model (4) (proposed by Fonseka et al. 1985) and the least squares function (5). The experimental data is indicated by dotted marker points. Data analysis is composed of measurements to sample failure for specimen type "A" potash rock.

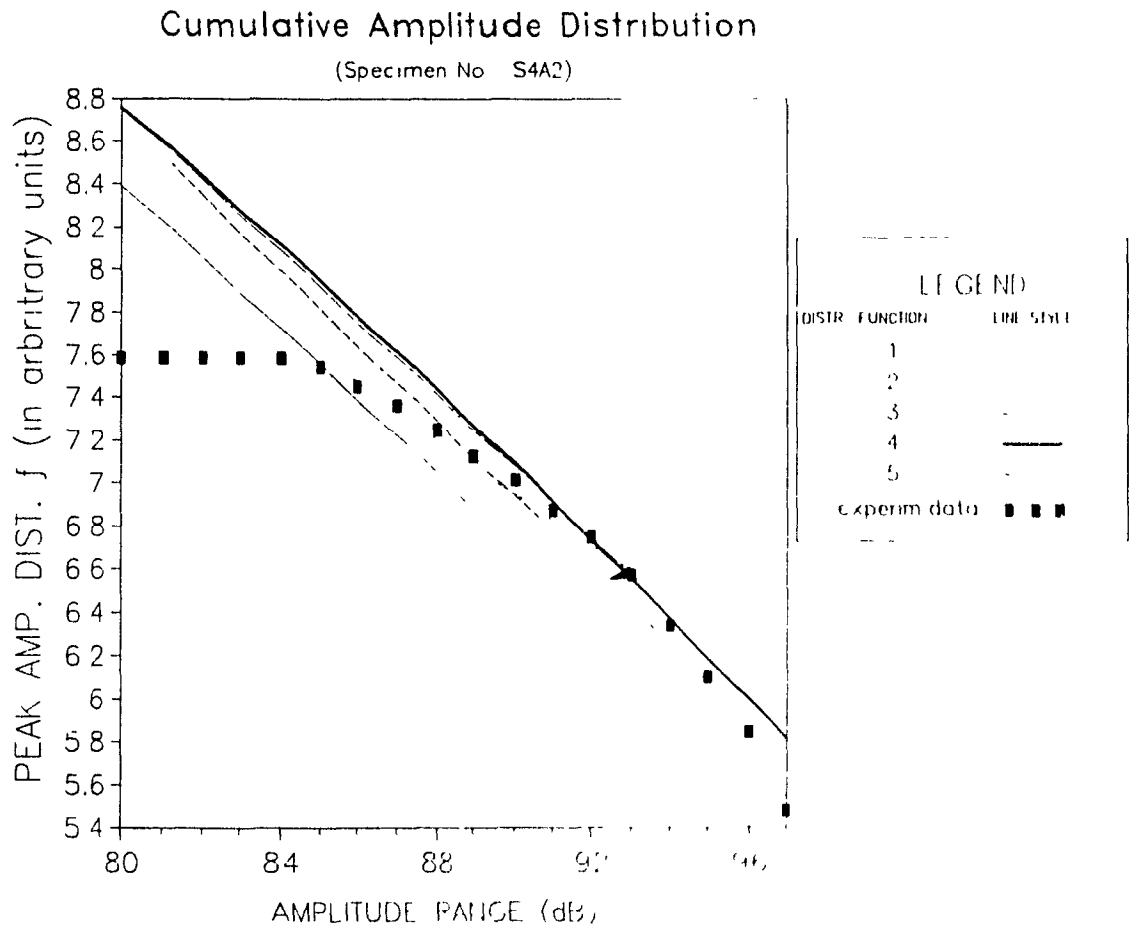


Figure 9.12: Cumulative distribution functions and corresponding plots for the power law function (1), the log normal distribution function (2), the Gutenberg-Richter model (3), the Gutenberg-Richter model (4) (proposed by Fonseka et al. 1985) and the least squares function (5). The experimental data is indicated by dotted marker points. Data analysis is composed of measurements to sample failure for specimen type "B" potash rock.

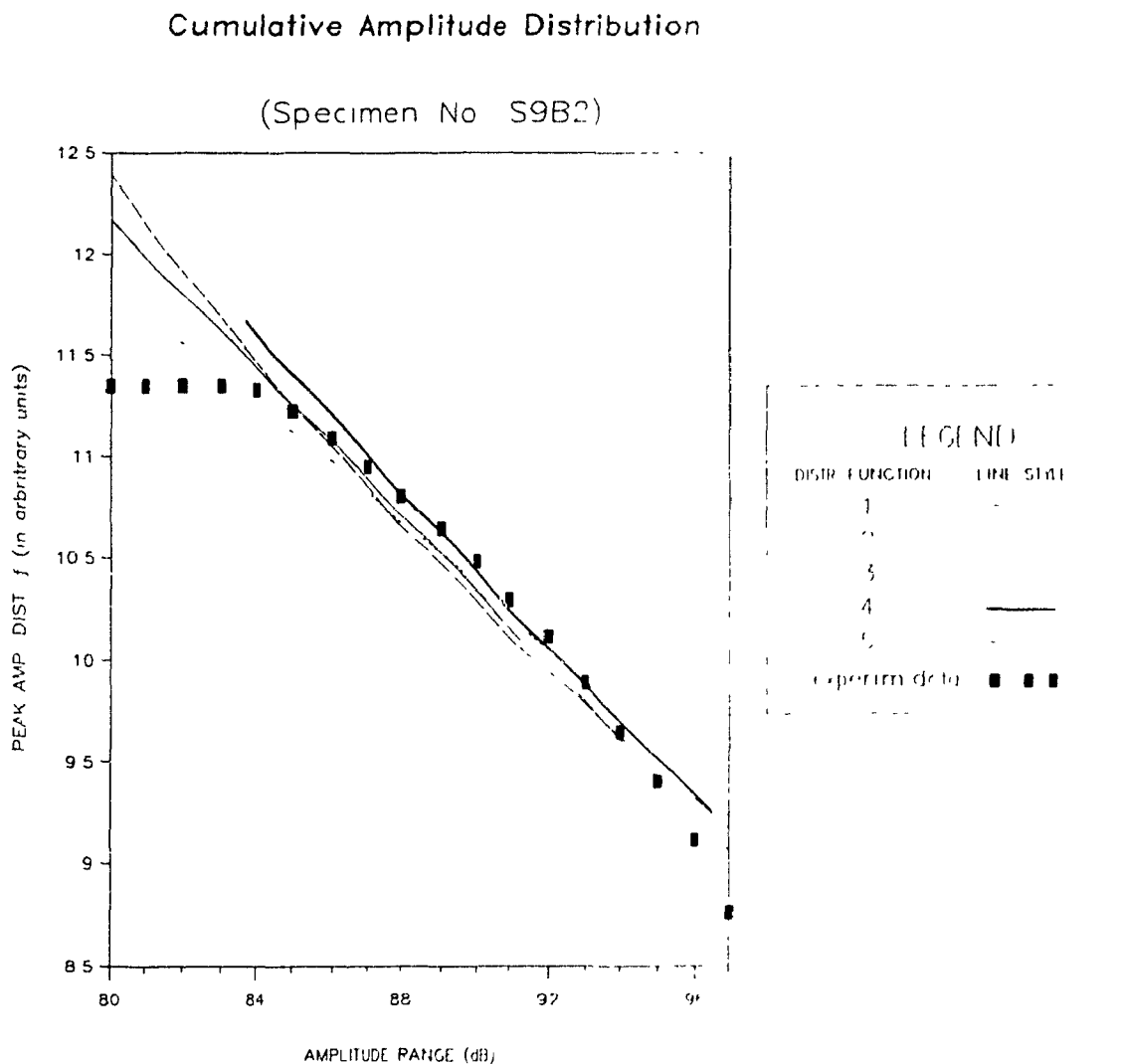
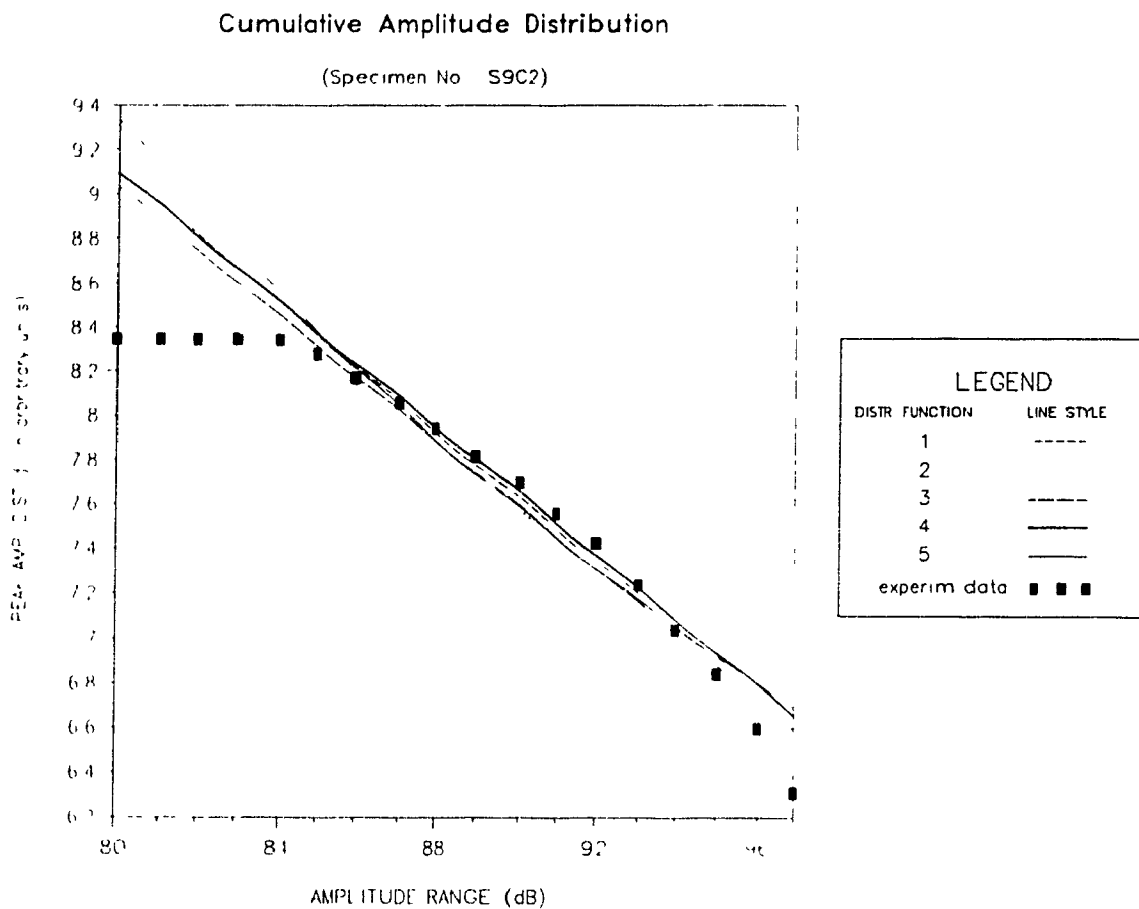


Figure 9.13: Cumulative distribution functions and corresponding plots for the power law function (1), the log normal distribution function (2), the Gutenberg-Richter model (3), the Gutenberg-Richter model (4) (proposed by Fonseka et al. 1985) and the least squares function (5). The experimental data is indicated by dotted marker points. Data analysis is composed of measurements to the elastic limit for specimen type "C" potash rock.



**Figure 9.14:** Cumulative distribution functions and corresponding plots for the power law function (1), the log normal distribution function (2), the Gutenberg-Richter model (3), the Gutenberg-Richter model (4) (proposed by Fonseka et al. 1985) and the least squares function (5). The experimental data is indicated by dotted marker points. Data analysis is composed of measurements to the elastic limit for specimen type "D" potash rock.

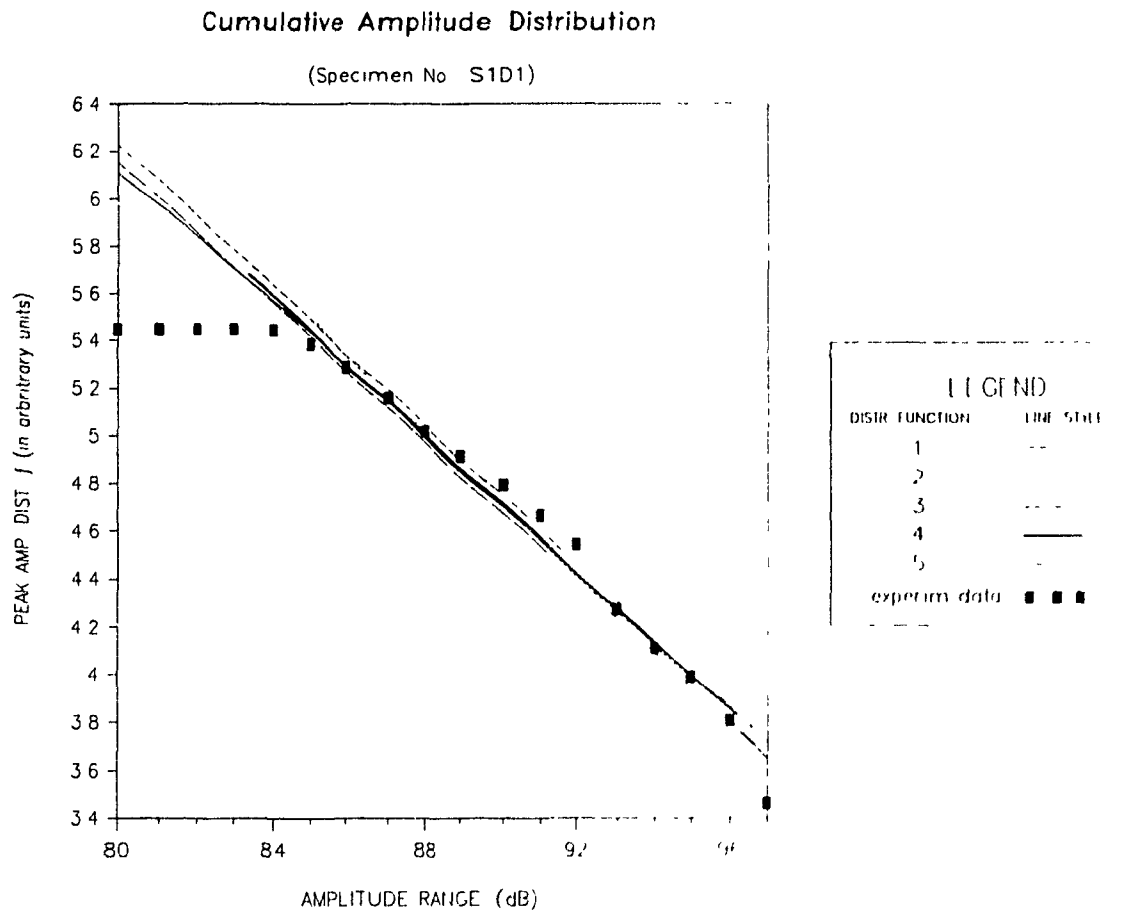


Table 9.4: Acoustic emission counts over 10 successive periods of increasing load levels calculated as a percentage of failure under uniaxial compression. Sample calculations are tabulated for small samples including S1B2, S1C4, S1D1 and S2A4. Calculations for large samples are also shown. These include samples S4A2, S9B5 and S9C5.

SAMPLE NO :S1B2  
AMPLITUDE RANGES

	1	2	3	4	5	6	7	8	
STRESS LEVEL	75-78	79-81	82-84	85-87	88-90	91-93	94-96	97-99	Amplitude Ratio
0-10	475	415	3	17	9	13	15	14	7.08
10-20	215	165	1	23	21	24	15	25	22.09
20-30	166	142	2	19	26	27	23	27	28.24
30-40	191	167	2	34	53	40	41	53	38.04
40-50	113	128	4	49	44	47	43	71	50.90
50-60	0	0	6	80	82	77	70	87	98.51
60-70	0	0	9	166	188	176	186	235	99.06
70-80	0	0	11	374	322	288	338	558	99.42
80-90	0	0	40	818	717	587	693	1303	99.04
90-100	0	0	94	1984	1890	1522	1597	2298	99.00

SAMPLE NO S1C4  
AMPLITUDE RANGES

	1	2	3	4	5	6	7	8	
STRESS LEVEL	75-78	79-81	81-84	84-87	87-90	90-93	93-96	96-99	Amplitude Ratio
0-10	1771	1374	8	135	145	143	122	174	18.57
10-20	56	39	7	35	39	38	39	40	65.19
20-30	33	26	2	35	40	34	33	43	75.20
30-40	41	13	4	51	49	46	44	52	79.87
40-50	35	26	5	83	84	101	71	72	86.16
50-60	54	29	8	73	168	168	131	136	89.50
60-70	22	16	17	377	378	339	282	278	96.78
70-80	0	0	40	1013	906	842	680	775	99.06
80-90	0	0	83	2382	2292	1855	1505	1407	99.13
90-100	0	0	340	7279	6495	5061	3668	3167	98.69

(continuation of Table 9.4)

SAMPLE NO S1D1  
AMPLITUDE RANGES

STRESS LEVEL	1	2	3	4	5	6	7	8	
	75-78	79-81	81-84	84-87	87-90	90-93	93-96	96-99	Amplitude Ratio
0-10	283	120	1	5	4	3	0	3	3.58
10-20	104	38	1	6	5	3	1	4	11.73
20-30	77	29	4	17	14	9	6	5	31.68
30-40	96	32	3	19	17	16	11	17	37.91
40-50	130	43	12	49	44	30	21	21	47.11
50-60	288	124	97	298	257	210	186	154	68.46
60-70	393	144	252	779	668	535	487	320	77.95
70-80	434	183	360	1378	1145	856	633	456	82.06
80-90	401	201	579	2030	1712	1135	811	458	83.88
90-100	76	167	1247	3776	2968	1939	1259	731	87.75

SAMPLE NO S2A1  
AMPLITUDE RANGES

STRESS LEVEL	1	2	3	4	5	6	7	8	
	75-78	79-81	81-84	84-87	87-90	90-93	93-96	96-99	Amplitude Ratio
0-10	88	76	0	6	2	6	1	1	8.89
10-20	41	22	0	1	2	0	1	0	1.62
20-30	32	25	0	4	2	2	1	0	6.77
30-40	31	34	1	4	3	6	3	1	11.41
40-50	55	36	2	10	8	2	3	1	12.00
50-60	98	61	10	45	32	24	8	6	28.68
60-70	161	138	49	179	138	100	98	44	46.94
70-80	271	182	100	383	307	259	176	102	45.66
80-90	464	308	196	799	590	482	239	153	45.16
90-100	262	161	512	1853	1353	1558	614	274	57.57

## (Continuation of Table 9.4)

SAMPLE NO S4A2  
AMPLITUDE RANGES

	1	2	3	4	5	6	7	8	
<b>STRESS LEVEL</b>	75-78	79-81	81-84	84-87	87-90	90-93	93-96	96-99	<b>Amplitude Ratio</b>
0-10	180	257	3	21	11	9	8	9	12.35
10-20	67	105	13	55	56	41	42	36	58.55
20-30	71	68	18	104	91	56	63	45	73.52
30-40	68	64	23	126	121	109	76	49	79.25
40-50	68	91	43	202	156	170	125	83	83.05
50-60	106	121	80	462	378	270	236	156	87.45
60-70	140	169	176	875	783	510	486	332	91.10
70-80	386	460	545	2641	2234	1194	1224	856	91.13
80-90	213	233	545	2555	1984	1102	911	495	94.45
90-100	785	1101	1024	3561	2559	1037	929	445	83.52

SAMPLE NO S9C5  
AMPLITUDE RANGES

	1	2	3	4	5	6	7	8	
<b>STRESS LEVEL</b>	75-78	79-81	81-84	84-87	87-90	90-93	93-96	96-99	<b>Amplitude Ratio</b>
0-10	1847	1057	14	73	67	44	32	31	7.80
10-20	568	341	25	140	121	107	66	65	34.82
20-30	475	291	34	217	149	131	99	86	46.02
30-40	492	294	46	353	271	195	143	137	56.91
40-50	638	346	95	570	496	383	259	258	64.56
50-60	915	538	202	1186	935	750	504	473	69.93
60-70	1334	722	284	1858	1556	1111	779	621	71.69
70-80	1859	912	496	3036	2278	1611	1005	696	72.53
80-90	2511	1311	722	4149	3074	2126	1179	767	71.31
90-100	1968	1210	1730	9410	6612	4475	2487	1560	83.34

SAMPLE NO S9B5  
AMPLITUDE RANGES

	1	2	3	4	5	6	7	8	
<b>STRESS LEVEL</b>	75-78	79-81	81-84	84-87	87-90	90-93	93-96	96-99	<b>Amplitude Ratio</b>
0-10	2477	2267	173	532	493	426	413	418	54.01
10-20	1362	1010	324	929	812	697	699	946	65.01
20-30	871	606	261	900	813	805	696	951	74.98
30-40	702	506	238	1087	927	830	706	986	79.81
40-50	627	390	225	1199	1067	939	762	1032	83.70
50-60	424	273	164	1085	890	803	636	780	86.21
60-70	369	212	129	1262	1056	898	686	753	89.17
70-80	374	224	122	1606	1476	930	853	853	90.71
80-90	399	246	98	2352	2121	1240	1197	954	92.51
90-100	333	331	83	3710	3400	2422	1459	1223	94.88

**Figure 9.15:** Graphical representation of the changes occurring in the ratio of high amplitude ranges (larger than 84 dB) over emissions of 75 dB for stress levels calculated as the percentage of failure stress for larger specimens tested.

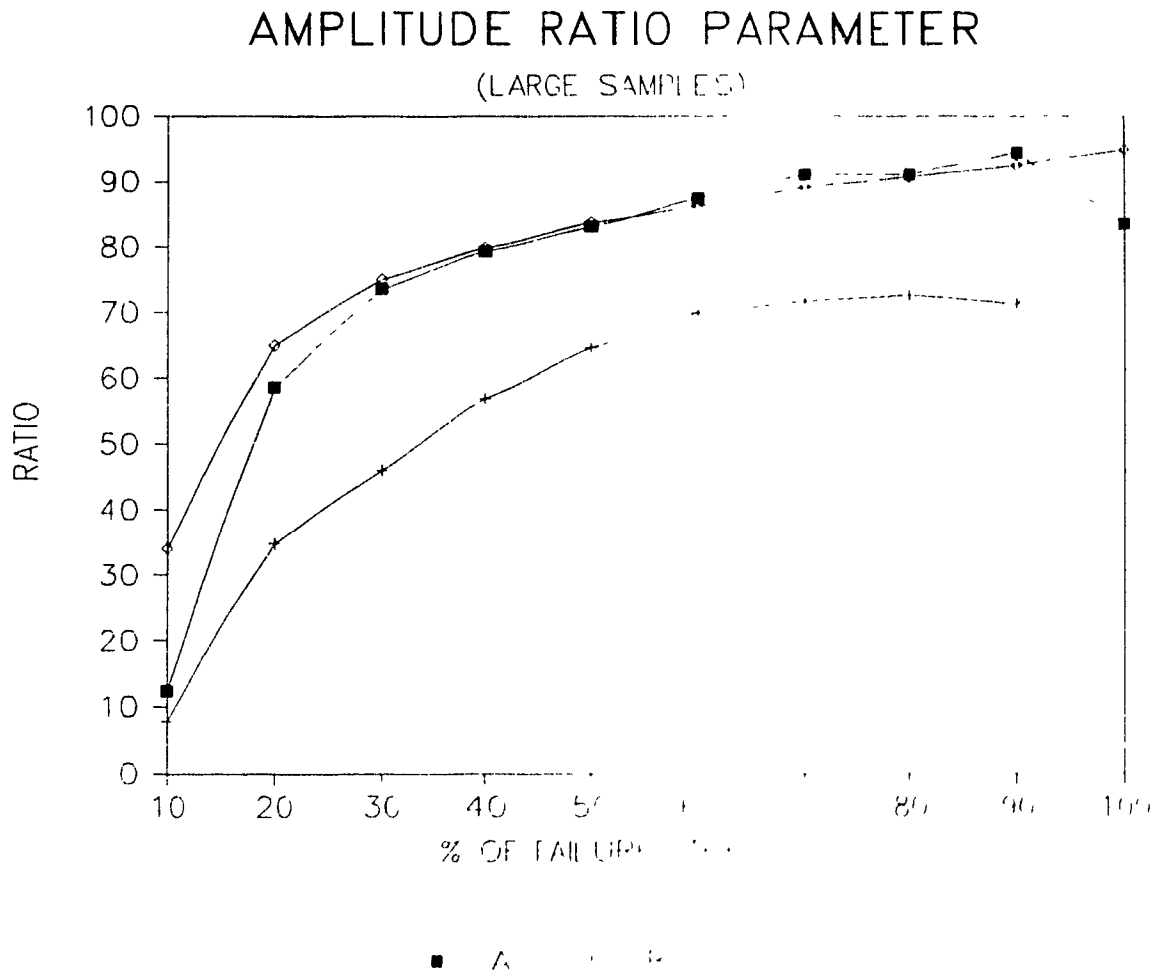


Figure 9.16: Graphical representation of the changes occurring in the ratio of high amplitude ranges (larger than 84 dB) over emissions of 75 dB for stress levels calculated as the percentage of failure stress for smaller specimens tested.

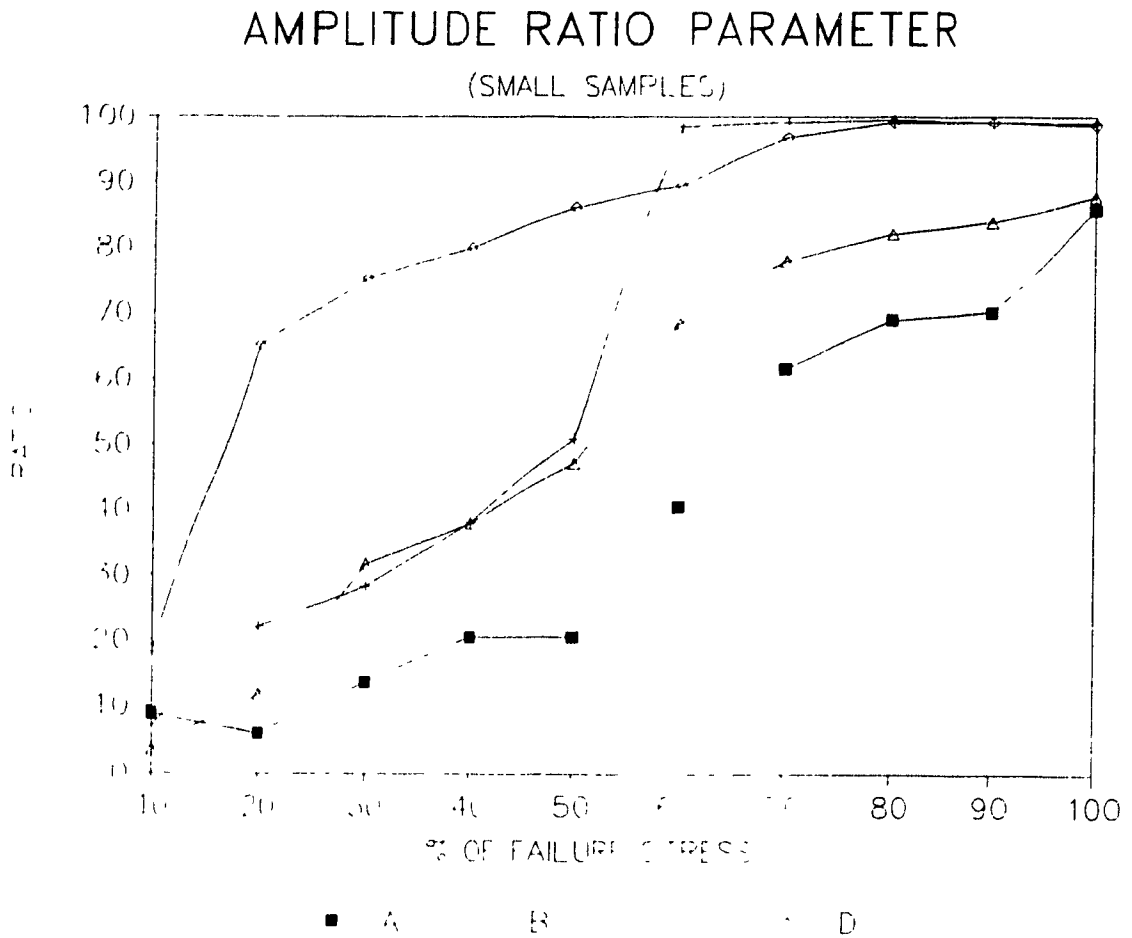


Figure 9.17: Isometric view of acoustic emission rate at each amplitude level versus increasing uniaxial compressive stress for sample S1B2.

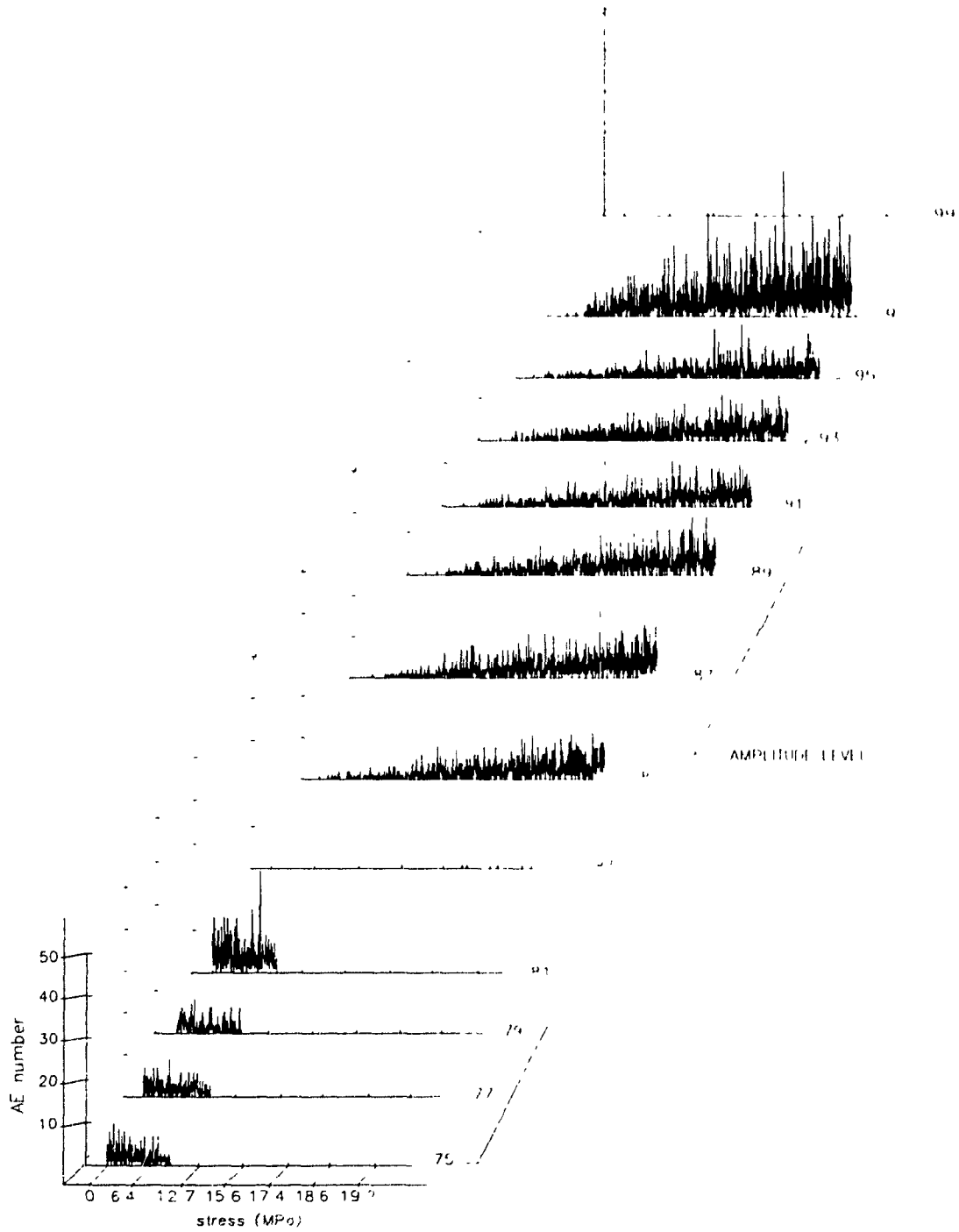


Figure 9.18: Graphical representation of energy distributions for acoustic emission data recorded up to the elastic limit.

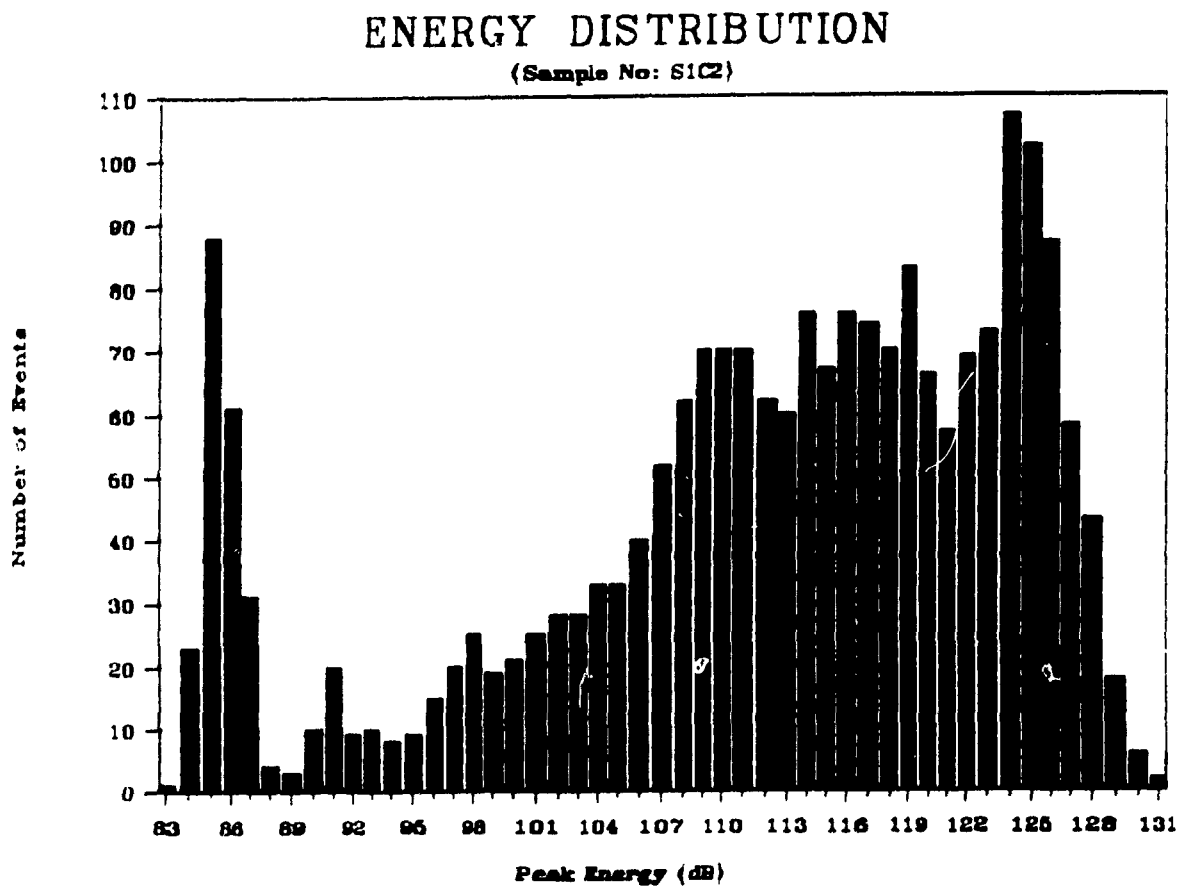


Figure 9.19: Graphical representation of energy distributions for acoustic emission data recorded to specimen failure.

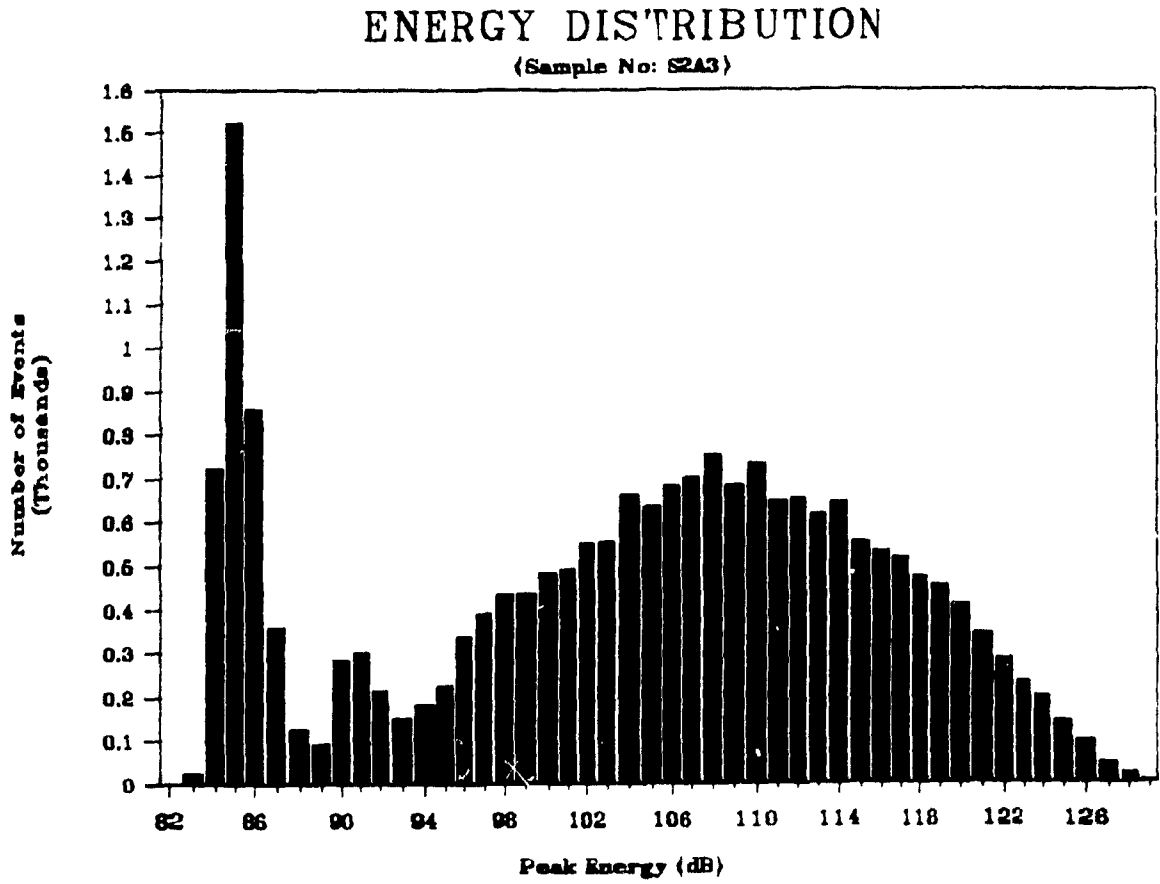


Figure 9.20: Graphical illustration of the cumulative energy distribution in relation to the log normal distribution function. The acoustic emission energy data for each event recorded in this example corresponds to sample S4A2. The data was recorded to specimen failure.

## Log-Normal Distribution

(Sample No. S4A2)

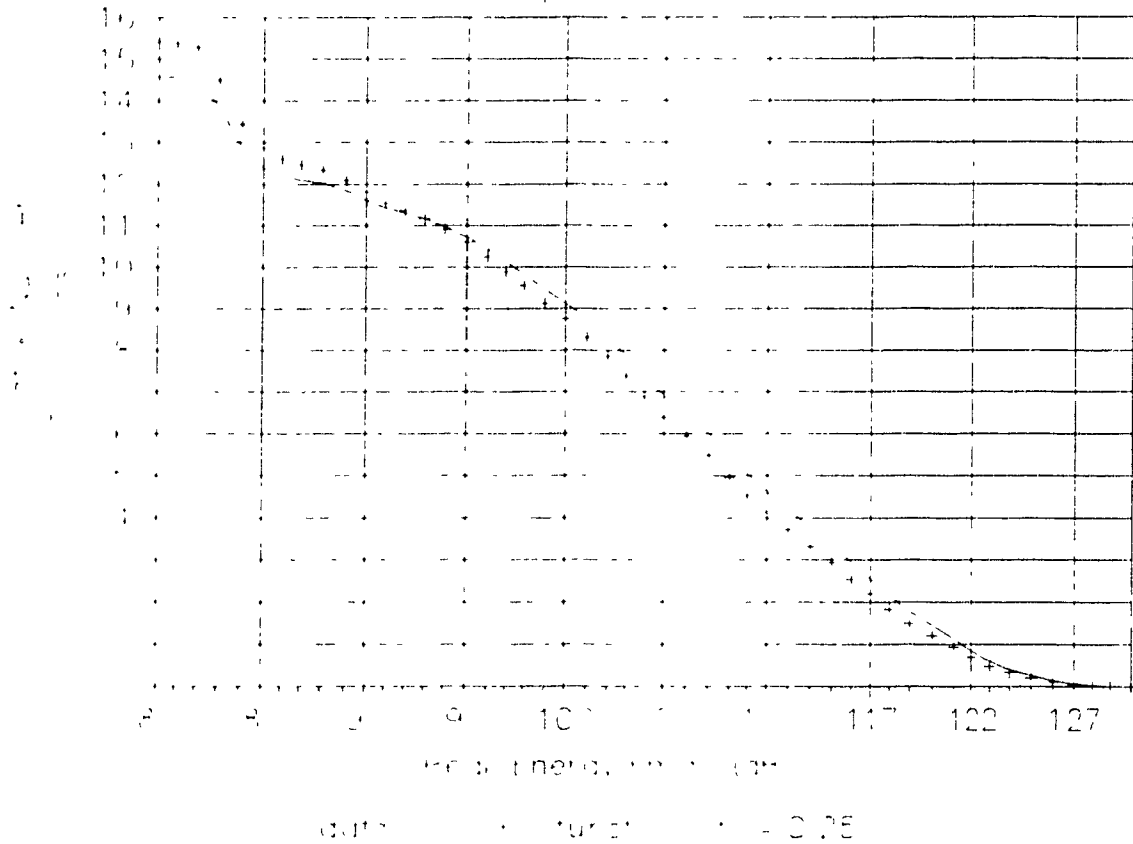


Table 9.5 Represented in the table below, labelled under stage 1), is the configuration and layout of the contingency table used for the analysis of acoustic emission time difference event data and acoustic emission amplitude. A sample calculation of Chi value (for Sample S1B2) is shown. Three stages are involved in the determination of the Chi value.

Stage 1) Observed values and calculations of totals for each row and column in the table

	TIME DIFFERENCE RANGES															16
	1	2	3	4	5	6	7	8	9	10	11	12	13	14	15	
AMPL RANGE	< 0005	0005 - 0 001	0 001 - 0 002	0 002 - 0 004	0 004 - 0 008	0 008 - 0 016	0 016 - 0 032	0 032 - 0 064	0 064 - 0 128	0 128 - 0 256	0 256 - 0 512	0 512 - 1 024	1 024 - 2 048	2 048 - 4 096	4 096 ->	101
84	0	0	0	0	0	1	0	1	0	0	0	0	0	0	0	2
85	1	2	1	19	34	48	28	20	13	19	9	1	3	0	0	198
86	35	68	84	160	200	201	175	116	94	46	25	6	0	1	1	1212
87	52	125	106	225	262	272	244	162	117	72	38	17	1	3	0	1696
88	31	96	101	213	260	283	239	166	118	73	34	12	3	4	0	1633
89	35	78	95	215	268	264	209	129	123	50	21	14	0	1	0	1502
90	28	95	74	177	209	195	109	117	96	53	30	10	1	1	0	1284
91	28	69	79	217	233	207	182	136	87	52	28	8	1	0	0	1327
92	21	65	66	171	205	181	137	110	81	36	27	10	0	1	0	1109
93	36	65	89	211	209	174	150	116	77	46	18	5	3	1	0	1200
94	18	59	77	140	180	166	140	95	77	54	22	8	3	0	0	1039
95	19	57	59	149	136	146	139	86	75	45	33	6	2	1	0	953
96	16	45	56	118	130	125	110	77	55	25	11	5	1	0	0	774
97	13	40	44	108	134	126	99	67	46	29	10	5	1	0	0	722
98	14	108	135	373	339	358	310	210	138	85	46	18	6	0	0	2140
99	14	102	140	140	300	340	400	380	250	120	50	12	5	0	0	2253
99	14	100	150	200	340	500	480	410	320	197	69	9	5	0	0	2787
Totals	375	1172	1356	2836	3439	3587	3240	2398	1767	995	471	146	35	13	1	21831

Stage 2) (Continuation of table 9.5) Tabulation of the expected value of each cell. The expected value is given by:  $\frac{(\sum \text{row} \times \sum \text{column})}{\text{total}}$

	1	2	3	4	5	6	7	8	9	10	11	12	13	14	15
003	0 11	0 12	0 26	0 32	0 33	0 30	0 22	0 16	0 09	0 04	0 01	0 00	0 00	0 00	0 00
3 40	10 63	12 30	25 72	31 19	32 53	29 39	21 75	16 03	9 02	4 27	1 32	0 32	0 12	0 01	0 01
20 82	65 07	75 28	157 45	190 92	199 14	179 88	133 13	98 10	55 24	26 15	8 11	1 94	0 72	0 06	0 06
29 13	91 05	105 34	220 32	267 17	278 67	251 71	186 30	137 27	77 30	36 59	11 34	2 72	1 01	0 08	0 08
28 05	87 67	101 43	212 14	257 24	268 31	242 36	179 37	132 17	74 43	35 23	10 92	2 62	0 97	0 07	0 07
25 80	80 64	93 29	195 12	236 61	246 79	222 92	164 99	121 57	68 46	32 41	10 04	2 41	0 89	0 07	0 07
22 06	68 93	79 75	166 80	202 27	210 97	190 56	141 04	103 93	58 52	27 70	8 59	2 06	0 76	0 06	0 06
22 79	71 24	82 42	172 39	209 04	218 04	196 94	145 76	107 41	60 48	28 63	8 87	2 13	0 79	0 06	0 06
19 05	59 54	68 88	144 07	174 70	182 22	164 59	121 82	89 76	50 51	23 93	7 42	1 78	0 66	0 05	0 05
20 61	64 42	74 54	155 89	189 03	197 17	178 10	131 81	97 13	54 69	25 89	8 03	1 92	0 71	0 05	0 05
17 85	55 78	64 54	134 97	163 67	170 72	154 20	114 13	84 10	47 35	22 42	6 95	1 67	0 62	0 05	0 05
16 37	51 16	59 19	123 80	150 12	156 59	141 44	104 68	77 14	43 44	20 56	6 37	1 53	0 57	0 04	0 04
13 30	41 55	48 08	100 55	121 93	127 17	114 87	85 02	62 65	35 28	16 70	5 18	1 24	0 46	0 04	0 04
12 40	38 76	44 85	93 79	113 74	118 63	107 15	79 31	58 44	32 91	15 58	4 83	1 16	0 43	0 03	0 03
36 76	114 89	132 92	278 00	337 11	351 62	317 60	235 07	173 21	97 54	46 17	14 31	3 43	1 27	0 10	0 10
38 70	120 95	139 94	292 68	354 91	370 19	334 37	247 48	182 31	102 69	48 61	15 07	3 61	1 34	0 10	0 10
47 87	149 62	173 11	362 05	439 63	457 93	413 63	306 13	225 56	127 02	60 13	18 64	4 47	1 66	0 13	0 13

Stage 3) Calculation of the final Chi value. Each cell in the table below is represented by the following equation:  $\frac{(\text{OBSERVED VALUE} - \text{EXPECTED VALUE})^2}{\text{EXPECTED VALUE}}$ . The Chi value is obtained by summing the totals of each column

003	0 11	0 12	0 26	0 32	1 37	0 30	2 77	0 16	0 09	0 04	0 01	0 00	0 00	0 00	
1 70	7 01	10 38	1 76	0 25	7 35	0 07	0 14	0 57	11 03	5 23	0 08	22 67	0 12	0 01	
9 66	0 13	1 01	0 04	0 43	0 02	0 13	2 20	0 17	1 55	0 05	0 55	1 94	0 11	16 07	
17 95	12 66	0 00	0 10	0 10	0 16	0 24	3 17	2 99	0 36	0 05	2 82	1 09	3 92	0 08	
0 31	0 79	0 00	0 00	0 03	0 80	0 05	1 00	1 52	0 03	0 04	0 11	0 06	9 43	0 07	
3 28	0 09	0 03	2 03	4 17	1 20	0 87	7 85	0 02	4 98	4 01	1 56	2 41	0 01	0 07	
1 60	9 86	0 42	0 62	0 22	1 21	0 29	4 10	0 60	0 52	0 19	0 23	0 54	0 07	0 06	
1 19	0 07	0 14	11 55	2 75	0 56	1 13	0 65	3 88	1 19	0 01	0 09	0 60	0 79	0 06	
0 20	0 20	0 12	5 04	5 26	0 01	4 62	1 15	0 86	4 19	0 39	0 90	1 78	0 17	0 05	
11 49	0 01	2 81	19 48	2 11	2 72	4 43	1 90	4 17	1 38	2 40	1 14	0 60	0 11	0 05	
0 00	0 19	2 41	0 19	1 63	0 13	1 31	3 21	0 60	0 93	0 01	0 16	1 07	0 62	0 05	
0 42	0 67	0 00	5 13	1 33	0 72	0 04	3 33	0 06	0 06	7 53	0 02	0 15	0 33	0 04	
0 55	0 29	1 31	3 03	0 53	0 04	0 21	0 76	0 93	2 99	1 94	0 01	0 05	0 46	0 04	
0 03	0 04	0 02	2 15	3 61	0 46	0 62	1 91	2 65	0 46	2 00	0 01	0 02	0 43	0 03	
14 09	0 41	0 03	32 46	0 01	0 12	0 18	2 67	7 16	1 61	0 00	0 95	1 92	1 27	0 10	
15 77	2 97	0 00	79 65	8 50	2 46	12 88	70 96	25 09	2 92	0 04	0 62	0 53	1 34	0 10	
23 97	16 46	3 09	72 53	22 34	3 87	10 65	35 24	39 52	31 22	1 31	4 98	0 06	1 66	0 13	
totals of each column															
102 23	51 93	21 88	236 02	53 58	23 19	38 02	143 01	90 95	65 51	25 27	14 24	35 49	20 85	17 01	939 1

CHI VALUE = 939.17 Sample S1B1

**Table 9.6:** Tabulation of Chi-Square values derived from samples tested under uni-axial compression. Data is derived from samples loaded until specimen failure.

Sample No.	Chi Value	Sample No.	Chi Value
S1A7	955.793	S1A1	415.23
S2A1	275.6953	S1A3	617.6507
S2A2	259.3458	S2A3	344.4121
S2A4	200.7832	S2A6	235.9487
S5A2	683.086	S4A1	302.0026
S5A3	521.7884	S4A2	482.1003
S5A4	301.431	S4A3	398.4427
S5A6	215.645	S4A4	225.7472
S5A7	362.9799	S4A6	412.8208
S5A8	498.0728	S5A1	255.6927
S6A1	324.3608	S5A5	302.7413
S1B1	939.1749	S5A9	363.5003
S1B2	303.2818	S9C1	659.8301
S1B3	250.5244	S9C2	1068.189
S6B1	291.5892	S9C5	583.1594
S1C1	837.2954	S9C6	1916.26
S1C2	818.6813	S9C7	386.3682
S1C3	239.755	S9B1	304.389
S1C4	367.8687	S9B2	574.8812
S7C1	190.8142	S9B3	350.9731
S1D1	361.6051	S9B4	1198.084
S1D2	273.3638	S9B5	837.3067
		S9BC1	678.7286

Figure 9.21: Contour diagram and three dimensional isometric view displaying the number of events with respect to time difference and amplitude for sample type "B" potash rock.

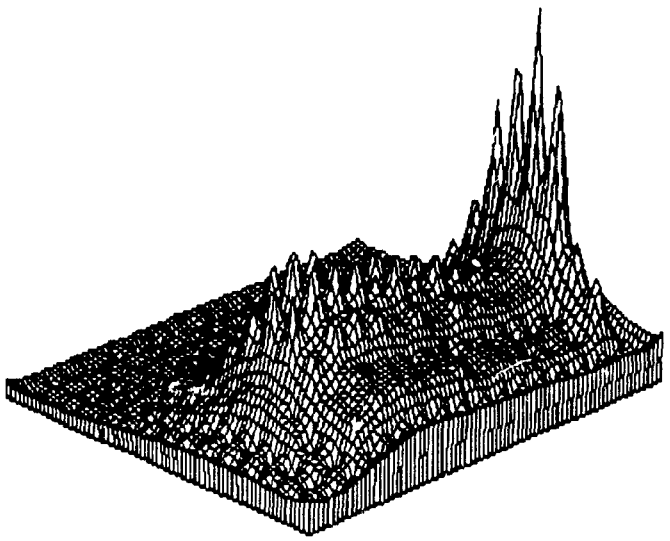
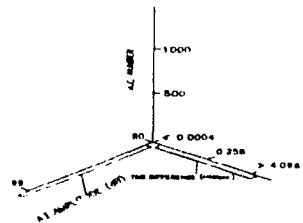
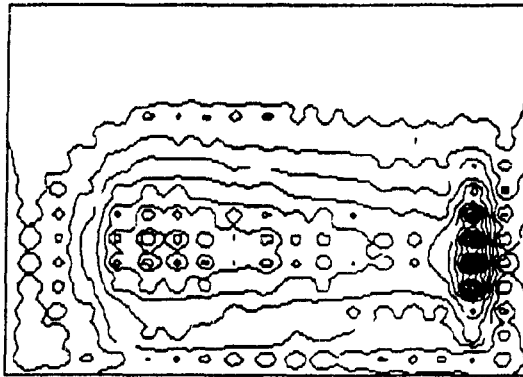
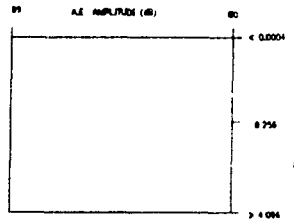


Figure 9.22: Contour diagram and three dimensional isometric view displaying the number of events with respect to amplitude and event duration for sample type "B" potash rock.

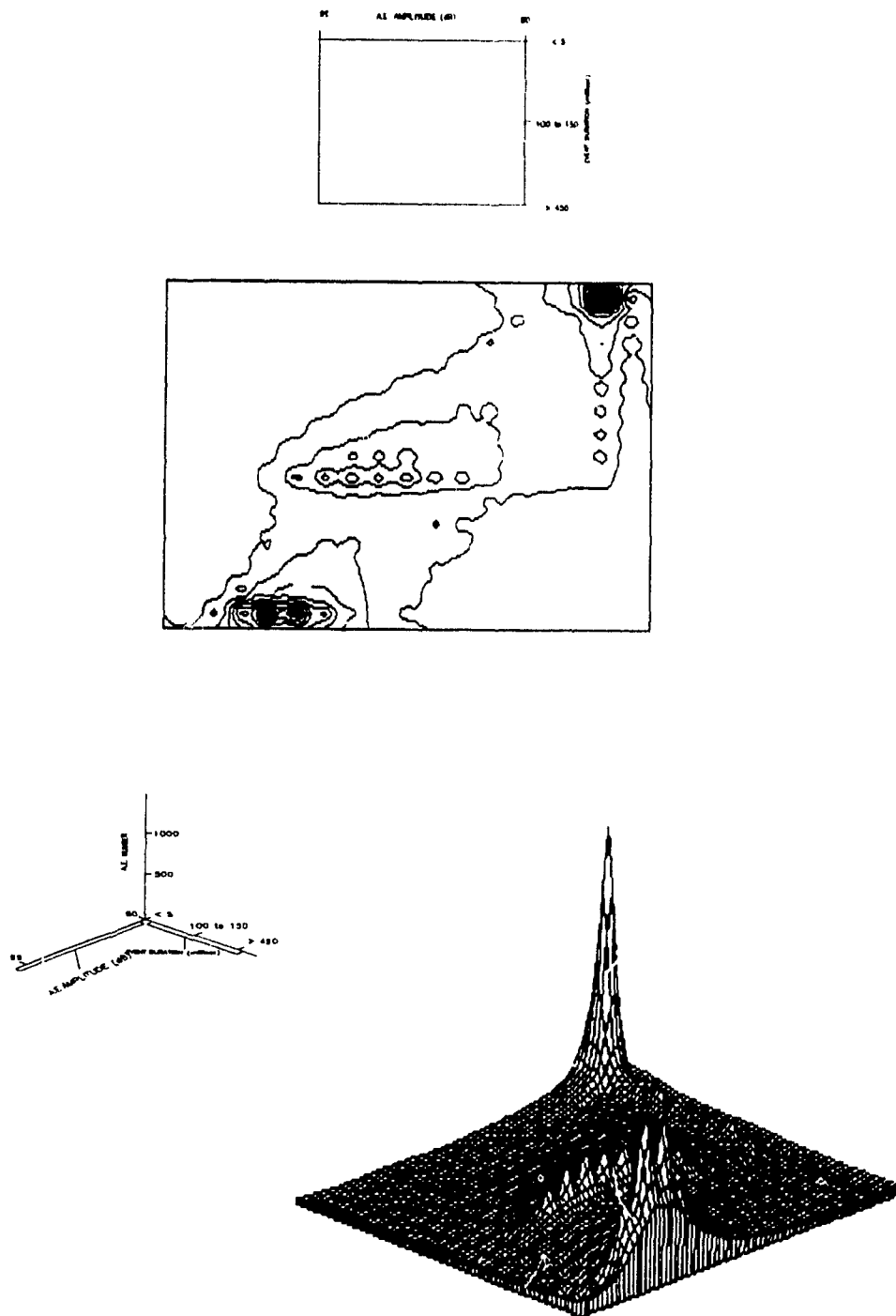


Figure 9.23: Contour diagram and three dimensional isometric view displaying the number of events with respect to energy and time difference for sample type "B" potash rock.

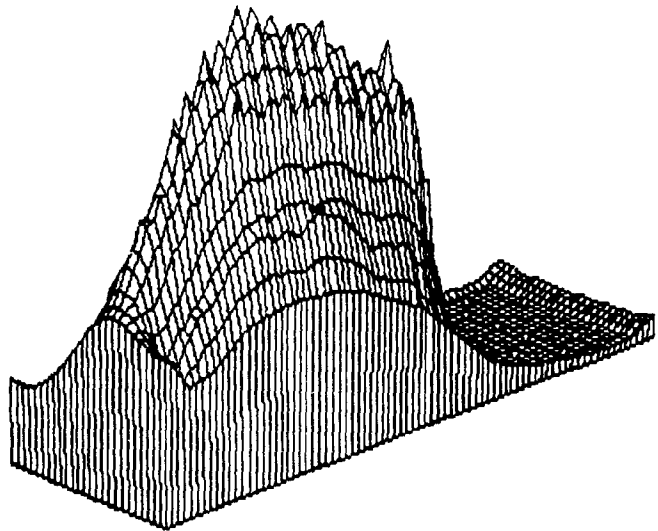
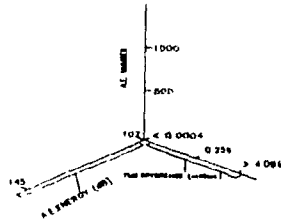
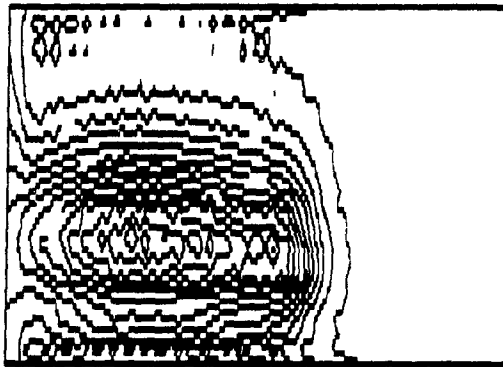
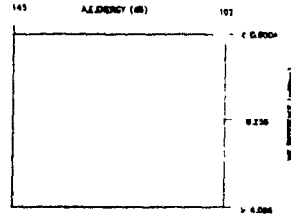
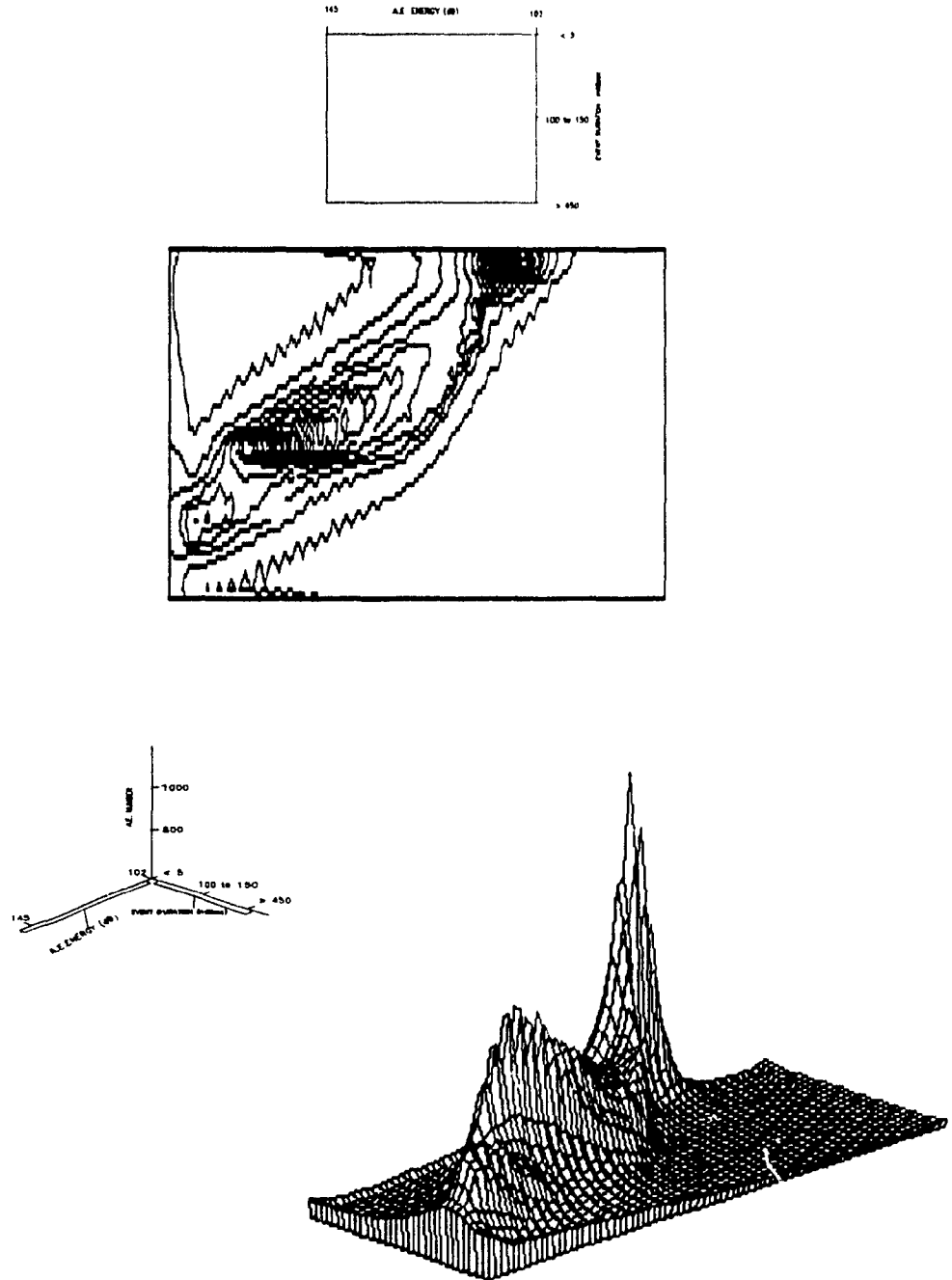
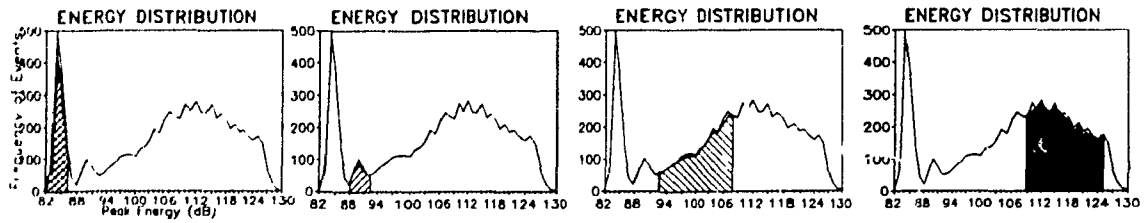


Figure 9.24: Contour diagram and three dimensional isometric view displaying the number of events with respect to energy and event duration for sample type "B" potash rock.

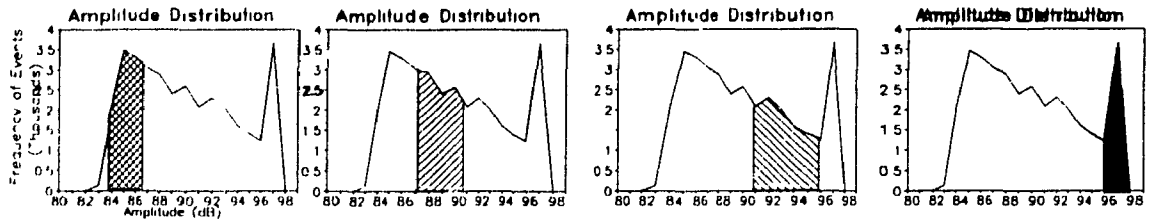


**Table 9.7: Summary displaying the relationships of amplitude, energy to time difference and event duration of acoustic emission events.**

BASED ON AMPLITUDE -- EVENT DURATION RELATIONSHIP



BASED ON ENERGY -- EVENT DURATION RELATIONSHIP



**1**  
**LOW ENERGY**  
**SIGNALS**

**2**  
**LOW-MODERATE**  
**ENERGY SIGNALS**

**3**  
**MODERATE TO**  
**HIGH ENERGY**  
**SIGNALS**

**4**  
**HIGH ENERGY**  
**SIGNALS**

-low amplitude events  
-(75 to 81 dB)  
-dominant in the pre-elastic stage

-low-moderate amplitude events  
-(83 to 91 dB)  
-steady rate present in the elastic stage  
-trending to increase near the elastic limit

-moderate amplitude events  
-(90 to 96 dB)  
-low but steady rate up to the elastic limit  
-increase at the elastic limit, and peaking at specimen failure

-high amplitude events  
-(96 dB < )  
-high steady rate within the plastic range and specimen failure

-A R very low, indicative of large amount of low ampl signals  
-low event duration (10 to 40 millisecc)  
low energy events

-A R increasing, but still dominated by low amplitude signals  
event duration between 150 to 250 millisecc  
generating signals of moderate energy

-A R moderately high, dominated by higher amplitude signals

-A R very high, high amplitude signals are generated near or at specimen failure  
-long event durations (250 to 450 millisecc and greater)

AMPLITUDE - TIME DIFFERENCE

-low time difference (0.016 to 0.032 millisecc)  
-high concentration of events

-low time difference (0.016 to 0.032 millisecc)  
-low concentration of events

-low time difference (0.016 to 0.032 millisecc)  
-low concentration of events

-range spanning from 0.0008 to 1.024 millisecc  
-high concentration of signals

ENERGY - TIME DIFFERENCE

-same concentrations as Amp-t-diff relationships

## **Fractographic Analysis of Potash Rock Loaded Under Uniaxial Compression**

### **10.1 Introduction**

The purpose of this section is to identify and classify microfracture development of potash rock loaded under uniaxial compression. A distinction is made between the various types of microfracturing phenomena observed in potash rock.

Deformational features observed in potash rock, resulting from uniaxial compression, can be explained by fracture processes. Evidence of these features can be sighted via optical and electron microscopy. Laboratory tests have also been conducted on specimens loaded to pre-defined stress levels in order to define these features [Fonseka et al. (1985), Kranz (1979), Montoto et al. (1984), Olsson and Peng (1976) and Tapponier and Brace (1976)]. These authors have developed a criteria used to interpret the nature and progressive development of microfractures by various mechanism.

This chapter is divided into three parts which will present the scheme utilized to organize the history of fracture development in potash rock into a sequential system.

The first part will introduce a classification scheme for fracture development in potash rock. This scheme incorporates various aspects of fracture development in potash rock into a systematic description. The fracture development stages are described with respect to increase in uniaxial load. Similarities as well as differences in terms of fracture development exist in all four types of potash rock.

The second part will present a thorough description of the fracture processes present in potash rock. Based on the criteria of the second part, the third section will organize the stages of fracture development and their interactions into names with respect to increasing uniaxial load on the samples.

### **10.2 Classification**

The criteria used to interpret the nature and development of microfractures has been explained based on several fracture descriptions tabulated in table 10.1. A microcrack by definition is any cavity within the rock that can not be seen without a microscope and that has an aspect ratio (cavity width divided by cavity length) of less than 0.05. Any cavity with a larger aspect ratio is considered to be a pore [Kranz (1979)].

Based on the categories shown in the table 10.1, a classification scheme has been devised. In order to avoid confusion with the nomenclature, the name based on the classification incorporates four elements.

The first element in naming the fracture incorporates the stress level at which the crack is observed. Bieniawski (1967) also observed crack development with respect to the stages of the load cycle under which the specimen was subjected. There are four regions or stages along the stress-strain curve for potash rock. These sections correspond to the preload, elastic, plastic or strain hardening region, and to the failure region. Figure 10.1 is a graphical representation of a stress-strain relationship of potash rock loaded under uniaxial compression. Figure 10.1 also shows the points on the stress-strain curve along which fractographic studies have been implemented to observe the fracture development corresponding to these four regions. A subdivision of the name of each stage has also been used in order to compensate for the progression of the development of any particular type of identified fracture. The progression of each crack with respect to its stage in the load cycle is identified as 'a', 'b', 'c' and 'd'. Stage 'a' corresponds to the earliest stage in the load cycle and 'd' the most advanced. The addition of the letter as a suffix is also indicative of the current stage of the crack's activity.

The second element in naming a fracture uses the location of the crack with respect to the textural position in the rock. Three groups are possible, transgranular cracks which run from grain boundaries or may transect an entire grain; intracrystalline cracks which begin and terminate totally within a grain and intercrystalline cracks which run over grain boundaries [Kranz (1979)].

The third element in naming the fracture identifies if the crack is a HARC or a LARC. Sprunt and Brace (1974) chose an aspect ratio of 0.1 as a value which separates high aspect ratio cavities (HARCs) from low aspect ratio cavities (LARCs). Other synonyms will be used if neither a HARC or LARC are applicable. These include names such as shear cracks, tension cracks and cleavage cracks.

### **10.3 Crack Classification**

#### **10.3.1 Stage 1a HARC - LARC**

Stage 1 designates the region along the stress-strain curve which corresponds to the pre-elastic stage of the load cycle. It is defined by closure of the intergranular pore space.

Two-dimensional low aspect ratio and high aspect ratio cracks are observed along the intergranular areas of the mosaic. The grain boundary is considered as a LARC and the triple junctions as HARCs. They display a decrease in the pore space of the rock. Under high magnification; detrital material, authigenic clay minerals and

red oxide grains occur as small compressed packets located within the grain boundary regions. These individual particles range in size from 4 microns to 100 microns. The grain boundary cracks range in widths from 10 microns to 1 mm and transect the length of the grain (refer to figures 10.2 and 10.3).

The density of these particles varies vertically within an individual sample and between various types of potash. In types "A" and "D" potash rock, the clay particles are found only partially cemented to adjacent walls of diagenetically altered sylvite and halite. However, their concentration is low. Types "B" and "C" display high concentration of these materials along the intergranular regions. When compressed under uniaxial load, the latter two types form sheaves of smaller LARCs and HARCs entirely enclosed within the grain boundary regions.

Stage 1b HARCs and LARCs are continually compressed within the elastic region of the stress-strain curve. These were identified due to the lack of new crack development along the grain boundary regions.

#### **10.3.2 Stage 2a Intercrystalline LARC A and B**

Stage 2 cracks originate within the early stages of potash samples loaded under uniaxial compression.

There are three types of stage 2a cracks: the stage 2a intergranular LARC A, the stage 2a intergranular LARC B and the stage 2a intergranular HARC. Cracks are initiated along the intergranular flaws. These result from the extension and sliding of intergranular space evident by the offset of adjacent grain boundary walls. The face of the walls are irregular to rough, intermingled with displaced material along the grain boundary areas.

The subclass 'a' is represented for cracks at the early to progressive stages within the loading cycle of the elastic region. These cracks progress by length and size within the onset of the plastic region. These are now designated as subclass 'b'. These cracks are also one of the sources of the development of transgranular cracks.

The first type designated as LARC A constitutes the initiation and the development of cracks located along the intercrystalline grain boundary regions. This is the dominant type of crack development observed in types "A" and "D" potash rock. The cracks have the appearance of long thin partially filled to unfilled openings of constant cross section. The crack pattern is continuous throughout the length of the samples. These cracks are also observed to form at low angles with respect to axial load, thus containing a diagonal to vertical orientation. The cracks conform to the shape of

the grain boundary. In type "A" potash rock, they range in length from 5 to 15 mm and in width from 50 to 500 microns. They typically match the vertically elongated lengths of the crystal grains predominantly in samples displaying a longitudinal anisotropic crystalline mosaic (refer to figures 10.4 and 10.5).

Similarly, type "D" potash rock displays intercrystalline cracking. A distinction between the two types of potash rock can be seen in that the cracks do not propagate throughout the entire length of the specimen in both types. Type "A" potash rock consists of an anisotropic texture along which intergranular cracks develop along vertically elongated grains. Type "D" potash rock displays a homogeneous crystalline mosaic. The lengths of the cracks in type "D" potash rock range from 1 to 5 mm, which represents approximately one half the average grain lengths.

Stage 2a intergranular LARC B displays similar crack morphology as the 'A' class. The distinction lies in that there is a high concentration of clay material located along the grain boundaries. Crack development along these areas coincides with the granulation of clay material and local loss of cohesion with adjacent grains. This is not the dominant type of fracturing. High magnification of the grain boundary region reveals sheaves of cracks that are entirely developed within the clay. Cracks are considered as a single grain boundary LARC due to the geometry of the crack observed under low magnification. The cracks are approximately one half the grain lengths and 30 to 200 microns in width.

The third variety of cracks apparent within this region of the loading cycle is referred to as the stage 2 intergranular HARC. These cracks are located along triple junctions of a crystalline mosaic. They consist of jagged adjacent grain faces, usually composed of a vertical to sub vertical LARC terminating along a subhorizontal face of a third grain. The triple junction along which the HARC is formed consists of halite and sylvite grains. The cracks range in diameter from 150 microns to 0.5 mm.

The LARCs form from a mode I extension and mode II sliding. Cracks terminating at a grain boundary often form a mode I activated HARC. The displacement between two adjacent grains against a third produces this HARC. Mode II and mode III are apparent by the shear displacement and rotation of intergranular material. Also, the orientation of jagged and broken grain boundary faces is an indication of the strain (refer to figure 10.6).

### **10.3.3 Stage 3a Intracrystalline LARC and Stage 3a Transgranular A, B and C Crack**

Stage 3 defined via the stress strain-curve is divided into two distinct regions: 'a' and 'b'. The stage 3a consists of a late elastic stage which progresses to the elastic limit and onto the onset of the plastic stage. Stage 3b is designated as the progressive plastic stage of deformation. Each region shows a change in the development of fracture growth.

There are two principal types of fracture development present within stage 3a. These include stage 3a transgranular cracks which are subdivided into types 'A', 'B' and 'C' and secondly, stage 3a intracrystalline LARCs.

In the early regions of stage 3b crack development, three types of cracks can develop within intracrystalline regions. These include stage 3b intracrystalline LARC, stage 3b fractures along cleavage planes and transgranular cracks which propagate through intragranular clay matrix and crystal grains. The cleavage cracks can propagate in two ways. These are referred to as stage 3b Cleavage A, Link A or Link B.

In the late stages of 3b, three types of transgranular crack interactions and shear cracks can occur. The former type includes stage 3b transgranular 'A', 'B' or 'C'. The shear cracks are subdivided into classes 'i' and 'ii'. Each type is defined by its location and geometric pattern along which it propagates through the material.

The stage 3a transgranular A cracks are produced by interacting intergranular cracks originated from stage 2. The 'B' subgroup represents transgranular cracks composed of interlinked intergranular-intragranular stage 2 cracks. The intragranular cracks are formed from cleavage cracks and irregularly shaped intragranular cracks. The final subgroup 'C' represents linkages between transgranular 'A' and 'B' with tectonic LARCs observed in some samples of the type "B" and "C" potash rock (refer to figure 10.8).

For stress levels up to the early plastic stage, new cracks appear to form continuously with increasing stress levels. Within potash rock types "A" and "D", the stage 3a transgranular crack dominates the development of fractures. The cracks emanate from a high angle interface of two adjacent grain boundary cracks and propagate at an acute angle to the direction of uniaxial load. Most grain boundaries whether at high or low angles are continuously cracked in a similar process. The cracks die out

with sharp ends along the grain boundary regions. Vertically oriented grain boundary areas and stage 2 intergranular LARCs are the structural flaws inducing this type of fracture development.

Most cracks form between 1.50 to 3.0 cm in length. The average cracks link between 2 to 4 adjacent grains. The crack density varies for different types of potash rock. Type "A" potash rock displays a regular transgranular fracture development in a direction parallel to load. Type "D" potash rock shows a moderately lower fracture density and a more irregular pattern oriented at higher angles to the direction of load. The latter ranges in length from 0.50 to 1.50 cm and shows an average linkage of 2 to 3 grains.

Stage 3a transgranular B crack is dominant in types "B" and "C" potash rock. In general, these cracks appear to develop by linkages of stage 2a and b intergranular LARCs and a new type of crack developed within stage 3 prior to, and during the transgranular crack development (identified as stage 3a Intracrystalline LARC). Cleavage and irregular LARCs form at oblique and at angles perpendicular to adjacent grain boundary regions of sylvite crystal grains.

In type "B" potash rock, the cracks can generally propagate 2 to 4 grain lengths. The cracks are generally oriented parallel to the load direction but display irregular trends due to their jagged appearance. The sudden change in direction of the transgranular crack is due to stage 2 intergranular LARC and passage through cleavage of sylvite porphyroblasts. The crystallographic orientation of sylvite grains is variable thus producing cleavage cracks in various directions. Serrate crack tips indicate termination of crack propagation.

Stage 3a transgranular C crack consists of interlinked tectonic LARCs interacting with intergranular and intracrystalline cracks from stage 2 and stage 3a respectively.

Inherent tectonic LARCs are cracks observed in some samples of types "B" and "C" potash rock. They appear as short regular shaped vertically oriented cracks evenly distributed throughout the specimen. They are approximately 0.3 to 2.0 cm in length with an average length of 0.71 cm, and a width ranging from 50 to 350 microns. They are not controlled by the texture or structure of the rock. They are possibly developed due to induced stresses activated during drift excavation.

Stage 3a transgranular C cracks also display slight trend irregularities in some of the cracks due to intermediate deviations of cracks through intracrystalline LARC cleavage cracks across sylvite grains. At this stage of the load cycle, the cracks range in length from 1 to 3 cm and display an average width of 400 microns.

The development of all the three types of transgranular cracks are induced by stage 2 cracks and flaws in the structure of the rock. The cracks progress in size with increasing load and are a prelude to the failure crack trends.

The formation of these cracks are primarily due to mode II and mode III fracture movements. The crack propagation direction, which produces the transgranular link, is developed due to local maximum tensile stress field surrounding the crack tips.

The crack development imposed by tectonic LARCs is due to mode I and mode II displacements. Also, interaction between the cracks resulting in transgranular type C cracks are produced by 'en-passant' and 'en-echelon' crack interactions. The 'en-echelon' crack interaction is the dominant type of crack observed due to crack distribution in the rock. Tensile linkages are a result of the 'en-echelon' array directed at an acute angle to the applied stress and shear linkages. The tensile linkages are in a vertical to near vertical direction as noted far more frequently as cracks branch and grow towards the maximum stress direction.

#### **10.3.4 Stage 3a Intragranular-Intracrystalline LARC**

Stage 3a intragranular-intracrystalline LARC type is more frequently observed at the 'b' stage of the three subdivisions of stage 3 loading cycle. They are also apparent in the 'a' stage, predominantly in potash rock types "B" and "C".

Stage 3a intragranular-intracrystalline LARC consists of straight microcracks hosted by sylvite grains. They have tapered ends and are oriented perpendicular to the grain boundary. The sylvite grains are generally adjacent to halite grains or clay matrix. The cracks form subparallel sets, all of which have approximately the same dimensions and planar orientation. They are generally restricted to development along cleavage planes and occasionally observed along glide planes of the grain. They are initially 10 to 100 microns in length (refer to figure 10.9).

The development of these cracks can be explained by the mismatch of elastic stiffness at the interface between sylvite, halite and/or clay, which induce high tensile stresses in the grains of higher stiffness. Such grains will be more densely cracked than those surrounded by grains of equal stiffness values.

### **10.3.5 Stage 3b Intragranular-Intracrystalline LARC**

Stage 3b is a region on the stress-strain curve represented from the progressive plastic stage to the advance plastic stage. Stage 3b intragranular- intracrystalline LARC are fractures that are initiated from within the crystal grain and are oriented perpendicular to the periphery of the grain. The crack propagates inward and across the grain. They are also found in samples loaded as early as the elastic limit and are directly a result of stage 3a transgranular B cracks.

These cracks are also found to occur in sylvite grains in samples containing a high concentration of sylvite and clay. They occur within halite grains, however in halitic rocks the fractures tend to occur at a later stage, and in this case stage 3b. These crack types appear in type "B" and "C" potash rock at stage 3a. Several crack configurations and interactions are also observed. Each one will be described individually in the following sections.

### **10.3.6 Stage 3b Intracrystalline LARC**

This is the progressive stage of stage 3a intracrystalline LARC. It has the same characteristics as the cracks observed in stage 3a, but their initial development is more commonly observed at this stage of the load cycle for potash rock types "A" and "D" and, occasionally "C".

These cracks form irregular cracks and short vertical intragranular cracks along cleavage planes. They occur in multiple sets located perpendicular to the periphery of the grain boundary. They are not fracturing through the fluid inclusions thus not affected by the intracrystalline fluid inclusion structure of the grains.

The cracks range in size from 100 microns to 2mm and are approximately 10 to 1750 microns apart. The cracks form at an acute angle to the load along regular planer flaws. These cracks promote various other types of microcrack and crack interactions. These cracks are observed in type "A" potash within halite grains. They are located in sylvite porphyroblastic grains in type "B" potash where they are spaced 2 to 5 mm apart. They are also observed within anhedral sylvite grains in types "C" and "D" potash rock. Type "D" potash rock also contains these cracks in halite grains (refer to figures 10.10a and 10.10b).

#### **10.3.6.1 Stage 3b Cleavage A**

Stage 3b cleavage A cracks are developed through crack interactions along cleavage (001) of sylvite and halite grains. They form parallel crack sets which are

interlinked by short perpendicular linkages usually along cleavage or another irregular plane. These are formed by two types of crack interactions mainly, 'en-echelon' and 'en-passant' crack interactions. The linkages are not promoted by pore structures within the grain. The major crack sets are planer in shape and are observed to occur along the same planer orientations as those observed by scanning electron microscopy (S.E.M.) along a crack surface. The linkages are described as follows:

#### **10.3.6.1.1 Stage 3b Link A**

The stage 3b link A crack is observed as (001) cleavage cracks oriented perpendicular to the major stage 3b cleavage A crack sets. They produce the multiple step pattern accomplished by a screw dislocation mode of deformation. The steps range in length from 800 microns to 1mm and are located between parallel sets of stage 3b cleavage A crack sets (refer to figure 10.11).

#### **10.3.6.1.2 Stage 3b Link B**

This is the second variation of linkage cracks produced by crack interactions. The stage 3b link B produces a cleavage step. The crack is parallel to the direction of crack propagation and perpendicular to the crack plane in which a twist boundary is present at an acute angle. Merging cleavage steps are produced along major cleavage planes transecting the diameter of the grain. This effect results in the formation of branching cleavage cracks. As observed, merging of the steps dictates the direction of crack propagation. This evidence shows that all cleavage cracks originate at the grain periphery (refer to figure 10.12).

In types "B" and "C" potash rock, the cracks linking the general crack sets occur within sylvite grains. The linkages are also longer ranging from 50 microns to 2 mm. A secondary cleavage linkage set present within the same grain can link up with similar crack interacting sets located at another section of the same grain but oriented along cleavage or glide planes. The linkage occurs along an oblique plane oriented along a possible shear plane.

The development of cleavage tongues can also be observed [Ewalds et al. (1984), Knott et al. (1973)]. These are apparent in sylvite porphyroblasts of type "B" potash rock. They are observed to form a deflection of the crack plane along a cleavage due to a solid inclusion. The inclusions are normally composed of solid crystalline inclusions or relic diagenetically altered clay globules hosted by sylvite. The crack is observed along an irregular plane, oriented at an oblique angle between two cleavage crack surfaces. They have an average surfacial width of 1mm.

### **10.3.7 Stage 3b Crack Development**

Stage 3b crack development coincides with the advanced plastic stage along the stress-strain curve. This stage is composed of various types of grain scale, crack interactions involved with the progression of transgranular crack development. These include the following: stage 3b transgranular A, stage 3b transgranular B and stage 3b transgranular C.

The distinction of crack characteristics in the 'b' stage in relation to the 'a' stage, comprises the coalescing of transgranular cracks.

It is also observed that the stage 3b intracrystalline A LARC and the stage 3b intracrystalline LARC are longer in length. Finally, a new third crack type is observed, at load ranges prior to specimen failure, classified as stage 3b shear cracks, with subclasses 'i' and 'ii'.

#### **10.3.7.1 Stage 3b Transgranular A**

The stage 3b transgranular A cracks are the progressive state of its predecessor. They consist of intergranular cracks linking through several grain lengths, the average linkage being three to four grains. These cracks are the dominant type observed in type "A" potash rock occupying 60% of the total crack population at this stage of the load cycle. The cracks also range in width from 1 to 2mm. They are straight, and only deviate slightly with respect to the grain boundary flaws of preceding grain structure (refer to figure 10.13).

#### **10.3.7.2 Stage 3b Transgranular B**

Stage 3b transgranular B cracks are also the progressive stage of transgranular cracks produced in the 'a' stage. The cracks consist of linkages of grain boundary cracks merging with intracrystalline cleavage cracks. The degree of crack lengths ranges from 2 to 6 grain lengths. Their size is dependent of the sample type and sylvite content. It is the dominant type of fracture observed in the types "B" and "C" potash rock. The cracks, in both these types of potash rock, are irregular and continuous. Irregularity in the trend is observed by the deviation of the crack from intergranular locations to cleavage planes. The degree of cleavage cracking varies from specimen to specimen. The variation is usually less than the degree of intergranular cracking for sample types with less than 15% of sylvite. Cleavage cracks are located in sylvite grains and are arrested by granoblastic clusters composed of a halite mosaic or clay

seam structure. The intergranular cracks were less easily terminated (usually 3 to 6 facets in length), only being halted when reaching a strong triple junction or clay seams.

#### **10.3.7.3 Stage 3b Transgranular C**

Stage 3b transgranular C crack consists of stage 3a and 3b tectonic LARCs, which progressively developed into stage 3a transgranular C. These cracks are predominantly observed in type "C" potash rock. The linkages consists of several stage 3a transgranular C cracks possibly produced by 'en-passant' crack interactions as observed by their orientation. They range in size from 1 to 4 cm at this stage in the load cycle. The trend of the group representing the sample distribution of these cracks is of regular, straight and vertical orientation, forming multiple parallel crack sets. The crack density is dependent on the initial percentage of the tectonic LARCs present in the sample, as much as 60% in some cases (refer to figure 10.13).

#### **10.3.8 Stage 3b Intracrystalline A and B LARCs**

Stage 3b intracrystalline A and B LARCs are cracks located within the sylvite crystal grains generally along cleavage A or along irregular planes B. These cracks are extensions of earlier stage 3a intracrystalline LARCs. They are larger, they propagate through the diameter of the grain accompanied by adjacent subparallel sets of similar cracks, and in many cases interact with each other (refer to figure 10.14).

These cracks occur near sample failure. They often link to form branching patterns extending the length of the grain and ranging in width from 50 microns to 2mm. These cracks are regular and straight in appearance, displaying constant cross sectional width, with long narrow tapered ends located adjacent to grain boundary flaws.

This crack type is typically observed in type "B" potash rock within sylvite porphyroblasts forming several sub-parallel sets of cracks along cleavage. They are less frequently observed in types "C" potash rock and sparsely in types "A" and "D". The latter two types display this crack formation as singular cleavage cracks transecting anhedral interstitial sylvite.

Most of these cracks appear to form by mode II mechanism. The cracks are oriented at low angles to the uniaxial load. They are also characteristically planer and regular in shape.

### **10.3.9 Stage 3a and b Shear Cracks (subclasses 'i' and 'ii')**

Stage 3a and b shear cracks (subclasses 'i' and 'ii') are cracks developed by simple shear deformation of the crystalline mosaic, at load levels just prior to failure of the specimen.

The result is the development of crack openings produced by tension in mode I, coupled with shear in mode II. The crack ends are oriented subparallel to the direction of applied load with subhorizontal crack openings. The ends are sharp with the middle portion displaying an opening with constant widths. These cracks can be observed within individual grains, subclass 'i', while subclass 'ii', cuts the structure and texture of the rock arbitrarily (refer to figure 10.15). The subclass 'i' displays jagged edges along with opposite faces comprising oblique cleavage of the grain. These are typically observed in type "A" potash rock within elongated halite grains. In type "B" potash rock these are smaller and found in sylvite porphyroblasts and, in type "C" they are found in both halite and sylvite grains. Subclass 'ii' are found in potash rock types "A", "C" and "D".

These fractures are sparsely distributed and both subclasses can be observed to occur within the same sample.

### **10.3.10 Stage 4 - Failure Crack Characteristics**

Stage 4 of the stress-strain curve coincides with the uniaxial compressive strength of the sample or the maximum stress the sample can attain. All samples tested display failure along longitudinal splitting (sheeting) which extends from 50% to 70% of the length of the specimen. At failure, the various types of transgranular cracks coalesce to produce various types of macroscopic interactions.

Failure is affected by flaking of longitudinal pieces of rock material. These fracture off evenly over the circumference and generally along the central location of the sample. The result produces samples shaped as double ended cones. Under microscopic scale, macroscopic shear fractures are observed. Cracking adjacent to these fractures produce cataclastic granulation. At high enough strain levels, faults are produced causing loss of cohesion. This is generally observed in samples containing a high concentration of interstitial clay. Individual crystal grains are shattered by the formation of multiple cleavage cracks in all three directions.

Variation occurs in the fracture pattern between the four types of potash rock. The fractures are generally symmetrically distributed around the circumference of the specimens. The dominant fracture characteristics along which failure occurs are observed to be either one of the transgranular fracture developments of prior stages.

Type "A" potash rock fails along coalescing stage 3b transgranular A cracks, with an almost vertical alignment of crystals. Displaying an anisotropic form of failure characterized by flaking failure (refer to figure 10.17).

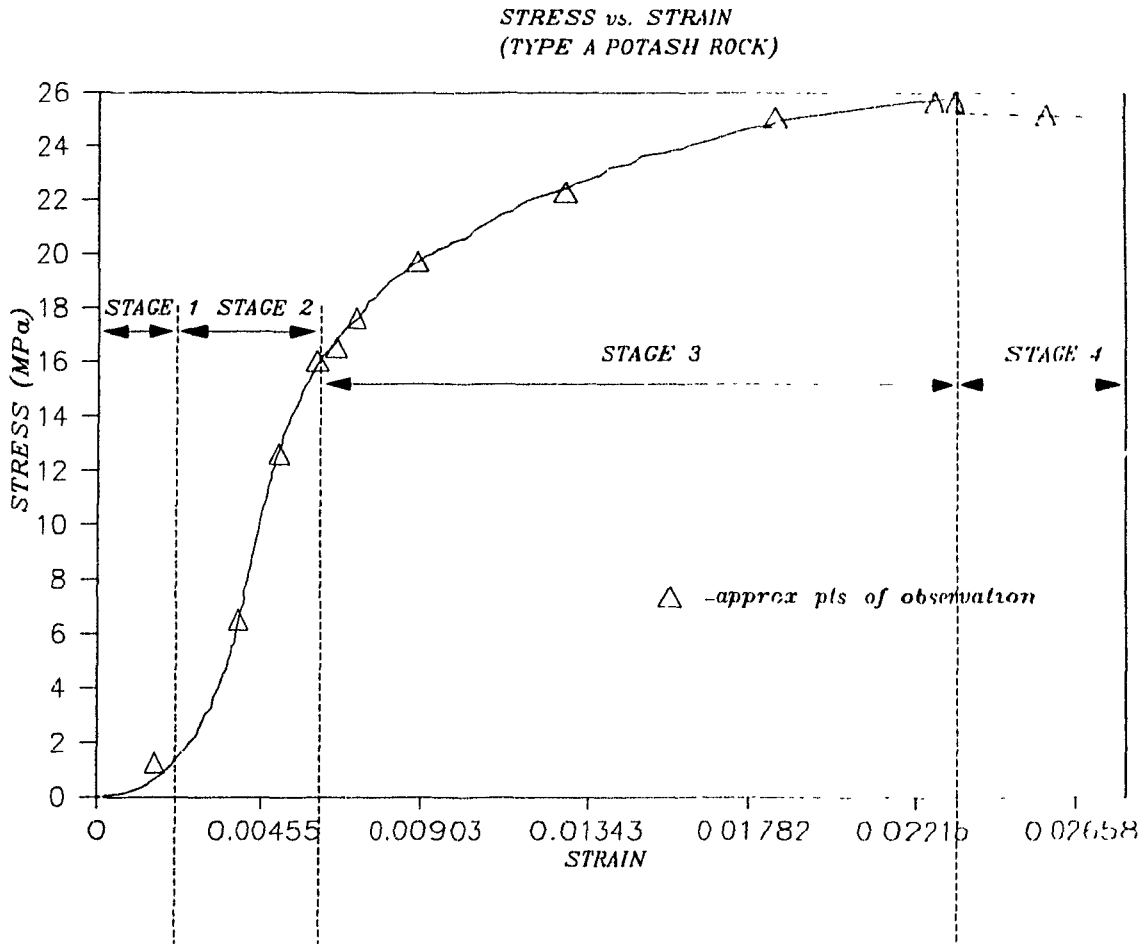
Types "B" and "C" potash rock are characterized by stage 3b transgranular B fracture patterns. Some type "C" potash rock samples also display transgranular C fracture patterns (refer to figure 10.16).

Finally, type "D" potash rock failure is characterized by stage 3b transgranular A and transgranular B crack patterns (refer to figure 10.17).

**Table 10.1 Summary of classification scheme of cracks observed in potash rock loaded under uniaxial compression.**

LOAD STAGE	PROGRESSIVE DEVELOPMENT OF CRACK TYPE	NAME OF CRACK	SUBCLASS DIVISION OF CRACK
(based on Stress Strain Curve)	(Progression of crack development to next stage in the load cycle)	(characteristic name of crack)	(textural suffix added to name)
<b>1</b>	<b>A</b>	Intercrystalline LARC Intercrystalline HARC Intergranular LARC	
	<b>B</b>	Intercrystalline LARC Intercrystalline HARC Intergranular LARC	
<b>2</b>	<b>A</b>	Intercrystalline LARC Intercrystalline HARC	
	<b>B</b>	Intercrystalline LARC Intercrystalline HARC Transgranular Tension Crack	
		Shear Crack	i - structure restricted to single grain ii - structure cross cutting crystalline mosaic
<b>3</b>	<b>A</b>	Intracrystalline LARC	A - crack along cleavage B - irregular crack
		Transgranular	A - intercrystalline to intercrystalline
			B - intercrystalline to intracrystalline
			C - intercrystalline to intracrystalline to tension cracks
	<b>B</b>	Intracrystalline LARC	A - crack along cleavage B - irregular crack
		Transgranular	A - intercrystalline to intercrystalline
			B - intercrystalline to intracrystalline
			C - intercrystalline to intracrystalline to tension cracks
<b>4</b>	Shear Cracks		
	Transgranular		
	Cataclastic (Cleavage, Intragranular, Shear plane)		

Figure 10.1: Definition of the stages of crack development and positions along which samples were observed on the stress-strain curve.



**LEGEND:**

- stage 1    pre-load adjustment
- stage 2    elastic region
- stage 3    plastic range / strain hardening region
- stage 4    failure and post-failure region

Figure 10.2: S.E.M. microphotograph of stage 1a HARC and LARC under moderate magnification, grain boundary junction consisting of intergranular clay particles.



**Figure 10.3:** S.E.M. microphotograph of stage 1a HARC and LARC under higher magnification , the shape of the particles are indicative of agglomerate clay material.

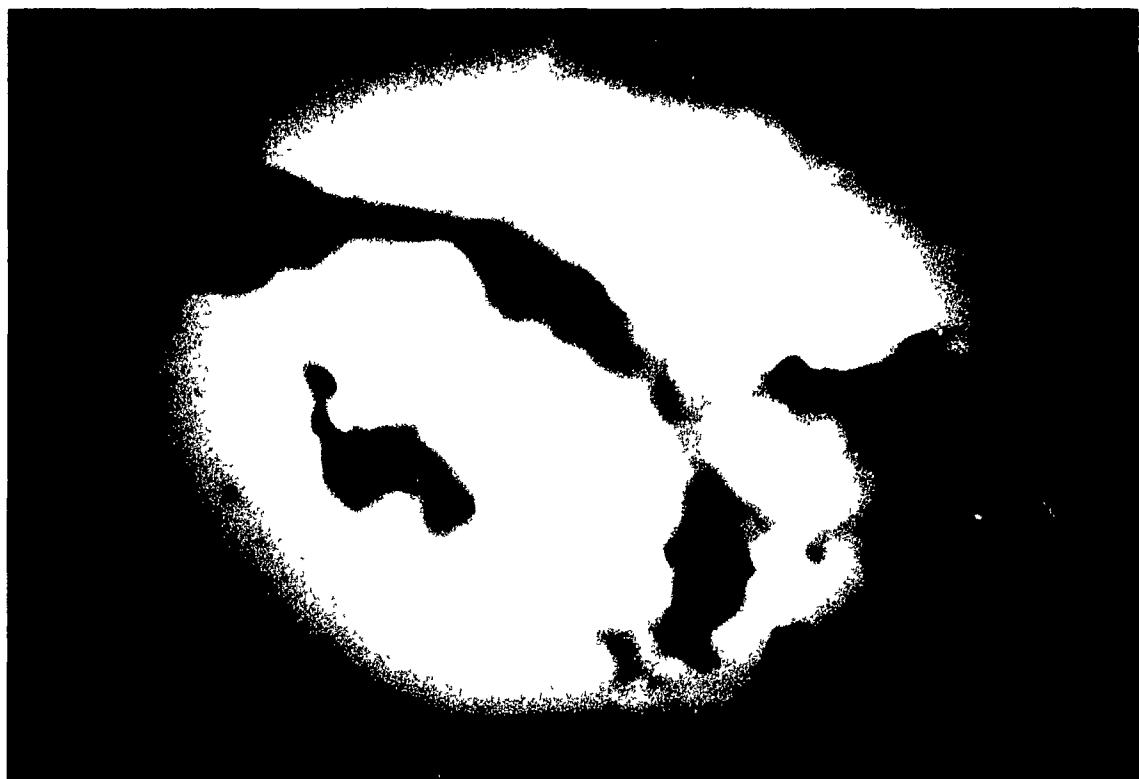


Figure 10.4: S.E.M. microphotograph of intergranular LARC A.



Figure 10.5: S.E.M. microphotograph of stage 2a intergranular LARC B .



Figure 10.6: Microphotograph of stage 2a HARC located at a triple junction of three grains: A) sylvite, B) halite, C) halite. Under a magnification of 65X and plane polarized light (PPL).



Figure 10.7: Summary of changes in crack development for progressive increase in uniaxial load for potash rock type "A" (fig.10.7a), type "B" (fig.10.7b), type "C" (fig.10.7c) and type "D" (fig.10.7d).

Figure 10.7a: Type "A" potash rock.

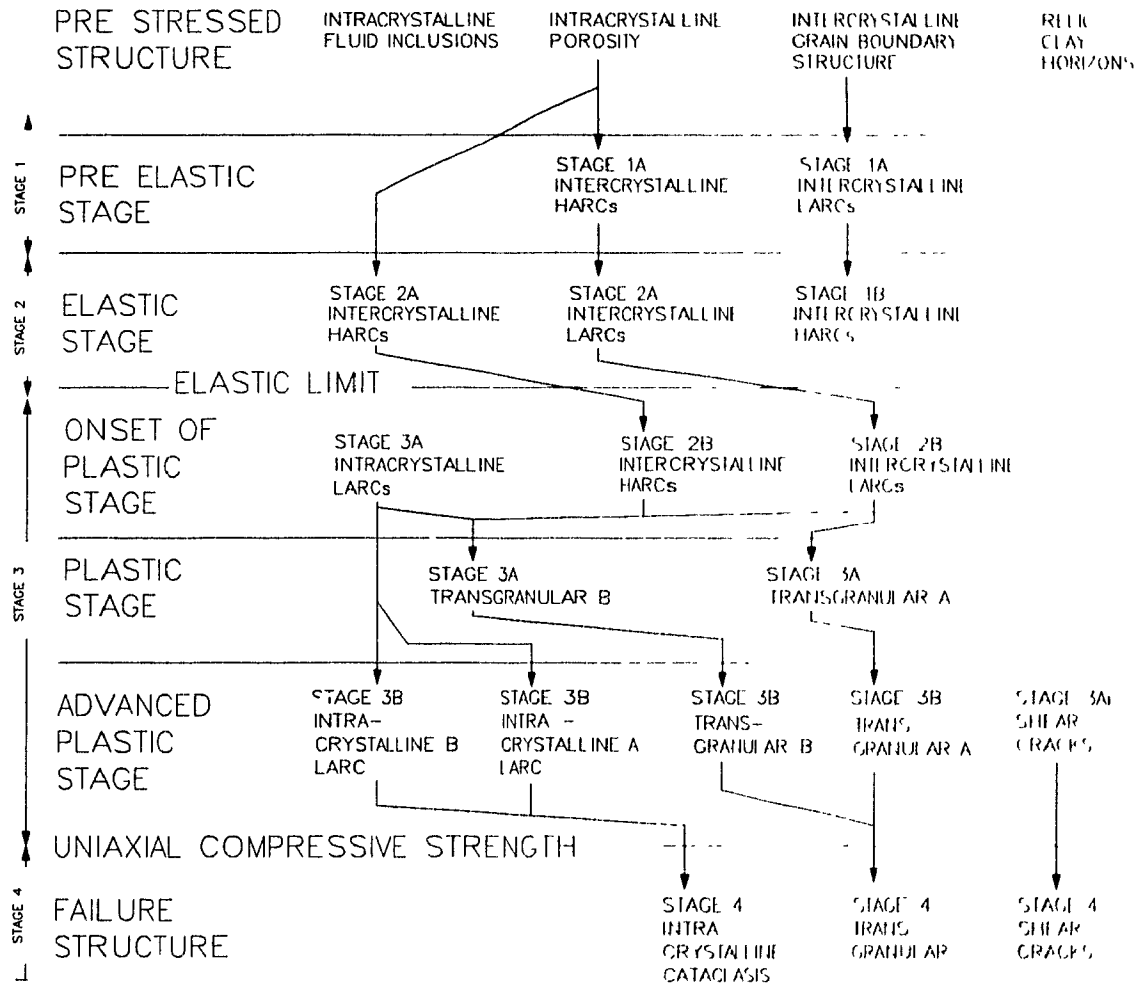


Figure 10.7b: Type "B" potash rock.

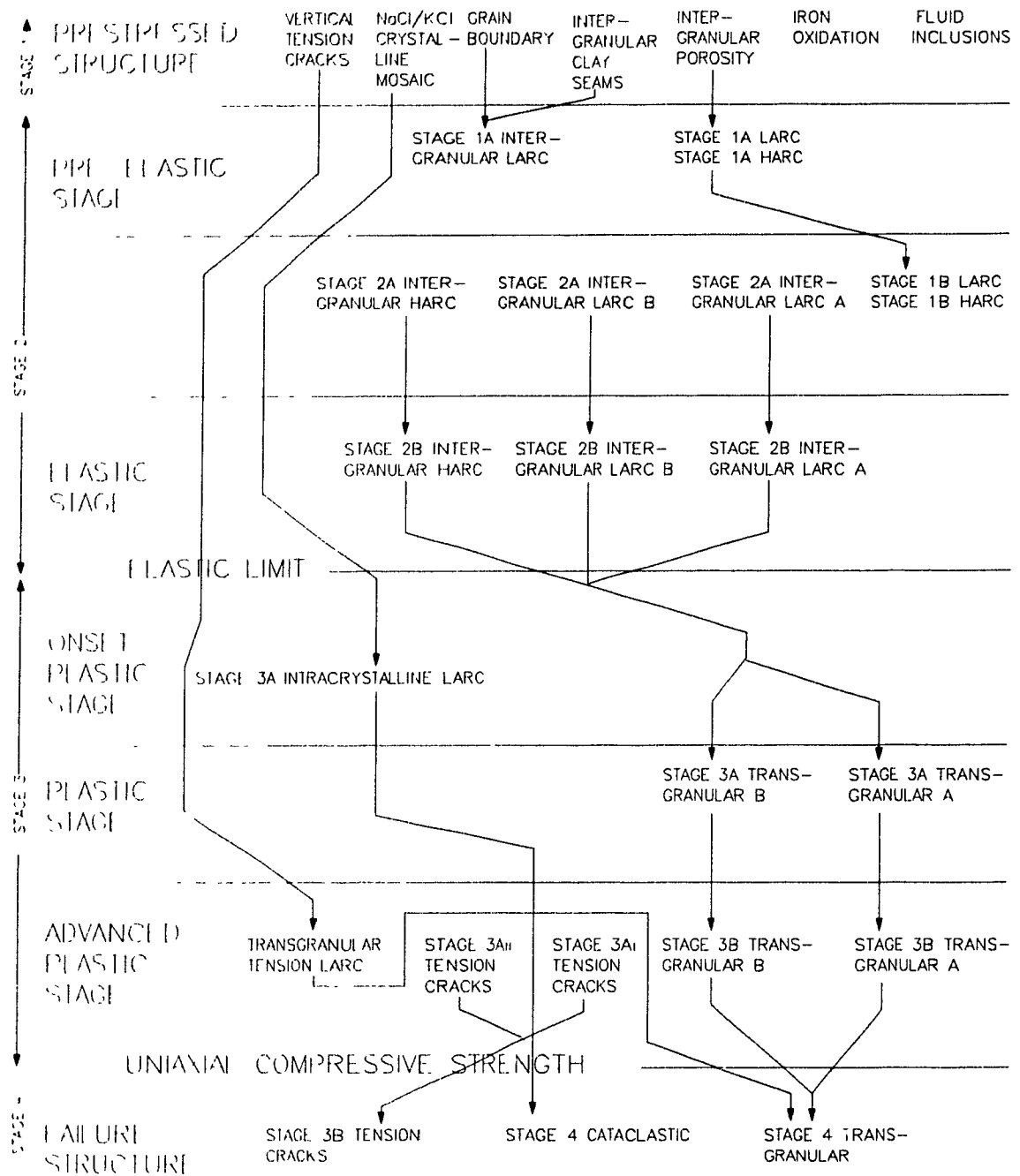


Figure 10.7c: Type "C" potash rock.

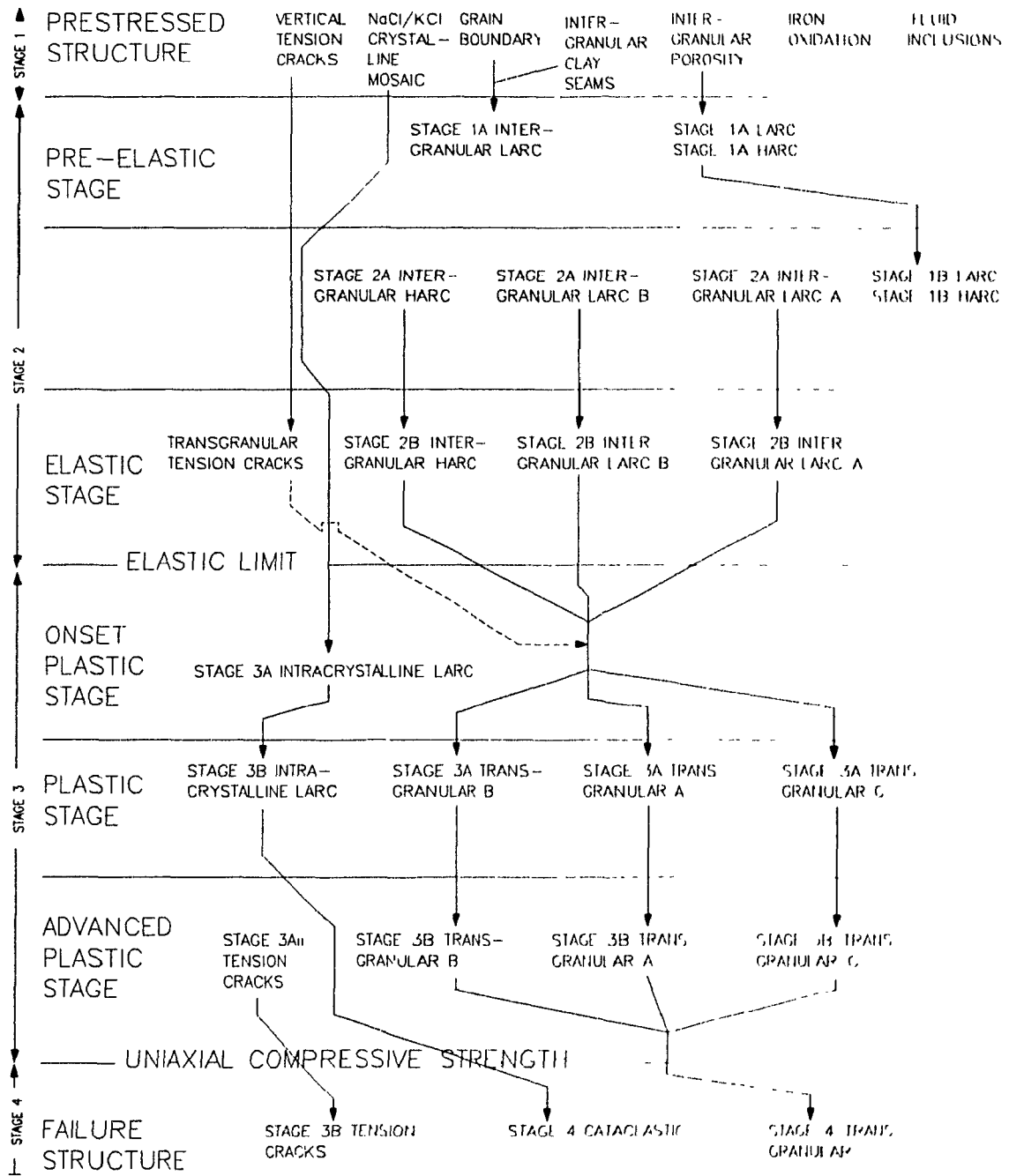


Figure 10.7d: Type "D" potash rock.

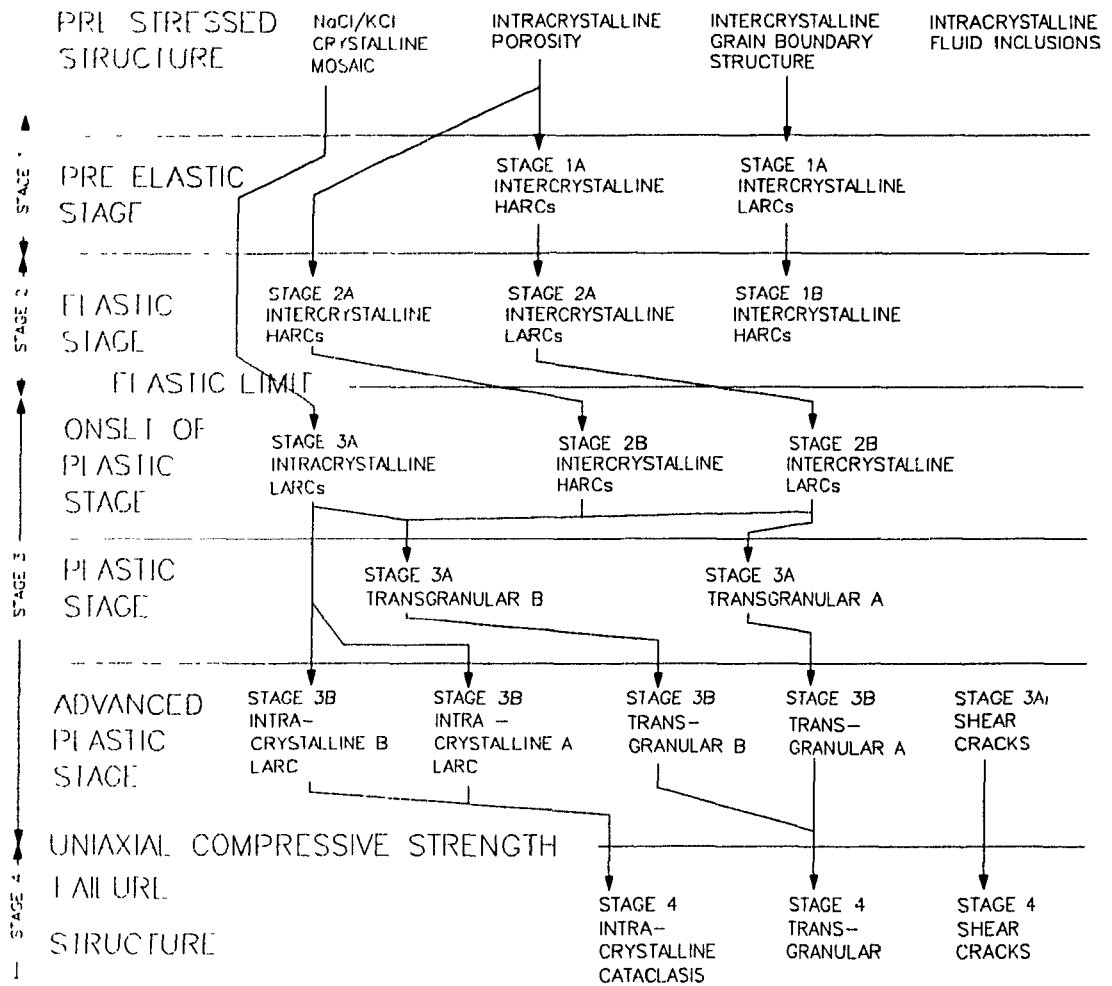
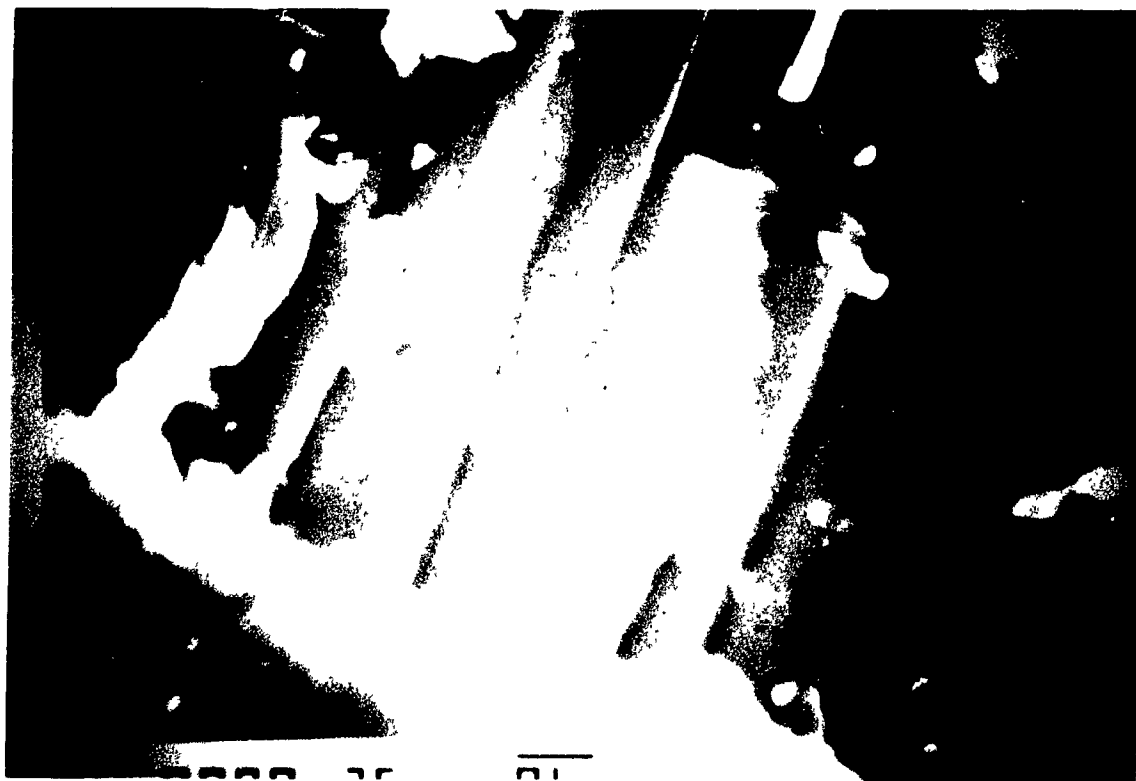


Figure 10.8: Photograph of planer polished vertical section of potash rock type "B" displaying tectonic cracks.



Figure 10.9: S.E.M. microphotograph of stage 3a intragranular LARCs, perpendicular to a clay rich grain boundary area.



**Figure 10.10a:** S.E.M. microphotograph of intracrystalline LARC at an advance stage 3 load cycle. The left aspect of the photograph displays two parallel LARCs on a planer surface of a crystal grain. The right aspect shows several parallel LARCs on multiple fracture surfaces.

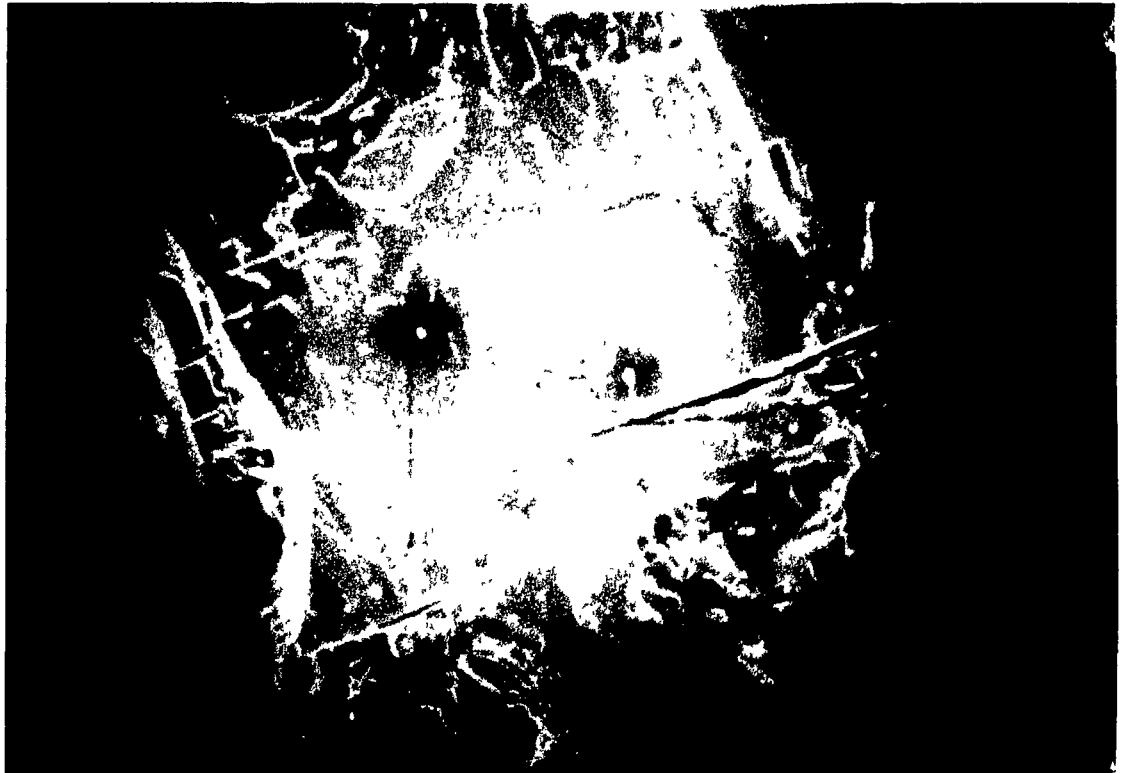


Figure 10.10b: S.E.M. microphotograph under lower magnification of a fractured crystal plane displaying cleavage fracture surfaces which are perpendicular to the plane [010]. The cracks are the same type as observed in figure 10.10a. They are categorized as intracrystalline LARCs.



Figure 10.11 S.E.M. microphotograph of stage 3b intracrystalline LARC link A type crack sets, displaying 'en-echelon' and 'en-passant' crack interactions.



Figure 10.12: Optical microphotograph of halite grain containing stage 3b intracrystalline LARC link B. Photograph taken under plane polarized light with 150 magnification.



Figure 10.13: Composite photograph displaying late stage 3b transgranular A, B and C. (a) displays type "A" potash rock with transgranular A fracture pattern, (b) and (c) shows transgranular B and C crack development within potash rock types "B" and "C"; and (d) potash rock type "D" consists of transgranular A crack pattern.

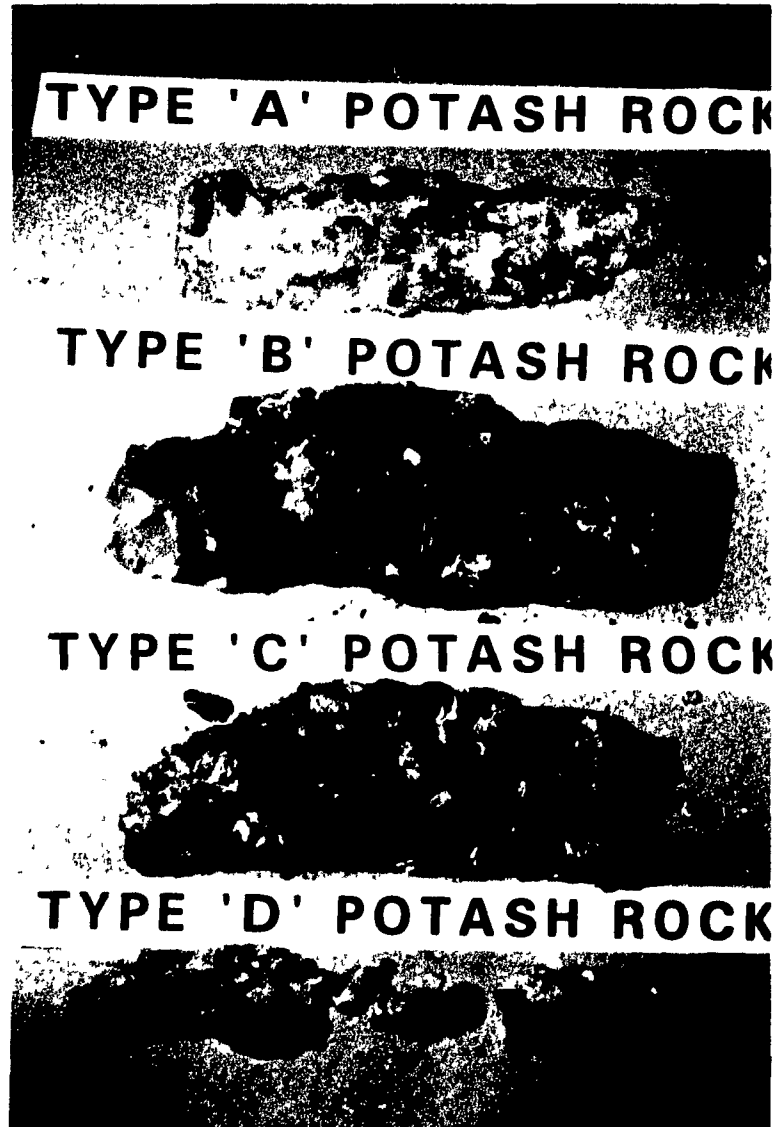


Figure 10.14: S.E.M. microphotograph of stage 3b intracrystalline A and B LARCs hosted by sylvite grains.

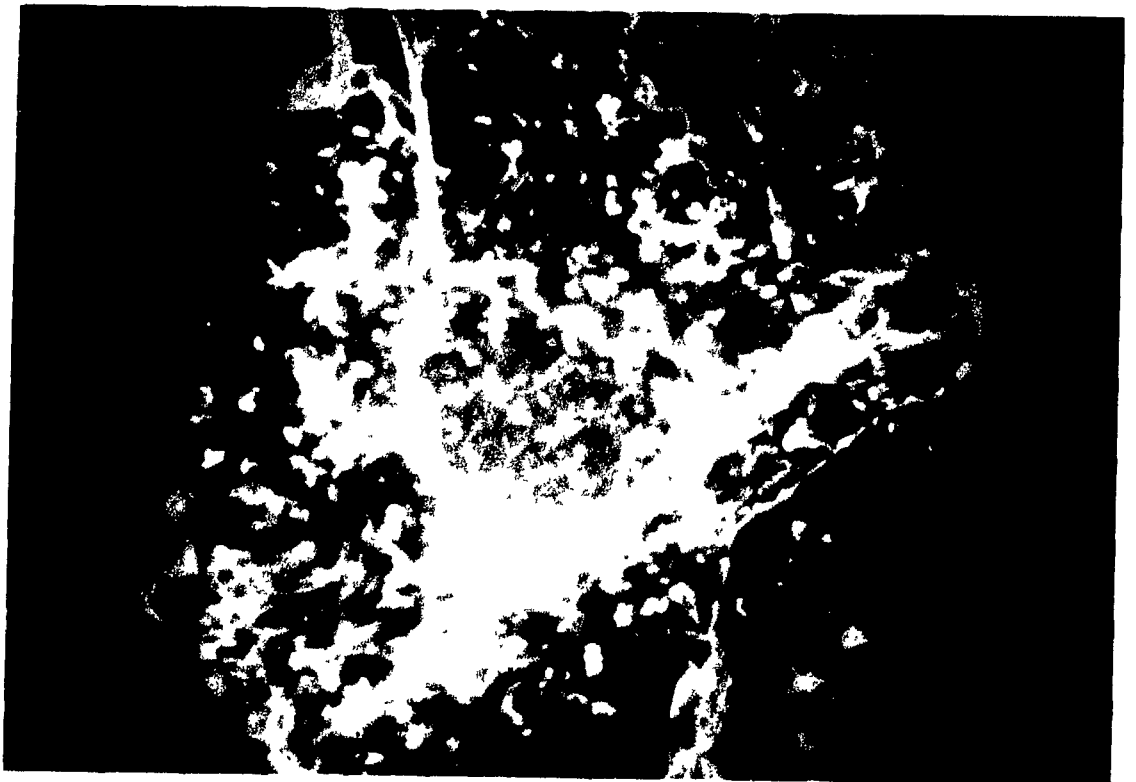


Figure 10.15: Photograph of stage 3b shear crack 'ii' class, crosscutting sylvite-clay interface (Magnification 10X).

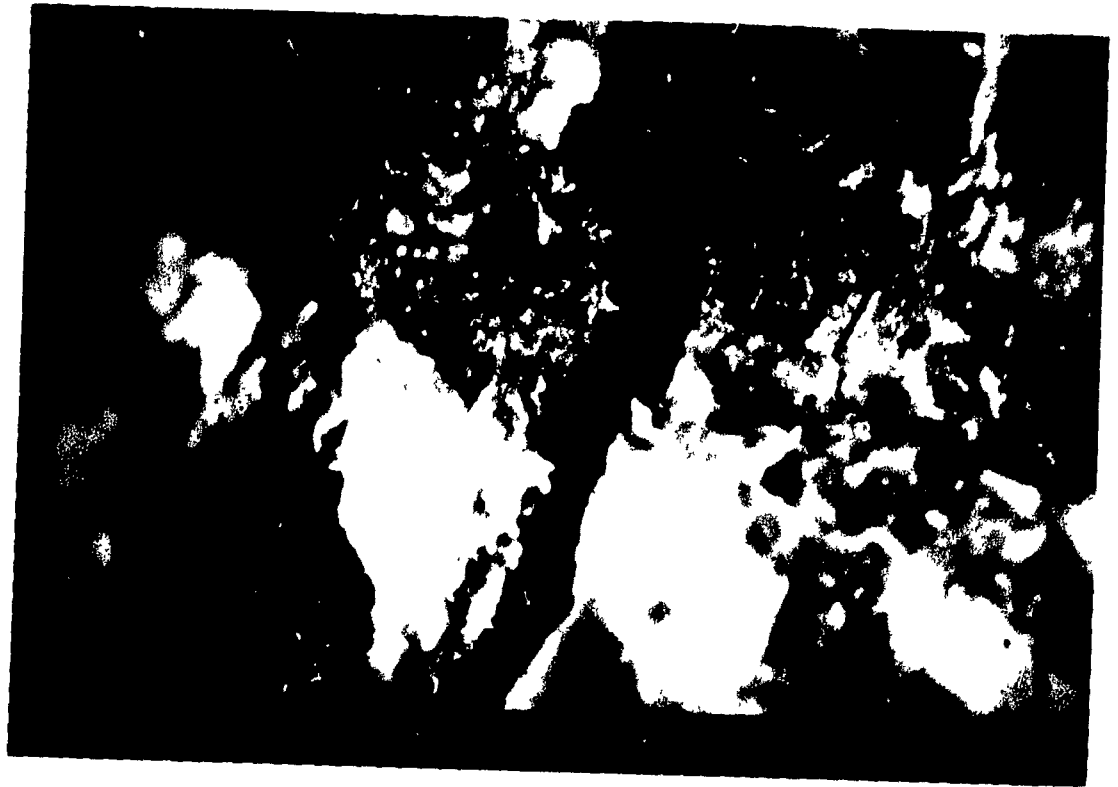
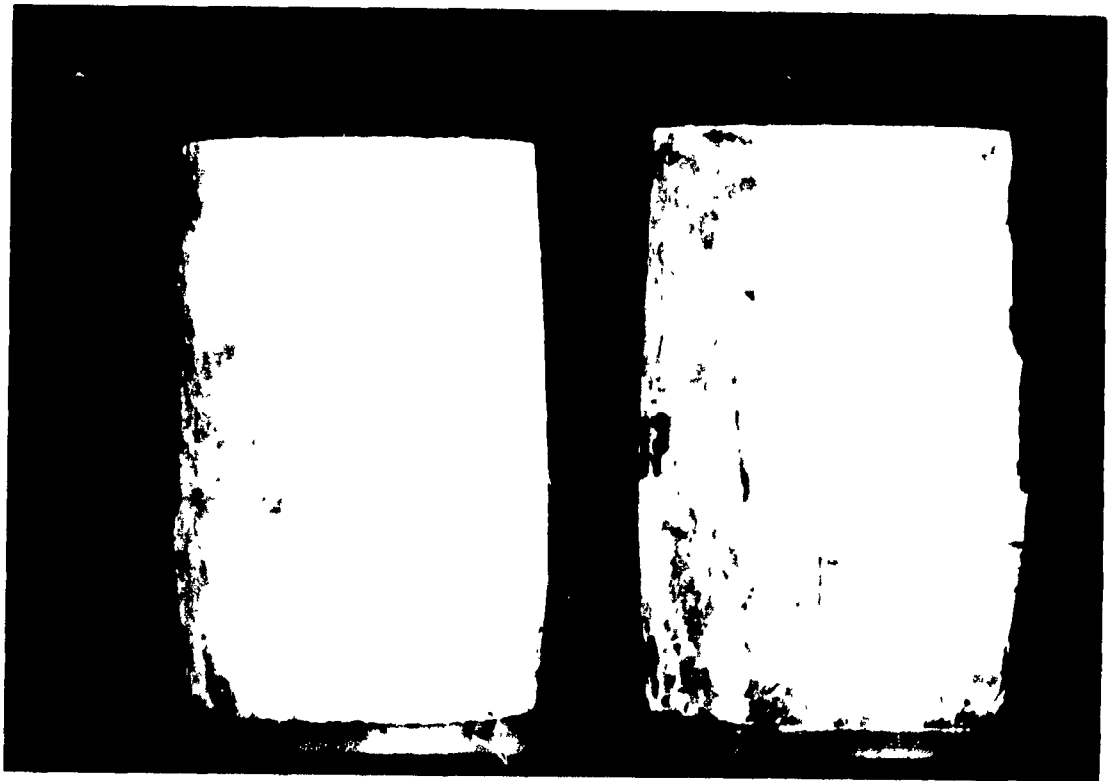


Figure 10.16: Photograph of types "C" and "B" potash rock and characteristic pattern of fracture development achieved at specimen failure. Potash rock type "B" is located on the right hand side of the photograph and type "C" on the left.



Figure 10.17: Photograph of types "A" and "D" potash rock and characteristic pattern of fracture development achieved at specimen failure. Potash rock type "D" is located on the right hand side of the photograph and type "A" on the left.



## Summary

The acoustic emission behavior in relation to microstructural characteristics of potash rock has been studied under laboratory testing conditions.

The prime objective of the investigation was to establish microscopic evidence of specimen damage and its possible correlation into the source of acoustic emission, under uniaxial load in a constant strain rate mode. Acoustic emission activity was monitored during the load experiments.

In this investigation, the potash rock consisted of four types distinguished by texture and compositional ratios of sylvite and halite. The specimens used for load testing were homogeneous and consisted of microstructural features that are uniformly distributed. The orientation of the samples tested consisted of right cylinders cored perpendicular to the bedding from the host rock.

The samples were tested on a stiff testing machine situated between two platens, one of which has a bevelled coupler in order to compensate for uneven sample end contact surfaces. Axial displacement due to uniaxial compression was measured with a linear variable differential transformer (LVDT), located parallel to the specimen. The displacement was measured from the contact of the upper platen. Acoustic emission was monitored via an piezoelectric transducer coupled to the vertical face of a specimen.

Samples utilized for load testing consisted of two sizes. A smaller sample set consists of a diameter of 7 cm and a larger set measuring at 15 cm. The length of the specimens was of a 2:1 length to diameter ratio. In compliance with this assumption, samples were tested under uniaxial compression with a constant strain rate of  $1.538 \times 10^{-3}$ .

The mechanical parameters measured in this testing program were axial displacement (axial strain), load (uniaxial stress) and Young's modulus of elasticity. A multiple regression analysis of experimental stress-strain data and their dependency to petrographic parameters was investigated.

The acoustic emission activity was monitored in the time domain over a frequency range of 100 to 300 kHz.

Acoustic emission rate, accumulated activity, amplitude, energy and event duration time difference were utilized as a means of studying the acoustic emission activity observed in potash rock. Acoustic emission data was individually analyzed and compared to other parameters in order to determine the sequence of acoustic emission characteristics with increasing load for the four types of potash rock.

Graphical interpretation and numerical analysis of acoustic emission rate versus stress and strain, amplitude distribution, energy distribution, contour plots of event frequency between energy, amplitude versus time difference and event duration were established for samples loaded to the elastic limit and specimen failure.

The model parameters including acoustic emission cumulative event count was determined using the least squares analysis of the experimental strain data and their dependency to stress [Scholz (1968a)].

Utilizing the cumulative amplitude distribution, the b-value parameters were established using several equation models to fit the distribution. These values were determined for data measured up to the elastic limit and sample failure. It is believed that the b-value has significance in delineating the source mechanisms.

The cumulative energy distribution and E-value parameter were examined in a similar method applied to the amplitude related b-value.

The amplitude parameter [Pollock (1976)] was also examined in order to observe the change in event amplitude with increasing stress level.

The mechanical behavior was compared to the b-value parameters. These were statistically analyzed using the least square analysis with the uniaxial compressive strength of the samples. This was modelled in order to establish the theory that the deformational mechanisms leading to specimen failure were interrelated to the progressive developmental pattern of generated acoustic emission.

The dependence of the polya-process and/or Poisson process was analyzed by the Chi distribution. Based on the time difference between consecutive acoustic emission events, it was concluded that the events were of an independent nature. Several patterns were discovered when a closer examination of the data showing the contouring of the frequency of events of their amplitude and corresponding time dif-

ferences was performed. Similar contour plots were established to show the density of events relating their amplitude and energy with respect to their time difference and event duration.

Finally, a study of the progressive microfracturing process during uniaxial load on potash rock was examined. In recognition of three stages along the stress-strain curve, along with the changing characteristics of acoustic emission rate, amplitude and energy characteristics, several tests of each potash rock type were arrested at intermediate levels of load in order to examine the fracture development within the samples. Specific points in reference to the stress-strain curve were chosen for this examination. A complete history of the fracture processes was established.

In conclusion, a comparative study relating the fracture process to the acoustic emission characteristics is proposed.

## CONCLUSION

Based on the experimental results for 72 specimens tested, the following conclusions can be drawn when relating microfracture to acoustic emission characteristics of potash rock:

- 1) Potash rock specimens derived from Saskatoon PCS can be petrographically subdivided into four types based on the compositional ratio between sylvite, halite and clay; textural homogeneity and structural interlocking.
- 2) The geomechanical behavior of the various potash rock types loaded under uniaxial compression are variable:
  - a) Based on the stress-strain curves, the material displays elastic-plastic behavior.
  - b) All four types of potash rock show a short elastic range up to 45 to 50% of the uniaxial failure strength, followed by a transitory stage at approximately 60% of the failure strength. Beyond this level a plastic behavior/strain hardening region is observed until sample failure.
  - c) Potash rock types "A" and "D" display a distinctive yield point whereas, types "B" and "C" do not.
  - d) Although the values for Young's modulus of elasticity are low, there are no distinctive patterns of values discernable. The values range from 1400 to 6400 GPa.
  - e) The uniaxial compressive strengths of potash rock types "A" and "D" are higher than types "B" and "C". Type "A" shows values ranging from 32 to 28 MPa. The lowest are registered for type "B" potash rock, showing a range from 22 to 14 MPa.
  - f) A multivariable regression analysis was performed to demonstrate the dependence of potash rock strength to various petrographic parameters. It was shown that only the concentration of sylvite notably affects the strength of the rock. Structural interlocking and textural homogeneity show insignificant dependence on the failure strength of potash rock.  
In general, an increase in the concentration of sylvite decreases the strength of potash rock.

- 3) Four stages along the stress-strain curve are recognizable with respect to the acoustic emission rate. These include:
- i) the initial stage - with little or no acoustic emission activity.
  - ii) the primary stage - the presence of very low acoustic emission activity located within the elastic range.
  - iii) the secondary stage - a region of rapid increase of acoustic emission activity activated at the onset of the region of plastic behavior.
  - iv) the final stage - a high and steady acoustic emission activity located at the post yield region.

The point of inflection defining a rapid increase in acoustic emission activity is less apparent within potash rock types "B" and "C".

- 4) The amplitude characteristics of potash rock are similar for all four types. The amplitudes recorded range from 77 to 99 dB. The distribution displays two major peaks at 85 dB and 97 dB.
- 5) The energy characteristics of potash rock are also similar for all four types. The energy values recorded range from 82 to 130. The distribution displays three peaks at 85, 90 and 100 to 112.
- 6) The b-value parameter was defined from the cumulative amplitude distribution. The value represents a constant in an equation formulated to fit the cumulative distribution curve. The b-values are significantly lower for events measured to specimen failure. But, there is insignificant variation in b-values between the various types of potash rock. This is indicative that the stress induced deformation mechanisms operating in the potash under uniaxial compression are similar for all four types.
- 7) The amplitude ratio [Pollock (1976)] has shown that low amplitude events (less than 84 dB) occur prior to the elastic limit of rocks loaded under uniaxial compression. An increase in the amplitude ratio is observed with increasing load, whereby it reaches a maximum of 94% at specimen failure. Also the majority of the events are generated within the plastic region of the stress-strain curve. This fact is also supported by the graphical interpretation of acoustic emission rates of individual amplitude ranges.

- 8) The statistical correlation between time difference and peak amplitude was established using a contingency table for the two parameters. Using the Chi distribution analysis technique, it was shown that there is an independence between the two parameters thus, conforming to a 'Poisson' fracture process or events generated independent of each other.
- 9) The frequency of events relating amplitude and consecutive time difference displayed several regions of high concentration of events. Large concentration of low amplitude (84 dB) and high amplitude (98 dB) constitute time differences of the 0.016 to 0.032 milliseconds range.
- 10) A frequency distribution between energy and time difference displayed similar concentration of events. These were concentrated along the same time difference range but events were clustered around the 98 energy level.
- 11) It was possible to determine the characteristics and occurrence of acoustic emission events with respect to increase in stress. Based on the amplitude ratio and acoustic emission rate of individual amplitude ranges, it was possible to determine at which stage in the load cycle various acoustic emission events occurred. It was also possible to determine the occurrence of energy of acoustic emission events with respect to load level by comparison of the event duration and amplitude of acoustic emission events via the contour diagrams.
- 12) Stress-induced microfracture process in all four types of potash rock are similar. It is the dominant fracture mechanisms and their initiation in relation the stress level, during a uniaxial compression load cycle, which differs.
- 13) The mechanisms have been identified by optical and electron microscopy from samples loaded to pre-determined stress levels. The deformational features observed within the whole range of the load cycle include intergranular pore closure, intergranular/intercrystalline microcrack displacement, intracrystalline microcracking and transgranular cracking.

Intergranular and intercrystalline pore closure are evident in all four types of potash rock in the pre-elastic stage. Within the early elastic stage of deformation, all four types of potash rock deform by intergranular displacement. Intergranular microcrack development progresses to the elastic limit and dominates the mode of deformation within types "A" and "D" potash rock. In contrast,

types "B" and "C" potash rock show development of intracrystalline microcracking in the late stages of the elastic zone and they represent the major mode of deformation in the plastic region of the stress-strain curve. Intergranular cracking dominates in types "A" and "D" potash rock up to the early plastic region of deformation.

Transgranular cracks consisting of intracrystalline crack interactions are the dominant crack development found in the progressive stages of the plastic region until specimen failure for potash rock types "B" and "C".

Transgranular cracks consisting of intergranular-intracrystalline cracks are the dominant mode of deformation for types "A" and "D". The latter also occurs within the plastic region to specimen failure.

- 14) In terms of acoustic emission signature, the progressive changes in crack development are apparent only in the analysis of acoustic emission rate and amplitude ratio. The analysis of the other acoustic emission parameters including the b-value, E-value, energy, amplitude distribution and event duration only provide refinements of the event characteristics of events recorded up to the elastic limit and specimen failure.

Acoustic emission rate has displayed a point of inflection located near the elastic limit, indicating increased activity due to initiation and development of intragranular microcracks.

The acoustic emission rate of individual amplitude ranges has shown that prior to the elastic limit, low amplitude signals are generated and high amplitude signals are associated with events generated after the elastic limit. The amplitude ratio also displays the ration of events below 84 dB over the total event count.

- 15) The comparison of fractographic and acoustic emission analysis has shown that intergranular phenomena present in the early stages in the loading cycle is associated with low amplitude events. High amplitude events present in the later stages of the loading cycle are associated with intragranular microcracking and transgranular cracking.

The amplitude ratio increases with increasing stress for types "A" and "D" potash rock early in the plastic deformation stage. This is apparent with an increase in the ratio from 30 to 60%. The same pattern is apparent just prior to the elastic limit for potash rock types "B" and "C".

The amplitude distribution also has shown that the number of high amplitude events recorded for types "B" and "C" potash rock are several magnitudes higher than for types "A" and "D". This ratio increases for events recorded to specimen failure.

The b-value is similar for all four types of potash rock. The results are similar since the parameter was determined at two specified limits whereby the mechanisms are the same for all four types of potash rock. It is proposed that the b-value would show a greater variation if it were calculated for stress levels prior to and after the elastic limit.

## BIBLIOGRAPHY

- Acoustic Emission Technology Corporation, (1988), "User's manual/ Operating Instructions, for the AET MODEL 5500 series, Microcomputer Based Acoustic Emission Monitoring System"; Sacramento, California
- Aki, K. and Richards, P.G., (1980), "Quantitative Seismology: Theory and Methods Volume One"; W.H. Freeman and Co., San Francisco.
- Armstrong R.W., (1968), "Grain boundary Strengthening and the polycrystalline deformation rate"; *Tire de dislocation Dynamics*, AR Rosenfield, Mcgrane Hill Book Co., pp. 293-309
- ASTM E569-82, (1982), "Standard Practice for Acoustic Emission Monitoring of Structures During Controlled Simulation"; *Annual Book of ASTM Standards, Part II*; ASTM, Philadelphia, Pennsylvania, pp.531-535.
- ASTM E610-77, (1978), "Standard Definitions of Terms Relating to Acoustic Emission"; *Annual Book of ASTM Standards, Part II*, ASTM, Philadelphia, Pennsylvania, pp.603-605.
- ASTM E650-78, (1979), "Standard Recommendation Practice for Monitoring Piezoelectric Acoustic Emission Contact Sensors"; *Annual Book of ASTM Standards, Part II*, ASTM, Philadelphia, Pennsylvania, pp.589-591.
- ASTM E750-80, (1980), "Standard Practice for Measuring The Operating Characteristics of Acoustic Emission Instrumentation"; *Acoustic Emission Annual Book of ASTM Standards, Part II*, ASTM, Philadelphia, Pennsylvania; pp.688-698.
- Atkinson, B.K., MacDonald, D. and Meredith, P.G., (1984), "Acoustic Response and Fracture Mechanics of Granite Subjected to Thermal and Stress Cycling Experiments"; *Proceedings Third Conference On Acoustic Emission/ Microseismic Activity in Geologic Structures and Materials*, Pennsylvania State University, Trans Tech Publication, Clausthal, Germany, pp.5-18.
- Attewell, P.B., SandFord, M.R., (1974a), "Intrinsic Shear Strength of a Brittle Anisotropic Rock -I- Experimental and Mechanical Interpretation"; *International Journal of Rock Mechanics and Geomechanical Abstract*, Vol.11, pp.423-430.
- Attewell, P.B., SandFord, M.R., (1974b), "Intrinsic Shear Strength of a Brittle Anisotropic Rock -II- Textural Data Acquisition and Processing"; *International Journal of Rock Mechanics and Geomechanical Abstract*, Vol.11, pp.431-438.
- Attewell, P.B., SandFord, M.R., (1974c), "Intrinsic Shear Strength of a Brittle Anisotropic Rock -III- Textural Interpretation of Failure"; *International Journal of Rock Mechanics and Geomechanical Abstract*, Vol.11, pp.439-451
- Aubertin, M., Gill, D.E., Ladamyi, B., (1987), "Le Comportement Rheologique du Sel: Revue Bibliographique: Tome I, Essais en Laboratoire et Modelisation Emperique"; EPM/R1-87/31, Ecole Polytechnique de Montreal.
- Baar, C.A., (1977), "Applied Salt Rock Mechanics I"; Elsevier Science Publ.
- Baram, J. and Rosen, M., (1980), "Effect of Grain Size on the Acoustic Emission Generated During the Plastic Deformation of Aluminum"; *Materials Science and Engineering*, 45, pp.255-262.
- Barron, K., (1970), "Detection of Fracture Initiation in Rock Specimens by the Use of Simple Ultrasonic Listening Device"; *International Journal of Rock Mechanics and Geomechanical Abstracts*, 8, pp.55-59.
- Beattie, A.G., and Jaramillo, R.A., (1974), "The Measurement of Energy in Acoustic Emission"; *Review of Scientific Instrumentation*, 45, #3, pp.352-357.
- Betourney, M., (1986), "Laboratory Studies of AE in Geologic Materials"; McGill University Report for Seminar Course, 306-620a, Montreal, Canada.

- Bieniawski, Z.T., (1967), "Mechanisms of Brittle Fracture of Rock. Part II-Experimental Studies"; International Journal of Rock Mechanics and Geomechanical Abstract, Vol.4, pp.407-423.
- Bombolakis, E.G., (1973), "Study of the Brittle Fracture Process under Uniaxial Compression", TectonoPhysics 18, pp.231-248.
- Brace, W.F., (1960), "An Extension of the Griffith Theory of Fracture to Rock"; Journal of Geophysical Research, Vol. 65, pp.3477-3480.
- Brace W.F., (1961), "Dependence of fracture strength of rocks on grain size"; Proc. 4th US Symposium on Rock Mechanics, University Park, pp. 99-103
- Brady B.H.G., and Brown E.T., (1985), "Rock Mechanics for Underground Mining"; George Allan and Unwin Publishers Ltd, London, 527p.
- Breyer, W.H., (1966), "CRC Handbook of Tables for Probability and Statistics"; Chemical Rubber Co., Clev. Ohio, 44114, 498p.
- Bunge, H.J., (1982), "Textural Analysis in Materials Science : Mathematical Methods"; London, Boston, Butterworths, 593p.
- Butcher B.M., (1980), "An elastic plastic mechanical constitutive description for rock salt triaxial compression"; SAND 80-1935, Sandia national laboratories, 44p
- Calder, P.N., Archibald, J.F., Madsen, D. and Bullock, K., (1988), "High Frequency Precursor Analysis Prior to a Rockburst"; Second International Symposium on Rockbursts and Seismicity in Mines, preprint papers, University Radisson Hotel-Minneapolis, Minnesota, pp.223-233.
- Carter N.L., Heard H.C., (1970), "Temperature and rate dependent function of halite"; Am.J.Sci., vol. 269 Oct, pp. 193-249
- Chugh, Y.P., and Heidinger, G.H., (1980), "Effect of Coal Lithology on Observed Microseismic Activity During Laboratory Tests"; Proceedings Second Conference On Acoustic Emission/ Microseismic Activity in Geologic Structures and Materials, Pennsylvania State University, Trans Tech Publication, Clausthal, Germany, pp.55-62.
- Dawson P.R., and Munson D.E., (1983), "Numerical simulation of creep deformations around a room in a deep potash mine"; I.J.R.M.M.S., vol.20, no.1, pp.33-42.
- Dean Water E., Schreiber C.B., (1978), "Marine evaporite, SEPM short course 1"; SEPM publication sales P.O. Box 4756 Tulsa OK. 74159, 188p.
- Dehoff R.T., and Rhine F.N., (1968), "Quantitative microscopy"; Mcgraw Hill book Co., New York, 550p
- Dellwig L.F., and Evans R., (1979), "Depositional processes in saline salt of Michigan, Ohio and New York"; Bull Am. Ass. Petrol. Geol., 53, pp.949-956
- Dellwig, L.F., (1955), "Origin of the Salina Salt of Michigan"; Journal of Sedimentary Petrology, vol.25, pp.83-110.
- Desia, J.D., and Gerberich, W.W., (1975), "Analysis of Incremental Cracking By the Stress Wave Emission Technique"; 7, pp.153-165.
- Dreyer W., (1972), "The science of rock mechanics part 1"; Trans Tec. Publ., Cleveland, USA, p.295
- Dunning, J., and Dunn, D., (1980), "Microseismicity of Stable Crack Propagation in Quartz"; Proceedings Second Conference on Acoustic Emission /Microseismic Activity in Geologic Structures and Materials, Pennsylvania State University, Trans Tech Publication, Clausthal, Germany, pp.1-10.
- Dürr, K., and Meister, D., (1984), "Evaluation of Pillar Deformation and Stability in a Salt Mine, Utilizing Acoustic Emission, Mine Survey and Rock Deformation Data"; Proceedings Third Conference On Acoustic Emission/ Microseismic Activity in Geologic Structures and Materials, Pennsylvania State University, Trans Tech Publication, Clausthal, Germany, pp.283-302.

- Eisenblätter, J., (1979), "Acoustic Emission Analysis : Introduction, Present Status and Future Development"; The Fourth Acoustic Emission Symposium, High Pressure Institute of Japan, Tokyo, pp.1-15.
- Eisenblätter, J., (1979), "The Origin of Acoustic Emission - Mechanisms and Models"; The Fourth Acoustic Emission Symposium, High Pressure Institute of Japan, Tokyo, pp.189-203.
- Erlenkämper, S., (1979), "Time and Amplitude Statistics of Acoustic Emission Signals in Fracture Mechanic Experiments"; The Fourth Acoustic Emission Symposium, High Pressure Institute of Japan, Tokyo, pp.165-187.
- Everitt, B.S., (1976), "Analysis of Contingency Tables"; London Chapman and Hall, John Wiley and Sons Inc., N.Y., 128p.
- Fleischmann, P., (1979), "Continuous Acoustic Emission during the Deformation of Pure Aluminum"; pp.39-51.
- Fonseka, G.M., Murrell, S.A.F., and Barnes, P., (1985), "Scanning Electron Microscope and Acoustic Emission Studies of Crack Development in Rocks"; International Journal of Rock Mechanics and Geomechanical Abstracts, 22, #5, pp.273-289.
- Fuzesy, L.M., (1983), "Petrology of Potash Ore in the Middle Devonian Prairie Evaporite"; Sask., Potash 83, Trans Tech Publication
- Gehle, R.M., and Thomas, R.L., (1984), "Monitoring Cyclic Load Effects on Rock Salt Insitu"; Proceedings Third Conference On Acoustic Emission/ Microseismic Activity in Geologic Structures and Materials, Pennsylvania State University, Trans Tech Publication, Clausthal, Germany, pp.339-346.
- Gerberich, W.W., and Hartbower, C.E., (1967), "Some Observations on Stress Wave Emission as a Measure of Crack Growth"; International Journal of Fracture Mechanics, 3, #3, pp.185-191.
- Gilbert, M.S., Farmer, I.W., (1981), "A Time Dependent Model for Living Pressure Basal on Strength concepts"; Proc. Int. Symp. on Weak Rock, Tokyo, pp.137-142.
- Graham, L.J., (1976), "Microstructural Effects on Acoustic Emission Signal Characteristics"; Science Center, RockWell International- Interdisciplinary Program for Quantitative Flaw Definition, Special Report Second Year Effort, pp.297-319.
- Greensmith, I.T., (1979), "Petrology of the sedimentary rocks, 6th edition"; London, George Allan and Unwin/Thomas Marby, 241p
- Greenfield, R.J., (1977), "Amplitudes and Spectra From Underground Sources"; Proceedings First Conference On Acoustic Emission/ Microseismic Activity in Geologic Structures and Materials, Pennsylvania State University, Trans Tech Publication, Clausthal, Germany, pp.405-426.
- Haimson B.C., and Kim K., (1977), "Acoustic Emission and Fatigue Mechanism in Rock"; Proceedings First Conference On Acoustic Emission/ Microseismic Activity in Geologic Structures and Materials, Pennsylvania State University, Trans Tech Publication, Clausthal, Germany, pp.35-56.
- Hardy, H.R. Jr., Leighton, F., (1977), "Acoustic Emission/MS Activity in Geologic Structures and Materials Proceedings of the 1st Conference"; Pennsylvania State University, Trans Tech Publication, Clausthal, Germany, pp.483.
- Hardy, H.R. Jr., Leighton, F., (1980), "Acoustic Emission/MS Activity in Geological Structures and Materials Proceedings of the 2nd Conference"; Pennsylvania State University, Trans Tech Publication, Clausthal, Germany, pp.486.
- Hardy, H.R. Jr., Leighton, F., (1984), "Acoustic Emission/MS Activity in Geologic Structures and Materials Proceedings of the 3rd Conference"; Pennsylvania State University, Trans Tech Publication, Clausthal, Germany, pp.814.

- Hardy, H.R. Jr., (1977), "Emergence of Acoustic Emission/ Microseismic Activity as a Tool in Geomechanics"; Proceedings First Conference On Acoustic Emission/ Microseismic Activity in Geologic Structures and Materials, Pennsylvania State University, Trans Tech Publication, Clausthal, Germany, pp.13-31.
- Hardy, H.R. Jr., and Leighton F., (1984), "Discussions Section"; Proceedings Third Conference On Acoustic Emission/ Microseismic Activity in Geologic Structures and Materials, Pennsylvania State University, Trans Tech Publication, Clausthal, Germany, pp.729-738.
- Hardy, H.R. Jr., (1982), "Theoretical and Laboratory Studies Relative to the Design of Salt Caverns for the Storage of Natural Gas"; Project PR 12 71 of the Pipeline Research Committee American Gas Association, 709p.
- Hardy, H.R. Jr., (1982), "Theoretical and laboratory studies relative to the design of salt caverns for the storage of natural gas"; Project PR - 12-71 of the pipeline Research committee, American Gas Association, 709p.
- Harris, D.O., Tetelman, A.S., and Darwish, F.A., (1972), "Acoustic Emission"; ASTM STP 505, Philadelphia, Pennsylvania.
- Harris, D.O., and Bell, R.L., (1977), "The Measurement and Significance of Energy in Acoustic Emission Testing"; Experimental Mechanics, 17, pp.347-353.
- Hassani, F.P., (1980), "A study of the Physical and Mechanical Properties of Rocks and Their Discontinuities Associated with Opencast Coal Mining Operations"; Ph.D. Thesis, University of Nottingham
- Hatano, H., (1974), "Quantitative Measurements of Acoustic Emission Related to its Microscopic Mechanism"; Journal of Acoustical Society of America, 57, #3, pp.639-645.
- Hatano, H., (1975), "Strain-rate Dependence of Acoustic Emission Power and Spectra in Aluminum Alloys"; Journal of Applied Physics, 47, #9, pp.3873-3876.
- Hatano, H., (1977), "Acoustic Emission and Stacking Fault Energy"; Journal of Applied Physics, 48, #10, pp.4397-4399.
- Hatton, L., Worthington, M.H., and Makin, J., (1986), "Seismic Data Processing: Theory and practice"; Blackwell Scientific Publishing, Oxford, London, Boston.
- Hertzberg, R.W., (1989), "Deformation and Fracture Mechanics of Engineering Materials"; 3d edition, New York Wiley, 680p.
- Hiroshi, T., Paris, P.C., Irwin, G.R., (1985), "The Stress Analysis of Cracks Handbook"; 2d edition, Saint-Louis, MO: Paris Productions Inc., Del Research Corporation
- Holcomb, D.J., (1981), "Memory, Relaxation and Microfracturing in Dilatent Rock"; Journal of Geophysical Research, 86, #B7, pp.6235-6248.
- Holt, J., and Evans, T.W.M., (1976), "Measurement and Interpretation of Amplitude Distribution of Acoustic Emission Signals"; RD/L/N40/76, Central Electricity Research Laboratories, Leatherhead, Surrey.
- Holter, H.E., (1969), "The Middle Devonian Prairie Evaporite of Saskatchewan"; Department of Mineral Resources, GSP, Province of Sask. Minister report, 130p
- Howarth, D.F., and Rowlands, J.C., (1987), "Quantitative assessment of rock texture and correlation with drillability and strength properties", Rock Mechanics and Rock Engineering 20, pp. 57-85
- Hugman, R.H., and Freeman, H., (1979), "Effects of texture and composition on mechanical behavior of experimentally deformed carbonate rock"; Amer. Ass of Petroleum Geologists Bulletin, vol. 63, no. 9, pp. 1478-1489
- Johnson, D.H., and Toksoz, M.N., (1980), "Ultrasonic P and S Wave Attenuation in Dry and Saturated Rocks Under Pressure"; Journal of Geophysical Research, 85, #B2, pp.925-936.

- Khair, A.W., (1984), "Acoustic Emission Pattern: an Indicator of Mode of Failure in Geologic Materials as Affected by Their Natural Imperfection"; Proceedings Third Conference On Acoustic Emission/ Microseismic Activity in Geologic Structures and Materials, Pennsylvania State University, Trans Tech Publication, Clausthal, Germany, pp.45-66.
- Kim, H.C., Elvin, D.E.C., and Rosenhouse, G., (1979), *Philos. Mag. A*, 40, pp.49-57.
- Knill, J.L., Franklin, J.A., and Malone, A.W., (1968), "A Study of Acoustic Emission From Stressed Rock"; *International Journal of Rock Mechanics and Geomechanical Abstracts*, 5, pp.87-119.
- Knott, J.F., (1973), "Fundamentals of Fracture Mechanics"; London, Butterworth, 273p.
- Kowallis, B.J., Raeloffs, E.A., Wang, H.F., (1982), "U Crack Studies of Basalts from the Iceland Research Drilling Project"; *Journal of Geophysical Research*, Vol.87, No.38, pp.6650-6656.
- Kranz, R.L., (1979), "Crack-Crack and Crack Pore Interactions in stressed granite"; *International Journal of Rock Mechanics and Geomechanical Abstract*, Vol.16, pp.37-47.
- Krembein, W.C., and Sloss, L.L., (1963), "Stratigraphy and sedimentation, San Francisco, W.H. Freeman and Co., 660p
- Kurita, K., and Fujii, N., (1979), "Stress Memory of Crystalline Rocks in Acoustic Emissions"; *Geophysical Research Letters*, 6, #1, pp.9-12.
- Lama, R.D., Vutukuri, V.S., (1978b), "Handbook of Mechanical Properties of Rocks"; Trans Tech Publication, Trans Tech House, Switzerland, Vol.II, 481p. (SBN 0878490213)
- Lama, R.D., Vutukuri V.S., (1978), "Handbook on mechanical properties of rocks, Volume three"; Trans Tech Publication, Trans Tech House, Switzerland,
- Lawn, B.R., Wilshaw, T.R., (1975), "Fracture of Brittle Solids"; Cambridge University Press, 1975, 204p.
- Le Compte, P., (1965), "Creep in Rock Salt"; *Journal of Geology*, Vol 73, No 3, pp.469-484
- Lepper, C.M., Poland, A.P., and Mullis, C.T., (1982), "A Microseismic System for Monitoring Slope Stability"; USBM Reports on Investigations on Microseismic Research, Volume I, RI 8641.
- Lindgren, B.W., (1976), "Statistical Analysis, 3rd Edition"; Macmillan Publ. Co., 609p.
- Lockner, D., and Byerlee, J., (1977), "Acoustic Emission and Fault formation in Rocks"; Proceedings First Conference On Acoustic Emission/ Microseismic Activity in Geologic Structures and Materials, Pennsylvania State University, Trans Tech Publication, Clausthal, Germany, pp.87-98.
- Lux, K.M., Rokahr, R., (1984), "Laboratory Investigations and Theoretical Statements as a Basis for the Design of Caverns in Rock Salt Formations"; 1st Conference on the Mechanical Behavior of Salt, Penn. State University, TTP, Germany, pp.275-309.
- Malott, C., (1984), "Theoretical Limitations of Microseismic Transducer Limitations"; Proceedings Third Conference On Acoustic Emission/ Microseismic Activity in Geologic Structures and Materials, Pennsylvania State University, Trans Tech Publication, Clausthal, Germany, pp.681-694.
- Matthews, J.R., (1983), "Volume 2: Nondestructive Testing Monographs and Tracts"; Acoustic Emission, Gordon and Breach Science Publishers, Inc.

- McCabe, W.M., (1980), "Acoustic Emission in Coal: A Laboratory Study"; Proceedings Second Conference On Acoustic Emission/ Microseismic Activity in Geologic Structures and Materials, Pennsylvania State University, Trans Tech Publication, Clausthal, Germany, pp.35-54.
- McGarr, A., Bicknell, J., Sembera, E., and Green, R.W.E., (1987), "Analysis of Exceptionally Large Tremors in Two Gold Mining Districts of South Africa"; Fred Leighton Memorial Workshop on Mining Induced Seismicity, Preprints, Queen Elizabeth Hotel, Montreal, Canada, pp.25-37.
- McGarr, A., and Bicknell, J., (1988), "Estimation of the Near Fault Ground Motion of Mining Induced Tremors from Locally Recorded Seismograms in South Africa"; Second International Symposium of Rockbursts and Seismicity in Mines, preprint papers, University Radisson Hotel-Minneapolis, Minnesota, pp.379-388.
- Meister, D., (1980), "Microacoustic Studies in Salt Rock"; Proceedings Second Conference On Acoustic Emission/ Microseismic Activity in Geologic Structures and Materials, Pennsylvania State University, Trans Tech Publication, Clausthal, Germany, pp.259-274.
- Mendelson, S., (1962), "Role of surface in plastic flow of Halite single crystals"; Jour. of Appl. Phys., vol.33, no.7, pp.2182-2186.
- Michel, B., (1966), "Recherche sur les proprietes mecanique Du sel gemme aux mines domainides de potasse d'Alsace, Proc. 1st Cong. Int. Soc. Rock Mech. Lisbon, pp. 595-600
- Middlebrooks, E.J., (1978), "Statistical Calculations: How to Solve Statistical Problems"; Ann Arbor Science Publishers, Mich., 48106, 120p.
- Mogi, K., (1962), "Study of Elastic Shocks Caused by the Fracture of Heterogeneous Materials and its Relations to Earthquake Phenomena"; Bull. Earthqu. Res. Inst., 40, pp.125-173.
- Mogi, K., (1986), "Chapter 4: How small Earthquakes Occur"; McGraw Hill Co., pp.63-67.
- Mogi, K., (1962), "Study of elastic shocks caused by the fracture of heterogeneous materials and its relation to earthquake phenomena, Bull. Earthaw. Res. Inst., Tokyo University, 40, pp. 125-173
- Montoto, M., Suarez del Rio, L.M., Khair, A.W., and Hardy, H.R. Jr., (1984), "AE in Uniaxially Loaded Granitic Rocks in Relation to Their Petrographic Character"; Proceedings Third Conference On Acoustic Emission/ Microseismic Activity in Geologic Structures and Materials, Pennsylvania State University, Trans Tech Publication, Clausthal, Germany, pp.83-100.
- Mottahed, P., and Vance, J.B., (1987), "MA/AE Research at PCS Mining Operations in Saskatchewan, Canada"; Fred Leighton Memorial Workshop on Mining Induced Seismicity, Preprints, Queen Elizabeth Hotel, Montreal, Canada, pp.259-263.
- Nakamura, Y., (1977), "Detection and Analysis of Acoustic Emission Signals"; Proceedings First Conference On Acoustic Emission/ Microseismic Activity in Geologic Structures and Materials, Pennsylvania State University, Trans Tech Publication, Clausthal, Germany, pp.445-458.
- Nakasa, H., (1979), "Application of Acoustic Emission Techniques to Structural Integrity Assessment"; The Fourth Acoustic Emission Symposium, High Pressure Institute of Japan, Tokyo, pp.311-325.
- Niggli, P., (1948), "Gesteins - und Minerallagerstätten"; Verlag Birkhawser, Basel, 1, 270p.
- Niwa, Y., Kobayashi, S. and Ohtsu, M., (1984), "Source Mechanism and Wave Motions of Acoustic Emission in Rock-Like Materials"; Proceedings Third Conference On Acoustic Emission/ Microseismic Activity in Geologic Structures and Materials, Pennsylvania State University, Trans Tech Publication, Clausthal, Germany, pp.101-116.

- Nockolds, S.R., Knox, R.W., Chimmer, G.A., (1978), "Petrology for Students"; Cambridge University Press, Great Britain, 435p.
- Ode, H., (1968), "Review of mechanical properties of salt relating to salt dome genesis"; Diapirism and Diapirism ed., Branstien J., O'Brien G.D., American Association of Petroleum Geologists, pp. 53-78
- Ohira, T., Kishi, T., and Horiuchi, R., (1979), "Acoustic Emission Analysis of Fatigue Crack Propagation in 7049 Al-Zn-Mg Alloy"; The Fourth Acoustic Emission Symposium, High Pressure Institute of Japan, Tokyo, pp.241-253.
- Olsson, W.A., Peng, S.S., (1976), "Microcrack Nucleation in Marble"; International Journal of Rock Mechanics and Geomechanical Abstract, vol.13, pp.53-59.
- Olsson, W.A., (1974), "Grain size dependence of yield in marble"; J. Geophys. Res., vol. 79, no. 32, p.4859-4861
- Onhaka, M., (1983), "Acoustic Emission During Creep of Brittle Rock"; International Journal of Rock Mechanics and Geomechanical Abstracts, 20, #3, pp.121-134.
- Onodera, T.F., Asoka, and Kimura H.M., (1980), "Relation between texture and mechanical properties of crystalline rocks"; Bull. Int. Assoc. Eng. Geol., No 22, pp. 173-177
- Palmer, I.G., and Heald, P.T., (1973), "The Application of Acoustic Emission Measurements to Fracture Mechanics"; Materials Science and Engineering, 11, pp.181-184.
- Passaris, E.K.S., (1980), "The Extrinsic Anisotropy of Rocksalt when Subjected Simultaneously to Tensile and Compressive Stress Fields"; Proc. 5th International Symposium on Salt, Hambourg, Vol.1, pp.477-485.
- Peng, S., Johnson, A.M., (1972), "Crack Growths and Faulting in Cylindrical Specimens of Chelmsford Granite"; International Journal of Rock Mechanics and Geomechanical Abstract, Vol.9, pp.37-86.
- Phillips, W.R., Griffen, D.T., (1981), "Optical Mineralogy, the Nonopaque Minerals"; W.H. Freedman and Co., San Francisco, 1981, 677p.
- Physical Acoustics Corporation, User's Manual to 3000 AE Systems, (1984), Princeton, N.J.
- Pollock, A.A., (1973), "Acoustic Emission Amplitudes"; Nondestructive Testing, 6, # 5, pp.264-269.
- Pollock, A.A., (1977), "Metals and Rocks: AE Physics and Technology in Common and in Contrast"; Proceedings First Conference On Acoustic Emission/ Microseismic Activity in Geologic Structures and Materials, Pennsylvania State University, Trans Tech Publication, Clausthal, Germany, pp.383-404.
- Pollock, A.A., (1980), "Physical Interpretation of AE/MS Signal Processing"; Proceedings Second Conference On Acoustic Emission/ Microseismic Activity in Geologic Structures and Materials, Pennsylvania State University, Trans Tech Publication, Clausthal, Germany, pp.399-424.
- Prugger, A.F., and Gendzwil, D.J., (1988), "Results of Microseismic Monitoring at the Cory Mine, 1981-1984"; Second International Symposium of Rockbursts and Seismicity in Mines, preprint papers, University Radisson Hotel-Minneapolis, Minnesota, pp.317-326.
- Radon, J.C., and Pollock, A.A., (1972), "Acoustic Emissions and Energy Transfer During Crack Propagation", Engineering Fracture Mechanics, 4, pp.295-310.
- Reymond, M.C., (1980), "Acoustic Emission in Rocks and Concrete Under Laboratory Testing Conditions"; Proceedings Second Conference On Acoustic Emission/ Microseismic Activity in Geologic Structures and Materials, Pennsylvania State University, Trans Tech Publication, Clausthal, Germany, pp.27-34.

- Richardson, A.A., (1980), "Using AE techniques in laboratory Investigations of Salt Behavior"; Proceedings Second Conference on Acoustic Emission/Microseismic Activity in Geologic Structures and Materials, Pennsylvania State University, Trans Tech Publication, Clausthal, Germany, pp.63-78.
- Richter, C.F., (1958), "Elementary Seismology"; California Inst., Tech., W.H. Freeman Publishing Co., San Francisco and London.
- Roberts, D.A., (1980), "Measuring Acoustic Emission in Salt During Primary and Secondary Creep"; Proceedings Second Conference On Acoustic Emission/ Microseismic Activity in Geologic Structures and Materials, Pennsylvania State University, Trans Tech Publication, Clausthal, Germany, pp.79-85.
- Rodgerson, P., (1974), "The significance of non-metallic inclusions in line pipe tails Part III"; metallurgical analysis, British Geo. Engineering research station, confidential report, pp 1-14
- Rong, C., (1979), "Acoustic Emission of Rocks Under Triaxial Compression with Various Stress Paths"; International Journal of Rock Mechanics and Geomechanical Abstracts, 16, pp.401-405.
- Rothman, R.L., (1977), "Acoustic Emission in Rock stressed to Failure"; Proceedings First Conference On Acoustic Emission/ Microseismic Activity in Geologic Structures and Materials, Pennsylvania State University, Trans Tech Publication, Clausthal, Germany, pp.109-134.
- Sangha, C.M., Talbot, C.J., and Dhir, R.K., (1974), "Microfracturing of a Sandstone in Uniaxial Compression"; International Journal of Rock Mechanics and Geomechanical Abstracts, 11, pp.107-113.
- Sano, O., Terada, M. and Ehara, S., (1982), "A Study on the Time Dependent Microfracturing and Strength of Oshima Granite"; Tectonophysics, 84, pp.343-362.
- Sarfarazi, M., Ghosh, S.K., (1987), "Microfracture in Polycrystalline Solids"; Eng. Fracture Mechanics, Vol. 27, pp.257-267.
- Schmalz, R.F., (1969), "Deep water evaporite deposition: a genetic model"; Bull. Am. Ass. Petrol. Geol., 53, pp. 798-823
- Schmidt-Thomas, K.G., Tensi, H.M., and Zeitler, H., (1976), "Acoustic Emission Analysis as a Metallurgical Method of Investigation"; The Fourth Acoustic Emission Symposium, High Pressure Institute of Japan, Tokyo, pp.17-37.
- Scholz, C.H., (1968)a, "The Frequency Magnitude Relation of Microfracturing in Rock and Its relation to earthquakes"; Bulletin of the Seismological Society of America, 58, #1, pp.399-415.
- Scholz, C.H., (1968)b, "Microfracturing and Inelastic Deformation of Rock in Compression"; Journal of Geophysical Research, 73, #4, pp 1417-1428
- Scholz, C.H., (1968)c, "Experimental Study of the Fracturing Process in Brittle Rock"; Journal of Geophysical Research, 73, #4, pp.1447-1486
- Sedgewick, R.T., (1968), "Acoustic Emission from Single Crystals of LiF and KCl"; Journal of Applied Physics, 39, #3, pp.1728-1740.
- Semadeni, T., Niewiadomski, J., and Rochon, P., (1988), "Waveform Analysis of Mine Induced Seismic Events Recorded at Rio Algom's Quirke Mine"; Second International Symposium of Rockbursts and Seismicity in Mines, preprint papers, University Radisson Hotel-Minneapolis, Minnesota, pp.379-388.
- Semadeni, T.J., And Calder, P.N., (1988), "High Frequency Microseismic Monitoring Applied to the Determination of Stress Levels in Hard Rock Mines"; Second International Symposium of Rockbursts and Seismicity in Mines, preprint papers, University Radisson Hotel-Minneapolis, Minnesota, pp 307-316.
- Serata, S., Gloyma, E.T., (1960), "Principals of structural stability of underground salt cavities"; Jour. of Geophysical Res , vol 65, no 9, pp.2979-2987

- Serata, S., (1964), "Theory and model of underground opening and support system"; Proc. 6th US Symposium on Rock Mech. Rolla, pp. 260-292
- Serata, S., (1968), "Application of continuum mechanics to design of deep potash mines in Canada"; S.I.J.R.M., C.S., vol. 5, pp. 293-314
- Serata, S. (1978b), "Geomechanical basic design of underground salt cavities"; ASME Publication, no 78, pet 59, 43p.
- Simmons, G., Richter, D., (1976), "Microcracks in Rock in the Physics and Chemistry of Rocks and Minerals"; Edited by R.G.J. Streus, Wiley, London.
- Sondergeld, C.H., (1981), "Desirable Sample Dimensions for Detailed Acoustic Emission Studies"; Geophysical Research Letters, 8, #7, pp. 695-697.
- Sondergeld, C.H., Estey, L.H., Halleck, P.M., Dey, T.N., and Blacic, J.C., (1984), "Monitoring of Acoustic Emissions During the Uniaxial Deformation of Large Samples"; Proceedings Third Conference On Acoustic Emission/ Microseismic Activity in Geologic Structures and Materials, Pennsylvania State University, Trans Tech Publication, Clausthal, Germany, pp 147-158
- Sondergeld, C.H., Grand, L., and Estey, L.H., (1984), "Acoustic Emissions During Compression Testing of Rock"; Proceedings Third Conference On Acoustic Emission/ Microseismic Activity in Geologic Structures and Materials, Pennsylvania State University, Trans Tech Publication, Clausthal, Germany, pp.131-146.
- Sondergeld, C.H. and Estey, L.H., (1981), "Acoustic Emission Study of Microfracturing During Cyclic Loading of Westerly Granite"; Journal of Geophysical Research; 86, #B4, pp.2915-2924.
- Spencer, E W., (1977), "Introduction to the Structure of the Earth"; Mcgraw Hill book Co., 639p.
- Sprunt, E S, Brace, W.F., (1974), "Direct Observation of Microcavities in Crystalline Rocks"; International Journal of Rock Mechanics and Geomechanical Abstract, Vol 11, pp.139-150.
- Stokes, R.J., (1966), "Mechanical Properties of Polycrystalline Sodium Chloride", Proc. British Ceramics Soc., Vol 6, pp.189-207
- Suárez Del Rio, L M., and Norin, J., (1985), "Technical Note: Bending Tests and Acoustic Emission for Heated Avesta-gniess"; International Journal of Rock Mechanics and Geomechanical Abstracts, 22, #1, pp.47-50.
- Supryniewicz, V.A., (1966), "Introduction to Electronics: For Students of Biology, Chemistry and Medicine"; Addison-Welsey Publ. Co., Reading, Massachusetts, U.S.A.
- Szpunar, J.A., and Tanner, B.K., (1984), "Grain Shape and Distribution of the Grain Boundary in Polycrystalline Materials"; Journal of Materials Science, 19, pp.3249-3254.
- Tandon, K.N., and Tangri, K., (1975), "Acoustic Emission during Deformation of Polycrystalline Silicon-Iron", Materials Science and Engineering, 20, pp.47-54.
- Taponnier, P., Brace, W.F., (1976), "Development of Stress-Induced Microcracks in Westerly Granite"; International Journal of Rock Mechanics and Geomechanical Abstract, Vol.13, pp.103-112
- Trombik, M., and Zuberek, W., (1977), "Microseismic Research in Polish Coal Mines", Proceedings First Conference On Acoustic Emission/ Microseismic Activity in Geologic Structures and Materials, Pennsylvania State University, Trans Tech Publication, Clausthal, Germany, pp 169-194.
- Underwood, E E., (1970), "Quantitative Stereology"; Reading Mass, Addison Wesley Pub Co., 274p.
- Vance, J B., (1983), "Application of Microseismic Techniques in Potash Mines"; First International Conference on Potash Technology, Pergamon Press, Toronto Ontario, pp.179-184

- Vance, J.B., and Mottahed, P., (1985), "AE/MS Applications to Potash Mining Problems"; Fourth International Conference on Acoustic Emission/ Microseismic Activity in Geologic Structures and Materials, State College, Pennsylvania.
- Varo, L., and Passaris, E.K.S., (1977), "The role of water in the creep properties of halite"; Conf. on Rock Eng., New Castle upon Tync, April 1977, pp.85-100.
- Vladut, T., (1988), "Suggested Method for Microseismic Monitoring"; Master content of the first draft of SMMM; Commission on Rock Testing- Working group on Microseismic Monitoring, pp.1-15.
- Wadley, H.N.G., Scruby, C.B., and Shrimpton, G., (1981), "Quantitative Acoustic Emission Source Characterization During Low Temperature Cleavage and Intergranular Fracture"; Acta Metallurgica, 29, pp.399-414.
- Wardlaw, N.C., and Scheverdtuer, W.M., (1966), "Halite-Anhydrite Seasonal Layers in the Middle Devonian Prairie Evaporite Formation, Sask., Canada,."; Geol. Soc. Am Bull., vol.77, pp.331-342
- Wawersik, W.R., Bracc, W.F., (1971), "Post Failure of a Granite and Diabase"; Rock Mechanics 3, pp.61-85.
- Williams H., Turner, F.J., and Gilbert, C.M., (1982), "Petrography- An Introduction to the Study of Rock in Thin Section- 2nd edition"; WH Freedman and Co. , San Francisco, 626p
- Wu, F.T., and Thomson, L., (1975), "Microfracturing and Deformation of Westerly Granite Under Creep Condition"; International Journal of Rock Mechanics and Geomechanical Abstracts, 12, pp.167-173.
- Yong, C., and Wang, C., (1980), "Thermally Induced Acoustic Emission in Westerly Granite"; Geophysical Research Letters, 7, #12, pp.1089-1092.